Terrestrial Planet Finder Interferometer Science Working Group Report

Edited by:

P. R. Lawson, O. P. Lay, K. J. Johnston, and C. A. Beichman

Jet Propulsion Laboratory
California Institute of Technology
Pasadena, California

1 March 2007

Abstract

Over the past two years, the focus of the project for the interferometric version of the Terrestrial Planet Finder (TPF-I) has been on the development of the scientific rational for the mission, the assessment of TPF-I architectures, the laboratory demonstration of key technologies, and the development of a detailed technology roadmap. The Science Working Group (SWG), in conjunction with European colleagues working on the European Space Agency's (ESA's) Darwin project, has reaffirmed the goals of TPF-I as part of a broad vision for the detection and characterization of Earth-like planets orbiting nearby stars and for the search for life on those planets. The SWG also helped to assess the performance of different interferometric configurations for TPF-I/Darwin. Building on earlier SWG reports, this document restates the scientific case for TPF-I, assesses suitable target stars and relevant wavelengths for observation, discusses dramatic new capabilities for general astrophysical observations, and summarizes how Spitzer has improved our knowledge of the incidence of zodiacal emission on the search for planets. This document discusses in some detail on laboratory advances in interferometric nulling and formation flying. Laboratory experiments have now achieved stable narrow- and broad-band nulling the levels of 10^{-6} and 2.0×10^{-5}, respectively. A testbed has demonstrated formation flying using two realistic spacecraft mockups. With a suitably funded program of technology development, as summarized herein and described in more detail in the *Technology Plan for the Terrestrial Planet Finder Interferometer* (2005), the National Aeronautics and Space Administration (NASA) and ESA would be able to start within the coming decade a full-scale TPF-I/Darwin mission capable of finding Earths orbiting more than 150 nearby stars, or a scaled back interferometer capable of studying more than 30 stars. Finding evidence for life on just one of those planets would revolutionize our understanding of our place in the cosmos.

Approvals
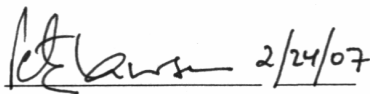
Prepared by: _[signature] 2/24/07_

Peter R. Lawson   date
TPF-I Systems Manager,
Terrestrial Planet Finder

Approved by:
NASA/JPL _[signature] 2/28/07_

Daniel R. Coulter   date
Project Manager,
Terrestrial Planet Finder

Approved by:
TPF-I SWG _[signature] 4/20/07_

Kenneth Johnston   date
TPF-I SWG Co-Chair,
US Naval Observatory

Approved by:
NASA/JPL _[signature] 24 Feb.2007_

Wesley A. Traub   date
Program Scientist,
Navigator Program

Approved by:
TPF-I SWG _[signature] 2/23/07_

Charles Beichman   date
TPF-I SWG Co-Chair,
California Institute of Technology

Approved by:
NASA/JPL _[signature] 2/26/07_
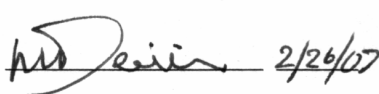
Michael Devirian   date
Manager,
Navigator Program

Acknowledgements

Twenty-two representatives from the astronomical community and one ex officio member were named to the TPF-Interferometer Science Working Group (TPF-I SWG). They work closely with the TPF project to develop the science rationale for the mid-IR observing program, to help guide the appropriate technology, and to interface with their counterparts on the European Space Agency's Terrestrial Exoplanet Science Advisory Team and Darwin project. As representatives of the broad astronomical community, the TPF-I SWG acts as the science conscience of the project, ensuring that the broad TPF-I science goals are worthy of the mission and that the mission will be able to fulfill them. Specific tasks of the TPF-I SWG includes, but are not limited to:

1. Refining, as necessary, TPF-I science goals as embodied in the Design Reference Mission and assessing the impact of altering mission design parameters (orbit, mission duration, telescope size, instrument complement, etc.) on these science goals.

2. Assessing design concepts, technology, and implementation plans relative to the overall scientific performance of the mission.

3. Assisting NASA in explaining the goals of TPF-I to the larger astronomy community and in preparing materials for review by external scientific advisory groups and oversight committees.

4. Producing a Science Requirements Document. This document will include the prioritized science objectives and requirements for the planet finding and characterization and general astrophysics aspects of the TPF-I mission.

The duration of the appointments of each TPF-I SWG member is approximately 3 years.

Table 1. Members of the TPF-I Science Working Group (2005–2008)

Name	Institution
Akeson, Rachel	Michelson Science Center, California Institute of Technology (CalTech)
Bally, John	University of Colorado
Beichman, Charles (ex officio)	Michelson Science Center, CalTech
Crisp, David	Jet Propulsion Laboratory
Danchi, William	Goddard Space Flight Center (GSFC)
Falkowski, Paul	Rutgers University
Fridlund, Malcolm	ESA/ESTEC
Hinz, Phil	University of Arizona
Hollis, Jan M. (Mike)	GSFC
Hyland, David	Texas A&M University
Johnston, Kenneth (chair)	US Naval Observatory
Lane, Ben	Massachusetts Institute of Technology (MIT)
Laughlin, Gregory	UC Santa Cruz
Liseau, Rene	Stockholm Observatory, Sweden
Mennesson, Bertrand	Jet Propulsion Laboratory
Monnier, John	University of Michigan
Noecker, Charley	Ball Aerospace
Quillen, Alice	University of Rochester
Röttgering, Huub	Leiden University, Netherlands
Serabyn, Gene	Jet Propulsion Laboratory
Wilner, David	Harvard-Smithsonian Center for Astrophysics
Woolf, Nick	University of Arizona

Table of Contents

3   Transforming Astrophysics with TPF-I

4   Design and Architecture Trade Studies

1   Introduction

Over 200 planets with masses ranging from the deuterium-burning limit of 13 Jupiter masses (M_{Jup}) down to 5.5 Earth masses ($M_\oplus$) have been detected through changes in the radial velocity or position of host stars, or through changes in the brightness of host stars due to transits or microlensing. These planets are found in orbits ranging from inside 0.05 astronomical units (AU) out to 5 AU with a wide range of orbital eccentricities. The physical characterization of a few of these planets has already begun with the detection at infrared wavelengths by the Spitzer Space Telescope of the secondary transits of three "Hot Jupiters" and the monitoring of the light curve of the "Hot Jupiter" companion of υ Andromedae (Figure 1-1). These results constrain the temperature, radius, and albedo of the planets and enable the study of the rotation and weather on distant planets.

But much more is possible beyond these initial measurements. The interferometric version of the Terrestrial Planet Finder (TPF-I) described in this report (Figure 1-2) will extend this measurement capability by many orders of magnitude, enabling the study of terrestrial planets in the Habitable Zone (1 AU from a G2V star) as well as to gas or icy giant planets out to 5 AU. TPF-I is currently envisioned
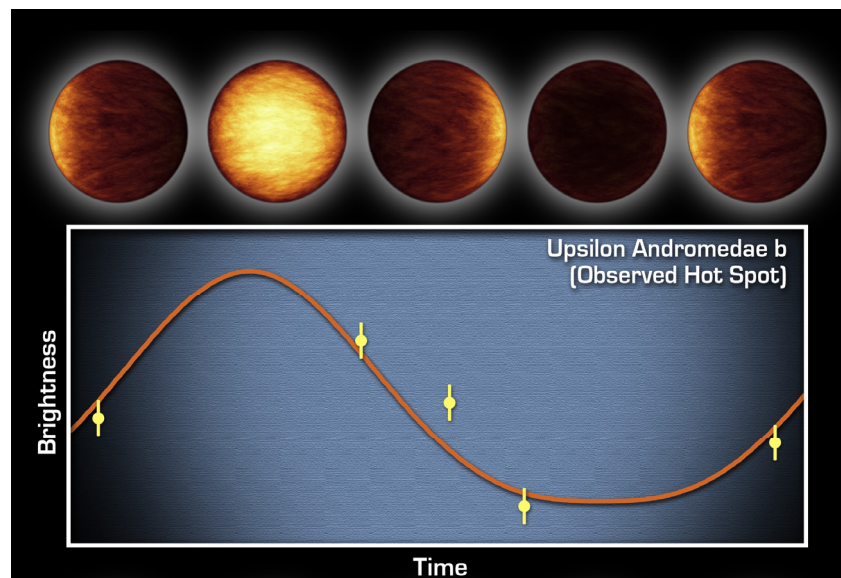
Figure 1-1. The Spitzer telescope has detected thermal emission throughout the entire 4-day period of the ''Hot Jupiter'' companion to the star Upsilon And (Harrington et al. 2006). The solid curve shows a model of a tidally locked planet with a sub-solar point that is considerably hotter than the backside due to relatively poor global circulation of winds. The TPF interferometer will extend these observations to Earth-sized planets in the habitable zone of nearby stars.

1
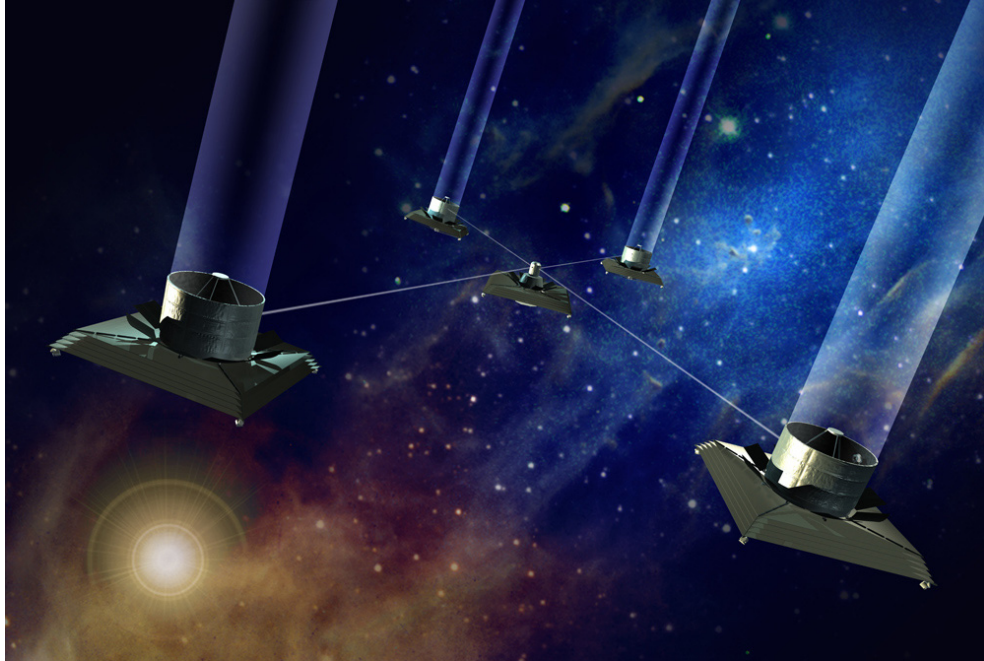
Figure 1-2. Artist's Impression of the Terrestrial Planet Finder Interferometer

as a cryogenic nulling interferometer consisting of four 3.5-m telescopes deployed on separate spacecraft with baselines in excess of 100 m (Figure 1-2). With TPF-I astronomers will be capable of characterizing planets and their atmospheres with the goal of identifying habitable or life-bearing planets around more that 150 nearby stars.

Ultimately, the detection and characterization of Earth-like planets and the search for life will require coordinated observations at optical and infrared wavelengths as well as dynamical measurements to determine planetary mass. Table 1-1 summarizes the measurements enabled by different planet-finding missions and how the mid-infrared observations of the interferometric version of the Terrestrial Planet Finder (TPF-I) fit into a broad vision of exo-planetology. Accomplishing the complete characterization of nearby planets is the unifying goal of TPF-I (which is being studied jointly with the TPF-I project by NASA and the Darwin project by the European Space Agency) and its sibling missions, the visible light coronagraph TPF-C and the astrometric mission Space Interferometry Mission (SIM)/Planetquest.

1.1 Purpose and Scope

This document is a collaborative effort between the TPF-I Science Working Group (SWG) and the TPF-I Project. Although the charter of the SWG was to advise NASA on science requirements and priorities, their advice also greatly influenced technical research within the project — in particular the project's ongoing reassessment of the interferometer architecture and the flow-down of science requirements to technical objectives. The science requirements and objectives are described by the SWG in the opening Chapters on *Exoplanet Science* (Chapter 2) and *Transforming Astrophysics with TPF-I* (Chapter 3). This work builds on earlier SWG reports (ExNPS 1996; Beichman et al. 1999; Beichman et al. 2002; Lawson

et al. 2004), and restates the scientific case for TPF-I, assesses suitable target stars and relevant wavelengths for observation, and summarizes recent results on the zodiacal emission that can impact detection of planets. The compelling general astrophysics that will be possible with TPF-I is described in Chapter 3; the balance between increased astrophysics capability and increased cost will be addressed at a later phase in the project. Through the stated science requirements and technical interchange meetings, the SWG was also influential in determining the architecture of the interferometer, described in detail in Chapter 4. The results of an extensive investigation of different architectures and the sources of systematic noise sources are presented and discussed. Chapter 4 also describes the baseline X-array architecture selected for detailed study as well as describing briefly a structurally connected option with limited capability.

The two subsequent chapters of this document consist primarily of contributions by TPF-I project members and provide a current view of progress with interferometer design studies (Chapter 5) and laboratory demonstrations of nulling interferometry and formation flying (Chapter 6). Included here are sections summarizing progress in critical testbed activities undertaken by the TPF-I project and reported on at various TPF-I Science Working Group meetings. Laboratory nulling has reached a broad-band level approaching 10^{-5} that is arguably within a factor of 2 needed for the TPF-I flight system. Chapter 6 also presents a summary of a technology roadmap developed by the TPF-I project

The concluding chapters resume with recommendations by the SWG for future studies. Chapter 7 includes a prioritized list of future scientific investigations, and Chapter 8 discusses the potential for international collaboration on TPF-I/Darwin in the context of concluding remarks.

Table 1-1. Synergy of Missions in the Navigator Program

Parameter	SIM	TPF-C	TPF-I
Orbital Parameters			
Stable orbit in habitable zone	*Measurement*	*Measurement*	*Measurement*
Characteristics for Habitability			
Planet temperature	Estimate	Estimate	*Measurement*
Temperature variability due to eccentricity	*Measurement*	*Measurement*	*Measurement*
Planet radius	Cooperative	Cooperative	*Measurement*
Planet albedo	Cooperative	Cooperative	Cooperative
Planet mass	*Measurement*	Estimate	Estimate
Surface gravity	Cooperative	Cooperative	Cooperative
Atmospheric and surface composition	Cooperative	*Measurement*	*Measurement*
Time-variability of composition		*Measurement*	*Measurement*
Presence of water		*Measurement*	*Measurement*
Solar System Characteristics			
Influence of other planets, orbit co-planarity	*Measurement*	Estimate	Estimate
Comets, asteroids, and zodiacal dust		*Measurement*	*Measurement*
Indicators of Life			
Atmospheric biomarkers		*Measurement*	*Measurement*
Surface biosignatures, e.g. red edge of vegetation		*Measurement*	

``*Measurement*'' indicates a directly measured quantity from a mission; ``Estimate'' indicates that a quantity that can be estimated from a single mission; and ``Cooperative'' indicates a quantity that is best determined cooperatively using data from several missions. (Beichman et al. 2006)

1.2 Science Objectives

The major scientific objectives of TPF-I are: (1) search for and detect any Earth-like planets in the habitable zone around nearby stars; (2) carry out a study of gas giants and icy planets, as well as terrestrial planets within the 5 AU of nearby stars (at a nominal distance of 10 parsecs (pc) from the Sun) within the field-of-view of a 10-μm interferometer; (3) characterize Earth-like planets and their atmospheres, assess habitability, and search for signatures of life; (4) carry out a program of comparative planetology; and (5) enable a program of "revolutionary" general astrophysics. A mission lifetime of 5 years, possibly extended to 10 years, is foreseen.

The core scientific goal of TPF-I is to detect directly and characterize Earth-like planets around nearby stars. The requirements that flow down from this goal define the characteristics of the observatory design and the mission. In particular, the ability to directly detect planets implies that TPF-I must be capable of separating the planet light from the starlight. Moreover, the facility must provide a sensitivity that will enable spectroscopic measurements of the light from the planet to determine the type of planet, its gross physical properties, and its main atmospheric constituents — the ultimate goal of course is to assess whether life or habitable conditions exist there. TPF-I will be designed so that, with a high degree of confidence, it will be capable of detecting Earth-like planets should they exist in the habitable zones of the stars in its survey.

1.3 Development of the Interferometer Architecture

The overall designs for planet-finding interferometers have changed substantially since Bracewell first proposed adding a π phase shift within an astronomical interferometer to create the first nulling interferometer (Woolf and Angel 1998). This Bracewell nuller has a symmetric response on the sky, making it difficult to separate the contribution of a planet from the emission from zodiacal dust orbiting the target star (the exozodiacal emission). It is also vulnerable to small drifts in the stray light level or in the gain of the system that can mimic the planet signal. The solution was the Linear Dual Chopped Bracewell design, comprising two single Bracewell nullers that are cross-combined with a relative phase of $\pm\pi/2$. By taking the difference in photon outputs of these two phase chop states, the resulting response is anti-symmetric, and is insensitive to the both the symmetric exozodiacal emission and instrumental drifts.

In parallel with the introduction of phase chopping, there was development of higher-order nulling configurations. The motivation here is to reduce the impact of stellar leakage on the null depth. Although light from the center of the star can be nulled completely, light from the edges will leak through to some extent. The Bracewell designs have a null that degrades away from the optical axis as θ^2, leading to relatively high stellar leakage. The Angel Cross combines the light from four collectors to give a null that degrades as θ^4, reducing the stellar leakage to a negligible level (Angel and Woolf 1997; Beichman, Woolf, and Lindensmith 1999). Variations on this design include the Degenerate Angel Cross (DAC) and Generalized Angel Cross (GAC). These basic nulling elements are cross-combined using phase chopping to generate configurations such as the Chopped Degenerate Angel Cross (a linear design based on DACs) and the six-collector Bow-Tie design that was favored by ESA for a while (Fridlund et al. 2006, and references therein).
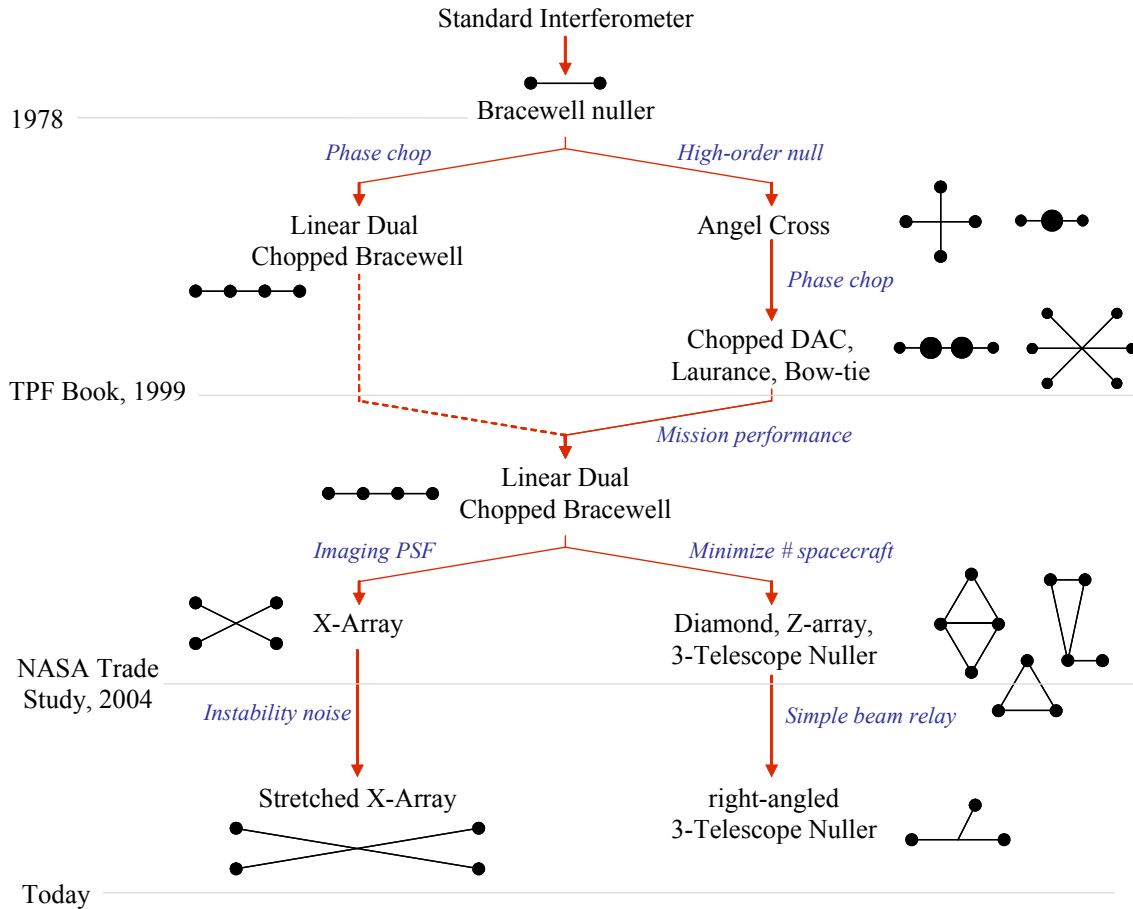
Figure 1-3. Schematic showing the evolution of the preferred nulling architecture for a TPF-I/Darwin mission.

These chopped high-order null configurations were thought to be superior in performance to the Linear Dual Chopped Bracewell configuration, but this proved not to be the case. Simulations to predict the number of stars that could be surveyed for planets showed that the Linear DCB could survey approximately twice the number of stars compared to a Bow-Tie with the same total collecting area. The reason is that the Linear DCB is much more efficient at converting planet photons into modulated output signal – it has a higher 'modulation efficiency'. This is offset by the higher stellar leakage, but this only has a significant impact on the bright nearby stars that occupy only a small fraction of the total integration time available.

The architecture evolution from this point has followed two parallel tracks. At ESA, the emphasis was on minimizing the number of spacecraft used. The Diamond and Z-Array are both DCB configurations in which the one spacecraft serves the function of both collector and combiner. In both cases the beams make multiple hops from collector to combiner to balance the path lengths. Another development was the three-telescope nuller. This is a departure from the DCB, in which the collectors are combined with phases of 0, $\pm 2\pi/3$, and $\pm 4\pi/3$. With three spacecraft, the equilateral triangle is the minimal configuration that still supports phase chopping, but the symmetry leads to undesirable imaging properties. It too uses multiple hops to relay the beams from collector to combiner. The design currently favored is the right-

angled Three Telescope Nuller with a dedicated beam combiner spacecraft to alleviate the complexity of the beam relay, and sufficient asymmetry to improve the imaging properties.

The focus at NASA was on improving the imaging properties of the array, which is important for separating the contributions from multiple planets, determining the orbit, and discriminating against lumps in the exozodiacal emission. This led to a rearrangement of the collectors in the Linear DCB to produce the X-Array – a configuration in which the nulling baselines lie along the short side of the rectangle and the imaging baselines (which determine the angular resolution) along the long dimension. The beams are relayed in a single hop from each collector to a central combiner. The decoupling of the nulling and imaging baselines makes the X-Array more flexible than other configurations. This flexibility was subsequently exploited to eliminate 'instability noise' with the 'Stretched X-Array' design. Instability noise—an analog of speckle noise in the coronagraph—arises from fluctuations in the path lengths, pointing, dispersion, etc. of the instrument, and drives the requirement on the null depth down to 10^{-6}. The long imaging baselines of the Stretched X-Array give the planet signals a unique spectral signature that can be effectively separated from the instability noise, and they also greatly improve the angular resolution of the instrument.

The configurations above are defined by the relative location of the collectors. Until recently, the combiner spacecraft was always located in the same plane as the collectors, normal to the direction to the target star. ESA then proposed the 'Emma' architecture, in which the combiner is moved out towards the star by about 1 km, and the collectors are reduced to a single spherical mirror. Most of the nulling configurations already described can be implemented in either the classic planar format or the out-of-plane Emma format. The Emma design offers significant advantages which are presently being studied independently by ESA and NASA. Preliminary results of these studies were first reported very recently, only in the later half of 2006, and are therefore not within the scope of this document. The appeal of the Emma design is primarily in its simplification of the telescope optics, eliminating the need for any deployables, and also in the design of the sunshields, which become folded into a hard shell—thereby reducing the risk of catastrophic failure. However, the simplification of the telescope optics increases the complexity of the beam combiner, and it currently is not known to what extent this will reduce the overall cost and risk of the mission. What is clear is that there exists obvious agreement in design principles between researchers at NASA and ESA, and the architectures for both TPF-I and Darwin appear to be converging in 2007.

1.4 References

Angel, R., and Woolf, N., "An imaging interferometer to study extrasolar planets," *Astrophys. J.* 475, 373–379 (1997).

Beichman, C. A., Fridlund, M., Traub, W. A., Stapelfeldt, K. R., Quirrenbach, A., and Seager, S., *Protostars and Planets V*, edited by Reipurth, B., Jewitt, D., and Keil, K., University of Arizona Press, Tucson, AZ, pp. 915 (2007).

Beichman, C. A., Woolf, N. J., and Lindensmith, C. A., *TPF: A NASA Origins Program to Search for Habitable Planets*, JPL Publication 99-3, Jet Propulsion Laboratory, Pasadena, CA (1999). http://planetquest.jpl.nasa.gov/TPF/tpf_book/index.cfm

Beichman, C. A., Coulter, D. R., Lindensmith, C. A., and Lawson, P. R., editors, *Summary Report on Architecture Studies for the Terrestrial Planet Finder,* JPL Publication 02-011, Jet Propulsion Laboratory, Pasadena, CA (2002). http://planetquest.jpl.nasa.gov/TPF/arc_index.cfm

Fridlund, C. V. M., d'Arcio, L., den Hartog, R., Karlsson, A. 2006, "Status and recent progress of the Darwin mission in the Cosmic Vision program," *Advances in Stellar Interferometry*, edited by Monnier, J. D, Schöller, M., Danchi, W. C., *Proc. SPIE* **6268**, 62680Q (2006).

Harrington, J., Hansen, B. M., Luszcz, S. H., Seager, S., Deming, D., Menou, K., Cho, J. Y.-K., and Richardson, L .J., "Phase dependent infrared brightness of the extrasolar planet υ Andromedae b," *Science* **314**, 623–626 (2006).

Kuchner, M. J., *General Astrophysics and Comparative Planetology with the Terrestrial Planet Finder Missions*, JPL Publication 05-01, Jet Propulsion Laboratory, Pasadena, CA (2005). http://planetquest.jpl.nasa.gov/documents/GenAst28b.pdf

Lawson, P. R., Unwin, S. C., and Beichman, C. A., editors, *Precursor Science for the Terrestrial Planet Finder*, JPL Publication 04-014, Jet Propulsion Laboratory, Pasadena, CA (2004) http://planetquest.jpl.nasa.gov/documents/RdMp273.pdf

Traub, W. A.; Ridgway, S. T., Beichman, C. A., Johnston, K. J., Kasting, J., Shao, M. *IAU Colloquium #200*, edited by Aime, C. and Vakili, F.: Cambridge University Press, Cambridge, UK, 399 pp. (2006).

Woolf, N. J., and Angel, J. R. P., "Astronomical searches for Earth-like planets and signs of life," *Ann. Rev. Astron. Astrophys*. **36**, 507–538 (1998).

A Road Map for the Exploration of Neighboring Planetary Systems (ExNPS) JPL Publication 96-22, Jet Propulsion Laboratory, Pasadena, CA (1996). http://origins.jpl.nasa.gov/library/exnps/index.html

2 Exoplanet Science

2.1 Science Requirements

2.1.1 Planetary Detection and Characterization

The objectives of the Terrestrial Planet Finder missions are to detect directly and characterize Earth-like planets around nearby stars. As illustrated in Fig. 2-1, TPF-C, a visible-light coronagraph, and TPF-I, a mid-infrared formation-flying interferometer, must first separate planet light from starlight. The requirement to characterize implies that the missions must determine the type of a planet and characterize its gross physical properties and its main atmospheric constituents, thereby allowing an assessment of the likelihood that life or habitable conditions exist there.

The combination of these two missions will provide a definitive characterization of planets. Measurements across such a broad wavelength range will yield not only physical properties (such as size and albedo), but they will also serve as the foundation of a reliable and robust assessment of habitability and the presence of life. The measurement requirements of the TPF-I mission for the detection and characterization of the constituents of extrasolar planetary systems (including terrestrial planets, gas giants, and zodiacal dust) are given in Table 2-1.

Types of Stars

On astrophysical grounds, Earth-like planets are likely to be found around stars that are roughly similar to the Sun (Turnbull 2004). Therefore, TPF target stars will include main sequence F, G, and K stars. However, M stars may also harbor habitable planets, and the nearest of these could be investigated using the high angular resolution of the interferometer.

Terrestrial Planets

Considering the radii and albedos or effective temperatures of Solar System planets, TPF-I must be able to detect terrestrial planets, down to a minimum terrestrial planet defined as having 1/2 Earth surface area and Earth albedo. In the infrared, the minimum detectable planet would be one with an infrared emission corresponding to the surface area and optical albedo, positioned in the orbital phase space stipulated below.

- *Habitable Zone*: The TPF missions should search the most likely range as well as the complete range of temperatures within which life may be possible on a terrestrial-type planet. In the Solar System, the most likely zone is near the present Earth, and the full zone is the range between Venus and Mars. The habitable zone (HZ) is here defined as the range of semi-major axes from

0.7 to 1.5 AU scaled by the square root of stellar luminosity. The minimum terrestrial planet must be detectable at the outer edge of the HZ.

- *Orbital Phase Space*: The distribution of orbital elements of terrestrial type planets is presently unknown, but observations suggest that giant-planet orbits are distributed roughly equally in semi-major axis, and in eccentricity up to those of the Solar System planets and larger. Therefore, TPF-I must be designed to search for planets drawn from uniform probability distributions in semi-major axis over the range 0.7 to 1.5 AU and in eccentricity over the range 0 to 0.35, with the orbit pole uniformly distributed over the celestial sphere with random orbit phase.

Giant Planets

The occurrence and properties of giant planets may determine the environments of terrestrial planets. The TPF-I field of view and sensitivity must be sufficient to detect a giant planet with the radius and geometric albedo or effective temperature of Jupiter at 5 AU (scaled by the square root of stellar luminosity) around at least 50% of its target stars. A signal-to-noise ratio of at least 5 is required.

Exozodiacal Dust

Emission from exozodiacal dust is both a source of noise and a legitimate target of scientific interest. TPF-I must be able to detect planets in the presence of zodiacal clouds at levels up to a maximum of 10 times the brightness of the zodiacal cloud in the Solar System. Although the average amount of exo-zodiacal emission in the "habitable zone" is not yet known (see Section 2.6), we adopt an expected level of zodiacal emission around target stars of 3 times the level in our own Solar System with the same fractional clumpiness as our Solar System's cloud. From a science standpoint, determining and understanding the properties of the zodiacal cloud is essential to understanding the formation, evolution, and habitability of planetary systems. Thus, TPF-I should be able to determine the spatial and spectral distribution of zodiacal clouds with at least 0.1 times the brightness of the Solar System's zodiacal cloud.

Spectral Range

The required spectral range of the TPF-I mission for characterization of extrasolar planets will emphasize the characterization of Earth-like planets and is therefore set to 6.5 to 18 μm in the infrared. The minimum range is 6.5 to 15 µm.

Spectrum

The TPF-I mission will use the spectrum of a planet to characterize its surface and atmosphere. The spectrum of the present Earth, scaled for semi-major axis and star luminosity, is used as a reference and suggests a minimum spectral resolution is 25 with a goal of 50. TPF-I must measure water (H_2O) and ozone (O_3) with 20% accuracy in the equivalent width of the spectral feature. Additionally it is highly desirable that TPF-I also be able to measure carbon dioxide CO_2) as well as methane (CH_4) (if the latter is present in high quantities predicted in some models of pre-biotic, or anoxic planets, e.g. Kasting et al. 2003).

Table 2-1. TPF-I Science Requirements

Parameter	TPF-I Requirement
Star Types	F, G, K, selected, nearby M, and others
Habitable Zone	0.7–1.5 AU scaled as $L^{1/2}$
Number of Stars to Search	150
Completeness for Each Core Star	90%
Minimum Number of Visits per Target	3
Minimum Planet Size	0.5–1.0 Earth Area
Geometric Albedo	Earth's
Spectral Range and Resolution	6.5–18 μm; R = 25 [50]
Characterization Completeness	Spectra of 50% of Detected or 10 Planets Maximum
Giant Planets	Jupiter Flux, 5 AU, 50% of Stars
Maximum Tolerable Exozodiacal Emission	10 times Solar System Zodiacal Cloud

Number of Stars to be Searched

To satisfy its scientific goals, TPF-I should detect and characterize a statistically significant sample of terrestrial planets orbiting F, G, and K stars. Although at this time, the fractional occurrence of terrestrial exoplanets in the Habitable Zone is not known, a sample of 150 stars within 30 pc (including a small number of nearby M stars) should suffice based on our present understanding.

Extended Number of Stars

It is desired to search as many stars as possible, beyond the required core sample. We anticipate that any mission capable of satisfying these objectives will also be capable of searching many more stars if the overall requirements on completeness are relaxed. It is desired that TPF-I be capable of searching an *extended group of stars* defined as those systems *of any type* in which all or part of the continuously habitable zone (see below) can be searched.

Search Completeness

Search completeness is defined as that fraction of planets in the orbital phase space that could be found within instrumental and mission constraints. We require each of the 150 stars to be searched at the 90% completeness level. For other targets in addition to the 150 stars, the available habitable zone will be searched as to limits in planet's orbital characteristics.

Characterization completeness

While it will be difficult to obtain spectra of the fainter or less well positioned planets, we require that TPF-I be capable of measuring spectra of at least 10 (~50%) of the detected planets.

Table 2-2. Illustrative Properties of a TPF-I Observatory Concept*

Parameter	4-Telescope Dual Chopped Bracewell Design
Telescopes	Four 4-m diameter telescopes, diffraction limited at 2 μm operating at 40 K
Array size	60–150 m center-to-center of outer telescope in linear array
Baseline range	40–100 m
Wavelength range	6.5–15 μm, with the goal of 6.5–18 μm
Angular resolution (maximum)	50–75 milli-arcseconds
Field-of-view	1 arcsec at 12 μm
Spectral resolution $\Delta\lambda/\lambda$	25 with a goal of 50
Sensitivity	0.35 μJ at 12 μm
Number of stars	150
Biomarkers	H_2O and O_3 with a goal of also measuring CO_2 and CH_4
Field of regard	±45° of anti-Sun direction
Orbit	L2 Halo orbit
Mission duration	5 years baseline with a goal of 10 years
Mission launch	2019 with Heavy-class launch vehicle, Delta 4050H

*Further details are available in Appendix B

Visitations

Multiple visits per star will be required to achieve required completeness, to distinguish it from background objects, to determine its orbit, and to study a planet along its orbit. TPF-I must be capable of making at least 3 visits to each star to meet the completeness and other requirements.

Multiple Planets

After the completion of the required number of visitations defined above, TPF-I should be able to characterize a planetary system as complex as our own with three terrestrial-sized planets assuming each planet is individually bright enough to be detected.

Orbit Determination

After the completion of the required number of visitations defined above, TPF-I shall be able to localize the position of a planet orbiting in the habitable zone with an accuracy of 10% of the semi-major axis of the planet's orbit. This accuracy may degrade to 25% in the presence of multiple planets.
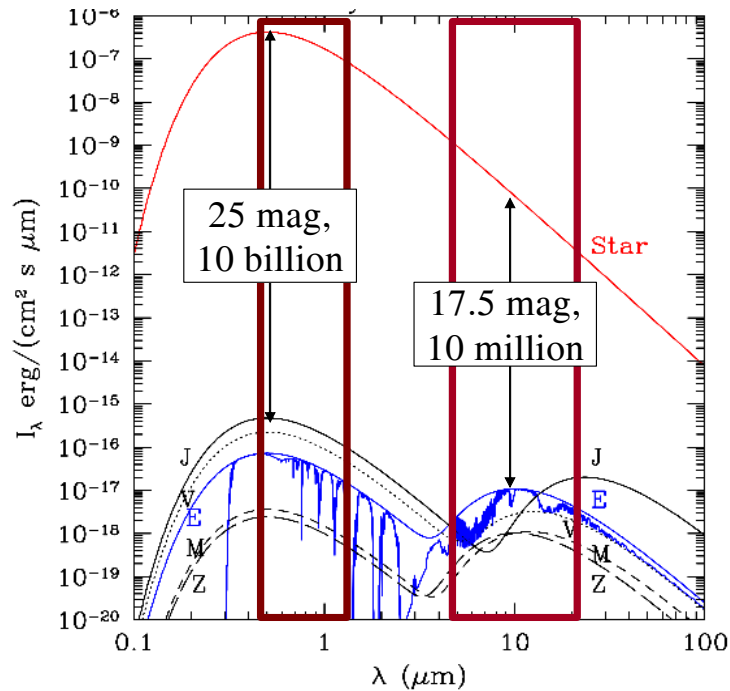
Figure 2-1. The Solar System seen from 10 pc illustrates the challenge of TPF-C and TPF-I, where the Earth-Sun contrast is 10^7 in the mid-infrared and 10^{10} in the visible. (Traub and Jucks 2002)

2.1.2 Observing Modes

Imaging

The interferometer will be capable of imaging in the nulling mode and in the classical mode of constructive interference. This is to meet major science goals in the areas of:

- Star and planet formation and early evolution.

- Stellar and planetary death and cosmic recycling.

- The formation, evolution, and growth of black holes.

- Galaxy formation and evolution over cosmic time.

Nulling

- Sensitivity: A point source of 1 µJy should be detectable with a signal divided by noise (S/N) of 5 in one hour's integration time

- Baseline Lengths: Maximum 200 meters

13

Classical interferometry

- Same as above

- Operate over the wavelength range of 3–15 µm

- A synthesized field of view (FOV) of 100–1000 resolution elements in two orthogonal coordinates

- A dynamic range of 100:1

- 1000 spectral elements

2.1.3 Mission Summary

Performance Requirement

As a minimum, TPF-I must be able to detect planets with half the area of the Earth, and the Earth's geometric albedo, searching the entire HZ of the core-group stars with 90% completeness per star. Flux ratios must be measured in three broad wavelength bands, to 10% accuracy, for at least 50% of the detected terrestrial planets. The spectrum must be measured for at least 50% of the detected terrestrial planets—to give the equivalent widths of H_2O, and O_3 to an accuracy of 20%.

Performance Goal

As a goal, TPF-I must be able to detect planets with half the area of the Earth, with Earth's geometric albedo, searching the entire HZ of the 150 stars with 90% completeness. The flux ratio must be measured in three broad wavelength bands to 10% accuracy for at least 50% of the detected terrestrial planets. The spectrum must be measured—for at least 50% of the detected terrestrial planets—to give the equivalent widths of H_2O, and O_3 in the infrared to an accuracy of 20%. Further, we desire that the mission search an *extended group of stars* defined as those systems *of any type* in which all or part of the HZ can be searched.

2.2 Wavelength Coverage

As shown in Figure 2-1, the Earth's brightness peaks at 10 µm. As discussed below, we specify the wavelength coverage for TPF-I as being between 6.5 and 15 µm to detect CH_4, O_3, and H_2O with a goal of 6.5–18 µm to include CO_2.
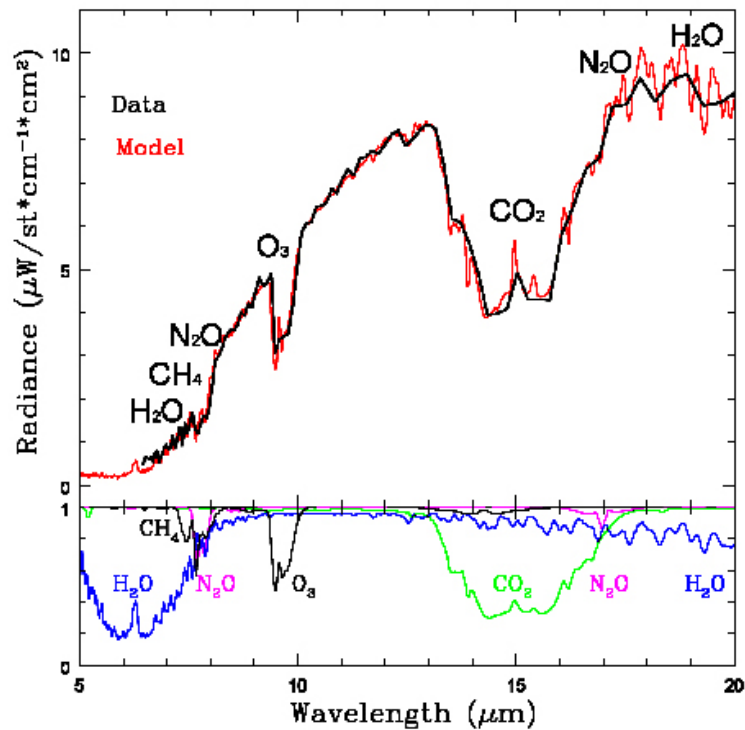
Figure 2-2. Model and disk-integrated spectrum in the mid-infrared. (Data by Christenson *et al.* 1997, reproduced from Kaltenegger *et al.* 2006).

2.3 Physical Characterization

The search for signs of life implies that one needs to gather as much information as possible in order to understand how the observed atmosphere physically and chemically works. Knowledge of the temperature and planetary radius is crucial for the general understanding of the physical and chemical processes occurring on the planet (e.g., tectonics, hydrogen loss to space). In theory, spectroscopy can provide some detailed information on the thermal profile of a planetary atmosphere. This however requires a spectral resolution and a sensitivity that are well beyond the performance of a first generation mission such as Darwin or TPF-I. Therefore, the following discussion will be limited to data that could be obtained with relatively low spectral resolution.

2.3.1 Temperature, Radius, and Albedo

One can calculate the stellar energy of the star F_{star} that is received at the measured orbital distance. This only gives very little information on the temperature of the planet which depends on its albedo. The surface temperature is likely to be enhanced by greenhouse gases. However, with a low-resolution spectrum of the thermal emission, plus a measure of the emitted flux, the effective temperature and the radius of the planet can be obtained by fitting the envelope of the thermal emission by a Planck function. The ability to assign an effective temperature to the spectrum relies on the existence and identification of spectral windows probing to the surface or to a common atmospheric level. Such identification is not

trivial in the absence of any other information on the observed planet. For an Earth-like planet there are some atmospheric windows that can be used in most of the cases, especially between 8 and 11 μm. This window would, however, become opaque at high H_2O partial pressure (e.g., the inner part of the HZ where a lot of water is vaporized) and at high CO_2 pressure (e.g., a very young Earth or the outer part of the HZ).

Let us look at the case of the three known terrestrial planets, Venus, Earth and Mars. For Mars, the temperature deduced from the shape of the infrared spectrum is a good approximation to the surface temperature, except in the CO_2 band. On Earth, the infrared spectrum is a mixture of surface and cloud emission, the latter occurring at lower temperature. The temperature given by the envelope of the spectrum is thus slightly lower, by about 10 K on average, than the average surface temperature. In the extreme case of Venus, the spectrum envelope gives a temperature of 277 K, much lower than the 740 K of the surface. The reason for this discrepancy comes from the fact that the atmosphere of Venus is completely opaque below 60 km because of the permanent cloud cover and the absorption continuum, induced at high pressure by CO_2–CO_2 collisions.

With low-resolution spectral observations, it is difficult to determine if the lower atmosphere contributes to the spectrum and therefore, if the temperature reflects the surface conditions. The accuracy of the radius and temperature determination will depend on the quality of the fit (and thus on the sensitivity and resolution of the spectrum), the precision of the Sun–star distance, and also the distribution of brightness temperatures over the planetary surface.

Finally, if the effective temperature is measured in the infrared, then the visible albedo can be inferred, using $F_{star}(1 - A) = 4\sigma T_{eff}^4$.

2.3.2 Orbital Flux Variation

The variation or constancy of infrared flux with orbital position (i.e., with phase angle) provides us some information about the surface of the planet. One approach is to note that the orbital flux variation in the infrared can distinguish planets with and without an atmosphere (Selsis et al. 2003, Gaidos and Williams 2004). A strong variation of the thermal flux with phase angle can be consistent with the absence of an atmosphere, because here we are looking at a rocky surface with low thermal inertia; and therefore, a strong day–night temperature variation. Examples are Mercury and the Moon. In such a case one has to readjust the inferred radius estimate of the planet by taking the viewing geometry of the system into account.

The opposite case, when the apparent effective temperature is constant along the orbit, implies a large thermal inertia from, for example an ocean, and/or a rapid circulation of incident energy through large scale atmospheric motions.

Therefore, habitable planets are potentially distinguishable from airless or Mars-like planets by the amplitude of the observed variations of effective temperature, however since Venus and Earth are roughly similar in this way, additional spectroscopy is needed to separate such cases.

An exception to the above cases is υ Andromedae b, a tidally locked hot Jupiter with an observed day–night temperature difference of about 1400 K (Harrington et al. 2006). Here, unlike Venus, the massive

atmosphere does not circulate its heat around the planet. That detection (as well as models) has shown that tidally locked planets are special cases and should exhibit strong temperature variations.

2.4 Biomarkers

The Terrestrial Planet Finder Interferometer (TPF-I) and Darwin missions, and the Terrestrial Planet Finder Coronagraph (TPF-C), are designed to directly detect terrestrial exoplanets around nearby stars and to measure their spectra (see, e.g., Beichman et al. 1999; 2006; Fridlund 2000; Kaltenegger and Fridlund 2005; Borde and Traub 2006). These spectra will be analyzed to establish the presence and composition of their atmospheres, to investigate their capability to sustain life as we know it (habitability), and to search for signs of life. These missions also have the capacity to investigate the physical properties and composition of a broader diversity of planets, to understand the formation of planets, and to search for the presence of potential biosignature compounds. The range of characteristics of planets is likely to exceed our experience with the planets and satellites in our own Solar System, and Earth-like planets orbiting stars of different spectral type might also evolve differently (Selsis 2000; Segura et al. 2003, 2005).

Biomarkers are detectable species whose presence at significant abundance requires a biological origin (Des Marais et al. 2002). They are the chemical ingredients necessary for biosynthesis (e.g., oxygen [O_2] and CH_4) or are products of biosynthesis (e.g., complex organic molecules, but also O_2 and CH_4). Our search for signs of life is based on the assumption that extraterrestrial life shares fundamental characteristics with life on Earth, in that it requires liquid water as a solvent and has a carbon-based chemistry (Owen 1980; Des Marais et al. 2002). Therefore we assume that extraterrestrial life is similar to life on Earth in its use of the same input and output gases, that it exists out of thermodynamic equilibrium, and that it has analogs to bacteria, plants, and animals on Earth (Lovelock 1975).

Candidate biomarkers that might be detected by a low-resolution TPF-I instrument include O_2, O_3, and CH_4. There are good biogeochemical and thermodynamic reasons for believing that these gases should be ubiquitous byproducts of carbon-based biochemistry, even if the details of alien biochemistry are significantly different than the biochemistry on Earth. Production of O_2 by photosynthesis allows terrestrial plants and photosynthetic bacteria (cyanobacteria) to use abundant H_2O as the electron donor to reduce CO_2, instead of having to rely on scarce supplies of hydrogen (H_2) and hydrogen sulfide (H_2S). Oxygen and nitrous oxide (N_2O) are two very promising bio-indicators. Oxygen is a chemically reactive gas. Reduced gases and oxygen have to be produced concurrently to produce quantities large enough to be detectable in disk-averaged spectra of terrestrial planet atmospheres, as they react rapidly with each other. N_2O is a biomarker in the Earth's atmosphere, being produced in abundance by life but only in trace amounts by natural processes. Although a relatively weak feature in the Earth's spectrum, it may be more pronounced in extrasolar terrestrial planet atmospheres of different composition or host-star spectral type (Segura et al. 2005). Currently, efforts are ongoing to explore the plausible range of habitable planets and to improve our understanding of the detectable ways in which life modifies a planet on a global scale.
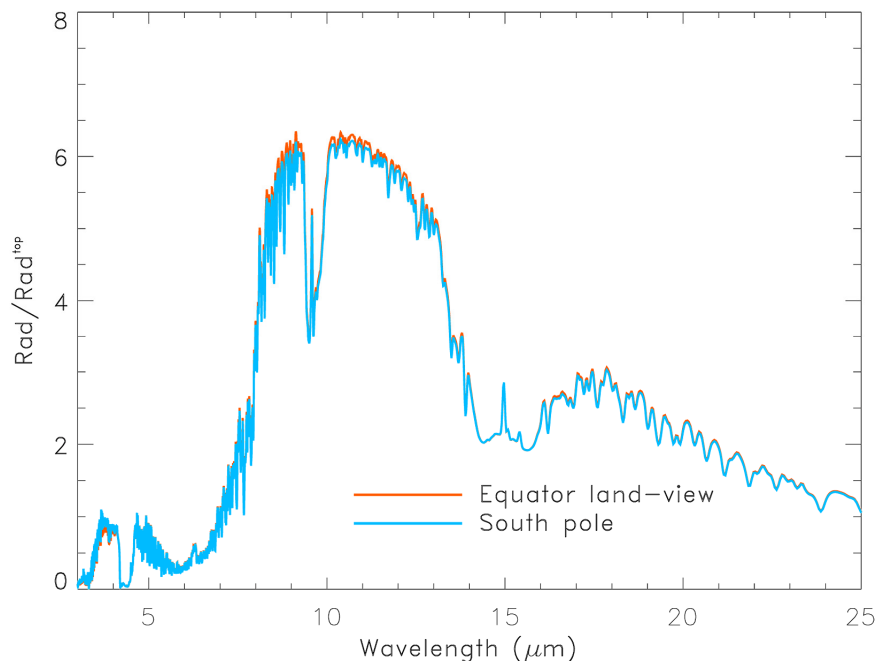
Figure 2-3. Simulated mid-infrared spectrum of an Earth-like planet showing the effects of viewing angle (Giovanna Tinetti, Institut d'Astrophysique de Paris).

2.4.1 Biomarker Signatures in the Mid Infrared

In the mid-IR, the classical signature of biological activity is the combined detection of the 9.6-μm O_3 band, the 15-μm CO_2 band, and the 6.3-μm H_2O band or its rotational band that extends from 12 μm out into the microwave region (Selsis and Despois 2002). Because oxygen is a chemically reactive gas, it follows that reduced gases and oxygen have to be produced concurrently to be detectable in the atmosphere, as they react rapidly with each other. The oxygen and ozone absorption features in the visible and thermal infrared, respectively, could indicate the presence of photosynthetic biological activity on Earth any time during the past 50% of the age of the Solar System. In the Earth's atmosphere, the 9.6-μm O_3 band is a poor quantitative indicator of the O_2 amount, but an excellent qualitative indicator for the existence of even traces of O_2. The Ozone 9.6-μm band is a very nonlinear indicator of O_2 for two reasons. First, for the present atmosphere, low-resolution spectra of this band show little change with the O_3 abundance because it is strongly saturated. Second, the apparent depth of this band remains nearly constant as O_2 increases from 0.01 times the present atmosphere level (PAL) of O_2 to 1 PAL (Segura et al. 2003). The primary reason for this is that the stratospheric ozone increases that accompanied the O_2 buildup lead to additional ultraviolet heating of the stratosphere. At these higher temperatures, the stratospheric emission from this band partially masks the absorption of upwelling thermal radiation from the surface.
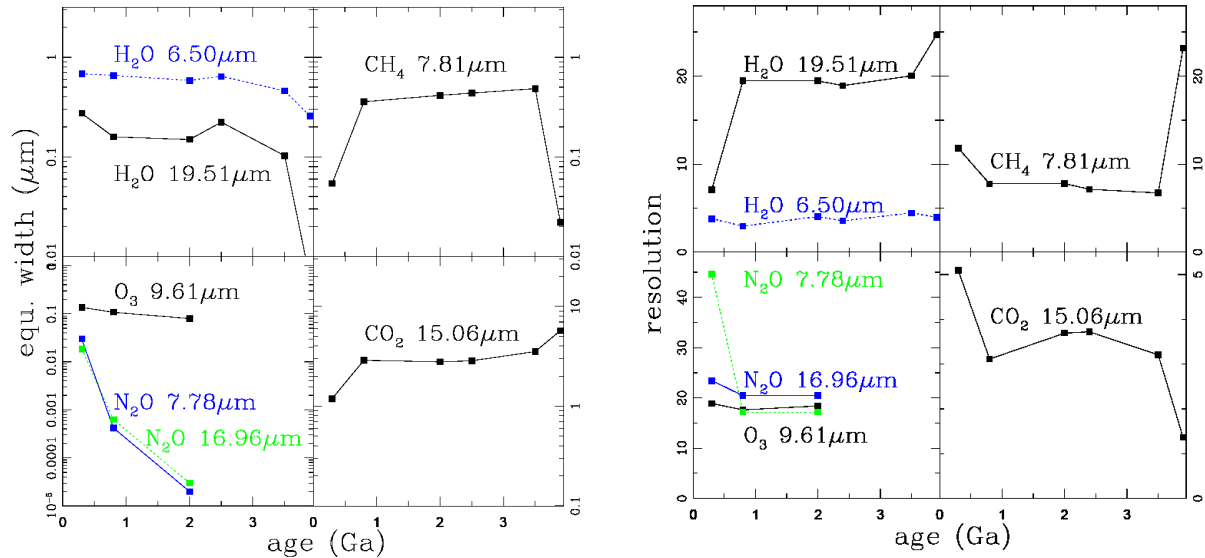
Figure 2-4. Equivalent width in microns (left) and resolution (right) of the main spectral features of atmospheric compounds over geological times in the thermal infrared for an Earth-analog with Earth clouds. (Kaltenegger et al. 2007)

Methane is not readily identified using low-resolution spectroscopy for present-day Earth, but the CH_4 feature at 7.66 μm in the IR is easily detectable at higher abundances (see e.g. 100× abundance in epoch 4 below). When observed together with molecular oxygen, abundant CH_4 can indicate biological processes (see also Lovelock 1975, Segura et al. 2003). Depending on the degree of oxidation of a planet's crust and upper mantle, non-biological mechanisms can also produce large amounts of CH_4 under certain circumstances.

N_2O is also a candidate biomarker because it is produced in abundance by life but only in trace amounts by natural processes. There are no N_2O features in the visible and three weak N_2O features in the thermal infrared at 7.75 μm, 8.52 μm, and 16.89 μm. For present-day Earth, one needs a resolution of 23, 23 and 44, respectively, to detect N_2O at thermal infrared wavelengths (Kaltenegger et al. 2007). Spectral features of N_2O also become more apparent in atmospheres with less H_2O vapor. Methane and nitrous oxide have features nearly overlapping in the 7-μm region, and additionally both lie in the red wing of the 6-μm water band. Thus N_2O is unlikely to become a prime target for the first generation of space-based missions searching for exoplanets, but it is an excellent target for follow-up missions. There are other molecules that could, under some circumstances, act as excellent biomarkers, e.g., the manufactured chloro-fluorocarbons (CCl_2F_2 [Freon 13] and CCL_3F [Freon 12]) in our current atmosphere in the thermal infrared waveband, but their abundances are too low to be spectroscopically observed at low resolution.

Other biogenic trace gases might also produce detectable biosignatures. Currently identified potential candidates include volatile methylated compounds (like methyl chloride [CH_3Cl]) and sulfur compounds. It is known that these compounds are produced by microbes, and preliminary estimates of their lifetimes and detectability in Earth-like atmospheres around stars of different spectral type have been made (Segura et al. 2003, 2005). However, it is not yet fully understood how stable (or detectable) these compounds

would be in atmospheres of different composition and for stars of different spectral type and incident ultraviolet flux. These uncertainties, however, could be addressed by further modeling studies.

2.4.2 Resolution Needed

This section provides quantitative information on the sensitivity necessary to detect spectral features on Earth or an Earth-like exoplanet. The equivalent width needed for optimal detection of each chemical signature in the thermal infrared is given in Figure 2-4 (Kaltenegger et al. 2007). Following standard practice, the total absorption in the feature is expressed in terms of equivalent width, (i.e., the spectral width of an equal area of a rectangular line with zero residual intensity and unity continuum). To detect a spectral feature with optimum signal to noise requires that the full width at half maximum (FWHM) of the spectrometer should be approximately equal to the FWHM of the spectral features. For an extrasolar planet this will not be known, but assuming an Earth-analog as a guideline, we can specify these numbers. We determine equivalent width for these species by integrating the difference between a model spectrum with and without the chemical of interest. The spectral resolution ($\lambda/\Delta\lambda$) needed for optimal detection of each changing spectral feature is given in Figure 2-4. Here λ is the central wavelength of a feature, and $\Delta\lambda$ is the FWHM of the feature after it has been smeared sufficiently to blend any sharp lines yet still retain its essential overall shape. These numbers are relevant for the design of the TPF-I and Darwin mission. Note that features like N_2O would have to be detected on top of another feature, implying an excellent signal-tonoise ratio (SNR) for detection. This example also illustrates that identification of the continuum region, as well as potentially overlapping species, is also an important part of biomarker detection, which in some cases may require higher spectral resolution, in addition to high signal to noise.

2.4.3 Planets Around Different Stars

The interferometric systems suggested for Darwin and the TPF-I mission operate in the mid-IR, and the coronagraph suggested for TPF-C operates in the visible. For the former it is thus the thermal emission emanating from the planet that is detected and analyzed, while for the latter the reflected stellar flux is measured. This means, that if you want to observe Earth-like planets in the Habitable Zone (HZ) around a given star, the thermal flux will to first order be constant for a given planetary size, while the reflected stellar flux will scale with the brightness of the star. The suppression of the primary's thermal emission will, on the other hand, be progressively easier for later and later spectral types. The contrast ratio is a factor of about 4 more for FV stars, 30 less for KV stars, and about 300 less for MV stars compared to the Sun–Earth contrast ration in the IR (Kaltenegger, Eiroa et al. 2007). Surprisingly enough, it may thus be easier for the IR interferometer concept to detect a habitable Earth around an M-Dwarf than around something more akin to our own Sun. This is true for interferometric systems like Darwin and TPF-I that can be adapted to each individual target system, since the HZ moves closer and closer to the star for later and later stellar types. The baseline of the interferometers have to increase to resolve M-star planetary-systems at larger distances, a constraint that is taken into account for the M target systems at largest distance in the target star catalogue.
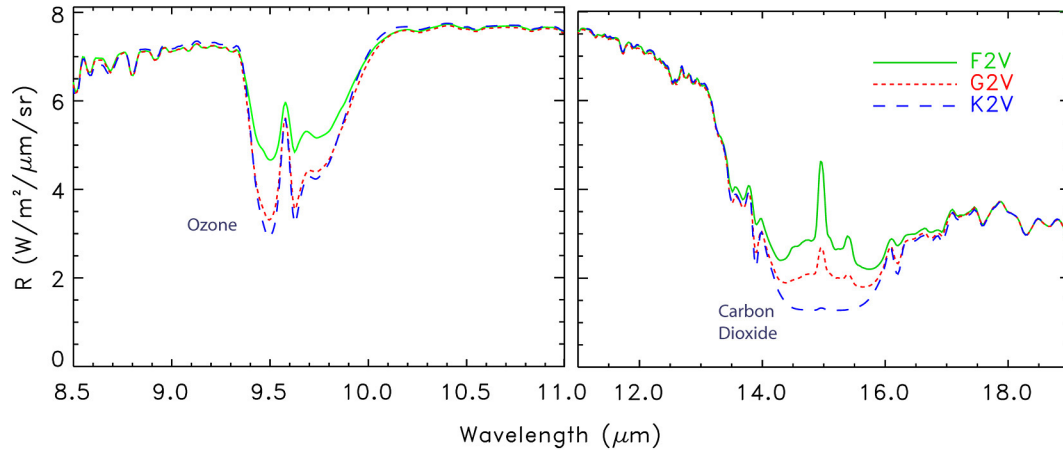
Figure 2-5. These spectra show the appearance of Earth-like planets orbiting within the habitable zones of stars of F2V, G2V, and K2V stellar type. In each case, a weakly-coupled radiative/photochemical atmospheric model was used to determine the equilibrium atmospheric composition and vertical structure for a planet with Earth's modern atmospheric composition, and radiatively forced by the UV to the far-infrared spectrum of a star of each spectral type. A sophisticated radiative transfer model was then used to create a synthetic spectrum of the global spectral appearance of the planet from space, using the equilibrium atmospheric composition as input. (Segura et al. 2003)

The results of modeling, illustrated in Figure 2-5, show the changes in detectability and shape of spectral features due to ozone, carbon dioxide, and methane for the "same" planet around stars of different spectral type. These observed changes in detectability are due to an interplay between the star's spectrum, the photochemistry of ozone, and coupled changes in the thermal structure of the planet's atmosphere. These models were run for host stars of F, G, K (Segura el al. 2003; Selsis et al. 2000) and M spectral type (Segura et al. 2005) and show that the detectable features around, e.g., a K star are deeper than the features around an F host star.

2.4.4 Detection of Water

There are two water features in the IR, the 6.3-µm H_2O band or its rotational band that extends from 12 µm out into the microwave region. Both water features are difficult to interpret and quantify for an extrasolar planetary atmosphere. A waveband region from 5 to 20 µm could detect both water features. The equivalent width for the two features is 1.66 and 0.66 respectively (Kaltenegger et al. 2007) for a current Earth model atmosphere with the average 60% cloud coverage.
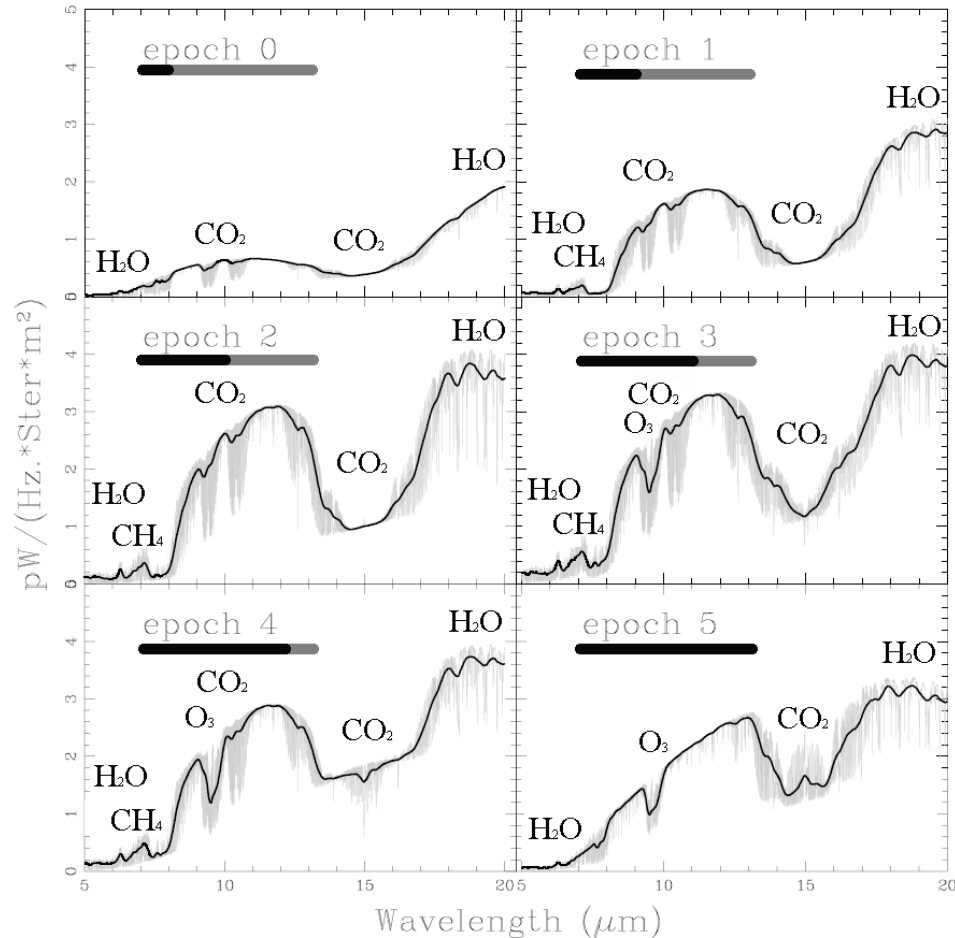
Figure 2-6. The mid-infrared spectral features on an Earth-like planet change considerably over its evolution from a CO_2-rich (epoch 0) to a CO_2/CH_4-rich atmosphere (epoch 3) to a present-day atmosphere (epoch 5). The black lines show a spectral resolution of 25 comparable to the proposed TPF-I mission concept designs. (Kaltenegger *et al.* 2006)

This would indicate a stronger feature at 6.3 μm. However, this feature is so strong that it is relatively insensitive to atmospheric water abundance. Models of Earth's atmosphere indicate that in the extreme clear-sky case, that the depth of this feature is very similar for water column abundances between 10% and more than 200% of the Earth's present water abundance.[1] Methane and nitrous oxide have features nearly overlapping in the 7-μm region, and additionally both lie in the red wing of the 6.3-μm water band. The 6.3-μm H_2O feature could act instead as a "true/false" indicator of the presence of even very small amounts of water if the atmosphere is an Earth-analog. Additionally the photons emission is very low at 6.3 μm (see section 2.2).The broad rotational band, extending between 12 and 200 μm, has little spectral structure. That makes it difficult to discriminate its absorption from other factors affecting the planetary spectrum, such as the temperature of the emitting layer, which could also result in reduced flux in this

---

[1] Victoria Meadows (Caltech), private communication.

wavelength region. The instrument design has to take the noise levels at both wavelength ends into account as well as the photons emitted from the planet. Preliminary studies indicate that it will be equally difficult to detect the water line at both features. To conclude this issue, considerable more detailed study is needed.

2.4.5 Biomarkers and Their Evolution over Geological Timescales

Terrestrial planets found around other stars may be observed at different stages in their geological and biological evolution. Earth's atmosphere has experienced dramatic evolution over 4.5 billion years, and other planets may exhibit similar or greater evolution, and at different rates.

Studies (see e.g., Des Marais et al. 2002; Schindler and Kasting 2000; Kasting and Catling 2003; Selsis, 2000; Pavlov 2000; Traub and Jucks 2002; Segura et al. 2003; Kaltenegger et al. 2007; Meadows 2006) are designed to guide the interpretation of an observed spectrum of such a planet by future instruments that will characterize exoplanets. Figure 2-6 shows theoretical mid-infrared spectra of the Earth at six epochs during its geological evolution (Kaltenegger et al. 2007). The epochs are chosen to represent major developmental stages of the Earth and life on Earth. If an extrasolar planet is found with a corresponding spectrum, we will have good evidence for characterizing its evolutionary state, its habitability, and the degree to which it shows signs of life. The oxygen and ozone absorption features could have been used to indicate the presence of biological activity on Earth anytime during the past 50% of the age of the Solar System. The dark lines show a resolution of 25 in the IR, as proposed for the Darwin/TPF-I mission.

2.5 Suitable Targets

Due to angular resolution and sensitivity constraints, the most suitable target stars around which TPF-I can search for exoplanets are the stars nearest the Sun. However, the nearest stars encompass a large variety of stellar types, classes, ages, and multiplicities (as well as distances); and so the set of all nearby stars needs to be trimmed or culled, for both scientific reasons and engineering/observational constraints. The current scientific source selection criteria, defined at a workshop held at the Naval Research Observatory in Washington, DC, in Nov. 2004, are summarized in this section.

2.5.1 Science Criteria

The identification of candidate scientific targets for TPF-I should begin with a complete list of nearby stars. The master list selected is the Hipparcos catalogue (ESA 1997) of nearby stars, out to a distance cutoff of 30 pc. This list does not include every star within 30 pc because dim stars at the larger distances do not fall within the Hipparcos sensitivity limit, implying that the list grows less and less complete as stellar temperatures decrease. However, for the primary targets of interest, "solar-like" F, G, and K stars, the list should be fairly complete.
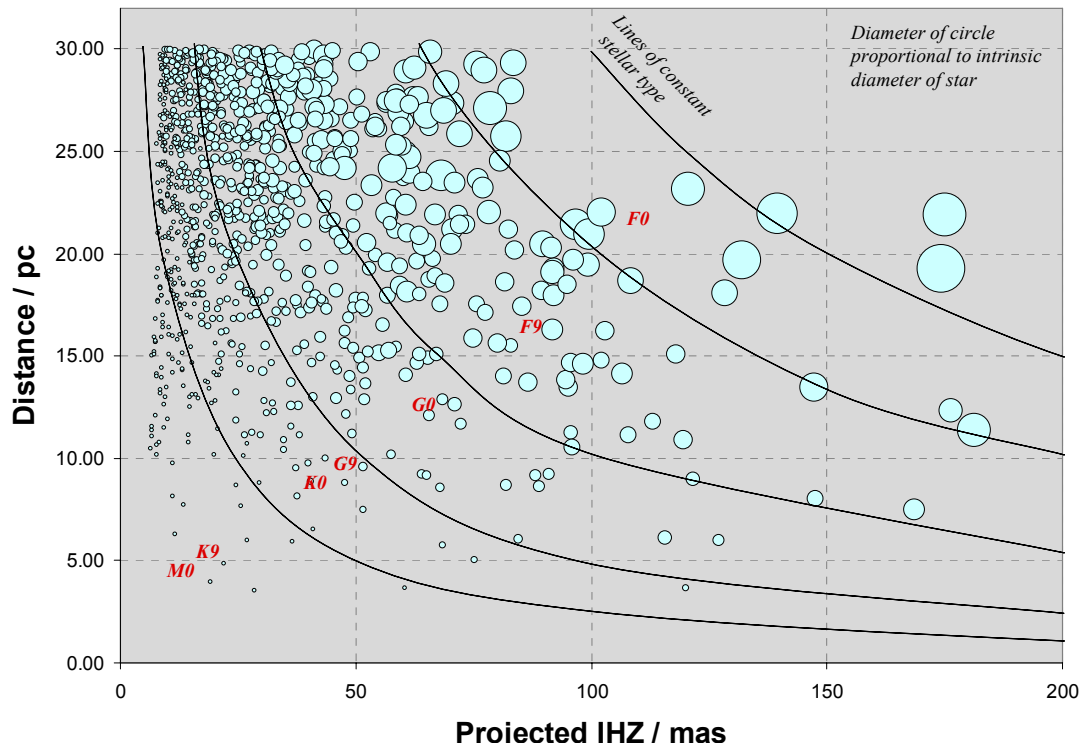
Figure 2-7. Candidate targets for TPF-I. Each of the 1014 candidate stars is represented by a circle with a diameter proportional to the diameter of the star (intrinsic, not angular diameter). Curves show loci of a given spectral type.

Beyond the distance criterion, at this early phase it is desirable to keep the number of culling criteria as small as possible. The scientific target stars can be summarized quite simply: bright, nearby, solar-like, main-sequence stars for which a binary companion is not too close. This statement translates in straightforward fashion to the detailed technical requirements listed in Table 2-3.

The final column in this table gives the number of potential target stars remaining after the set of culls down to a given line has been applied. Even after all applicable science culls have been applied, over 1000 suitable targets remain. These 1014 stars are plotted in Fig. 2-7 on a space of stellar distance vs. projected inner habitable zones size, from which it can be seen, e.g., that for a sizable candidate population of stars to be observable, an inner working angle of 50 milliarcsecond (mas) or smaller is needed. The final candidate list of 1014 stars was used to predict the performance of different TPF-I architectures.

2.5.2 Engineering Criteria

Next one also needs to include instrumental or engineering constraints which can eliminate certain classes of stars. With the current baseline design of TPF-I, these fall into two categories. First, sunshade constraints limit observations to stars within 45° of the ecliptic. Second, control of stray light implies that any bright companion stars must be more than 10 arcsec away from the target star of interest. As Table 2-2 shows, this eliminates about 40% of the scientifically interesting stars.

**Table 2-3. Science and Engineering Criteria for
Selection of TPF-I Candidate Targets**

Parameter	Constraint	Remaining Stars
Science Culls		
Distance (Hipparcos catalog)	< 30 pc	2350
Apparent magnitude	< 9	1299
Bolometric luminosity	< 8	1284
Luminosity class	IV, V	1247
B-V index	> 0.3	1184
Variability	< 0.1	1143
Companions further than	50 AU	1014
Engineering Culls		
After science culls		1014
Field of regard	|Ecliptic latitude| < 45 deg	650
Multiplicity	Separation > 10"	620

2.6 Exozodiacal Dust

2.6.1 Zodiacal Dust as a Constituent of Planetary Systems

The presence of dust around a mature, main-sequence star is a reminder that the star was born by accretion in a dense protostellar disk of gas and dust and that any planets possessed by the star were born out of that same material. The dust around a mature star is not itself primordial, since radiative forces will remove small dust grains in a few thousands to a few millions of years. However, the parent bodies of the observed small dust grains—large numbers of either asteroids or comets—are the remnants of primordial material, and the debris within them provides hints to the origin of planetary systems. Additionally, this solid material is important in the evolution of life, since the cold outer reaches of a planetary system are rich in water and volatiles needed for the creation of habitable environments in the inner reaches of the system. Thus, we want to study the exozodiacal clouds of nearby stars for their intrinsic scientific importance using a variety of observational facilities, including TPF-I/Darwin and TPF-C. Yet the brightness of the exozodiacal cloud is also a potential problem for the detection of terrestrial planets due to increased photon noise and confusion between planets and structures in the zodiacal cloud.

Thus, the incidence, distribution and composition of material in the habitable zones of nearby stars are important for the design of TPF-I or TPF-C and for the feasibility of studying individual targets. After a brief discussion about the impact of photon noise from exozodiacal emission on both visible-light and mid-IR instruments, we summarize recent observational results, discuss theoretical expectations for the level of exozodiacal emission, and describe future observational programs relevant to determining the level of exozodiacal emission around typical TPF targets. We will show that TPF-I can operate in the

presence of zodiacal clouds 10–20 times as bright as our own without undue difficulty and that systems with this amount of emission, *or considerably less*, are likely to be common among mature solar-type stars.

2.6.2 Zodiacal Emission as a Source of Noise

For a cryogenic nulling interferometer operating in an orbit near 1 AU the three dominant noise sources are (Angel and Woolf 1997; Beichman and Velusamy 1999): stellar light that leaks past the interferometric null because of the finite diameter of the star, $S_{*,Leak}$; emission from the local zodiacal dust, S_{LZ}; and emission from the exozodiacal dust in the target system that leaks past the interferometer, $S_{EZ,Leak}$ (Figure 2-8). At short wavelengths (<8 μm), the stellar leak may dominate all other noise sources while at wavelengths longward of 20 μm, emission from the interferometer itself may become important. But over a broad range of wavelengths, the balance between $S_{*,Leak}$, $S_{EZ,Leak}$, and S_{LZ} controls the photon-noise-limited noise floor. In the infrared case, the brightness of the planet itself is small (<1%) compared with the backgrounds and can be ignored. Similarly, detector read noise and dark current can be ignored for broad-band detection.

In the background limit considered here, the total noise is given by the square root of the sum of all the individual photon fluxes reaching the detector. Rather than evaluate the absolute signal-to-noise ratio, S/N, we consider here the ratio of the S/N in the presence of exozodiacal emission, SNR(EZ), to the S/N in the absence of such emission, SNR(0):

$$\left.\frac{SNR(EZ)}{SNR(0)}\right|_{IR} = \frac{\sqrt{S_{*,Leak} + S_{LZ}}}{\sqrt{S_{*,Leak} + S_{LZ} + S_{EZ,Leak}}} = \frac{\sqrt{1 + S_{*,Leak}/S_{LZ}}}{\sqrt{1 + S_{*,Leak}/S_{LZ} + S_{EZ,Leak}/S_{LZ}}}$$

In the above, $S_{*,Leak}$ depends on the nulling configuration, the wavelength of operation and the angular size of the star. Null depths of 10^{-5} to 10^{-6} have been demonstrated in the laboratory) and for the purposes of illustration, it suffices to take $S_{*,Leak} = 10^{-5}F_*$. The emission from the local zodiacal cloud, S_{LZ}, is very complex in detail (Kelsall et al. 1998), but can be parameterized for our purposes as follows:

$$S_{LZ} = \tau_{LZ} B_\nu(255\ K)\ \Omega_{tel}$$

where B_ν is the Planck function; τ_{LZ} (~10^{-7}; Backman 1998) is the vertical optical depth looking out from the mid-ecliptic plane at 1 AU; and Ω_{tel} is the diffraction limited solid angle of an individual telescope in the interferometer. A typical value of the zodiacal cloud brightness toward the ecliptic pole from our mid-plane location is 12 MJy sr^{-1} at 12 μm (Kelsall et al. 1998).
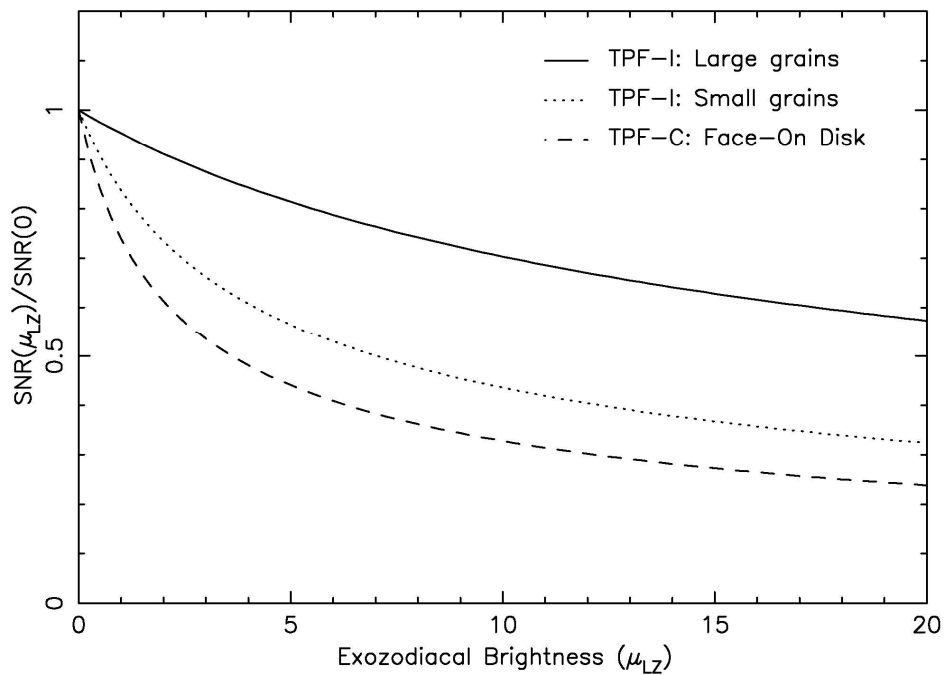
Figure 2-8. The variation of signal-to-noise for planet detection as a function of exozodiacal brightness for three cases: TPF-I for large grain emission; TPF-I for small grain emission; and TPF-C. The parameter μ_{LZ} is the ratio of surface brightness of the exozodiacal cloud in the habitable zone of a target star to that of our own zodiacal cloud.

In the absence of more detailed information, the vertical optical depth of the exozodiacal dust in any system can be parameterized as a factor, μ_{EZ}, times the optical depth of our Solar System's dust cloud. The emission from exozodiacal dust is then $S_{EZ}(r) = 2\,\mu_{EZ}\,\tau_{LZ}(r)\,B_\nu(T(r))\,\Omega_{tel}$, where the factor of two accounts for the fact that in the exozodiacal case we are looking through the entire cloud and not from the vantage of the mid-plane as we do locally. By analogy with the local zodiacal cloud (Backman 1998), the vertical optical depth is assumed to fall off radially as $\tau_{LZ}\,(r) = \tau_{LZ}\,(1\ \mathrm{AU})r_{AU}^{-0.3}$. We also take $T(r) = T_0 r_{AU}{}^{\beta}$ as the equilibrium temperature for grains heated by stellar radiation and emitting in the infrared. Typical 1-AU values of (T_0, β) for large and small silicate grains are (255 K, –0.5) and (362 K, –0.4), respectively (Draine and Lee 1984; Backman and Paresce 1993; Beichman et al. 2006a). For reference, it is worth nothing that the integrated signal from a Solar-System-equivalent exozodiacal cloud is a few hundred times brighter than the signal from an Earth twin. The effect of exozodiacal emission is, however, reduced by the fringe pattern of the interferometer which attenuates the bright central portion of the exozodiacal disk. To account for this effect, we incorporate the fringe pattern of a particular nulling scheme, $\xi(\theta,\varphi)$, where θ and φ are the radial and azimuthal variables, respectively. In the simplified case of a face-on disk, the signal reaching the detector, $S_{EZ,\ Leak}$, is then given by the integral of S_{EZ} over the fringe pattern and the telescope solid angle:

$$S_{EZ,Leak}(d) = 2\int_0^{2\pi} d\varphi \int_0^{\theta\max} \mu_{EZ}\tau_{EZ}(\theta d)B_\nu(T(\theta d))\xi(\theta,\varphi)\theta d\theta$$

for a star at a distance d pc. Figure 2-8 (Beichman et al. 2006b) shows an illustrative example of the effect of EZ emission on the S/N of a TPF-I detection where we have adopted the fringe pattern, $\xi(\theta,\varphi)$, for the Dual Chopped Bracewell interferometer (Lay and Dubovitsky 2004; Lay et al. 2005) and a diffraction-limited beam size of $\theta_{max} = 0.6\lambda/D = 0.5''$ for a $D = 3$-m telescope at 12 μm. For a solar-type star at $d = 10$ pc, the ratio of the exozodiacal contribution to that from the Solar System's own dust is 0.06 μ_{EZ} or 0.24 μ_{EZ}, for large and small grains, respectively. For a particular temperature, smaller grains are located further from their parent star than the cooler, larger (blackbody) grains; and thus, emission from small grains is less effectively blocked by the central null of an interferometer. Small grains thus produce more noise than large grains for a given total exozodiacal brightness. Figure 2-8 shows the variation of S/N as a function of exozodiacal brightness, μ_{EZ}, for two grain sizes. When the surface density of the exozodiacal dust, μ_{EZ}, is 10 times that of our Solar System, corresponding to a 20-fold brightness increase, the S/N is reduced by a factor of ~2–3, necessitating an increase in integration time by a factor of ~4–9 to recover the original S/N. Since many hours of integration time are needed to detect an Earth-sized planet in the presence of a $\mu_{EZ} = 1$ cloud, and days to carry out a spectroscopic program, it is clear that studying systems with $\mu_{EZ} = 10$–20 will be difficult.

A similar analysis can be used to assess the effects of exozodiacal emission at visible wavelengths; for details see Beichman et al. (2006b) or Brown (2005). Figure 2-8 also shows the variation in S/N for TPF-C assuming a 3.5- × 8-m telescope observing a planet 25 mag fainter than a V = 4.5 mag solar twin at 10 pc and a local zodiacal brightness of 0.1 MJy sr^{-1} at 0.55 μm (Bernstein, Freedman, and Madore 2002). As with the interferometer, the effect of zodiacal emission in the target system is to lower the S/N by a factor of ~2–3 at $\mu_{EZ} = 10$. In this particular example, the relative effect of the exozodiacal emission is more pronounced for the TPF-C than for the TPF-I because the interferometer is dominated by the strong *local* zodiacal background until very bright exozodiacal emission is observed. The intrinsic background level within the visible-light coronagraph is low (by assumption of an excellent 10^{-10} rejection ratio) so that the exozodiacal emission quickly plays a significant role in setting the system noise.
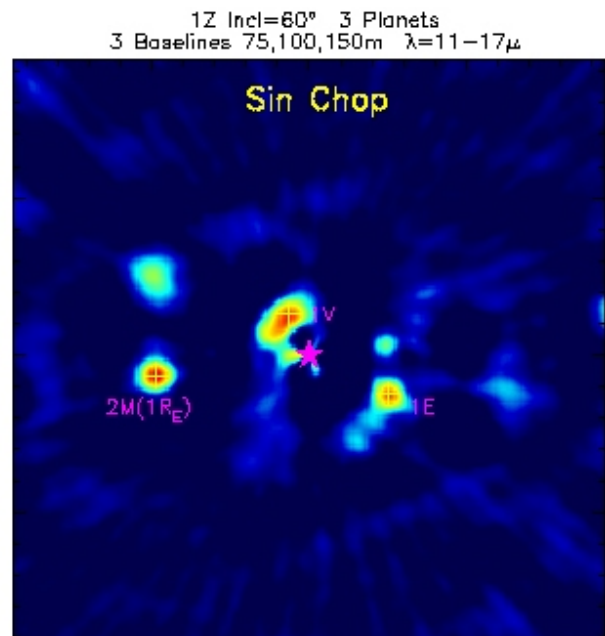
Figure 2-9. Use of a four-element interferometer with chopping allows rejection of symmetrical emission from the zodiacal cloud and allows detection of three planets.
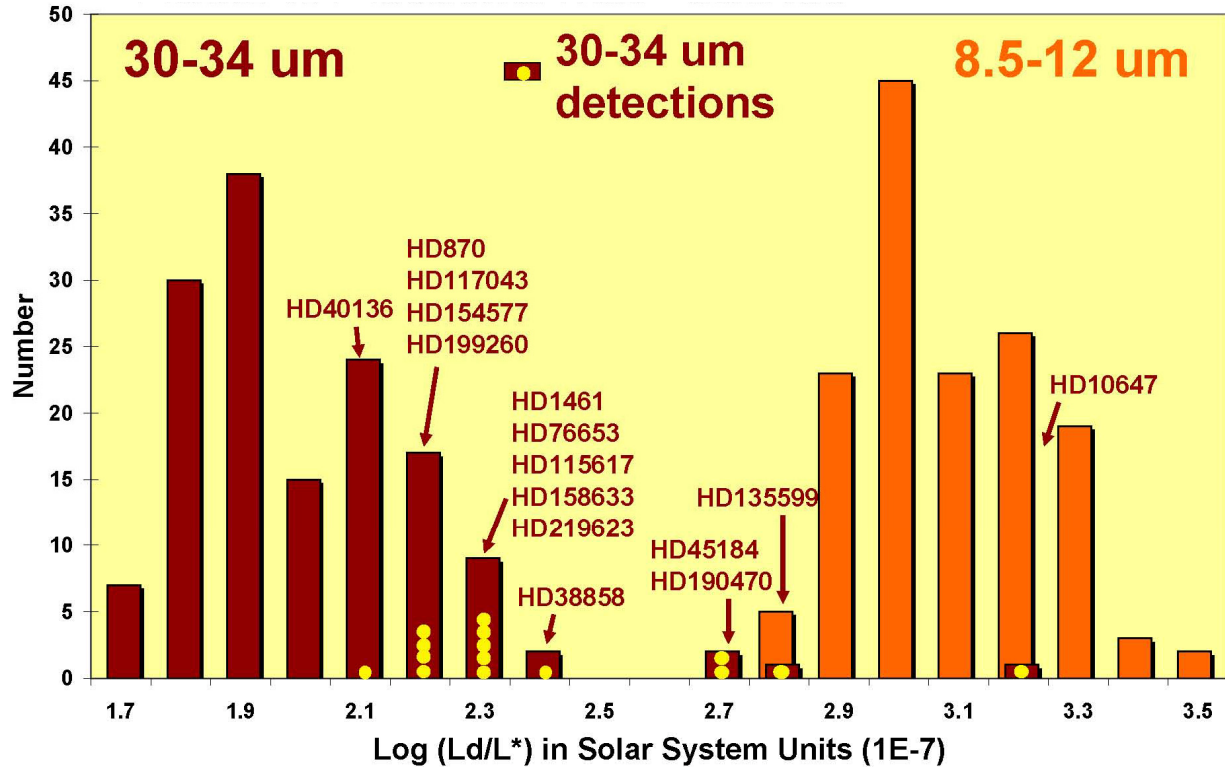
Figure 2-10. Upper limits (or detections) of zodiacal emission in the habitable zone based on Spitzer/IRS results are around 1,000 times the level of our Solar System (Beichman et al. 2006a).

A more detailed examination of the effects of the exozodiacal emission on the detectability of planets would include inclination effects as well as the possibly confusing effects of structures within the zodiacal cloud. It is already well known, for example, that observing an inclined exozodiacal disk though a simple Bracewell interferometer produces a nulled output signal that mimics that of a planet (Angel and Woolf 1997). This is one of main drivers for more complex modulation schemes such as the Oases (Angel and Woolf 1997), Dual Chopped Bracewell, and X-array designs (Lay 2005), and composite designs (Velusamy, Beichman, and Shao 1999). As these studies have shown, with sufficient angular resolution and uv-plane complexity, structures such as wakes and gaps can be distinguished from the signatures of planets. This necessity, along with the need to distinguish multiple planets in a system, is one of the key drivers for observing with TPF-I using a variety of baselines up to at least 100 m. As suggested by Figure 2-9, good angular resolution and diversity in *uv*-plane coverage are an important aspect of properly characterizing planetary systems.

A simple order of magnitude estimate of the brightness of structures in the zodiacal cloud shows that this confusion will not be a problem in clouds like our own, $\mu_{EZ}\sim1$, but it could become one in brighter clouds. TPF will image or resolve away structures larger than $\Theta_{TPF} \sim \lambda/B = 25$ mas at 10 μm on a $B\sim100$ m baseline, or roughly 0.25 AU at 10 pc. The flux density associated with an over-density in a patch of zodiacal emission, $I_{EZ} \sim 2\varepsilon\mu_{EZ}I_{LZ}$, would result in a noise level of $\sigma_{struct}\sim 2\varepsilon\mu_{EZ}I_{LZ}\Theta_{TPF}^2$. Resonant structures associated with planets in our Solar System are a few tenths of an AU in size with over-densities of ~10% for a wake behind the Earth (Dermott et al. 1994; Reach et al. 1995; Backman 1998)
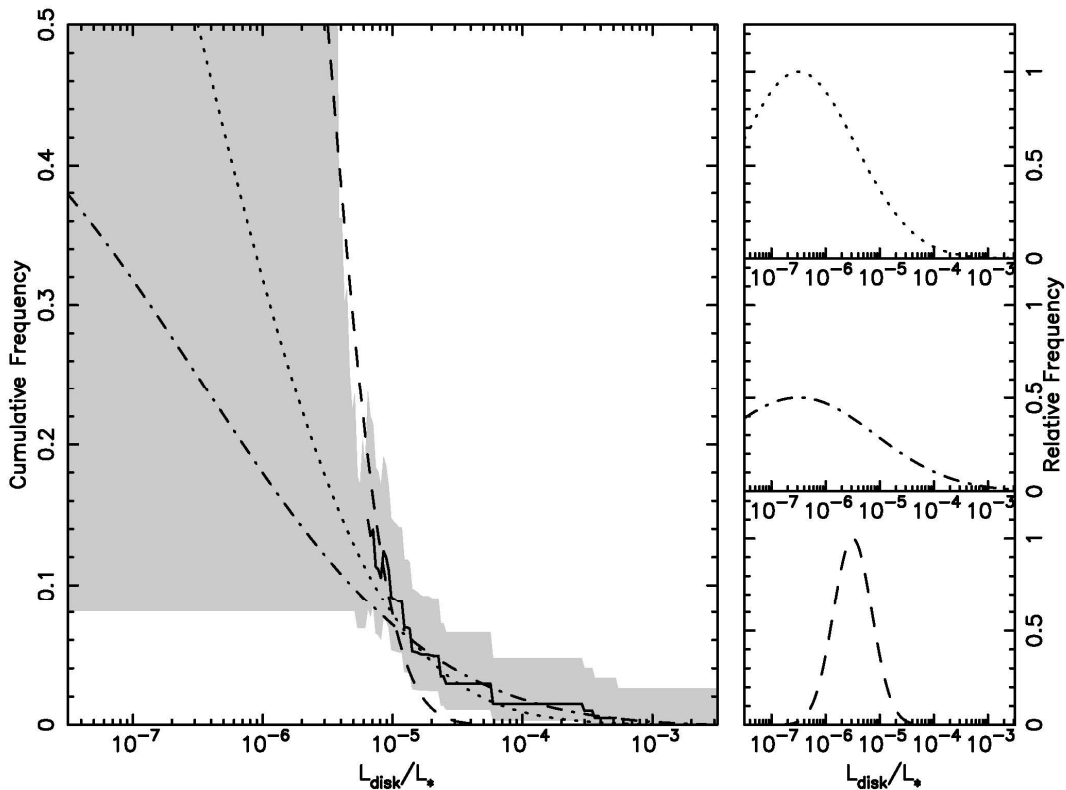
Figure 2-11. Observations constrain different distributions of exozodiacal emission (Bryden et al. 2006). The grey areas are ruled out at the 3-sigma level. Three different luminosity functions are shown to the right.

and <2% for a wake behind Mars (Kuchner et al. 2000). Taking an illustrative value of $\varepsilon = 0.05$ and a nominal zodiacal brightness of $I_{LZ} = 12$ MJy/sr at 12 μm, then the noise floor due to structured zodiacal emission is $\sigma_{struct} \sim 0.01$ μJy, or roughly 1/30 of the brightness of an Earth twin. If the fractional over-density, ε, remains constant as the brightness of the zodiacal cloud, $\mu_{EZ}I_{LZ}$, increases, then the noise level σ_{struct} will increase until the point where, at $I_{EZ} \sim 30 \times I_{LZ}$, the irreducible noise floor becomes equal to the brightness of an Earth twin. At this point no amount of additional integration can help the detection problem, and improved angular resolution is required to see through the confusing zodiacal structure. Additional modeling and observation of zodiacal clouds in the range of 1–100 times the brightness of our cloud will be necessary to assess the importance of this effect.

2.6.3 Summary of Current Observational Results on EZ Disks

Results from the Spitzer Space Telescope have greatly advanced our understanding of the incidence of EZ clouds as a function of age, spectral type, and metallicity. At 70 μm Spitzer is sensitive to levels of EZ emission from ~35–75 K dust with $L_{disk}/L_* \sim 10^{-6}$ to 10^{-5}, or roughly 5–10 times the expected level of emission of our own Kuiper Belt. A wide variety of Spitzer programs have found the following characteristics of EZ emission:

- Approximately 14±3% of mature, solar type stars (F5–G5) have detectable 70-μm zodiacal emission at the $L_{disk}/L_* = 10^{-5}$ to 10^{-6} level (Bryden et al. 2006). This rate is somewhat higher

among A and early F stars (~25%) and smaller for stars later than K (<4%) (Su et al. 2007; Beichman et al. 2006b).

- Emission at 10 μm, corresponding to dust in the habitable zone and thus most relevant to TPF, is rare at the Spitzer sensitivity level at mature stars. However, the unfavorable contrast ratio at this wavelength means that Spitzer can detect emission only at a level ~1,000 times brighter than our own zodiacal cloud (Figure 2-10). Initial estimates based on Infrared Astronomical Satellite (IRAS) (Mannings and Barlow 1998; Fajardo-Acosta, Beichman, and Cutri 2000) and Infrared Space Observatory (ISO) (Laureijs et al. 2002) observations were that <2% of systems have detectable disks at 10 μm, while the largest Spitzer sample studied to date of 150 stars suggests a rate of less than ~1% (Beichman et al. 2006b). While a few individual objects (including A stars like beta Pic and beta Leo and the 2–4 Gyr old K0 star HD 69830 (Beichman et al. 2005b) show bright emission from small grains in the habitable zone, stars like this are very rare.

- Zodiacal emission is both more intense and more frequent (up to 30% at 24 μm) at ages less than ~150 Myr (Rieke et al. 2005; Siegler et al. 2007), but at stellar ages greater than about 1 Gyr, the incidence of EZ emission shows little dependence on age.

- Despite the detection of exozodiacal emission in association with planet-bearing stars (Beichman et al. 2005a), there is little dependence on the incidence of EZ emission on metallicity despite the clear dependence on the incidence of planetary systems on metallicity (Beichman et al. 2006b).

- Relatively featureless spectra are seen toward most disks using the Spitzer/IRS spectrometer (Jura et al. 2004; Chen et al. 2006; Beichman 2006a) with a few dramatic exceptions (Beichman et al. 2005). Disk emission becomes detectable around 25–30 μm in Spitzer/Multiband Imaging Photometer for SIRTF [now Spitzer] (MIPS) 24-μm photometry and Spitzer/infrared spectrograph (IRS) spectra implying temperatures of 75 K and an inner edge to the emitting region around 7–14 AU.

2.6.4 Theoretical Implications of Current Observations

While it is true that we cannot yet observe zodiacal disks at the level of our own cloud, particularly in the habitable zone, the existing observations begin to rule out some disk "luminosity functions" of L_{disk}/L_* that are much brighter than our own. Figure 2-11 shows constraints on possible distributions of L_{disk}/L_* based on Spitzer results (Bryden et al. 2006). The cumulative distribution shown on the left hand side of the figure rules out a log-normal distribution of zodiacal brightness centered on a level that is 100 times brighter than our Solar System level. Future observations will be needed to constrain similar log-normal distributions centered on levels of emission more similar to those of our own Solar System.

Theory based on the evolution of debris disks as revealed by ISO (Dominik and Decin 2003) and Spitzer (Wyatt et al. 2006) can also guide our expectations. Figure 2-12 shows models based on a cascade of collisions between planetesimals leading to the production of small grains that are ultimately lost to the system due to either Poynting-Robertson drag or radiative blowout. For a canonical set of parameters (Wyatt et al. 2006) appropriate to a solar type star, the curves show the evolution of $f = L_{disk}/L_*$ as a function of time while holding all but one of the parameters constant. The predicted level of zodiacal emission drops well below 10 times that of our system by the time the star reaches a few Gyr. The right-hand curves show the variation of expected emission for different disk sizes (1, 3, 10, 30 AU). The 3-AU

31
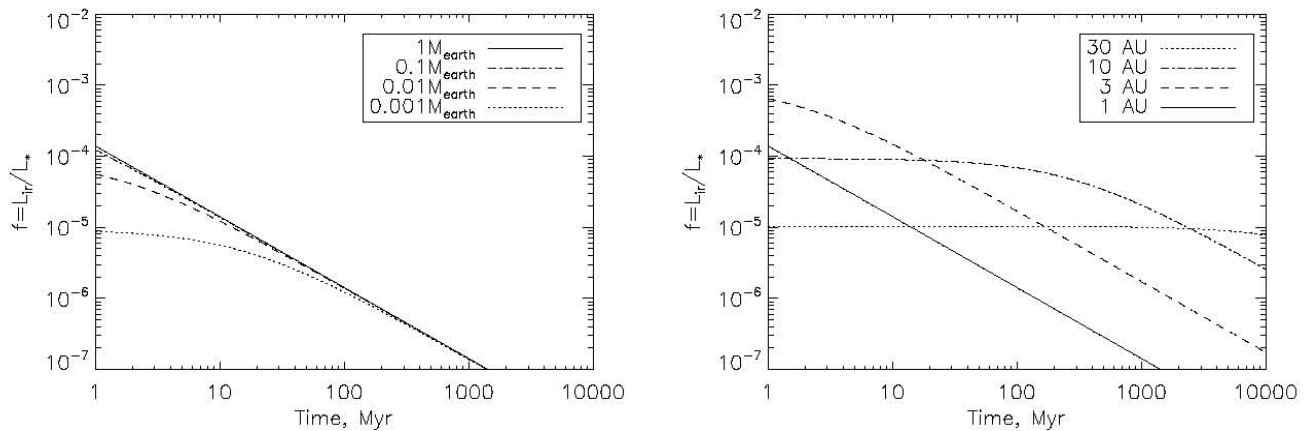
Figure 2-12. Models of the evolution of total exo-zodiacal emission as a function of time as a function of total disk mass (left) and disk location (right; Wyatt et al. 2006) show that after a few Gyr solar-type stars with disks interior to 10 AU reach zodiacal levels comparable to our own, $f = L_{disk}/L = 10^{-7}$.

case corresponds to the location of our asteroid belt and reproduces almost exactly the level of emission in our own Solar System, L_{disk}/L_*, a few $\times$ 10^{-7}. The 10- and 30-AU cases predict a higher level of zodiacal emission than is presently seen in the Solar System; however, this model ignores the clearing action of the Jupiter and Saturn which would either have incorporated much of the planetesimal material into a solid core, or ejected the material. While our theoretical understanding is far from complete, curves such as these, validated by present and future observations of disks, should give us confidence that the expected level of emission will be at or below the desired ~10–20 EZ level needed for the detection of terrestrial planets around many nearby stars.

2.6.5 Prospects for Future Observations

It will take observations with facilities other than Spitzer to push to lower levels of zodiacal emission. The Herschel telescope will measure cold Kuiper Belt disks to Solar System levels while ground-based interferometers, such as the Keck Interferometer (KI) and the Large Binocular Telescope Interferometers (LBTI), will spatially suppress the stellar component to measure definitively the 10-μm exozodiacal emission that arises in the habitable zone and that might cause problems for TPF.

The Keck Interferometer (KI; Colavita et al. 2006) is currently implementing a nulling interferometry mode at 10 μm specifically targeted at observations of exozodiacal emission around nearby main-sequence stars. In this mode, the central star is placed on a destructive fringe, allowing detection of the much fainter surrounding emission while rejecting intense photospheric emission. The size scales probed by 85-meter baseline in this mode are 25 to 200 mas, corresponding to the habitable zone for many nearby main-sequence stars. Initial observations using this mode have been made, and the final detection level is expected to be 100 times the level of our Solar System with a sensitivity limit of 2 Jy for the target star. At this sensitivity limit and within the declination range of the telescope, there are 53 main-sequence stars with A through K spectral types, which can be observed with KI, including: 10 A stars, 18 F stars, 10 G stars, and 6 K stars. The KI observations will be sensitive to dust in the habitable zone at a factor of 10 lower levels than the Spitzer observations. The sample of available stars will determine the

frequency of disks at the 100 Solar System level and will test the theoretically predicted spatial distributions such as those described in section D and Figure 4-5. In a few years after implementation of the KI nuller, the Large Binocular Telescope Interferometers (LBTI; Hinz et al. 2003) will become operational. LBTI also works at 10 μm and eliminates the stellar flux through interferometric combination, but its unique design of co-mounted telescopes on a 15-meter baseline gives it a large field-of-view with ~100 mas resolution. LBTI is expected to push to sensitivity levels a factor of 10 below KI's and complement KI by looking at material at ~2 times greater distances from the star.

With Spitzer and Herschel measuring excesses from 200 to 20 μm down to near Solar System levels, and with KI and LBTI pushing to near Solar System levels at 10 μm, we can confidently expect to understand the statistical properties of TPF targets well enough to know whether or not there exists, as theory suggests, a population of stars with low levels of zodiacal emission. We will also have detailed information on many individual targets, particularly at northern declinations accessible to KI and LBTI.

2.7 References

2.7.1 Science Requirements

Kasting, J. F., Catling, D., "Evolution of a habitable planet," *Ann. Rev. Astron. Astrophys.* **41**, 429–463 (2003).

Turnbull, M. C., *The Searth for Habitable Worlds: From the Terrestrial Planet Finder to SETI,* Ph.D. dissertation, University of Arizona, Tucson, AZ (2004).

2.7.2 Physical Characterization

Gaidos, E., and Williams, D. M., "Seasonality on terrestrial extrasolar planets: inferring obliquity and surface conditions from infrared light curves," *New Astronomy* **10**, 67–77 (2004).

Harrington, J., Hansen, B. M., Luszcz, S. H., Seager, S., Deming, D., Menou, K., Cho, J. Y.-K., and Richardson, L. J., "Phase dependent infrared brightness of the extrasolar planet υ Andromedae b," *Science* **314**, 623–626 (2006).

Selsis, F., "The atmosphere of terrestrial exoplanets: Detection and characterization," *Extrasolar Planets Today and Tomorrow,* ASP Con. Ser. **321**, Beaulieu, J.-P., Le Cavalier des Etangs, A., and Terquem, C., editors, Astronomical Society of the Pacific, San Francisco, CA, 170–182 (2004).

2.7.3 Biomarkers

Beichman, C. A., Woolf, N. J., and Lindensmith, C. A., eds., *The Terrestrial Planet Finder (TPF): a NASA Origins Program to Search for Habitable Planets*, JPL Publication 99-3, Jet Propulsion Laboratory, Pasadena, California (1999).

Beichman, C. A., Fridlund, M. , Traub, W. A., Stapelfledt, K. R., Quirrenbach, A., and Seager, S. "Comparative planetology and the search for life beyond the solar system," *Protostars and Planets V*, editors Riepurth, B., et al., University of Arizona Press, Tucson, AZ, 915–928 (2006).

Bordé, P. J., and Traub, W. A., "High-contrast imaging from space: Speckle nulling in a low-aberration regime," *Astrophys. J.* **638**, 488–498 (2006).

Christensen, P. R., and Pearl, J. C., "Initial data from the Mars Global Surveyor thermal emission spectrometer experiment: Observations of the Earth," *J. Geophys. Res.* **102**, 10875–10880 (1997).

Des Marais, D. J., Harwit, M. O., Jucks, K. W., Kasting, J. F., Lin, D. N. C., Lunine, J. I., Schneider, J., Seager, S., Traub, W. A., and Woolf, N. J., "Remote sensing of planetary properties and biosignatures of extrasolar terrestrial planets," *Astrobiology* **2**, 153–181 (2002).

Falkowski, P. G., "Evolution: Tracing oxygen's imprint on Earth's metabolic evolution," *Science* **311**, 1724–1725 (2006).

Fridlund, M., *DARWIN The InfraRed Space Interferometer*, ESA-SCI (2000)12, 47 European Space Agency: Noordwijk, The Netherlands (2000).

Jucks K. W., Johnson D. G., Chance K. V., Traub W. A., Margitan J. J., Osterman G. B., Salawitch R. J., and Sasano, Y., "Observations of OH, HO_2, H_2O, and O_3 in the upper stratosphere: implications for HOx photochemistry," *Geophysical Research Letters* **25**, 3935–3938 (1998).

Kaltenegger, L., Eiroa, C., Stankov, A., Fridlund, M., "The Darwin target star catalog," *Astron. Astrophys.* submitted (2007).

Kaltenegger, L., and Fridlund, M., "The Darwin mission: Search for extra-solar planets," *Advances in Space Research* **36**, 1114–1122 (2005).

Kaltenegger, L., Traub, W. A., and Jucks, K., "Spectral evolution of an Earth-like planet," *Astrophys. J.* in press (2007).

Kasting, J. F., and Catling, D., "Evolution of a habitable planet," *Ann. Rev. Astron. Astrophys.* **41**, 429–463 (2003).

Lovelock J. E., "Thermodynamics and the recognition of alien biospheres [and discussion]," *Proc. R. Soc. Lond. B* **189**, 167–181 (1975).

Meadows, V., "Modelling the diversity of extrasolar planets," *Direct Imaging of Exoplanets: Science and Techniques*, *Proc. IAU Colloquium 200*, editors Aime C., and Vakili, F., Cambridge University Press, Cambridge, UK, pp. 25–34 (2006).

Montanes-Rodriguez P., Pallé, E., and Goode P. R., "Globally integrated measurements of the Earth's visible spectral albedo," *Astrophys. J.* **629**, 1175–1182 (2005).

Owen, T., "The search for early forms of life in other planetary systems," in *Strategies for Search for Life in the Universe*, editors Papagiannis, M. D., Springer: Dordrecht, The Netherlands, p. 177 (1980).

Pavlov, A. A., Kasting, J. F., Brown, L. L., Rages, K. A., Freedman, R., "Greenhouse warming by CH4 in the atmosphere of early Earth," *J. Geophys. Res.* **105**, 11981–11990 (2000).

Schindler, T. L., and Kasting, J. F., "Synthetic spectra of simulated terrestrial atmospheres containing possible biomarker gases," *Icarus* **145**, 262–271 (2000).

Segura, A., Krelove, K., Kasting, J. F., Sommerlatt, D., Meadows V., Crisp D., Cohen, M., and Mlawer, E., "Ozone concentrations and ultraviolet fluxes on Earth-like planets around other stars," *Astrobiology* **3**, 689–708 (2003).

Segura, A., Kasting, J. F., Meadows, V., Cohen, M., Scalo, J., Crisp, D., Butler, R. A. H., and Tinetti, G., "Biosignatures from Earth-like planets around M Dwarfs," *Astrobiology* **5**, 706–725 (2005).

Selsis, F., "Physics of Planets I: Darwin and the Atmospheres of Terrestrial Planets," *Darwin and Astronomy: The Infrared Space Interferometer*, ESA SP **451**, European Space Agency, Noordwijk, The Netherlands, pp. 133–140 (2000).

Selsis, F., Despois, D., and Parisot, J.-P., "Signature of life on exoplanets: Can Darwin produce false positive detections?"*Astron. Astrophys.* **388**, 985–1003 (2002).

Tinetti, G., Meadows, V. S., Crisp, D., Kiang, N., Bosc, E., Fishbein, E., and Turnbull, M. C., "Detectability of planetary characteristics in disk-averaged spectra. I: The Earth model," *Astrobiology* **6**, 34–47 (2006).

Tinetti, G., Meadows, V. S., Crisp, D., Kiang, N., Kahn, B. H., Bosc, E., Fishbein, E., Velusamy, T., and Turnbull, M. C., "Detectability of planetary characteristics in disk-averaged spectra. II: Synthetic spectra and light-curves of Earth," *Astrobiology* **6**, 881–900 (2006).

Traub, W. A., and Jucks, K., "A possible aeronomy of extrasolar terrestrial planets," *Atmospheres in the Solar System: Comparative Aeronomy*, AGU Monograph Series **130**, editors Mendillo, M., Nagy A., and Waite J. H., American Geophysical Union: Washington, DC, 369–380 (2002).

Turnbull, M. C., Traub, W. A., Jucks, K. W., Woolf, N. J., Meyer, M. R., Gorlova, N., Skrutskie, M. F., and Wilson, J. C., "Spectrum of a habitable world: Earthshine in the near-infrared," *Astrophys. J.* **644**, 551–559 (2006).

Woolf, N. J., Smith, P. S., Traub, W. A., and Jucks, K. W., "The spectrum of Earthshine: A pale blue dot observed from the ground," *Astrophys. J.* **574**, 430–433 (2002).

2.7.4 Suitable Targets

European Space Agency, *The Hipparcos and Tycho Catalogues*, ESA SP-1200 (1997)
        http://www.rssd.esa.int/Hipparcos/catalog.html

2.7.5 Exozodiacal Dust

Angel, R. and Woolf, N., "An imaging interferometer to study extrasolar planets," *Astrophys. J.* **475**, 373–379 (1997).

Backman, D. E., "Terrestrial-temperature dust around main sequence stars," in *Exozodiacal Dust Workshop; Conference Proceedings*, editors. Backman, D. E., Caroff, L. J., Sandford, S. A., Wooden, D. H., p. 107 (1998).

Backman, D. E. and Paresce, F., "Main-sequence stars with circumstellar solid material — The Vega phenomenon," in *Protostars and Planets III,* Space Telescope Science Institute, Baltimore, MD, pp. 1253–1304 (1993).

Beichman, C. A., Woolf, N. J., Lindensmith, C. A. eds., *The Terrestrial Planet Finder (TPF) : a NASA Origins Program to search for habitable planets*, JPL Publication, 99-3, Pasadena, CA (1999).

Beichman, C. A. and Velusamy, T. "Sensitivity of the TPF Interferometer for planet detection," *Working on the Fringe: Optical and IR Interferometry from Ground and Space*, editors. S. Unwin and R. Stachnik, Proc. ASP Conference **194**, Brigham Young University Press, Provo, Utah, pp. 408–422, (1999).

Beichman, C. A., Bryden, G., Rieke, G. H., et al., "Planets and infrared excesses: Preliminary results from the Spitzer MIPS survey of solar-type stars," *Astrophys. J.* **622**, 1160–1170 (2005).

Beichman, C. A., Bryden, G., Gautier, T. N., et al., "An excess due to small grains around the nearby K0 V star HD 69830: Asteroid or cometary debris?" *Astrophys. J.* **626**, 1061–1069 (2005).

Beichman, C. A., Tanner, A., Bryden, G., et al., "IRA spectra of solar-type stars: A search for asteroid belt analogs," *Astrophys. J.* **639**, 1166–1176 (2006).

Beichman, C. A., Bryden, G., Stapelfeldt, K. R., et al., "New debris disks around nearby main-sequence stars," *Astrophys. J.* **652**, 1674–1693 (2006b).

Bernstein, R. A., Freedman, W. F., and Madore, B. F., "The first detections of the extragalactic background light at 3000, 5500, and 8000 angstroms," *Astrophys. J.* **571**, 85–106 (2002).

Brown, R. A., "Single-visit photometric and obscurational completeness," *Astrophys. J.* **624**, 1010–1024 (2005).

Bryden, G., Beichman, C. A., Trilling, D. E., et al., "Frequency of debris disks around solar-type stars: First results from a Spitzer MIPS survey," *Astrophys. J.* **636**, 1098–1113 (2006).

Chen, C., Sargent, B. A., Bohac, C., et al., "Spitzer IRS spectroscopy of IRAS-discovered debris disks," *Astrophys. J. Supp. Ser*. **166**, 351–377 (2006).

Colavita, M., Serabyn, G., Wizinowich, P. L., and Akeson, R. L., "Nulling at the Keck Interferometer," in Advances in Stellar Interferometry, Edited by J. D. Monnier, M. Schöller, and W. C. Danchi, *Proc SPIE* **6268**, 03 (2006).

Dermott, S. F., Jayaraman, S., Xu, Y. L., Gustafson, B. A. S., and Liou, J. C., "A circumsolar ring of asteroidal dust in resonant lock with the Earth," *Nature* **369**, 719–723 (1994).

Draine, B. T. and Lee, H. M., "Optical properties of interstellar graphite and silicate grains," *Astrophys. J.* **285**, 89–108 (1984).

Dominik, D., and Decin, G., "Age dependence of the Vega phenomenon: Theory," *Astrophys. J.* **598**, 626–635 (2003).

Fajardo-Acosta, S. B., Beichman, C. A., and Cutri, R. M., "Discovery of new candidate Vega-type systems from IRAS and the 2 Micron All-Sky Survey," *Astrophys. J.* **538**, L155–L158 (2000).

Hinz, P. M., Angel, R.. P., McCarthy, D. W., Hoffmann, W.F., and Peng, C. Y., "The Large Binocular Telescope Interferometer," in *Interferometry for Optical Astronomy II*. Edited by Wesley A. Traub. *Proc. SPIE* **4838**, 108–112 (2003).

Jura, M., Chen, C. H., Furlan, E., et al., "Mid-infrared spectra of dust debris around main-sequence stars," *Astrophys. J.* **154**, 453–457 (2004).

Kelsall, T., Weiland, J. L., Franz, B. A., et al., "The COBE Diffuse Infrared Background Experiment search for the cosmic infrared background. II. Model of the interplanetary dust cloud," *Astrophys. J.* **508**, 44–73 (1998).

Kuchner, M. J., Reach, W., and Brown, M., "A search for resonant structures in the zodiacal cloud with COBE DIRBE: The Mars wake and Jupiter's Trojan clouds," *Icarus* **145**, 44–52 (2000).

Laureijs, R., Jourdain de Muizon, M., Leech, K., et al., "A 25 micron search for Vega-like disks around main-sequence stars with ISO," *Astron. Astrophys.* **387**, L285–L293 (2002).

Lay, O., Gunter, S. M., Hamlin, L. A., et al., "Architecture trade study for the Terrestrial Planet Finder Interferometer," *Techniques and Instrumentation for Detection of Exoplanets II,* Edited by D. R. Coulter, Proc. SPIE **5905**, 59052 (2005).

Lay, O., and Dubovitsky, S., "Nulling interferometers: the importance of systematic errors and the X-array configuration," in *New Frontiers in Stellar Interferometry*, *Proc. SPIE* **5491**, editor W. A. Traub, 874–885 (2004).

Mannings, V., and Barlow, M. J., "Candidate main-sequence stars with debris disks: A new sample of Vega-like sources," *Astrophys. J.* **497**, 330–341 (1998).

Reach, W. T., Franz, B. A., Weiland, J. L., et al., "Observational confirmation of a circumstellar dust ring by the COBE satellite," *Nature* **374**, 521–523 (1995).

Rieke, G. R., Su, K. Y. L., Stansberry, J. A., et al., "Decay of planetary debris disks," *Astrophys. J.* **620**, 1010–1026 (2005).

Siegler, N., Muzerolle, J., Young, E. T., et al., "Spitzer 24 micron observations of open cluster IC 2391 and debris disk evolution of FGK stars," *Astrophys. J.* **654**, 580–594 (2007).

Su, K. Y. L., Rieke, G. H., Stansberry, J. A., Trilling, D. E., *Protostars and Planets V*, editors. Reipurth, B., Jewitt, D., and Keil, K., LPI Contribution No. 1286, p. 8118, University of Arizona Press, Tucson, AZ, (2007).

Velusamy, T., Beichman, C. A., and Shao, M., "A dual three-element nulling interferometer for TPF," in *Working on the Fringe: Optical and IR Interferometry From Ground and Space*, Proc. ASP Conference **194**, Edited by S. Unwin and R. Stachnik. ISBN: 1-58381-020-X, p. 430–436 (1999).

Wyatt, M. C., Smith, R., Greaves, J. S., Beichman, C. A., Bryden, G., Lisse, C. M., "Transience of hot dust around Sun-like stars," *Astrophys. J.* accepted (2006).

3 Transforming Astrophysics with TPF-I

The milli-arcsecond (mas) angular resolution of TPF-I/Darwin in the 5- to 15-μm wavelength regime will enable transformational science in the era of the Atacama Large Millimeter Array ALMA) and (ground-based extremely large telescopes (ELTs) in the visual to near-IR wavelength region) on topics ranging from our home planetary system; star and planet formation, evolution, and death; the formation, evolution, and growth of black holes; and the birth and evolution of galaxies over cosmic time. TPF-I/Darwin will provide milli-arcsecond resolution, a gain of about two to three orders of magnitude over filled aperture telescopes such as the James Webb Space Telescope (JWST). This mission will enable imaging to at least 20th magnitude around a wavelength of 10 μm, a million-fold improvement over the best ground-based sensitivity in this wavelength regime. These gains in resolution and sensitivity are comparable to those attained at visual wavelengths over the last four centuries as astronomy evolved from the naked-eye era before Galileo to the charged couple device (CCD) era in the latter half of the twentieth century. The TPF-I/Darwin infrared interferometer will be a pathfinder to ultra-high-resolution imaging in space.

3.1 Introduction

Infrared interferormetry in space with a constellation of telescopes and an image combiner flying in formation will be a gateway to milli-arcsecond (mas) angular resolution astronomical imaging and spectroscopy of the future. The TPF-I from NASA and Darwin from ESA are the first formation-flying interferometer concepts to be seriously investigated for both technical feasibility and scientific potential. These missions were conceived for a very specific goal – the detection and characterization of terrestrial planets in terrestrial orbits around about 150 spectral-type G stars within 30 pc of the Sun. However, the stringent performance requirements imposed on these missions by planet finding and characterization makes TPF-I/Darwin a powerful tool for many other astronomical applications. Space enables phase-stability unachievable by Earth-based system that will be limited only by the metrology used in establishing the flux-collector-combiner separations. TPF-I/Darwin will be a technological pathfinder for future micro-and nano-arcsecond resolution instruments at infrared and other wavelengths. Here, we explore the general astrophysics enabled by milli-arcsecond angular resolution and micro-jansky sensitivity in the 5 to 15 μm wavelength regime with possible extension to wavelengths from 2 to 30 μm.

We start by summarizing the assumed parameters of the TPF-I/Darwin interferometer. Consider the four science areas where this instrument will provide revolutionary observations, followed by a listing of additional research areas where high-impact observations could be made.

3.1.1 Darwin/TPF-I Properties

We assume a baseline TPF-I architecture consisting of four free-flying telescopes plus a beam combiner. The apertures are approximately D = 4 meters, the maximum baselines are approximately B = 500 m, and the operating wavelength range is between 5 and 15 μm with a spectral resolution of at least R = 50. Although the current prime-mission (planet finding) requires a nulling interferometer configuration, we will assume that imaging interferometry without nulling will also be possible. Additionally, we will consider upgrades in spectral resolution, wavelength coverage, baseline length, and multi-beam interferometry of two or more objects distributed over the field-of-view of each telescope.

These parameters translate to a primary-beam (diffraction spot size of each telescope) $\theta_P = \lambda / D = 0.25$" to 0.75", and a synthesized beam (interferometric angular resolution) of $\theta_I = \lambda / B = 0.002$ to 0.006" (2 to 6 milli-arcseconds or mas) over the assumed operating wavelength range of 5 to 15 μm and B = 500 m. The sensitivity is about 20th magnitude, and may be considerably better if the coherence time can be improved.

Extension of the operating wavelength range down to 2 μm (the wavelength beyond which thermal emission from the atmosphere makes ground-based observations difficult for all but the brightest sources), or extension of maximum baselines to 1,000 m would enable an angular resolution of 1 mas to be reached or exceeded. Note however, that excess thermal noise introduced by the increasing visibility of the thermal shields of the telescopes on long baselines will likely result in loss of sensitivity and contrast. Studies are therefore needed to assess the maximum baselines that can be used. The nulling mode will be useful in the study of the environments of bright object such as quasars, stars, and luminous pre- and post-main sequence objects, such as the Becklin-Neugebauer object in Orion or the massive post-LBV, eta-Carinae. Multi-object interferometry will enable the precise determination of relative positions, parallax, and proper motions.

Ground-based interferometers suffer from the randomly phased fluctuations introduced by the atmosphere. Even extreme adaptive optics (AO) systems will exhibit residual phase noise that limits sensitivity. In comparison, space-based interferometry has the enormous advantage of exquisite phase-stability limited only by metrology and path-length-difference compensation errors. On-the-fly recording of fringes will enable excellent sampling of the *u-v* plane required for high-fidelity imaging of complex sources.

3.1.2 Diagnostics in the TPF-I/Darwin Bands

The wavelength region between 5 and 15 μm is rich in diagnostics for probing physical conditions in astrophysical environments. Emission from warm dust in the range 100 to 1,000 K, the characteristic temperature of grains located in and near the habitable zones of stars (about 0.3 to 3 AU for Solar-luminosity stars) peaks in this spectral domain. TPF-I/Darwin will be the most powerful probe of dust in star forming-cloud cores heated by young stars and clusters. This instrument is ideally suited for imaging of the region from 0.1 to 10 AU where planets form around Solar-mass stars located within a few hundred pc of the Sun, warm dust located from 10 to 1000 AU around massive stars located anywhere in the Galaxy, and the dust surrounding the Active Galactic Nucleus (AGN) and extragalactic star-forming regions in our locale in the Universe.

A variety of molecular bands and solid-state features (arising from grains and ices) will provide powerful diagnostics of composition and molecular structure (amorphous vs. crystalline). This wavelength region contains bands produced by PAHs polycyclic aromatic hydrocarbons (PAHs), the bands of amorphous and crystalline silicate dust around 10 μm, and a variety of ice features due to water, carbon monoxide, carbon dioxide, and methanol, molecular vibrational bands of many common organic and inorganic substances, fine structure lines of many elements and ions, and the spectral lines of atomic and molecular hydrogen.

TPF- I/Darwin will be highly complementary to giant ground-based facilities being deployed during the next decades. The ALMA (Atacama Large Millimeter Array) will probe molecules and cold dust in the outer portions of protostellar environments and disks beyond 10 AU, but with only 0.05" to 0.5" resolution. Future ground-based ELTs (Extremely Large Telescopes with apertures of 30 m or more that are equipped with extreme AO) may probe the hot gas, dust, and plasma that shine below a wavelength 2 μm with a resolution approaching 0.01". While ELTs will probe stars and plasmas at a narrow band centered at 10 μm, TPF-I/Darwin will be uniquely suited to investigate warm dust, ices, molecules, and a variety of atomic and ionic species with at least an order of magnitude better angular resolution over the much wider spectral range of 5–15 μm. TPF-I/Darwin is especially well suited for probing in the planetary region between 0.1 and 10 AU around forming, maturing, and dying stars with more than an order of magnitude better angular resolution than any other conceived facility.

The TPF-I/Darwin spectral domain contains the lines of may ions and atoms (H, He, Ne, Ar), including several ionization stages of hard-to-deplete noble gases, the rotational and vibrational transitions of a variety of molecules including H_2, forbidden fine-structure lines, continua from dust, and a variety of solid state features from ices and PAH molecules (at wavelengths of 6.2, 7.7, 8.6, 11.3, 12.7, 14.2, and 16.2 μm). Combined, these tracers can be used to map temperature, density, metallically and kinematics of gas at intermediate to cold temperatures (10 to over 10,000 K) and moderate densities (10 to over 10^6 cm^{-3}).

Extension of the wavelength coverage from about 2 μm to as long as 30 μm should be considered. Extension to the shorter wavelengths would permit overlap with ground-based AO-assisted interferometry, improved resolution, and access to the vibrational transitions of H_2, CO, and other molecules and ices. Extension to longer wavelengths would permit observations of cooler, more embedded targets; would provide access to the 24-μm iron complex, the ground-rotational transitions of H_2, and the 20 micron silicate feature, and would extend the use of PAH, [Ne II], Brackett α-based distance, and metallicity determinations to very high redshifts. Darwin/TPF-I capabilities will revolutionize our ability to observe the formation and maturation of stars, planetary systems, and star clusters ranging from loose associations to super-star clusters that evolve into globular systems.

The spectral energy distributions of normal nearby galaxies peak at a rest-frame wavelength of a few microns. For galaxies at high redshifts, this peak will be shifted to observed wavelengths of 5−10 μm. High resolution sensitive measurements at 5−10 μm are crucial for tracing the formation and evolution of high redshift galaxies. At the highest redshifts, rest-frame visual wavelength emission will fall into the Darwin/TPF-I windows. Therefore, this mission will diagnose the very first stars and galaxies to emerge from the "Dark Ages" of the Universe with an angular resolution sufficient to resolve the ionized bubbles they create (star-forming regions of ioninzed hydrogen, HII) and other global properties. A central feature of TPF-I/Darwin is its ability to resolve a length scale of order 100 pc – the size of giant molecular

clouds or an OB association – anywhere in the Universe, enabling the detailed investigation of the cosmic evolution of galactic structure.

3.2 Transformational Astrophysics

We highlight four research areas where TPF-I/Darwin will make revolutionary advances, namely:

- Star and planet formation and early evolution.
- Stellar and planetary death and cosmic recycling.
- The formation, evolution, and growth of black holes.
- Galaxy formation and evolution over cosmic time.

3.2.1 Star and Planet Formation and Early Evolution

Darwin/TPF-I will have a resolution of 1 AU at a distance of 500 pc, the distance to the Orion massive star-forming region. In the nearest regions of low-mass star formation (~125 to 150 pc), 0.25 AU structures will be resolved.

Stars are the fundamental building blocks of the baryonic Universe. Short-lived massive stars and clusters are responsible for the nucleosynthesis of elements heavier than helium, for the ultraviolet (UV) radiation that re-ionized the Universe at the end of the cosmic Dark Ages, and for regulating the physical and chemical state of the interstellar media (ISM) of galaxies. Their powerful stellar winds and terminal supernova explosions dominate the generation of random motions in the ISM. Long-lived low-mass stars provide the stable environment needed for the formation of planetary systems and the evolution of life.
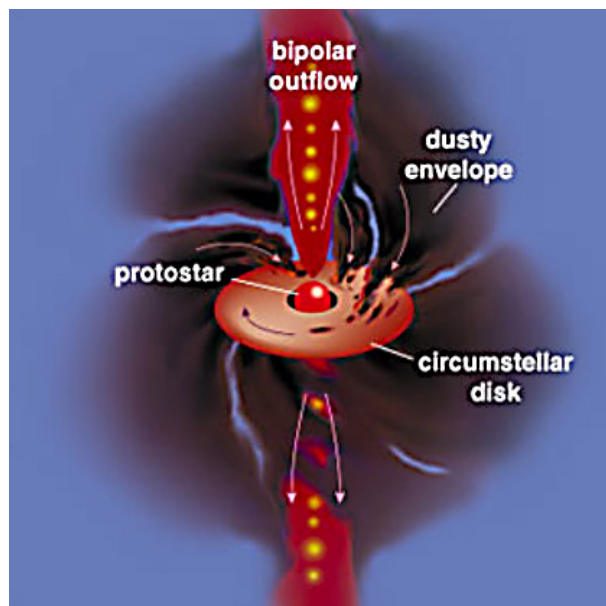
Figure 3-1. Schematic of the circumstellar environment of an isolated young star.

Figure 3-2. HST image of the giant galactic nebula NGC 3603 shows the various stages of the life cycles of stars in one single view, from a starburst cluster of young hot Wolf-Rayet stars and early O-type stars (center) to the evolved blue supergiant Sher 25 (upper right), which marks the end of the life cycle.

Star formation is the process that determines the mass-spectrum (initial mass function —IMF; Kroupa 2000) of stars. Star formation determines how galaxies consume their interstellar media and how they convert this material into long-lived low-mass stars, and star formation controls the rate and nature of galactic evolution.

In the standard model of star formation (Figure 3-1), the inside-out gravitational collapse of a rotating *cloud core* leads to the formation of a *protostellar core* on a time-scale of about 10^4 years. The infall of high-angular-momentum gas forms a spinning, circumstellar disk through which most of the star's final mass spirals onto the protostar on a time-scale of $\sim 10^5$ years. Entrained and dynamo-generated magnetic fields launch powerful jets and bipolar outflows along the rotation axis of the system for a period of order 10^5 to 10^6 years (Reipurth and Bally 2001). Planetary systems form and mature from remnants of the disk in about 10^6 to 10^8 years; low-mass stars reach the main-sequence (MS) in 10^7 to $> 10^8$ years (see the Grenoble stellar evolutionary tracks, Siess, Dofour, and Forestini 2000).

During the last decade, observations have shown that most stars form in highly over-dense, but short-lived clusters that form from the collapsing and fragmenting cores of turbulent molecular clouds (MacLow and Klessen 2004). Furthermore, the birth and early evolution of most stars occurs in the close proximity of luminous, massive stars that irradiate the birth environments with intense UV radiation and which explode as supernovae on time-scales ranging from 3 to 40 Myr, the same time-scale on which
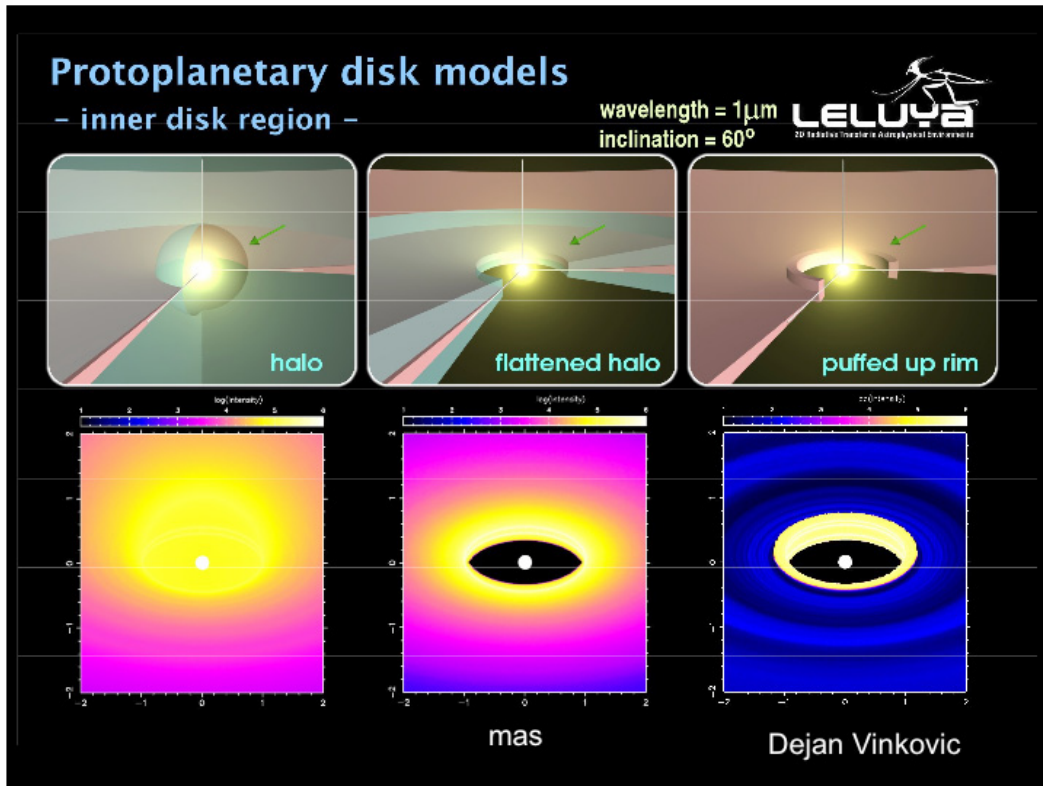
Figure 3-3. Three possible geometries for the centers of T Tauri disks and synthetic images of these models in scattered light. TPF-I could distinguish among these possibilities, shedding light on the origin of close-in planets (Dejan Vinkovic, Princeton Univ.).

planetary systems mature, their central stars reach the main-sequence, and birth clusters and associations disperse (Lada and Lada 2001; Adams et al. 2004). While in the *standard model* for the formation of low-mass stars, they evolve gradually from accreting (Class 0 and I) protostars into Class II and III T Tauri stars, in the modern *clustered formation paradigm*, catastrophic events such as dynamical interactions with sibling stars (Reipurth 2000; Tan 2004), evaporation of envelopes and disks by the intense radiation fields (Johnstone, Hollenbach, and Bally 1998), winds, and supernova explosions punctuate early stellar and planetary system evolution (Hollenbach et al. 2000). Contrary to being hazardous, UV radiation in from both the central protostar and nearby massive stars may actually promote the formation of planetesimals by selectively removing light gases and small particles (Throop and Bally 2005).

Massive stars appear to be preferentially formed in ultra-dense proto-cluster environments where cluster - stellar densities are higher than 10^5 stars per cubic parsec. Interstellar separations are frequently less than a few thousand AU. Darwin/TPF-I 2- to 10- mas resolution in the thermal infrared will resolve a projected interstellar separation of 10 to 50 AU at a distance of 5 kpc, enabling the cores of embedded proto-clusters to be resolved, and their structure analyzed anywhere in the Galaxy. Does the high multiplicity fraction of massive stars originate in the primordial fragmentation of the parent cloud core, or does it develop later in the evolution of the cluster by means of stellar dynamical processes such as three-body encounters?
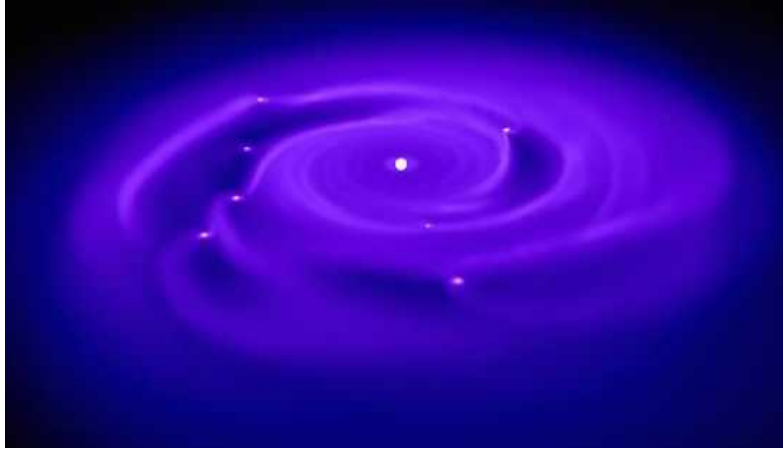
Figure 3-4. A computer simulation showing how a protoplanetary disk surrounding a young star begins, in a relatively short time, to fragment and form gas giant planets with stable orbits (Courtesy of Lucio Mayer, ETH Zürich).

Thermal IR interferometry will resolve the acceleration region where stellar winds are produced in pre-main-sequence stars, Wolf-Rayet stars, and giants. Many such systems are in multiple systems where phenomena associated with wind–wind interactions can be directly imaged. Interferometric spectro-imaging of highly ionized species will provide unique diagnostics of these systems that will complement radio-wavelength observations.

Darwin/TPF-I will resolve forming super-star clusters and starbursts in our Galaxy and in nearby galaxies. Milli-arcsecond angular resolution will enable TPF-I to peer inside clusters to determine the volume density of stars and to directly test formation models for the most massive stars in such systems, even when the clusters are still highly embedded and their stars are still accreting. Do massive stars sink rapidly to the cluster center due to on-going accretion and dynamical friction? Do massive stars always form by accretion, or do stellar interactions and mergers contribute? The multiplicity fraction of massive stars as a function of location within a cluster, and as a function of cluster age, will provide clues.

TPF-I/Darwin will have the capability to resolve the structure of circumstellar and planet-forming disks, and to trace the shadows cast by the "dust walls" formed at the disk inner edge (Figure 3-3), spiral waves, gaps created by forming giant planets, and the compositional variations resulting from condensation sequences (Figure 3-4). The inner radii associated with the evaporation of various ices (such as water, ammonia, and methanol) should be detectable by their characteristic spectral bands. Polarization measurements will enable the measurement of magnetic field geometries by their power to align dust grains. These observations will produce direct tests of planetary system formation models to distinguish between competing paradigms, such as core-accretion and formation via gravitational instability.

The ionization and shock fronts produced by ionizing radiation will be resolved and diagnosed by the analysis of spectral-line ratios. The highest resolution observations should resolve the inner regions where jets and disk winds are launched, thereby providing direct tests of outflow generation models. Are jets formed by ordinary stellar winds, the magnetic X-points where stellar magnetospheres interact with

the circumstellar disk, or are they launched by magnetic fields entrained or dynamo-amplified in the disk itself? Detection of molecular bands from simple molecules (as well as PAH and silicate features) will enable the characterization of chemical and physical gradients in disks.

Darwin/TPF-I will be especially sensitive to young planets, which tend to be larger, hotter, and therefore brighter than mature objects. Forming gas and ice giants will be easy to detect. Even forming or young, rocky terrestrial planets are expected to be brighter, especially following recent accretion events or impacts.

Observations of more mature planetary systems and debris disks with ages ranging from a few million to several hundred million years will lead to direct tests of planetary system evolution models. The Darwin/TPF-I planet-finding capability will enable the direct detection of forming and evolving planets. Large impacts on rocky planets are expected to produce global "lava oceans" that will glow at 10 μm for thousands of years. Thus, direct observations of the conditions following giant impacts and equivalents of the "Late-Phase Heavy Bombardment" suspected to have occurred about 800 Myr after the birth of our own Solar System may be observable in other planetary systems. Source selection would rely on the detection of extensive debris disks that may indicate a high rate of collisions.

The Darwin/TPF-I observations of forming and evolving planetary systems will complement the prime mission of planet detection and characterization by providing direct tests of planet formation and evolution models.

3.2.2 Stellar and Planetary Death and Cosmic Recycling

As stars of all masses evolve off the main sequence, they develop cool, extended envelopes that reprocess most of the emitted starlight into infrared radiation observable with TPF-I. Low- and intermediate-mass stars ($M = 0.8 - 8 M$) make up more than 90 per cent of all the stars that have died in the Universe up to the present time. At the end of their main sequence life-time, they enter the high-luminosity asymptotic giant branch (AGB) phase. During the short so-called superwind phase, the stars eject their hydrogen-rich outer layers to reveal the chemically enriched deeper layers of the star. These stars obtain the highest luminosity and the largest diameter in their existence with the size or nearly an AU. AGB stars are expected to either vaporize, or swallow their planetary systems. Emission from silicates, silicon carbide (SiC), PAHs, and some ices will provide powerful probes of physical and chemical evolution of these objects. In the closest AGB stars, TPF-I/Darwin will resolve the photospheres; in more distant objects, it will probe their winds and dying planetary systems in great details.

After this final burst of activity, these stars evolve into hot, compact white dwarfs with masses in the range of $0.6-1.4 M_o$. The expanding ejecta surrounding the star becomes ionized and forms a planetary nebula before dispersing into the interstellar medium (ISM).

Recently, the Spitzer Space Telescope had detected infrared excess emission from about 15 to 20% of old white dwarf stars near the Sun (Reach et al. 2006; Mullally et al. 2006). This emission indicates the presence of debris disks consisting of mostly large-solid particles that have resisted being dragged into the central white dwarf by the Poynting-Robertson drag for the age of the white dwarf. Such debris disks surrounding aging white dwarfs may trace the remnants of planetary systems that were destroyed during the post-main-sequence red-giant phase of their parent stars. There are hints that in-spiraling solids may
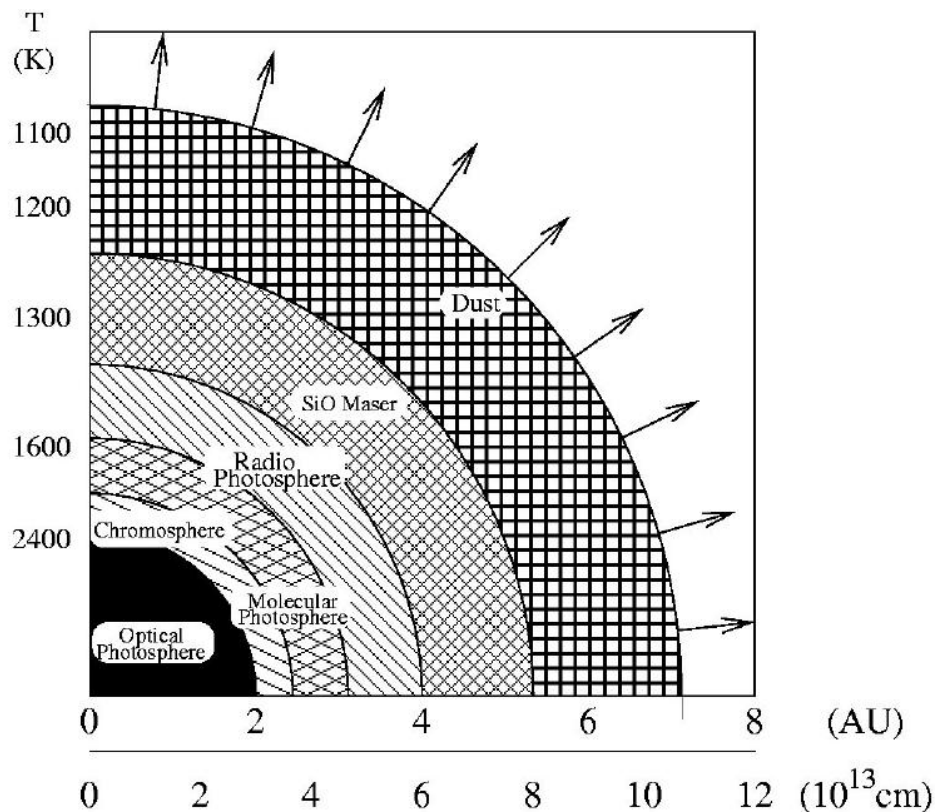
Figure 3-5. Schematic of the atmospheric spatial structure and temperature profile of a typical Mira star (Reid and Menten 1997).

be responsible for anomalous metal-abundances in white dwarf atmospheres. TPF-I/Darwin interferometric imaging may resolve these disks, determine their structure, and constrain their compositions. Such observations may shed independent light on the abundances of planetary systems and that have been destroyed millions to billions of years ago.

AGB mass-loss (e.g., Zijlstra et al. 2006) determines the mass distribution of stellar remnants, including the lower mass limit of type II supernovae progenitors. Stellar mass loss also drives Galactic evolution through replenishment and chemical enrichment of the ISM. Such mass loss contributes roughly half the total gas recycled by all stars (Maeder 1992), creates an amount of carbon roughly equal to that produced by supernovae and Wolf-Rayet stars (Dray et al. 2003; Gavilán, Buell, and Mollá 2005), and is the main source of carbonaceous interstellar dust (Dwek 1998; Edmunds 2001).

TPF-I/Darwin will resolve AGB stars at the distance of the Galactic center. These observations will directly measure the impacts of the high-pressure Galactic-center environments, radiation, and outflows on the structure of AGB star envelopes. VLA and ground-based [NeII] observations have already revealed cometary tails around some evolved stars such as IRS7 (Yusef-Zadeh and Morris 1991). Interferometry will enable the study of such tails to be used as diagnostics of the environments.

There are about 200 moderately evolved AGB stars (Mira variables) known within 1 kpc. Both oxygen-rich (M-type) and carbon-rich (C-type) AGB stars show spectral features around 9.7 μm and 11.3 μm due
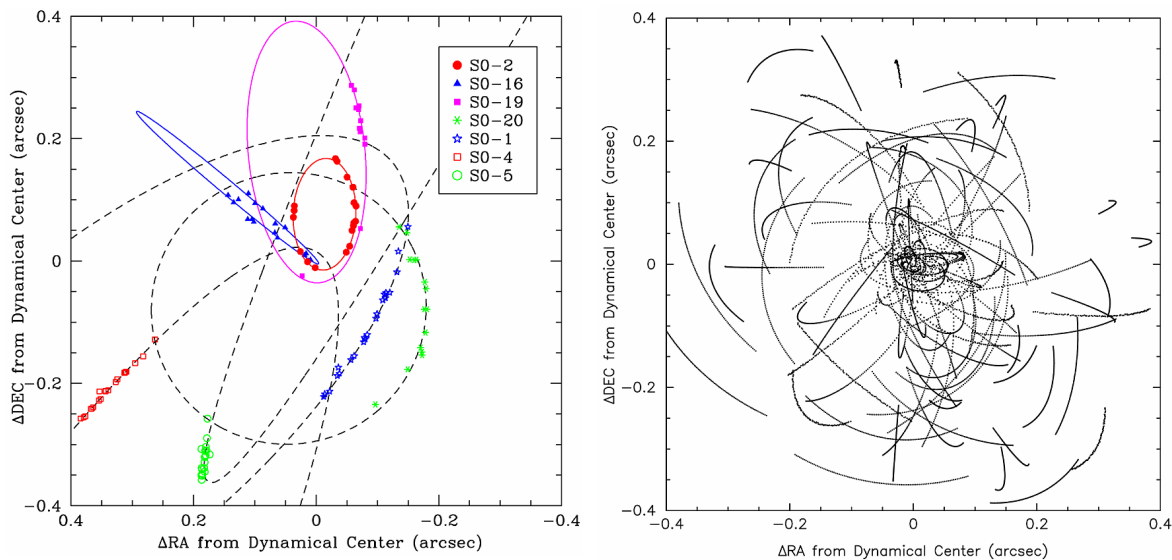
Figure 3-6. (Left panel) Astrometric positions and orbital fits for eight stars that show accelerated proper motion within the central 0.8" × 0.8" of the Galaxy (Ghez et al. 2003). (Right panel) Astrometric positions for a simulated sample of 100 stars detectable with TPF-I. Motions are over a 10-yr baseline assuming ten observations per year per star.

to silicate particles and SiC grain as well as spectral lines from other atomic and molecular species. IRAS detected more than 10^5 new AGB candidates. The improved spectral resolution of ISO and Spitzer allowed the study of the AGB population of the Magellanic Clouds and other Local Group galaxies at mid-infrared wavelengths.

Darwin/TPF-I will detect the circumstellar envelope of AGB stars located well beyond the Local Group where these stars are being found photometrically as galaxy members (e.g., in the Sculptor group at 2.5 Mpc and in the M81 group at 4 Mpc). Furthermore, Darwin/TPF-I will provide detailed maps of the distribution dust and gas within the envelopes of AGB stars within the Galaxy. This will be essential information to tie basic stellar parameters to the properties of mass-loss. This is not only important for the usage of the properties of mass loss for addressing key astrophysical questions (see above), but also to advance theoretical models (e.g. Sandin and Hofner 2003) that cannot predict mass-loss rates from stellar parameters. The later is largely due to the complicated physics of the interplay of stellar pulsation, shock waves, dust formation and radiation pressure which combined all drive the mass-loss.

3.2.3 Formation, Evolution, and Growth of Black Holes

How do black holes form? Do they form first, and trigger the birth of galaxies around them, or do galaxies form first and stimulate the formation of black holes? How do black holes grow? Do they grow in a merger tree as galaxies collide, or do they accumulate their mass by hydrodynamic accretion from surrounding gas and stars in a single galaxy? TPF-I will image the circum-nuclear disks of systems such as M106 (NGC 4258). The H_2O maser disk in that galaxy requires significant IR pumping near 10 μm— thus its disk will be very bright. TPF-I will compliment ELT imaging. The high contrast between the AGN and the disk requires high-fidelity imaging: TPF-I will enable a search for the dominant mode of AGN feeding and probe the launch and collimation regions of AGN jets.
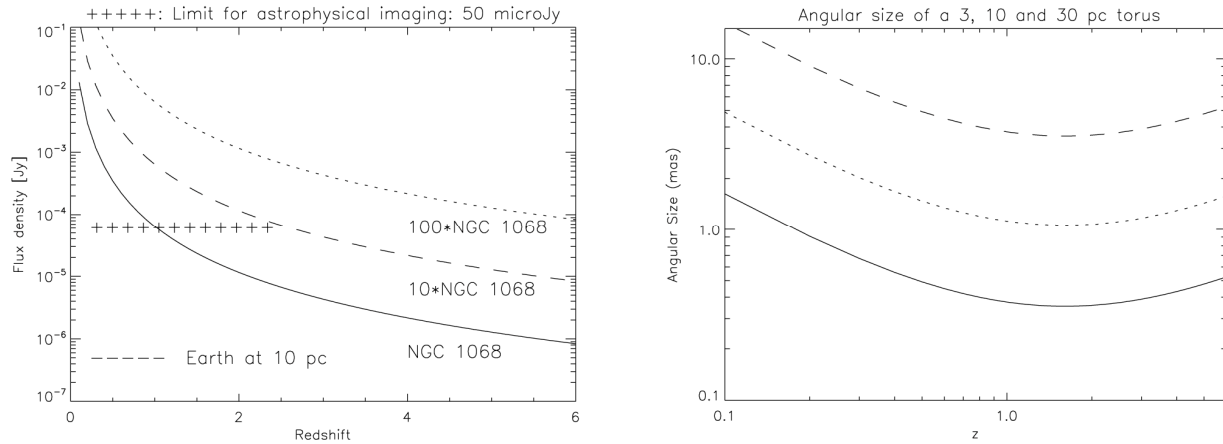
Figure 3-7. The 10-µm flux density (left) and angular scale (right) of dusty tori as a function of redshift. The lines indicated are for AGN as luminous and 10 and 100 times as luminous at 10 µm as NGC 1068. Also the fiducial flux density of an Earth at 10 pc is indicated.

The Galactic center contains the nearest massive black hole (3.6×10^6 M$_o$), a uniquely dense star cluster containing up more that 10^7 stars/pc^3, and a remarkable group of high-mass stars with Wolf-Rayet-like properties. Darwin/TPF-I will be able to trace the distribution of lower mass stars, and probe the distribution of dust and plasma in the in the immediate vicinity of the central black hole. A simulation of a possible sample of stars near the Galactic center is shown in Fig. 3-6.

Galaxies contain exotic systems in which one or more stars orbits an exotic star or a collapsed object such as a white dwarf, neutron star, or black hole. Mass transfer can result is mass ejections in the form of excretion disks such as those seen around contact binaries and symbiotic systems. In others, mass transfer produces accretion disks, which drive powerful winds or jets. In accreting neutron-star or black-hole systems, mass transfer can produce relativistic jets which often mimic the behavior of quasars (hence the term micro-quasar). However, in these systems, phenomena occur on time-scales orders of magnitudes shorter than in the AGN. Exotic and symbiotic systems include massive stars that have undergone recent eruptions (such as eta Carinae), Roche-lobe overflow systems that have shed circumstellar disks (such as WeBo1), and micro-quasars (such as SS 433). Infrared emission can be produced by warm dust in circumstellar tori, by molecules, by highly ionized species such as neon and argon, or by continuum processes such as synchrotron radiation or the inverse Compton effect. Darwin/TPF-I will revolutionize the investigation of these systems by probing the inner AU-scale regions where these flows are energized.

Supermassive black holes are found in the centers of many galaxies. When these objects are fed by strong accretion flows, they eject relativistic jets and powerful winds; these phenomena can drive intense luminosity. Darwin/TPF-I will enable the diagnosis of physical and chemical properties of active galactic nuclei (AGN) at all redshifts. Its 2- to 10-mas angular resolution will produce resolutions ranging from under 1 pc for the nearest AGN to tens of pc for the most distant. Darwin/TPF-I will provide a look at the stellar and interstellar environments of these 10^6 to 10^{10} Solar mass black holes in unprecedented detail. Emission lines (such as Br α, [Ne II], and Argon) will trace the ionized and shock-excited components of the circum-nuclear environment. Are mini-spirals, such as that seen in our own Milky Way, common?

Continuum interferometry will map the circum-nuclear distributions of stars. Synchrotron emission produced by relativistic particles gyrating in nuclear magnetic fields will trace non-thermal continua. The distributions of silicate dust, ices, and PAHs can be used to trace the warm-gas and dust distributions in the circum-nuclear environments of AGN with unprecedented resolution.

Interferometric measurements of the lensed objects may provide the highest resolution studies of stars and interstellar media in the distant Universe. By combining the milli-arcsecond resolution of Darwin/TPF-I with the natural magnification of a gravitational lens, linear resolutions of less than 1 pc can be achieved in the high-redshift Universe.

3.2.4 Galaxy Formation and Evolution

Current galaxy-formation models assume that the large-scale mass distribution in the early Universe is driven by the gravity exerted by dark matter. The evolution of the dark-matter distribution follows from conditions in the early Universe. Gas dynamics, shocks, and radiative heating and cooling all play fundamental roles in the emergence of the first stars and proto-galaxies. The first stars are thought to be massive (10 to 100 Solar masses), and hotter than their modern counterparts. Thus, the first stars are though to create giant HII regions whose red-shifted hydrogen and helium emission lines should be readily observable by Darwin/TPF-I.

While NASA's JWST is expected to make the first detections of these objects, its angular resolution will be limited to the diffraction spot size of its 6.5-m primary mirror, about 0.2". Darwin/TPF-I will resolve scales of order 10 to 100 pc at all redshifts. The IR response will enable the detection of rest-frame near-IR to visual wavelength emission at very high redshifts ($z > 5$). Thus, Darwin/TPF-I will provide the hundred-fold gain in resolution needed to resolve these primordial HII regions. Models suggest that the birth of the very first stars may inhibit further star formation until these primordial stars die, a few million years after their birth. High angular resolution follow-up of JWST-detected "First Light" objects by Darwin/TPF-I will test the current paradigm for the formation of the first stars. Are they truly isolated, single objects, or are they surrounded by young clusters of stars?

Soon after the formation of the very first stars, their supernovae will pollute the surrounding medium, causing the condensation of dust. Dust heated by starlight, and the HII regions surrounding the very first stars will be visible and resolvable by Darwin/TPF-I. Subsequent growth of primordial galaxies occurs by a combination of merging and in-fall of primordial gas.

The baryonic matter in young galaxies is expected to be dominated by gas. As the first generations of stars explode in supernova explosions, they will pollute their environments with metals. Dust and molecule formation will drive star formation to increasingly resemble star formation in the current epoch. Hot dust, giant HII regions, and warm molecular clouds are expected to emerge. Darwin/TPF-I will play a crucial role in mapping the distributions of stars, clusters, super-giants, post-main sequence stars, supernovae, and emerging black holes in the highest redshift galaxies being detected at sub-mm wavelengths with today's instruments (Smail et al. 1997, Hughes et al. 1998, Barger et al. 1998) or in the future by the Atacama Large Millimeter Array (ALMA) and in the thermal IR by JWST.

Darwin/TPF-I will be especially sensitive to forming super-star clusters, the suspected progenitors of today's globular cluster systems. While JWST may detect galaxies containing such clusters at high red-
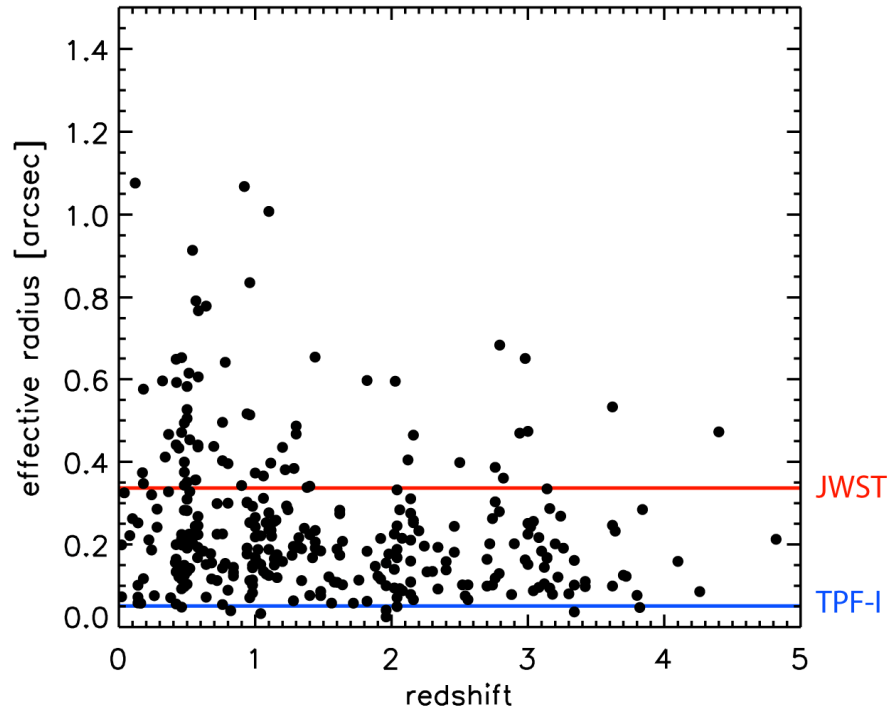
Figure 3-8. Effective radii measured in the K-band as a function of redshift for a subsample of FIRES/VLTsurvey with $K_{AB} > 25$. TPF-I can resolve most of these galaxies, many more than JWST.

shifts, Darwin/TPF-I will be needed to determine their galactic locations, to determine their relationships to other galactic structures, and to characterize their global properties.

Current theory, modeling, and observations indicate that galaxies grow and evolve by merging. How do these processes impact global and local star formation and the formation, growth, and evolution of black holes? Darwin/TPF-I will obtain milli-arcsecond resolution observations that can be directly compared to models.

Scheduling flexibility will enable Darwin/TPF-I to respond to targets of opportunity and transient phenomena such as ultra-high redshift, possibly population III, supernovae, flaring activity in the AGN, or even currently unanticipated time-dependent phenomena. Darwin/TPF-I will provide milli-arsecond characterization of these phenomena and their immediate environments.

Galactic evolution will remain a central theme of astrophysics for decades to come. The investigation of large samples of distant galaxies will be crucial for such studies. The "Lyman break technique" has defined samples of more than 1000 galaxies between $2.5 < z < 5$ (e.g., Steidel et al. 1999). Lyα and Hα emitting galaxies have also been found with deep imaging through narrow-band filters (e.g.. Venemans et al. 2002; Kurk et al. 2003) or by selection of very red J−K colors (Franx et al. 2003). Spectroscopic follow-up of Submillimetre Common-User Bolometer Array (SCUBA) galaxies, radio galaxies (e.g. de Breuck et al. 2001), and X-ray emitters (e.g. Rosati et al. 2002) have yielded significant samples of $z > 2$ objects.
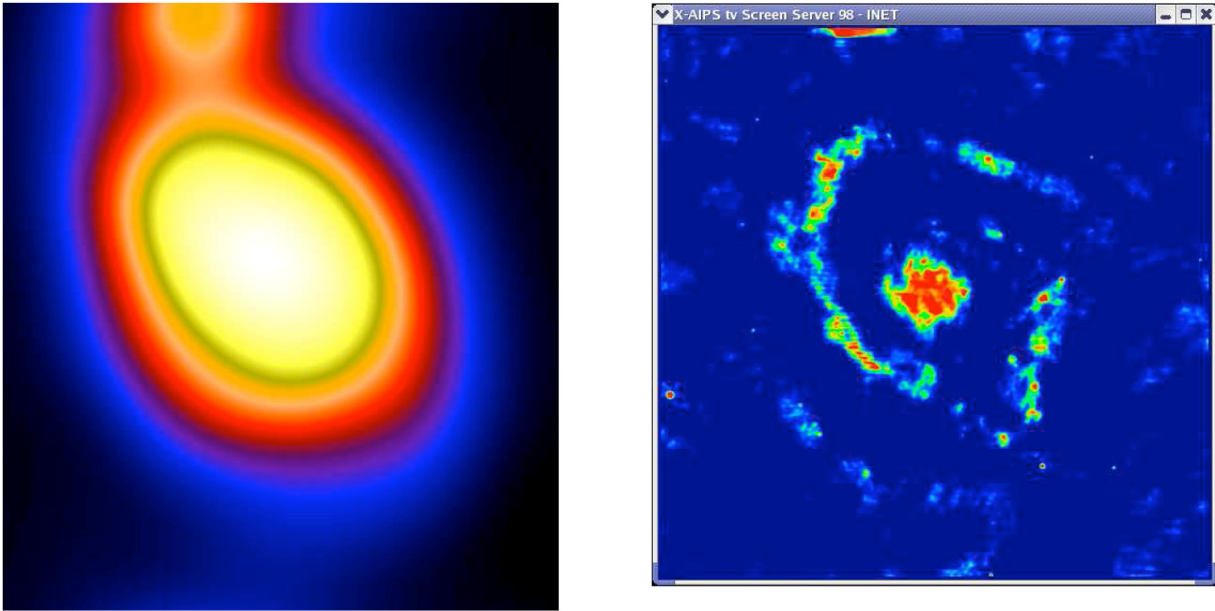
Figure 3-9: Simulated images of a M51-type galaxy at z = 3 as observed with JWST (left) and Darwin (right).

The Faint Infra Red Extra-galactic Survey (FIRES, Franx et al. 2000), a very deep infrared survey centered on the Hubble Deep Field South using the Infrared Spectrometer and Array Camera (ISAAC) instrument mounted on the Very Large Telescope (VLT) (Moorwood 1997) demonstrates that there will be plenty of targets to investigate with Darwin/TPF-I. With integration times of more than 33 hours for each of the infrared bands (J, H, and K), limiting AB magnitudes of 26.0, 24.9, and 24.5, respectively, are reached (Labbé et al. 2003). Recently, this field has been imaged at 3 to 8 μm with the Infrared Array Camera (IRAC) on the Spitzer Space Telescope with the aim of accurately determining stellar masses for distant red galaxies (see Fig. 3-8 and Labbé et al. 2005). From these studies, we conclude that, for the brighter objects, it is possible to obtain good images with a signal-to-noise ratio of 50 within integration times of 25–50 hours using Darwin/TPF-I.

Darwin/TPF-I will resolve individual OB associations, massive star clusters, and their associated giant HII regions. By observing multiple fields, interferometric maps of entire galaxies can be obtained at selected redshifts. By carefully selecting targets of a specific type, the evolution of galaxy structures can be tracered as functions of redshift and environment. The evolution of metallicity with cosmic age (and redshift) can be mapped using the various molecular tracers, ices, PAH bands, and noble-gas lines that fall into the pass-band of Darwin/TPF-I.

3.2.5 Other Science Opportunities

- **Our home planetary system**: TPF-I/Darwin will easily measure the diameters, and properties of dwarf planets (Kuiper Belt Objects), moons, asteroids, and comet nuclei. Low-resolution spectro-photometry will constraint the natures of surfaces, atmospheres, and environments.

- **Parallax and proper motions in the Galactic Plane**: Establish a network of Galactic fiducial distance markers using IR-bright stars.

- **Resolve milli-arcsecond separation of multiple stars**: Search for compact binaries formed during the dynamical decay of non-hierarchical multiple star systems and the ejection of high velocity stars in embedded young clusters.

- **Are there intermediate black Holes (IMBHs) in the Galactic Center?** Is there a 1000–10,000 Solar mass black hole in the IRS13 cluster in the GC, or in other clusters in this region? The presence of IMBHs may explain how dynamical friction has enabled the migration of massive stars into the immediate vicinity of SgrA*. TPF-I will measure the mass functions and measure proper motions of cool stars and red-giants in the IRS 13 cluster, complementing measurements with ELTs to determine the presence or absence of IMBHs.

- **Image stellar micro-lensing events**: (target of opportunity, TOO, program). Another unique application for TPF-I will be resolving micro-lensing events detected in future infrared galactic plane surveys. Currently, most microlensing surveys are executed in the visible wavelengths; thus, they have been limited to fields out of the galactic plane (e.g.,the galactic Halo and the Large Magellanic Cloud). However, infrared detection is necessary to observe inner bulge stars or to investigate the massive astronomical compact halo object MACHO population in the central galaxy. TPF-I/Darwin will have the resolution to resolve some of the lensing events allowing the mass-distance ambiguity to be lifted in the gravitational lens model (Boden et al. 1988; Dalal and Lane 2003) and to detect the lensing star directly in some cases (Nguyen et al. 2004).

- **Excretions disk and exotic high luminosity objects in the Milky Way and the Local Group**: Eta-Carinae-like objects, LBVs, Be star excretion disks, and other objects.

- **Micro-quasars**: TPF-I/Darwin will probe excretion disks produced by Roche-Lobe overflow and trace the inner portions of relativistic jets by means of IR synchrotron emission and ions entrained in the jet sheath.

- **SNe**: TPF-I/Darwin will be able to image the formation and evolution of dust in supernova ejecta and trace the structure of the circumstellar environment into which the blast is propagating. The dust, molecules, atoms, and ions launched by the supernova progenitor are illuminated by both the supernova flash and by the advancing shock front of the ejecta. Over a wide range of conditions, the resulting emission from the circumstellar environment peaks in the IR.

- **Dark Matter and dark energy**: Darwin/TPF-I studies of gravitational lensing by galaxy clusters, AGN, and ordinary galaxies may provide a unique tool for probing the nature of dark matter. Measurements of background time-variable objects in gravitationally lensed systems will enable accurate characterizations of differential time-delays along different ray paths, giving clues about the geometry of the space-time in the lensing objects. These measurements, when made with milli-arcsecond resolution, will provide unprecedented constraints on the structure of dark matter haloes.

3.3 Conclusions

Darwin/TPF-I will open a gateway to future space-based interferometry to deliver ever increasing angular resolution throughout the electromagnetic spectrum. The baseline design will provide order-of-magnitude improvements in angular resolution over any other instrument. Combined with sensitivity to objects as faint as magnitude 20, Darwin/TPF-I capabilities have the potential for revolutionary advances in all areas of astrophysics and planetary science. This mission will transform our understanding of galaxy formation and evolution, stellar and planetary system origins, the cycles of matter and energy in the cosmos; and it will enable the detailed mapping of surfaces and weather patterns in Solar System objects. The utility of this instrument for general astrophysics and planetary science will only be limited by the lack of available observing time.

3.4 References

Adams, F. C., Proszkow, E. M., Fatuzzo, M., and Myers, P. C., "Early evolution of stellar groups and clusters: Environmental effects on forming planetary systems," *Astrophys. J.* **641**, 504–525 (2006).

Barger, A. J., Cowie, L. L., Sanders, D. B., et al., "Submillimetre-wavelength detection of dusty star-forming galaxies at high redshift," *Nature* **394**, 248–251 (1998).

Boden, A. F., Shao, M., and van Buren, D., "Astrometric observations of MACHO gravitational microlensing," *Astrophys. J.* **502**, 538–549 (1998).

Dalal, N., and Lane, B. F., "Bringing closure to microlensing mass measurements," *Astrophys. J.* **589**, 199–209 (2003).

De Breuck, C., van Breugel, W., Röttgering, H., et al., "Spectroscopy of ultra-steep-spectrum radio sources," *Astron. J.* **121**, 1241–1265 (2001).

Dray, L. M., Tout, C. A., Karakas, A. I., and Lattanzio, J. C., "Chemical enrichment by Wolf-Rayet and asymptotic giant branch stars," *Mon. Not. R. Astron. Soc.* **338**, 973–989 (2003).

Dwek, E., "The evolution and elemental abundances in the gas and dust phases of the Galaxy," *Astrophys. J.* **501**, 643–665 (1998).

Edmunds, M. G., "An elementary model for the dust cycle in galaxies," *Mon. Not. R. Astron. Soc.* **328**, 223–236 (2001).

Franx, M., Labbé, I., Rudnick, G., et al., "A significant population of red, near-infrared high-redshift galaxies," *Astrophys. J.* **587**, L79–L82 (2003).

Gavilán, M., Buell, J. F., and Mollá, M., "Low and intermediate mass star yields: The evolution of carbon abundances," *Astron. Astrophys.* **432**, 861–877 (2005).

Ghez, A. M., Salim, S., Hornstein, S. D., et al., "Stellar orbits around the Galactic central black hole," *Astrophys. J.* **620**, 744–757 (2005).

Granato, G., Danese, L., and Franceschini, A., "Thick tori around active galactic nuclei: The case for extended tori and consequences for their x-ray and infrared emission," *Astrophys. J.* **486**, 147–159 (1997).

Hollenbach, D. J., Yorke, H. W., and Johnstone, D., "Disk dispersal around young stars," in *Protostars and Planets IV*, editors, Mannings, V., Boss, A. P., and Russell, S. S., University of Arizona Press: Tucson, AZ, 401 (2000).

Hughes, D. H., Serjeant, S., Dunlop, J., et al., "High-redshift star formation in the Hubble Deep Field revealed by a submillimeter-wavelength survey," *Nature* **394**, 241–247 (1998).

Johnstone, D., Hollenbach, D., and Bally, J., "Photoevaporation of disks and clumps by nearby massive stars: Application to disk destruction in the Orion nebula," *Astrophys. J.* **499**, 758–776 (1998).

Kroupa, P., "The initial mass function of stars: Evidence for uniformity in variable systems," *Science* **295**, 82–91 (2002).

Labbé, I., Franx, M., Rudnick, G., et al., "Ultradeep near-infrared ISAAC observations of the Hubble Deep Field South: Observations, reduction, multicolor catalog, and photometric redshifts," *Astron. J.* **125**, 1107–1123 (2003).

Labbé, I., Huang, J., Franx, M., et al., "IRAC mid-infrared imaging of the Hubble Deep Field-South: Star formation histories and stellar masses of red galaxies at $z>2$," *Astrophys. J.* **624**, L81–L84 (2005).

Lada, C. J., and Lada, E. A., "Embedded clusters in molecular clouds," *Ann. Rev. Astron. Astrop.* **41**, 57–115 (2003).

Maeder, A., "Stellar yields as a function of initial metallicity and mass limit for black hole formation," *Astron. Astrophys.* **264**, 105–120 (1992).

MacLow, M.-M., and Klessen, R. S., "Control of star formation by supersonic turbulence," *Reviews of Modern Physics* **76**, 125–194 (2004).

Moorwood, A. F., "ISAAC: a 1–5 μm imager/spectrometer for the VLT," Optical Telescopes of Today and Tomorrow, *Proc. SPIE* **2871**, Ardeberg; A. L. editor, 1146–1151 (1997).

Mullally, F., Kilic, M., Reach, W. T., et. al., "A Spitzer white dwarf infrared survey," *Astrophys. J. Supp. Ser.* astro-ph/0611588 (2006).

Nguyen, H. T., Kallivayalil, N., Werner, M. W., Alcock, C., Patten, B. M., and Stern, D., "Spitzer Space Telescope observations of the aftermath of microlensing event MACHO-LMC-5," *Astrophys. J. Supp. Ser.* **154**, 266–270 (2004).

Reach, W. T., Kuchner, M. J., von Hippel, T., Burrows, A., Mullally, F., Kilic, M., and Winget, D. E., "The dust cloud around the white dwarf G29-38," *Astrophys. J.* **635**, L161–L164 (2005).

Reid, M. J., and Menten, K. M., "Radio photospheres of long-period variable stars," *Astrophys. J.* **476**, 327–346 (1997).

Reipurth, B., "Disintegrating multiple systems in early stellar evolution," *Astron. J.* **120**, 3177–3191 (2000).

Reipurth, B., and Bally, J., "Herbig-Haro flows: Probes of early stellar evolution," *Ann. Rev. Astron. Astrophys.* **39**, 403–455 (2001).

Rosati, P., Tozzi, P., Giacconi, R., et al., "Chandra Deep Field South: The 1 million second exposure," *Astrophys. J.* **566**, 667–674 (2002).

Röttgering, H. J. A., D'Arcio, L., Eiroa, C., et al. "Astrophysical Imaging with the Darwin IR interferometer," *Towards Other Earths: Darwin/TPF and the Search for Extrasolar Terrestrial Planets*, Proc. ESA-SP 539, European Space Agency: Noordwijk, The Netherlands, pp. 299–308 (2003).

Sandin, C. and Höfner, S., "Three-component modeling of C-rich AGB star winds. I. Method and first results," *Astron. Astrophys.* **398**, 253–266 (2003).

Siess, L., Dufour, E., and Forestini, M., "An internet server for pre-main sequence tracks of low- and intermediate-mass stars," *Astron. Astrophys.* **358**, 593–599 (2000). (http://astropc0.ulb.ac.be/~siess/index.html)

Smail, I., Ivison, R. J., and Blain, A. W., "A deep sub-millimeter survey of lensing clusters: A new window on galaxy formation and evolution," *Astrophys. J.* **490**, L5–L8 (1997).

Steidel, C. C., Adelberger, K. L., Giavalisco, M., Dickinson, M., and Pettini, M., "Lyman-break galaxies at z>4 and the evolution of the ultraviolet luminosity density at high redshift," *Astrophys. J.* **519**, 1–17 (1999).

Tan, J. C., Krumholz, M. R., and McKee, C. F., "Equilibrium star cluster formation," *Astrophys. J.* **641**, L121–124 (2006).

Tan, J. C, "The Becklin-Neugebauer Object as a runaway B star, ejected 4000 years ago from the θ1 Orionis C system," *Astrophys. J.* **607**, L47–L50 (2004).

Throop, H. B., and Bally, J., "Can photoevaporation trigger planetesimal formation?" *Astrophys. J.* **623**, L149–L152 (2005).

Venemans, B. P., Kurk, J. D., Miley, G. K., et al., "The most distant structure of galaxies known: A protocluster at z=4.1," *Astrophys. J.* **569**, L11–L14 (2002).

Yusef-Zadeh, F., and Morris, M., "A windswept cometary tail on the Galactic supergiant IRS 7," *Astrophys. J.* **371**, L59–L62 (1991).

Zijlstra A. A., Matsuura, M., Wood, P. R., et al., "A Spitzer mid-infrared spectral survey of mass-losing carbon stars in the Large Magellanic Cloud," *Mon. Not. R. Astron. Soc.* **370**, 1961–1978 (2006).

4 Design and Architecture Trade Studies

There are many different ways in which a mid-IR nulling interferometer can be implemented, each with strengths and weaknesses. This chapter describes the main issues involved and the trade study that was conducted to select the best configuration. The first section describes the principle of operation of a nulling interferometer observing planets around nearby stars. Section 4.2 introduces the performance models that are used to assess the capability of each design. The configurations considered are outlined in Section 4.3. Subsequent sections address key elements of the trade: aperture diameter and array size (Section 4.4), co-planar vs. non-co-planar arrays (Section 4.5), beam combiner design (Section 4.6), the impact of stray light (Section 4.7), the nature and mitigation of instability noise (Section 4.8), and the imaging properties of these phased arrays (Section 4.9). These elements are all combined in the trade study that was conducted in 2004 to select the best architecture as summarized in Section 4.10.

4.1 Principle of Operation

In this section we describe how planet photons can be isolated from their parent star using a nulling interferometer.

Figure 4-1 shows the simplest nulling interferometer – the single Bracewell configuration – proposed by Bracewell in 1979. This comprises two collecting apertures separated by baseline length B, phased such that the light from an on-axis source is canceled in the single-mode spatial filter at the beam combiner output. This is the nulled or dark output port; all the on-axis photons exit from the bright port to the left of the figure. To implement this scheme requires that a phase difference of π, independent of wavelength, be introduced between the two arms. The corresponding response of the interferometer on the sky is shown in both upper panels. It is a sinusoidal corrugation with a null running through the star at the center, and an angular periodicity of λ / B. If the array is rotated about the line of sight to the star, then this corrugated pattern rotates with respect to the star and the offset planet. While the star remains on the null, the planet follows the circular locus and the detected planet photon rate (lower right) rises and falls as the peaks and troughs of the response sweep through the location of the planet. The main disadvantage of the single Bracewell configuration is that the response on the sky is symmetric. As a result there is ambiguity in the location of the planet, the exozodiacal dust emission can have a similar signature to the planet, and (most important) it is not possible to implement an effective chopping scheme.
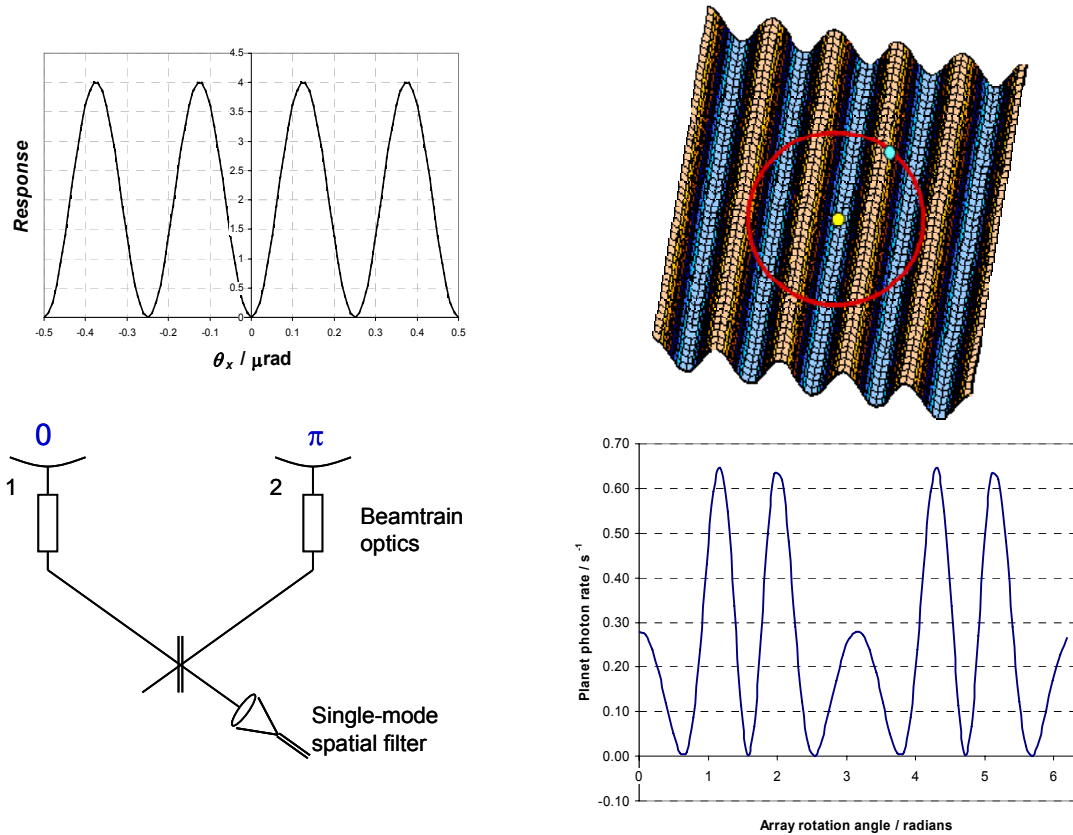
Figure 4-1. Single Bracewell configuration. The schematic of the interferometer is shown, lower left. A cross-section through the fringe response on the sky is shown, upper left. The fringe pattern is rotated around the star (hidden behind a central null) to detect a planet. The Planet follows the red locus as the array is rotated about line of sight to star, upper right; the corresponding photon rate vs. rotation angle is shown at lower right.

These disadvantages are overcome with the Dual Bracewell configuration, an example of which is illustrated in Figure 4-2. There are now four collecting apertures. In this case, they are deployed along a line with equal spacing, phased as indicated. This configuration is essentially two single Bracewell baselines, which are then cross-combined with a third beam combiner with a relative phase shift of $\pi / 2$. The resulting response on the sky of this four-element phased array is shown in the top panel. The structure is more complex than before, and there is a clear left–right asymmetry. We will refer to this as the 'left' chop state, since there is a large peak in the response immediately to the left of the star.
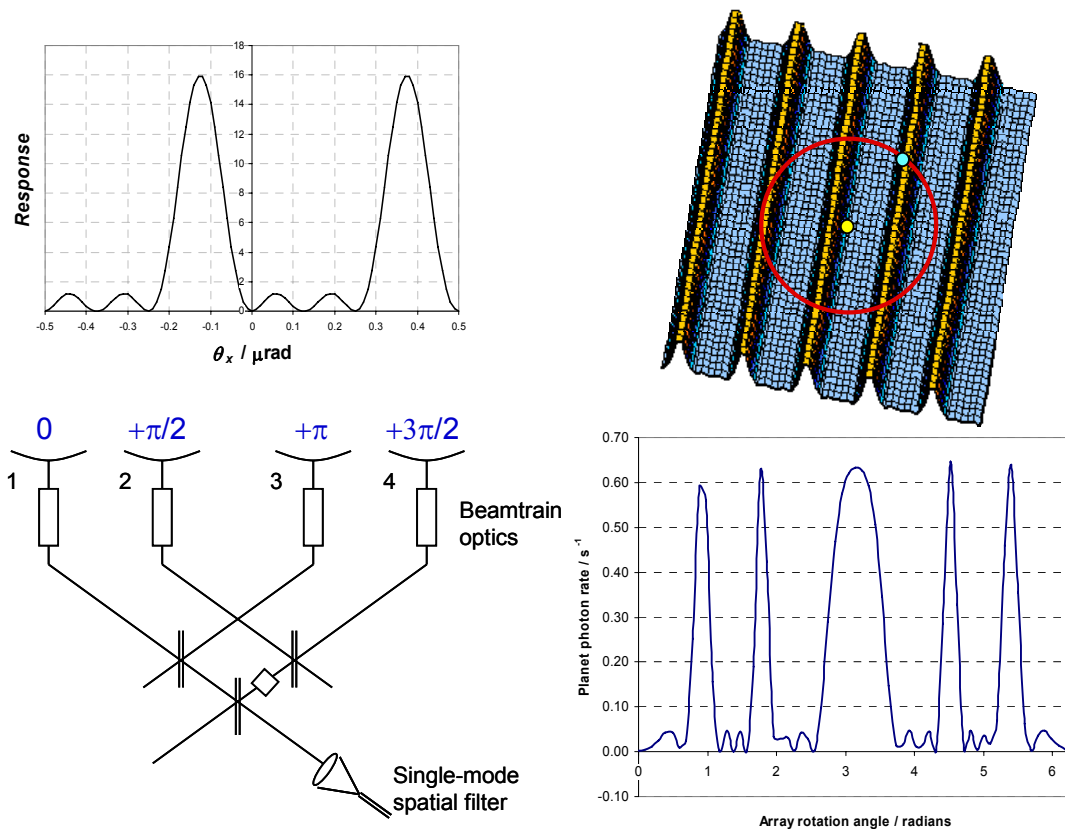
Figure 4-2. Dual Bracewell configuration. Lower left – schematic of interferometer; upper left – section through response on the sky; upper right – response on sky showing star at central null and planet offset. The Planet follows the red locus as the array is rotated about the line of sight to the star; the corresponding photon rate vs. rotation angle is shown at lower right.

By negating the relative phases of the collectors, we obtain the mirror image response on the sky, as shown by the dashed line in Figure 4-3. This is the 'right' chop state. By switching the phasing of the instrument back and forth between these two states, the response on the sky is chopped from left to right and back. Taking the difference of the photon rates obtained gives the 'chopped' response denoted by the heavy line in Figure 4-3 (upper left panel) and the 3D view shown in the upper right. The chopped response is purely asymmetric, and the chopped photon rate has both positive and negative excursions. It is now possible to distinguish the side of the star on which the planet is located, and to discriminate against any symmetric sources of emission (e.g., star, exozodiacal dust). Any source of noise (e.g., stray light) that contributes equally to the left and right chop states is also removed.
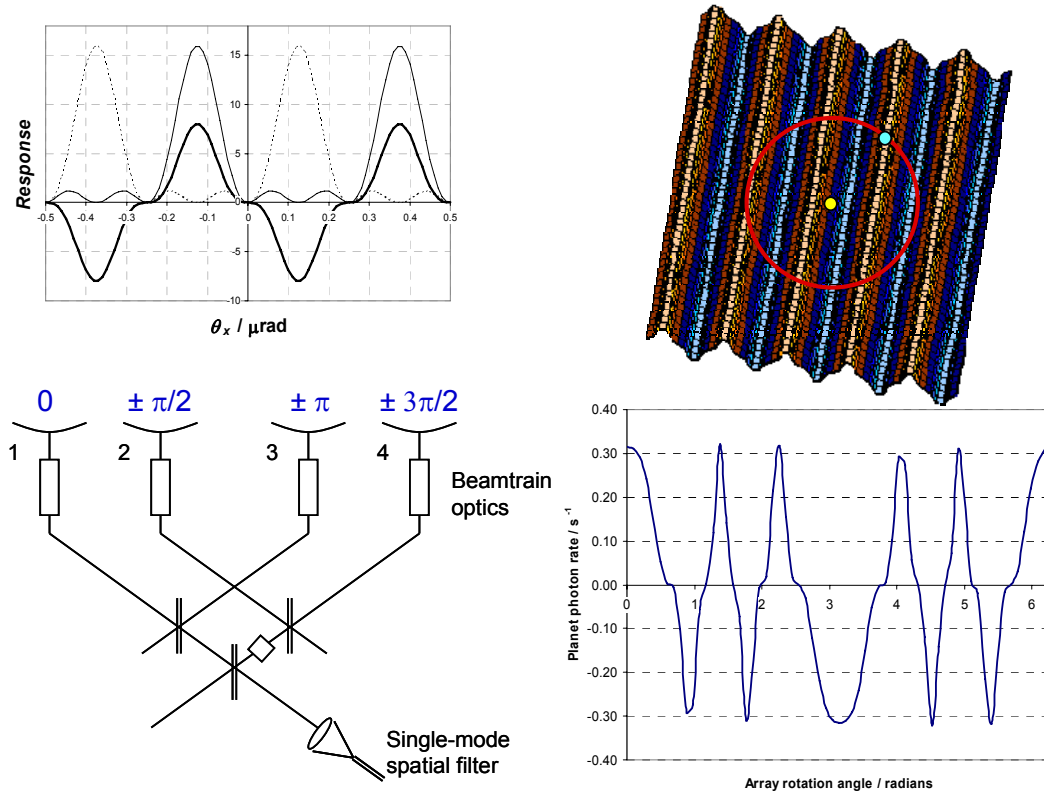
Figure 4-3. Chopped dual Bracewell configuration. Lower left – schematic of interferometer; upper left – section through response on the sky; upper right – response on sky showing star at central null and planet offset. The planet follows the red locus as the array is rotated about the line of sight to the star; the corresponding photon rate vs. rotation angle is shown at lower right.

The lower right panel of Figure 4-3 shows the variation of the chopped planet photon rate with the rotation angle of the array. This characteristic signature depends on the location of the planet relative to the star. As we change the 'azimuthal' offset of the planet, the signature pattern is shifted left or right with respect to the array rotation angle. Increasing the radial offset of the planet from the star means that the circular locus in the upper right panel of Figure 4-3 expands and passes through more peaks and valleys of the response, resulting in a signature pattern with higher 'frequency'. In general, the data must be inverted to obtain the fluxes and locations of any planets that are present.

The approach that has been used most commonly to do this is correlation mapping, first suggested by Angel and Woolf (1997). The principle is described in Figure 4-4. The process is closely analogous to the Fourier transform used for standard interferometric image synthesis. The cross-correlation process generates a "dirty map" (a term borrowed from radio synthesis imaging), which must be deconvolved to extract the point-like planets. The example in Figure 4-4 shows the noise-free dirty map for a single point source, and therefore represents the point-spread function (PSF) for the array. Because we are dealing
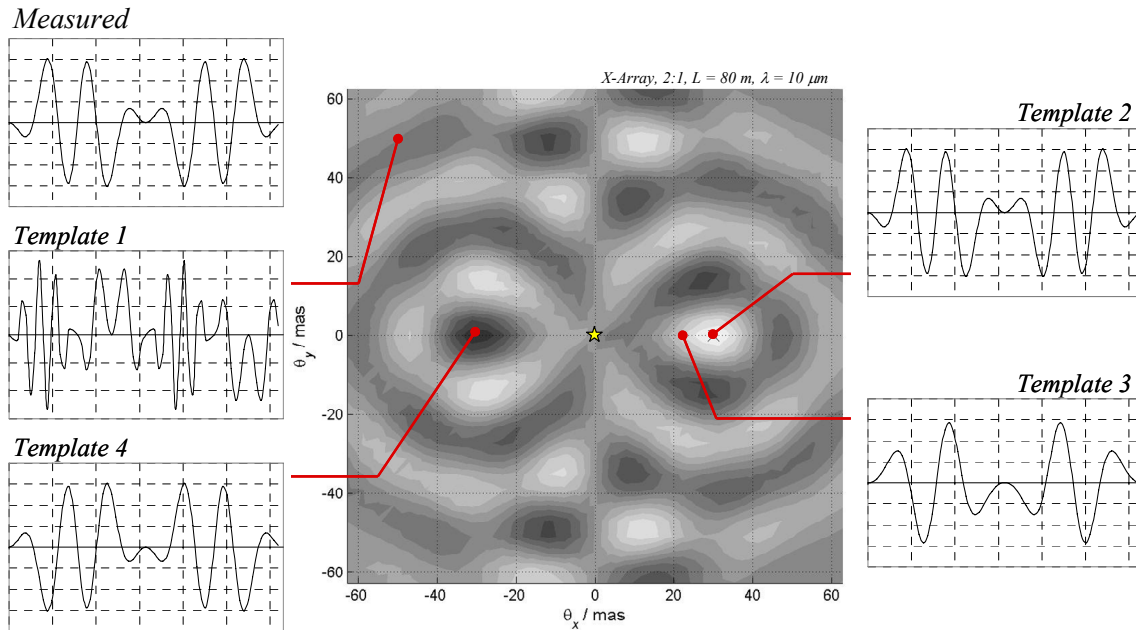
Figure 4-4. Calculation of the cross-correlation map. The measured chopped planet photon rate vs. array rotation angle is shown in the upper left (no noise). For each possible location of a planet in the map, we can generate a template for the signal that would be obtained. This grid of templates is cross-correlated with the measured signal, and the level of correlation is plotted as the grey-scale. Template 1 would result from a planet in the upper left of the plot. The template is clearly a poor match to the measured signal, and the correlation is low. The highest correlation is obtained with template 2, which corresponds to the actual location of the planet. Template 3 is from a slightly offset location and has reduced correlation. Template 4 is from the opposite side of the star and has a perfect anti-correlation with the measured signal.

with a phased array in which more than two collectors are combined in a single output, the PSF is more complex than for a standard imaging array in which each baseline is measured independently. There are satellite peaks in addition to the main peak, each of which has sideobes, and the PSF varies with the position in the map. Section 4.9.2 shows how these properties depend on the array configuration. Approaches to deconvolution are described in Section 4.9.4.

Up to this point the analysis has been for a single wavelength. The measurements in practice span a broad range of wavelengths (nominally 6.5–18 μm). Independent of the desire to do spectroscopy, the measurement must be broken out into a number of spectroscopic channels to avoid smearing together the different planet signatures (photon vs. array-rotation angle) obtained at each wavelength. Each of these channels is processed independently to obtain a correlation map. The correlation maps can then be co-added (with appropriate weighting) to obtain the net correlation map. The wide range of wavelengths greatly extends the *u-v* coverage of the array, suppressing the sidelobes of the PSF.
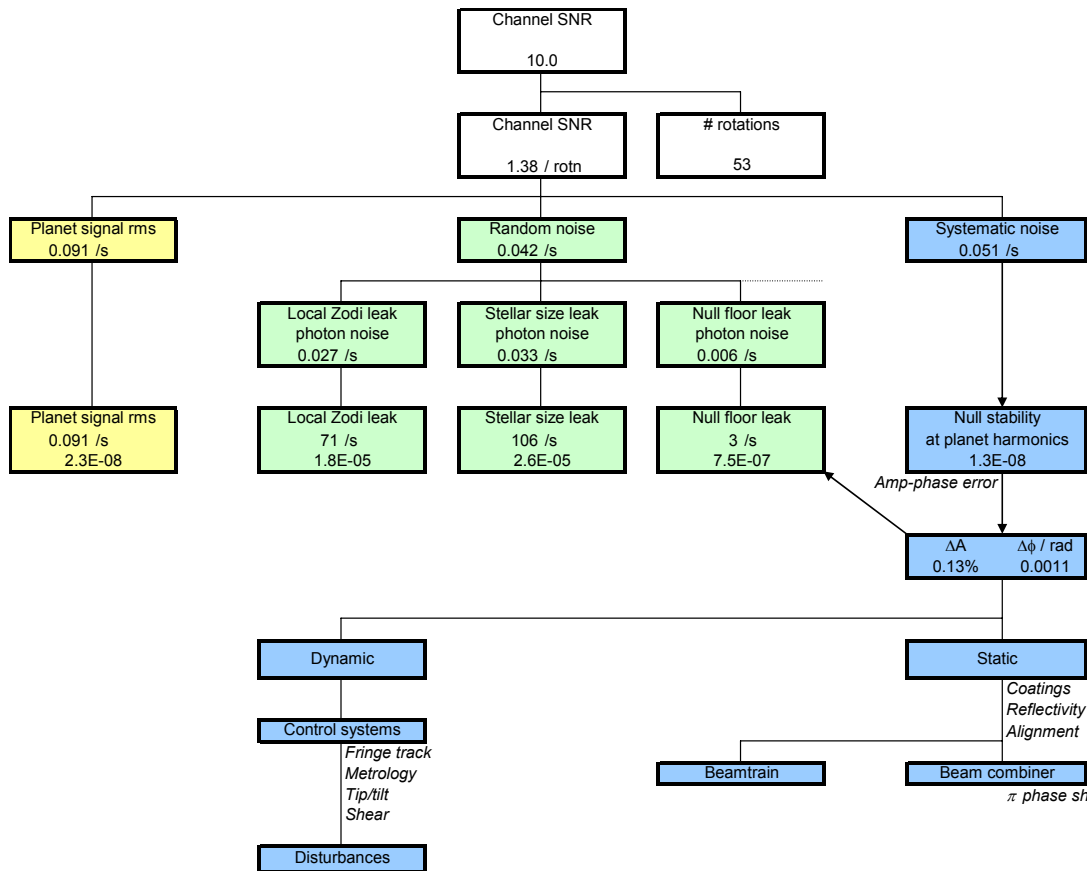
Figure 4-5. Simplified TPF-I error budget for the signal-to-noise ratio (SNR) required for ozone detection at 10-μm wavelength.

4.2 Performance Models

The two key performance models are described in this section: the Interferometer Performance Model (IPM) for predicting the SNR on a specified target; and the Star Count Model for estimating the number of targets that can be surveyed over the duration of the mission.

4.2.1 Interferometer Performance Model

The TPF Interferometer Performance Model (IPM) is maintained as a series of Excel spreadsheets and is used both to estimate the performance of different architectures, and to derive the requirements for the baseline design. The spreadsheet performance model is run as a bottom-up calculation; that is, the overall performance is calculated based on the specified low-level inputs (as opposed to a top-down suballocation approach). The inputs can be adjusted and balanced until the desired output performance is obtained, at which point the input values assumed become the requirements on the instrument.

Figure 4-6. Full TPF-I Error Budget for a Single Spectral Channel

Figure 4-5 shows a simplified version of the TPF-I error budget. The values shown result in an SNR of 10 for an ozone spectral channel spanning 9.5 to 10.0 μm, which currently represents the driving requirement on the integration time. The Earth-like planet orbits a G2 Sun-like star with an angular separation of 50 mas at 15 pc distance. The ecliptic latitude is 30 degrees (this determines the contribution from local zodiacal dust). The array has a linear Dual Chopped Bracewell configuration, comprising four 4-m diameter collectors spaced at 30-m intervals with phases of 0, π, π/2, and 3π/2, for a total array size of 90 m.

The overall SNR is built up from 53 rotations of the array, each with a period of 50,000 s. The total observing time is 31 days (which does not currently include any overhead for calibration). The SNR for a single rotation is broken out into the root-mean-square (rms) of the planet signal variations and the contributions from random and systematic noise. The rms planet signal in this spectral band is less than 0.1 photons/s, corresponding to a fraction 2.3×10^{-8} of the stellar signal in the same channel. In this example, the random noise has approximately equal contributions from the stellar size leakage and from local zodiacal dust. Other contributions (including exozodiacal dust emission, instrument thermal emission and stray light) have been omitted for clarity. The conversion from leakage photon rate to leakage photon noise is based on shot noise for a rotation of 50,000 s. The null floor leak term represents the photon noise arising from mismatches in the instrument beamtrains. The null floor makes a much lower contribution to the random noise budget than the local zodiacal emission and stellar leakage since it is driven by need to minimize the systematic error.

The instability noise contribution to the error budget is indicated by the blue boxes, and it is chosen to be similar in magnitude to the random error. The contribution of 0.051 photon/s corresponds to a null fluctuation of order 10^{-8} at frequencies similar to the planet signal. These null fluctuations result primarily from nonlinear combinations of amplitude (ΔA) and phase ($\Delta\phi$) errors of the electric fields from the collectors. Analysis shows that the electric fields delivered by each collector must be matched in amplitude to within an rms error of less than 0.13% (equivalent to 0.26% intensity error), and matched in phase to within 1 milliradian at $\lambda = 10$ μm (equivalent to 1.5 nm of path). These conditions must be met simultaneously for all wavelengths in the science band, for both polarization states, and over all timescales (including direct current [DC] offsets and vibrations in the kilohertz frequency range). The null depth resulting from this level of control is 7.5×10^{-7}. Meeting these amplitude and phase requirements is the primary technical challenge for the TPF-I system, and these requirements drive almost all aspects of the instrument design. Instability noise and its mitigation are described in more detail later in this document.

In Figure 4-5 the amplitude and phase errors have been further categorized into static and dynamic terms. Static errors arise from mismatches in the coatings, the reflective and transmissive optics, and the static alignment of the system, including both dispersive and birefringent effects. Introducing an achromatic π phase shift in the nulling beam combiner has been a focus of research, but matching the transmission of the different beamtrains – each of which contains on the order of 30 optical elements – across the full range of wavelengths and polarization is also a formidable challenge. The dynamic terms include all time-variable effects. The formation-flying system is continually in motion, and a series of control systems must be used to stabilize the optical path at the 1-nm level and to manage the tilt and shear of the wavefront that couples into the single-mode spatial filter. It is clearly important to validate the static terms over an optical bandwidth that is representative of the flight system. Conversely, if the instrument can be
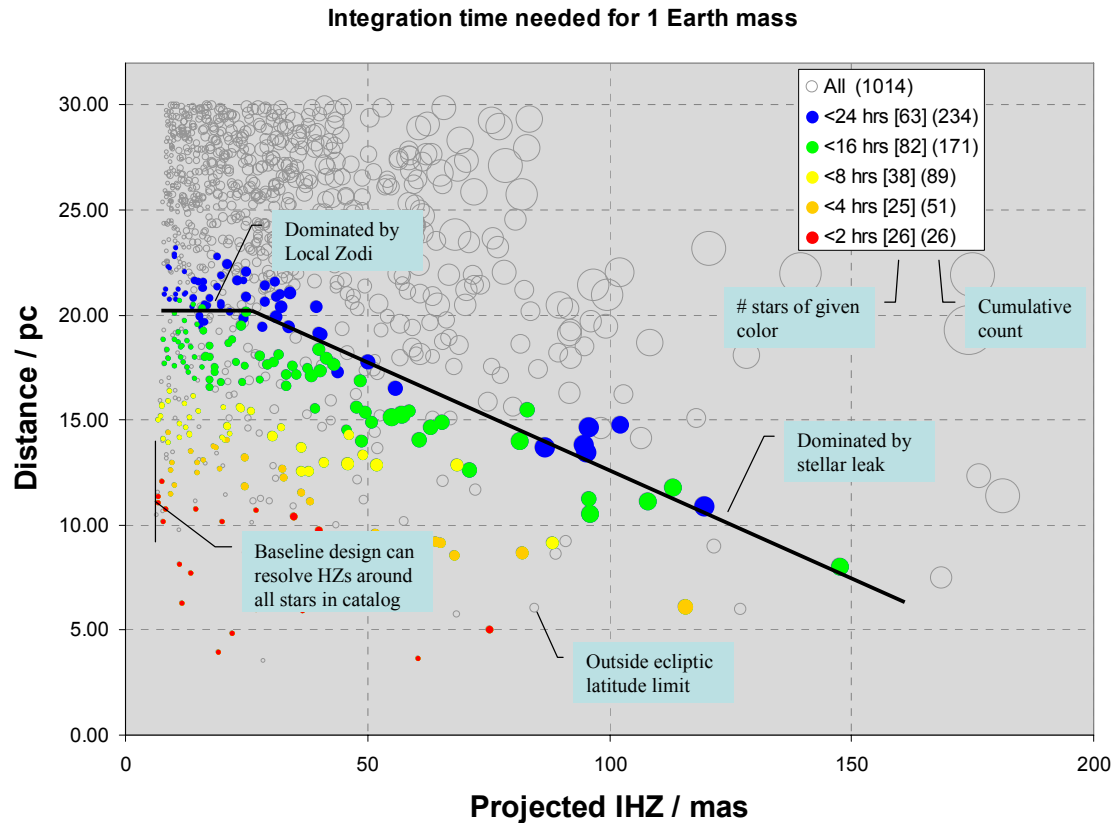
Figure 4-7. Integration times for detection of Earth-sized planet around TPF-I candidate target stars. The array is a linear dual Bracewell configuration with a 4-m collector diameter.

demonstrated to be stable at one wavelength, then we can argue that it will be stable at all wavelengths (with the exception of time-varying dispersive terms, which should be small).

The actual error budget is somewhat more detailed than the one shown previously in Fig. 4-5. One of the summary pages is reproduced in Fig. 4-6. The SNR is calculated over a number of spectral channels spanning the full bandwidth of the instrument. The model is flexible and can compute the SNR for arbitrary array geometries, with and without phase chopping, using the method of baseline decomposition (see Lay 2004). Noise sources include photon noise from local zodiacal emission, stellar leakage, exozodiacal emission, instrument thermal emission, stray-light, detector read noise, and dark current, as well as a sophisticated calculation of the instability noise. The contributions from local and exozodiacal dust are based on the models of Kelsall et al. (1998). The signal and noise sources have different dependences on wavelength, distance, array size, and collector diameter, leading to complex variation in the broad-band SNR. Zodiacal and exozodiacal emission started appearing.

4.2.2 Star Count Model

The purpose of the star count model is to predict the number of stars that can be surveyed for the presence of planets during a specified mission duration. Here we provide a brief description. A more detailed explanation can be found in Dubovitsky and Lay (2004).
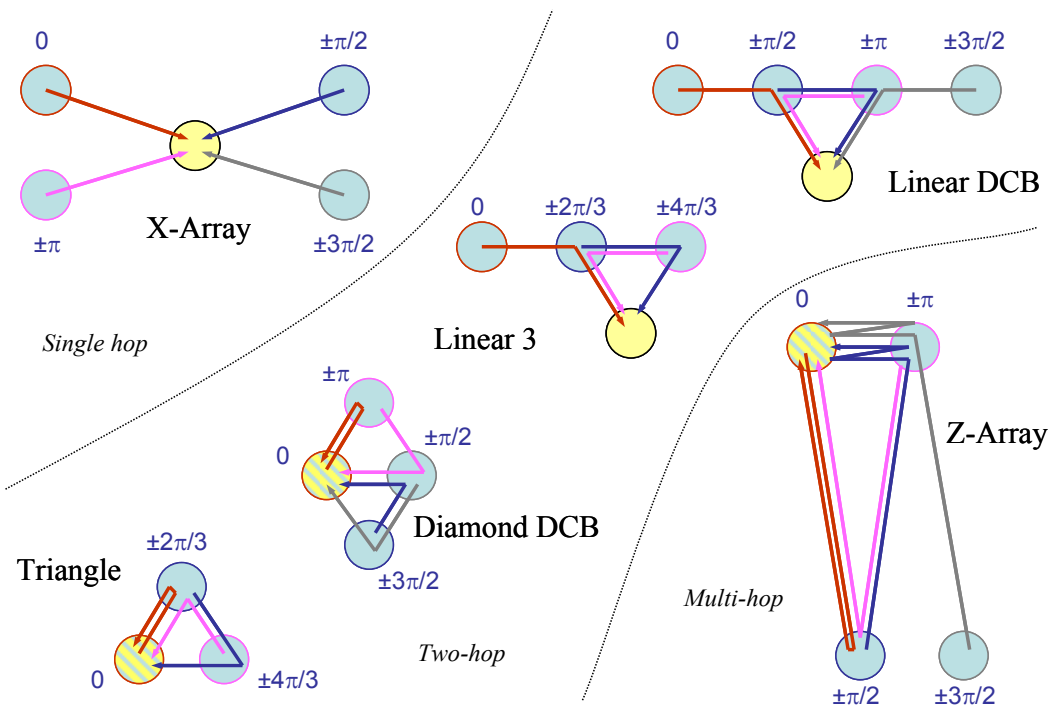
Figure 4-8. Nulling configurations considered in the trade study. The target star is in the direction normal to the page. The phasing of each collector is given for each of the two chop states. Pale blue circles represent collector spacecraft; yellow circles are dedicated combiner spacecraft; hatched yellow and blue circles are collector spacecraft with combining optics. Colored lines indicate the beam relay paths for each aperture. A number of other configurations were ruled out, as described in the main text.

Originally implemented in MathCad, the model has now been migrated to MatLab. The starting point is the catalog of 1014 TPF-I candidate target stars described in Section 2.5 and illustrated by the circles in Figure 4-7. Given a specific nulling configuration and collector diameter, the program cycles through each star, determining first whether it meets the criteria for ecliptic latitude (solar shading constraint) and inner working angle. It then estimates the time needed to achieve an SNR of 5 for a broad-band detection of an Earth-sized planet, using a simplified version of the full performance model. The list of targets is then sorted in ascending order of integration time. With 2 years of mission time available for the initial survey, we assume that 50% of this time will be spent integrating on targets and that each target will be visited three times to ensure a completeness in excess of 90%. The number of targets that can be surveyed is therefore given by the star in the sorted list by which the cumulative integration time has reached 2 x 50% / 3 = 122 days.

The colored circles in Figure 4-7 indicate the integration time needed to detect an Earth-sized planet around the star. The mid-IR signal from an Earth-sized planet in the mid-Habitable Zone depends only on the distance to the system. The noise is dominated by contributions from the local zodiacal dust (invariant with distance) and stellar size leakage (which decreases with distance but increases for the earlier spectral types). As a result the easiest targets in red are the nearby K stars. Integration times increase with distance and with the intrinsic size of the star. The solid line shows schematically a contour

of constant integration time; targets to the left are limited by local zodiacal emission, while those to the right are limited by stellar leakage.

This technique can also be extended to predict the number of targets that can be spectroscopically characterized in a given amount of time. This depends on the prevalence of Earth-like planets in the Habitable Zone. If planets are rare then the average distance to the systems being characterized is high, the integration times are long, and only a few systems can be accommodated in the time available. If planets are very common, however, then we will be able to characterize a much larger number of nearby systems. The simple algorithm to account for this is described in Dubovitsky and Lay (2004).

A more sophisticated model to predict and optimize the program completeness is now underway. Based on similar analysis for the TPF-C mission, the algorithm assesses the observability for each of 1000 planets around each star. For each week of the mission, only the most productive stars are selected in order to maximize the number of planets found.

4.3 Nulling Configurations

We define an *architecture* by the combination of nulling configuration, collector aperture diameter, beam routing between spacecraft, beam combiner design, number of launches, and type of launch vehicle. The nulling configuration includes the number and relative locations of the collectors, and the amplitudes and phases with which each collector beam is combined. All are significantly constrained in geometry by the need for equal optical path lengths from each collector to the combiner.

The six basic architectures compared in this study are listed in Figure 4-8, ranging from three to five spacecraft. The first four are all part of the Dual Chopped Bracewell (DCB) family, in which the four apertures have phases of 0, $\pi/2$, π, and $3\pi/2$ radians. The Linear DCB (Beichman et al. 1999) can be phased in two ways, with either separated or interleaved nulling baselines. In the analysis we choose the optimal case for each observing scenario. The X-array (Lay and Dubovitsky 2004) chosen for study has a fixed 2:1 aspect ratio (a tunable aspect ratio is discussed in Section 7). The Diamond DCB and Z-Array were both proposed by Anders Karlsson (ESA) as a means of reducing the number of spacecraft; the hatched circle in the schematic indicates a spacecraft that functions as both a collector and combiner. The Z-Array uses multiple relays between the collectors to balance the path lengths. The four DCB architectures have identical beam combiners. The Triangle and Linear 3 are based on a three-way nulling strategy with phases of 0, $2\pi/3$, and $4\pi/3$ (Karlsson et al. 2004). The other three-spacecraft designs have been proposed by Serabyn and Mennesson (2004). In all cases, the spacecraft are confined to a plane perpendicular to the target star direction for thermal reasons. The beams must be routed such that the path lengths from the star to the combiner are equal; this is achieved with a single hop from the collector to the combiner in the X-array, two hops for the Linear DCB, Diamond DCB, Triangle and Linear 3, and as many as four hops for the Z-Array.

Many nulling configurations were not considered in the trade study. The single Bracewell nuller is attractive for its simplicity (only two collectors), but it cannot accommodate a phase chop, making it extremely vulnerable to slow systematic effects (a variation of 1 photon per second of scattered light can look like a planet, for example). There are also a number of configurations with higher-order nulls, in which the central null of the response on the sky has a broader null than the quadratic profiles seen in

Figures 4-1–4-3. The motivation was to reduce the stellar size leakage which is often the dominant source of noise. Examples are the Angel cross, OASES, Laurance, and Bow-Tie configurations. Although they reduce the noise, they are also less efficient at detecting modulations in the planet photon rate. The star count model (Section 4.2.2) demonstrated that these higher-order null configurations were significantly less capable than the dual chopped Bracewell designs.

A given nulling configuration may be implemented as either a free-flying formation of spacecraft or as a single, structurally-connected system. The length of a practical structure limits the inner working angle and angular resolution, and it severely restricts the number of targets that can be surveyed and characterized. For this reason, a structurally-connected option was not considered in the trade study. In addition, formation-flying arrays may be implemented in either co-planar or non-co-planar forms (as described in Section 4.5), although only co-planar forms were considered in the trade study.

4.4 Collector Aperture Diameter and Array Size

The performance of a given configuration depends strongly on the aperture diameter and constraints on the minimum and maximum array size. The aperture diameter is constrained by the launch vehicle and the number of spacecraft needed. We adopted the Boeing Delta IV-Heavy as the standard launch vehicle. We further assumed that the collector primary mirrors were circular and monolithic (i.e., no deployable
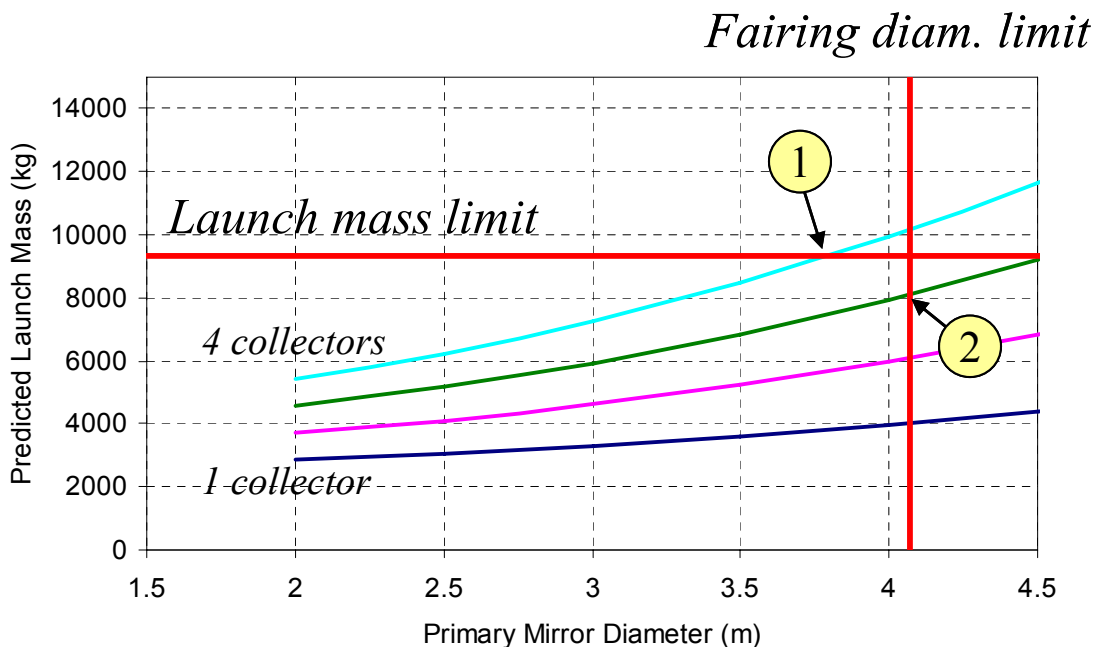
Figure 4-9. Launch mass as a function of primary mirror diameter and the number of collectors for the case where there is a separate combiner spacecraft. Mass and fairing diameter constraints are shown for a Delta IV-Heavy launcher, assuming 30% mass margin. The maximum aperture diameter is 3.8 m for the Linear DCB and X-Array configurations, constrained by the launch mass (Point 1). The Linear 3 configuration has a maximum diameter of 4.1 m, constrained by the fairing diameter (Point 2). A modified set of curves was used for the combiner-less configurations.

segments). The dynamic envelope of the fairing has a diameter of 4.6 m. Allowing a total of 50 cm for other structures, the maximum launchable aperture diameter is 4.1 m, represented by the vertical line in Figure 4-9. A parametric model was constructed to predict the total mass as a function of aperture diameter, number of collectors and whether or not a dedicated combiner spacecraft was needed. The model was based on the mass budget from a detailed design study for a 4-m diameter collector, using scaling laws of $D^{2.5}$ for the collector primary, $D^{1.5}$ for the secondary and support structure, and $D^{2.0}$ for the solar shade. The mass of the combiner spacecraft and optics, and the collector spacecraft bus were assumed to be independent of the aperture size. The curves predicted by the model in the case where there is a separate combiner spacecraft are shown in Figure 4-9. Also shown is the 9600-kg launch mass limit. The Linear DCB and X-array are mass-limited to an aperture of 3.8 m, while the other architectures are constrained by the fairing diameter to 4.1 m aperture. The fairing height of 17 m was not the limiting constraint for any of the architectures considered, although the current five-spacecraft single launch stack design still has some risk. A two-launch scenario was also considered for the Linear DCB and X-array; the aperture diameter is increased to 4.1 m, but there is the additional cost and complication of supporting two launches and a rendezvous in deep space.

The array size is defined by the longest baseline between any two collectors (center-to-center). The minimum sizes are determined by the closest separation we are willing to tolerate between spacecraft without significant risk of collision. A minimum spacecraft separation of 20 m was chosen, corresponding to a 'tip-to-tip' spacing of 5 m between sunshades that are 15 m across. The maximum array size for nulling is limited by stray light: the thermal emission from the solar shades of one spacecraft is scattered into the science beam on another spacecraft by contamination on the optics. This scattered light easily overwhelms the other sources of noise unless the optics are baffled to completely block the thermal emission. As the separation between spacecraft is increased, the angular offset between the solar shade and the exit point of the science beam is reduced, and the shade becomes harder to block. A maximum spacecraft separation of 160 m was imposed, based on the practical dimensions of the light baffle.

4.5 Planar vs. Nonplanar

The architectures compared in the trade study were all co-planar; the collector and combiner spacecraft are all located in a plane normal to the direction of the target star. The cold optics are kept shaded from the Sun by large sunshades (also in the plane of the array), and observations are restricted to targets that lie within a cone of the anti-Sun direction (Figure 4-10a). Architectures in which the combiner spacecraft sat above the plane of collectors were discounted because the hot sunshade of the combiner would generate an unacceptably high flux of thermal photons on the cold side of the collector spacecraft.

A new non-planar scheme was recently proposed by ESA that may avoid these issues, and it provides significant simplification in the design of the collector spacecraft. This has been dubbed the 'Emma' architecture (after Emma, the wife of Charles Darwin) and is illustrated in Figure 4-10b. The collector spacecraft carries a single optic – a spherical primary with a focal length of ~ 1 km – that focuses the light from the target system to the combiner spacecraft. The large separation of the combiner from the collector spacecraft minimizes the impact of thermal radiation from one to the other. The Sun is now nominally off to the side, at 90 degrees from the target star direction. The collectors have compact shades around their perimeter, and the combiner has a set of shades on the Sun-ward side of the spacecraft. As the array of collectors rotates about the line of sight to the target, the combiner must remain stationary to preserve its

shading. The formation-flying system must carefully maintain the position and pointing of the collector spacecraft to ensure that the beams are delivered to the correct locations on the combiner.

The Emma architecture has a number of attractive features, but also has some disadvantages:

Pros:	**Cons:**
+ Simplified collector	– Increased combiner spacecraft complexity
No deployable optics	– Smaller maximum array size
Compact sun-shade	– Increased demands on formation flying
+ Flexible collector array geometry	– No collector standalone observing
+ Increased sky coverage	– Stray light from collector sunshades
+ Smaller minimum array size	

The Emma concept has been pursued by the Alcatel study group for Darwin, and it has now become the subject of a design study at JPL.
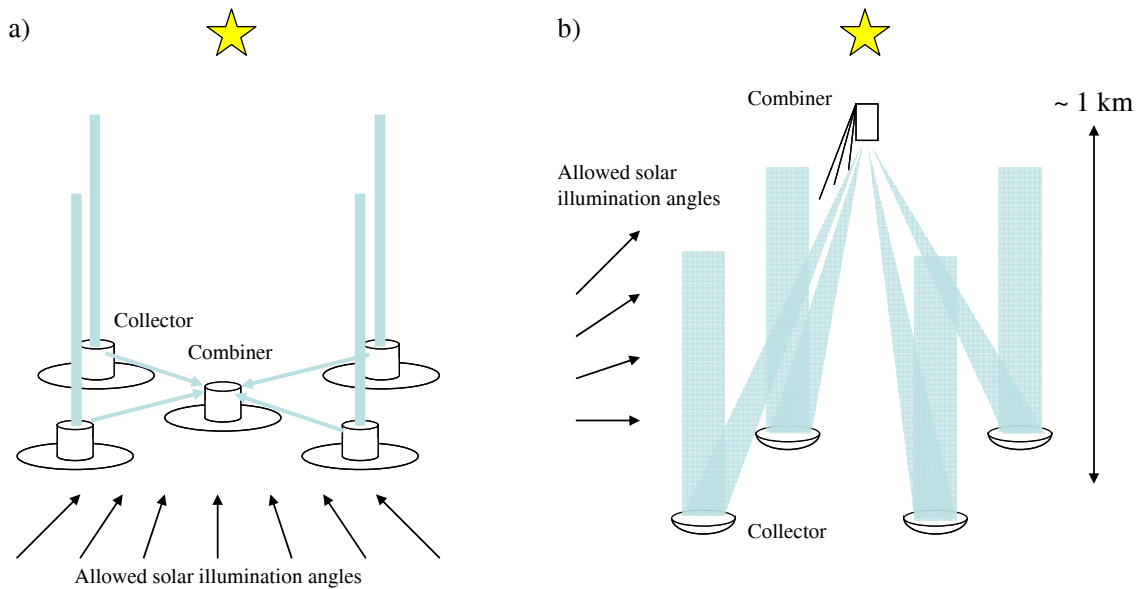
Figure 4-10. (a) Classic co-planar architecture, (b) the out-of-plane Emma concept.

4.6 Beam Combiner Design

In nulling interferometry, excess starlight is blocked using an interferometric cancellation technique, improving the star-to-planet contrast ratio to enable planet detection over an observation time typically of several hours. To reduce the stellar leakage signal to a level comparable to the zodiacal background the nuller should be capable of reaching null depths of at least 10^{-5}. To reach deep nulls, a number of parameters must be controlled, some inside the nuller and some in other associated systems. An important feature of a successful nulling beam combiner will be identical treatment of both input beams in terms of phase shifts, reflections and transmissions, angles of incidence, polarizations, etc. Different nuller designs are being tested in the laboratory and in the field. A modified Mach-Zehnder design (MMZ) has been deployed on the Keck telescopes, and this design seeks to achieve a high degree of symmetry in the beam combination by causing each input beam to be both transmitted once and reflected once from near-identical beamsplitters (this design achieved 2 million to 1 laser nulls at 10.6 μm).

A different design (also using conventional beamsplitters), the rooftop nuller, was built at JPL for SIM and achieved high performance nulls (laser transient nulls at 633 nm near 10^{-6} and 18% bandwidth red-light nulls of 10^{-4}) in the visible waveband. A newer concept, the fiber beam combiner is currently being tested in the laboratory for deployment on a large ground-based telescope. This design seeks to achieve high beam symmetry by dispensing with the beamsplitters and combining the incoming beams directly on the tip of a single-mode optical fiber, and this design has already achieved laser nulls of 10^5 in the visible.
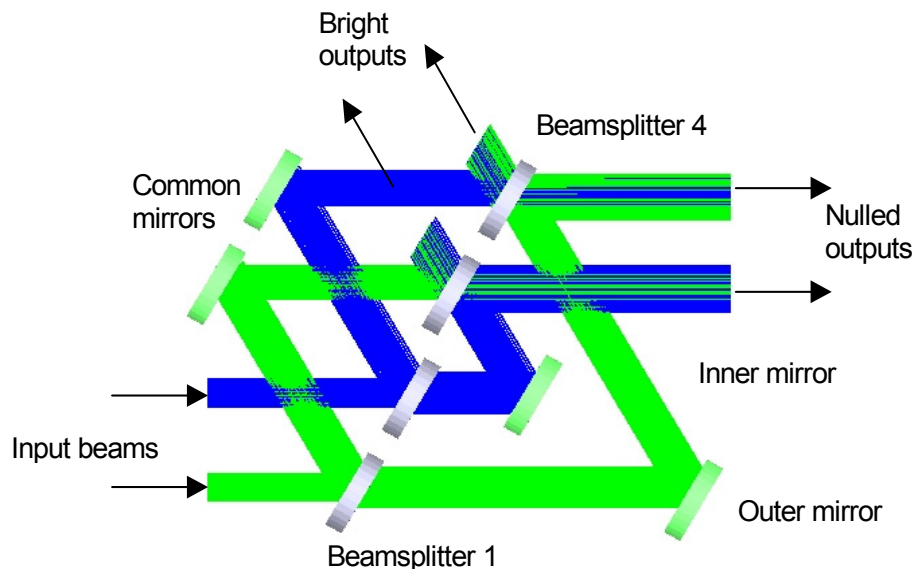
Figure 4-11. Modified Mach-Zehnder nuller used on Keck Telescopes.
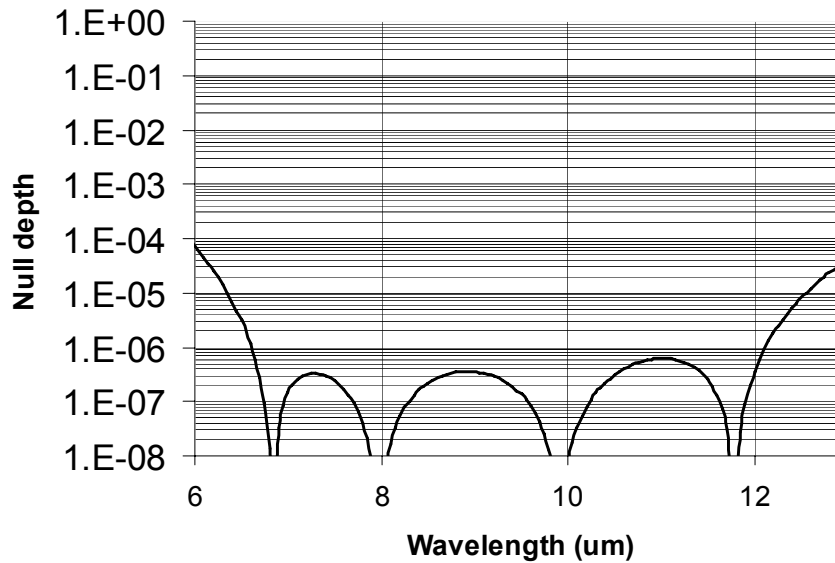
Figure 4-12. Calculated null depth across the band for NaCl and AgCl wedges between 6 and 13 μm.

A second key component of a beam combiner design is the field-inversion system which inverts the electric field of one of each pair of incoming beams by exactly π across the waveband, allowing the beam combiner to form a null (destructive fringe) rather than a constructive fringe. Several different methods of field inversion have been proposed, and at least two have been tested in the laboratory. One method uses a periscope-like arrangement of mirrors to produce the field inversion. This has the advantage of being effective across a very wide waveband. A second method uses pieces of glass of carefully controlled thickness known as phase plates to produce the field inversion. Figure 4-12 shows the calculated null depth for a set of silver chloride (AgCl) and sodium chloride (NaCl) phase plates. Other glass combinations potentially yielding deep nulls are also known.

A third key component for the beamcombiner is the ability to control the optical path and maintain the null fringe on the star. Light at a different wavelength from the nulling band is used for this purpose, for example between 2 and 4 μm. If this light follows as much of the beam train as possible, then the phase of the null fringe can be better controlled, leading to deeper more stable nulls, important for faint planet detection. In the flight design study described next, the fringe tracking light follows the science path almost exactly and is interfered on the same beamsplitters as the nulling light.

4.6.1 Co-axial Combiners for a Formation-Flying Interferometer

For the formation-flying interferometer design work, a simplified nuller was used rather than the highly symmetric MMZ design. The main benefits would be that only one internal laser metrology beam would be needed for each beam of the interferometer rather than two, the attenuation or round-trip insertion loss would be less for the metrology light, and the science light would emerge on only two beams rather than four, offering a small but significant improvement in signal-to-noise ratio at the detector. There would also be associated engineering simplifications. Because of the wide spectral band to be covered by TPF-I, the nuller is actually divided into two units stacked next to one another, one operating on the wavelength range 7 to 11 μm and the other on the range 11 to 17 μm. This arrangement necessitates an additional

Figure 4-13. Schematic layout of simplified beam combiner.

metrology path and possibly a second fringe tracking system. By splitting the spectrum we generate less demanding coating requirements on the beamsplitters which must, for the highest efficiency, give a near reflection/transmission ratio (R/T) across the band. Also, single spatial mode filters (which cover these spectral bands) are becoming available.

The simplified nuller uses a beamsplitter/compensator plate arrangement to obtain a near match of optical path across the waveband. Residual error in the R/T ratio is taken up using one specially fabricated coating on one side of the compensator plate. Models showed that the throughput could then be matched across the spectral band on both incoming beams to better than 1%. The residual amplitude and phase errors are then well within the compensation range of the adaptive nuller.

Science detector and fringe tracking

The science detector operates on the two complementary outputs of the cross-combiner. Light emerging from the cross-combiner is focused through the single-mode spatial filter (the subject of a TPF-I technology development effort) and then is dispersed through a prism before being detected on the science array. Since only two beams are output from each cross-combiner, a single science detector array (nominally a silicon:arsenic [Si:As] array) can handle all four beams from the pair of cross-combiners. The nuller layout includes a fringe tracking camera, which detects the phase on each nuller and on the cross-combiner.

One beam from each nuller is extracted from the rejected light output (all the 7–17 μm wavelength starlight exits the system from this output) and is dispersed onto the camera array. From the cross-

combiner, two beams are extracted, so a total of four beams are sensed at the array. For the second cross-combiner a second fringe tracker would be needed unless a laser metrology could be used to transfer measured phase to the second nuller.

4.6.2 Multi-Axial Beam Combiners

In contrast to classical beamsplitter-based beam-combiner designs, it is also possible to combine optical beams using single-mode fibers. Technology at long wavelengths has not advanced to the point where each of the various beams to be combined can be injected into separate fibers and then combined using cross-couplers. However, another approach is feasible. Separate beams can be directly combined into a single fiber simply by using a common focusing optic, as in Figure 4-14. Each of the individual beams must couple to the same spatial mode in the single-mode fiber. Thus, if the beams (in the two beam case) arrive with a relative phase shift of π radians, the two beams entering the fiber mode will cancel each other. Note that a large number of beams can be combined in one step, as a number of beams around the periphery of a common focusing optic can all be simultaneously focused onto the common fiber tip (Figure 4-15; Karlsson et al. 2004; Wallner et al. 2004). This method of "fiber nulling" has now been verified in the optical regime, where deep narrowband nulls close to one part in a million have already been obtained (Haguenauer and Serabyn 2006) , and in the near-infrared, where broad-band nulls of a few 10^{-4} have been obtained across the H band (Figure 4-16; Mennesson et al. 2006). However, while simple and easy to use, this nulling approach also has disadvantages, including lower efficiencies in the case of a small number of beams, and the lack of a complementary, or "bright" output. Thus, more experience with this type of combiner is required to fully understand the trade-offs relative to classical beamcombiners.
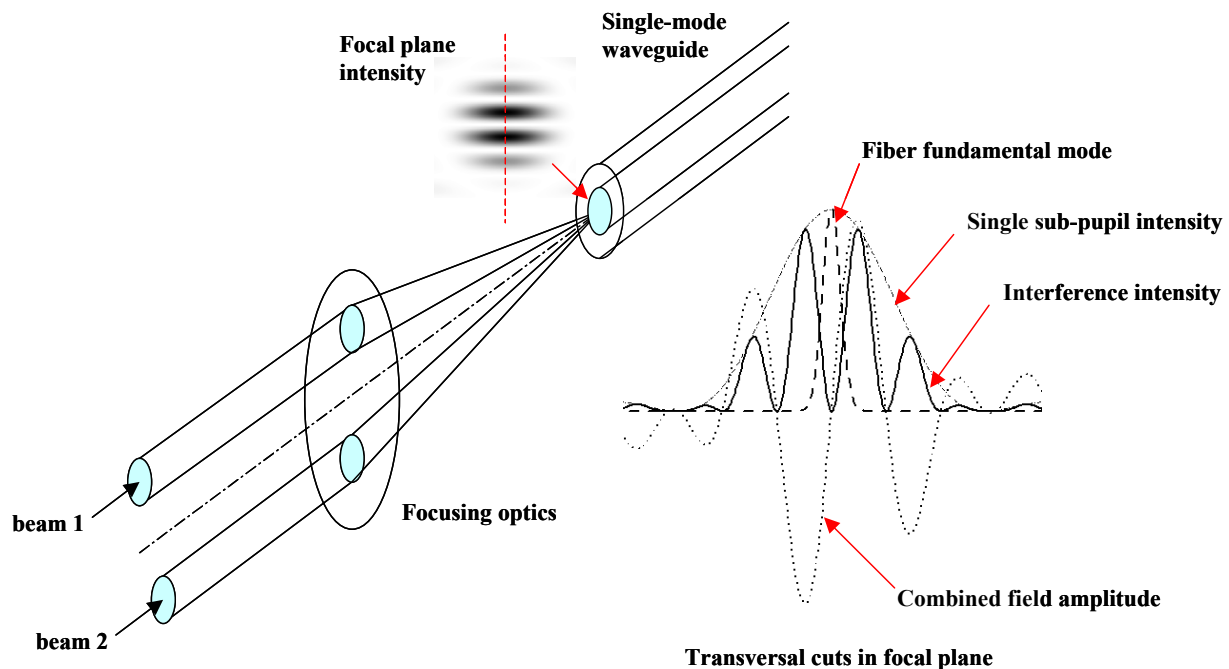
Figure 4-14. Principle of single-mode fiber beam combination. The two beams are combined by the same focusing element onto the core of a single-mode fiber.
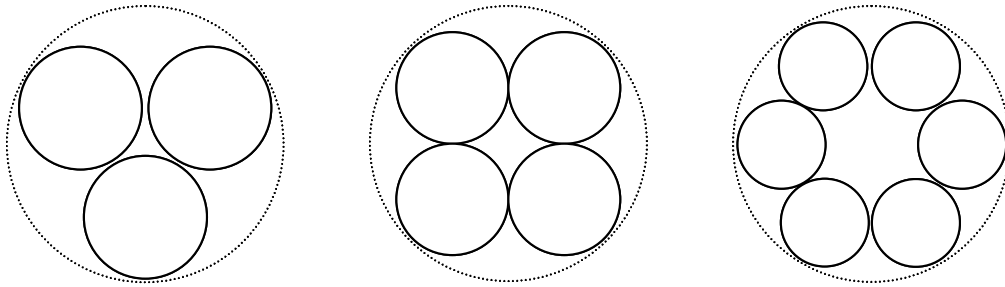
Figure 4-15. Layout for multi-beam combination. The beams (small circles) are all focused onto the core of a single-mode fiber by the same focusing optic (large circle).
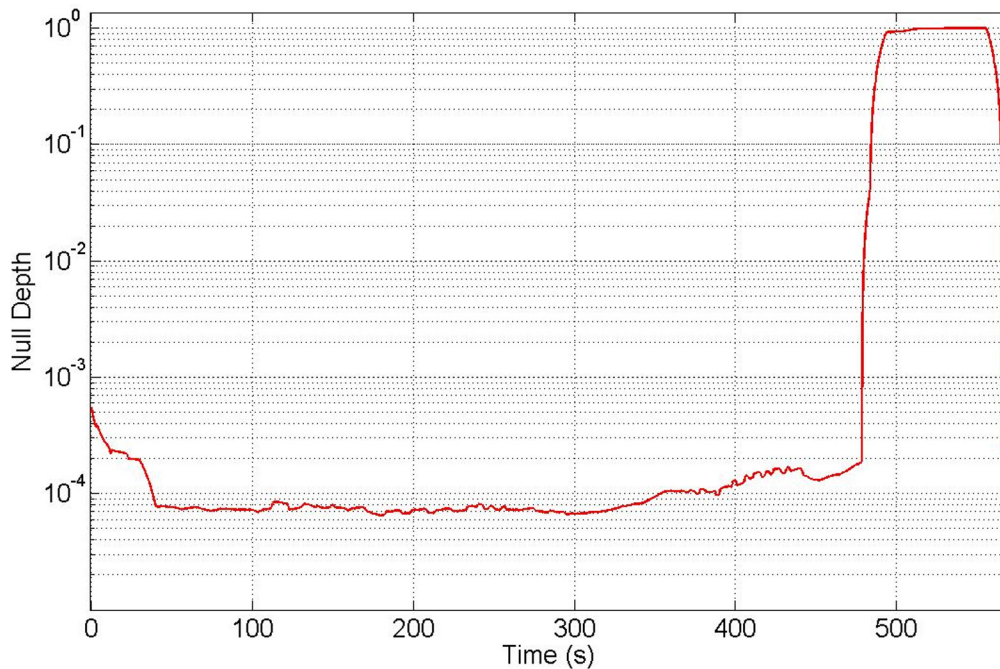
Figure 4-16. Measured H-band null depths. The best null in this 10-s running average is 6.5×10^{-5} (Mennesson et al. 2006).

4.7 Stray Light

The light that is collected by each telescope is relayed through free space to the central beam combiner where interference fringes are formed. The optics of the beamcombiner must restrict the field of view looking *back* toward each telescope in order to strongly attenuate or block sunlight that might be reflected off the outer edges of the telescope spacecraft – in particular off the rim of the sunshields. The adopted solution has been to place the relayed light paths as far above the plane of the heat shields as possible,

therefore increasing the dark field of view seen from the combiner spacecraft. Strategies for minimizing stray light have been detailed by Noecker *et al.* (2004, 2005).

4.8 Instability Noise and Mitigation

In an ideal nulling interferometer, the electric fields of the light from the collecting telescopes are combined with a prescribed set of amplitudes and phases that produce a perfect null response at the star (Figure 4-17a). In this case the integration times needed for planet detection and spectroscopy depend on the planet signal strength and the level of photon shot noise (from local and exozodiacal emission, stellar leakage around the null, and instrument thermal emission).
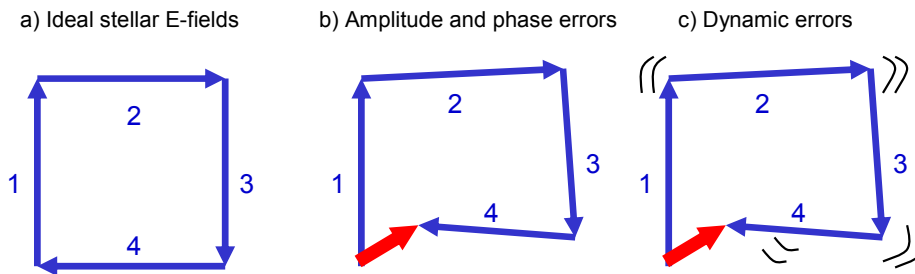
Figure 4-17. a) Summation of electric fields in the spatial filter for an ideal Dual Chopped Bracewell nulling configuration. b) Amplitude and phase errors in the contributions from the different collectors lead to a residual leakage of photons. c) As the amplitude and phase errors vary with time, the residual photon leakage rate fluctuates and can mimic the presence of a planet.

4.8.1 Origin of Instability Noise

In practice, it will not be possible to maintain the exact set of amplitudes and phases – vibrations and thermal drifts result in small path-length errors and time-variable aberrations. The null "floor" is degraded, and there is a time-variable leakage of stellar photons that can mimic a planet signal (Fig. 4-17b and c). This is known as 'instability noise' (previously "systematic error" or "variability noise"), and it increases the integration time required. The analysis of instability noise is somewhat complex (Lay 2004). Some components are removed by phase-chopping. Others, such as the "amplitude-phase cross terms" and the "co-phasing error," are not removed and result in leakage photon rates proportional to $\delta A_i \delta \phi_j$ and $\delta \phi_j$, respectively, where δA_i represents an amplitude error from the ith collector and $\delta \phi_j$ is a phase error from the jth collector. The analysis shows that a null depth of ~10^{-5} is generally sufficient to control the level of photon noise from the stellar leakage, but that a null depth of ~10^{-6} is needed to prevent instability noise from becoming the dominant source of noise. A 10^{-6} null requires rms path control to within ~1.5 nm, and rms amplitude control of ~0.1%. It is therefore instability noise, not photon noise that drives the performance of the instrument.

Table 4-1 lists the mechanisms responsible for amplitude and phase errors, along with their spectral dependence and temporal nature. For example, vibrations in the optical path difference (OPD) result in a phase error that scales as the inverse of wavelength and are inherently time varying. Beam shear also

gives a time-varying amplitude error (less light is coupled to the detector) but is approximately independent of wavelength. Mismatches in dispersion, birefringence, and reflectivities between the collector beams may have a more complex spectral dependence, denoted by $f(\lambda)$, but are inherently static. These static effects can be compensated by an adaptive nuller (Peters et al. 2006) or similar device. The dynamic terms combine via amplitude-phase ($\delta A \, \delta \phi$) and co-phasing ($\delta \phi$) mechanisms to form the time-variable instability noise:

$$
\begin{aligned}
IN(t) &= \left[\alpha_1(t)\lambda^{-1} + \alpha_2(t)\lambda^{-2} + \alpha_3(t)\lambda^{-3} \right] F_*(\lambda) \\
&= \left[\beta_1(t)\nu + \beta_2(t)\nu^2 + \beta_3(t)\nu^3 \right] F_*(\nu)
\end{aligned}
\tag{1}
$$

where ν is the optical frequency, the α and β coefficients vary randomly with time, and F_* is the stellar flux (since the star is the source of these leakage photons). Other instability mechanisms, such as an unbalanced chop, may also be important, but will have a similar spectral dependence. The important conclusion is that at any given time the instability noise has a spectral signature that varies slowly with wavelength. This slow dependence with wavelength forms the basis of the first mitigation strategy, described in the following section. Ben Lane has proposed an alternative scheme described in Section 4.8.3.

Table 4-1. Sources of Instability Noise and Their Spectral Dependence

Phase			Amplitude		
Mechanism	**Spectrum**	**Static / dynamic**	**Mechanism**	**Spectrum**	**Static / dynamic**
OPD Vibration	λ^{-1}	dynamic	Tip / tilt	λ^{-2}	dynamic
Fringe tracker offset	λ^{-1}	dynamic	Focus	λ^{-2}	dynamic
Control noise	λ^{-1}	dynamic	Higher order	λ^{-2}	dynamic
Dispersion mismatch	$f_1(\lambda)$	static	Beam shear	λ^0	dynamic
Birefringence mismatch	$f_2(\lambda)$	static	Reflectivity / transmittivity	$f_3(\lambda)$	static

4.8.2 Stretched X-Array and Spectral Filtering

In the stretched X-array and spectral filtering approach, we use the spectral dependence as the means to distinguish between the planet signal and the instability noise. To make this effective, the array must be stretched significantly with respect to previous designs. The X-array is the natural choice, since it can be stretched along its long dimension while preserving the short nulling baselines needed to minimize the stellar leakage. In principle, all instability noise can be eliminated. The nulling requirement can be relaxed from 10^{-6} to 10^{-5}, while at the same time the sensitivity is improved and the angular resolution of the array is significantly increased. The technique is described below. A more complete analysis can be found in Lay (2006).

Figure 4-18a shows the stretched X-array geometry, consisting of four collectors located on the corners of a rectangle and a central combiner, observing a star normal to the plane of the page. The aspect ratio has been stretched to 6:1, with 35-m nulling baselines. The corresponding instrument response at a wavelength of 10 μm, projected onto the plane of the sky, is shown in Fig. 4-18b. This is the "chopped" response – the phasing of the array is switched rapidly between two states, and the difference is taken. The star is located in the middle of the central, vertical null stripe (mid-grey); on either side the response
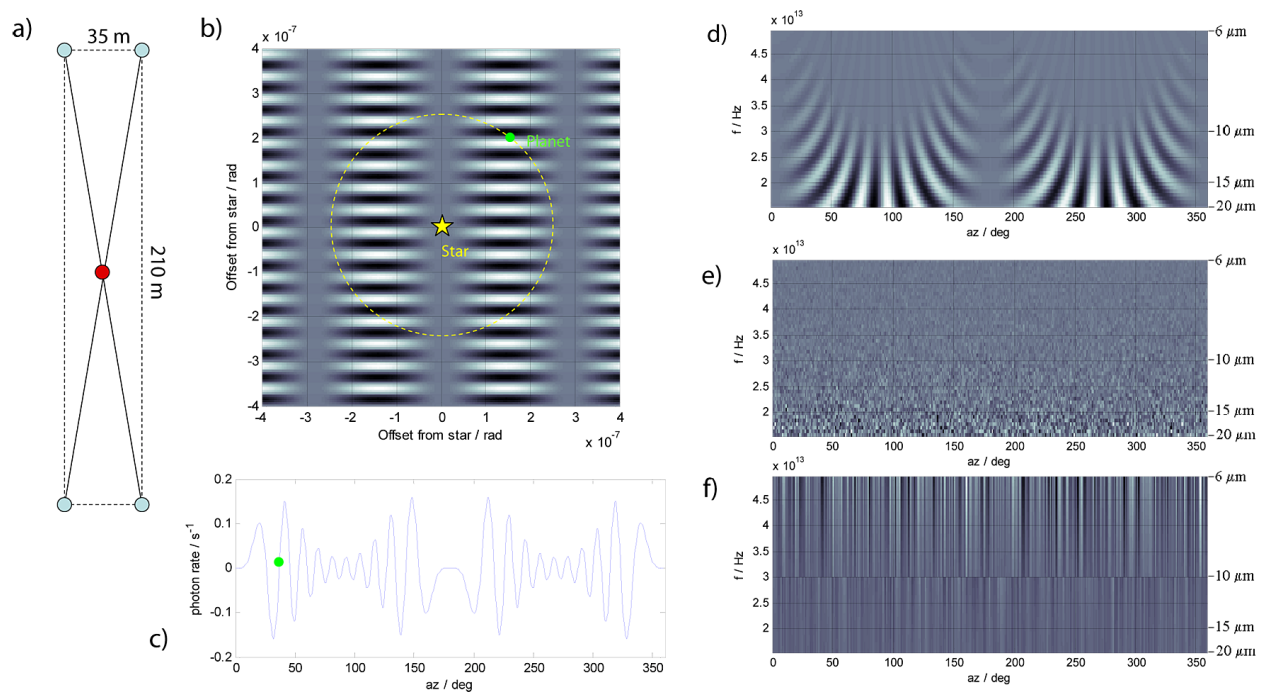
Figure 4-18. (a) Stretched X-array configuration. The aspect ratio is 6:1 in this example. (b) Chopped response of the stretched X-array configuration on the sky for a wavelength of 10 μm. The target star is located on a null (mid-grey); white and black represent positive and negative regions of the response. The planet has an offset of 250 nrad, or ~ 50 mas. (c) Chopped planet photon rate as the array is rotated. Peaks and valleys correspond to the white and black regions encountered along the circular locus shown in (b). (d) Chopped planet photon rate (grey-scale) as a function of optical frequency (left axis) or wavelength (right axis) and array rotation azimuth. Similar wavelength-azimuth plots are shown for (e) photon noise and (f) instability noise.
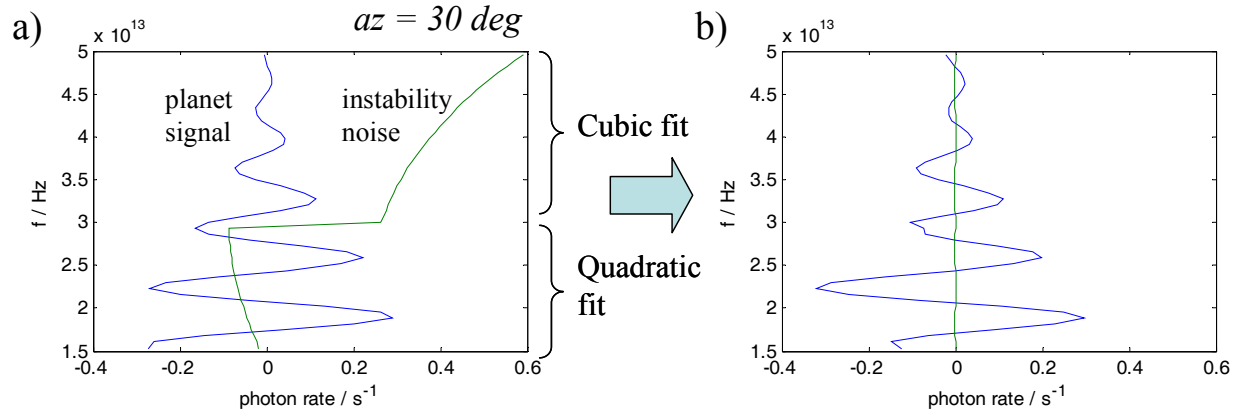
Figure 4-19. (a) Vertical cuts through wavelength-azimuth plots of Fig. 4-18 d and f at an azimuth of 30 degrees. Planet signal shows characteristic oscillatory behavior. Instability noise follows low-order polynomial dependence, with independent contributions to the two halves of the spectrum (separate hardware). (b) Result of removing low-order fits. Most of the planet signal remains, but the instability noise is almost completely removed.

has both positive (white) and negative (black) regions. A single planet is shown with a radial offset of 50 mas (2.5×10^{-7} rad) from the star. The detected photon rate from the planet as a function of rotation azimuth of the array is shown in Fig. 4-18c. The circular symbol gives the photon rate for the rotation angle shown in Fig. 4-18b. The peaks and valleys of Fig. 4-18c correspond to the white and black parts of the response along the circular locus in Fig. 4-18b. As the wavelength is increased from 10 μm, the instrument response of Fig. 4-18b is scaled about the center, with increased spacing between the peaks and valleys of the response. The photon rate from the planet is also changed according to its spectral distribution. Figure 4-18d combines these effects to show how the planet photon rate depends on both the wavelength (or optical frequency) and the array rotation azimuth. The example is based on a planet with a 265-K black-body spectrum, which has a substantially higher photon rate at 20 μm compared to 6 μm. A horizontal section through this distribution at a wavelength of 10 μm gives the profile shown in Fig. 4-18c. The wavelength-azimuth plot is a convenient representation of the data obtained from spectral channels of TPF-I as the array is rotated.

In addition to the planet signal, there are two distinct classes of noise (Section 4.2.1). The photon (shot) noise is shown in Fig. 4-18e, and is proportional to the square root of the overall photon rate. Important contributors are the local and exozodiacal backgrounds and stellar leakage. The instrument instability noise is shown in Fig. 4-18f. We assume that the full spectral range of 6 to 20 μm has been split for practical reasons into two bands for nulling: 6–10 μm and 10–20 μm. (It is difficult to cover the full range with one set of glasses and single-mode spatial filters.) Over each of these bands the instability noise at any instant is represented by a low-order polynomial series in the optical frequency multiplied by the stellar spectrum, according to Eq. 1. The coefficients vary randomly with time as the instabilities (path length, tilt, etc.) evolve. In Fig. 4-18f we show instability noise that is random from one azimuth to the next and from one band to the other (i.e., having a white noise spectrum). In practice the spectrum is not exactly white, and there will be some correlation, both with azimuth and between the spectral bands, but we will not rely on this correlation for the analysis presented here. In general, the instability noise increases at high optical frequencies / short wavelengths. The smooth variation with wavelength, coupled with the white-noise spectrum in azimuth, result in the distinctive vertical striping seen in the plot.

Table 4-2. Impact of Null Depth on SNR (after instability noise removed)

Null depth @ 10 µm	Broadband SNR (relative)	Ozone SNR (relative)
10^{-6}	1.00	1.00
10^{-5}	0.97	0.92
10^{-4}	0.80	0.60

Figure 4-19a shows vertical cuts through the wavelength-azimuth plot at an azimuth of 30 degrees, and depicts both the planet signal and an example of instability noise. The instability noise is a smooth, slowly varying function within the two halves of the spectrum, whereas the planet signal oscillates with wavelength. We exploit this difference to remove the instability noise. Removing a low-order polynomial fit from each half of the spectrum gives the curves shown in Fig. 4-19b. In each case, the instability noise signature has been almost totally removed, and the signal remains largely intact, although somewhat modified. The impact of the fitting on the planet signature is predictable and can be corrected. Some of the planet signal is removed by the fitting process (which impacts the sensitivity), and it is this that motivates the need for a stretched array. As the array size is reduced, there are fewer oscillations of the planet signal across the spectrum, and more of the planet signal is removed by the low-order fit. The 6:1 aspect ratio described here is a compromise between the array size and the amount of planet signal that is lost.

With the effective removal of the instability noise, it is possible to relax the required null depth. Table 4-2 lists the SNR obtained for both broad-band detection and ozone spectroscopy, relative to the SNR with a 10^{-6} null depth. In the absence of instability noise, the SNR is determined by photon noise, with principal contributions from stellar size leakage, local zodiacal dust, and stellar-null floor leakage. Only the stellar-null floor leakage depends on the null depth. Relaxing the null depth to 10^{-5} has only a small impact on the SNR. At a null depth of 10^{-4} the stellar-null floor leakage is becoming the dominant source of photon noise. But even with this relaxation by a factor of 100, the mission is still viable, albeit with reduced sensitivity.

A significant added benefit of the stretched array is that the angular resolution is improved by a factor of ~3. The benefits of this will be described in Section 4.9.

4.8.3 Post-Nulling Calibration

As previously explained, instability noise can wash out any planet signal unless the various electric fields are matched in all particulars at the level of ~0.1%. The difficulty of attaining such levels of control (e.g., ~1 nm path control) has motivated some research into ways to measure and remove nulling leakage after beam combination (Guyon 2005; Lane, Muterspaugh and Shao 2006).

One such approach, dubbed "coherent calibration", is outlined in Figure 4-20. In this approach, one takes advantage of the fact that light leaking through the null is coherent with light from the star, but not with light from the planet. Hence it is possible to use the bright output from the nuller (which would otherwise simply be discarded) as a "reference beam" to be mixed with part of the nulled output from the interferometer. This mixing process will yield an interferometric fringe, the amplitude of which is a direct measure of the amount of starlight leaking through the nuller.

Simulations of coherent calibration shown in Fig. 4-21 indicate that it is possible relax the required levels of field matching, possibly by factors of 10 or more. However, further work is required to demonstrate the approach in the laboratory, and to understand the ultimate limits to the level of calibration precision that can be attained before other limitations become manifest.
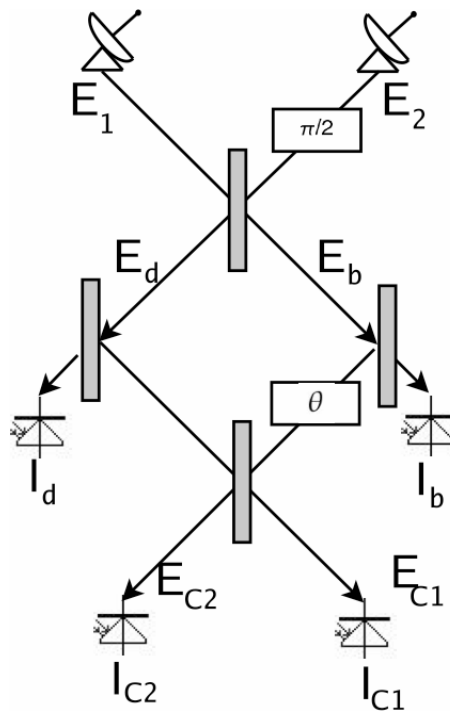
Figure 4-20. Schematic outline of coherent calibration. Part of the science beam (I_d) is mixed with a reference beam (I_b) taken from discarded starlight; the resulting fringes are measured at I_{C1} and I_{C2} and used to infer the amount of starlight leaking through the null and contaminating the science measurement. Although only a single-Bracewell nuller is shown, the concept can be applied to more complicated nulling architectures (e.g., the X array) in a straightforward manner.

It should be noted that this calibration approach does carry some cost in the form of a more complex beam-combination system (i.e., inserting a Mach-Zender interferometer into the system directly behind the nuller) and some loss of photon flux (a fraction of the science beam must be mixed with the reference beam). However, the amplitude and path-control requirements on this second beam combiner are nowhere near as stringent as of the nulling system.
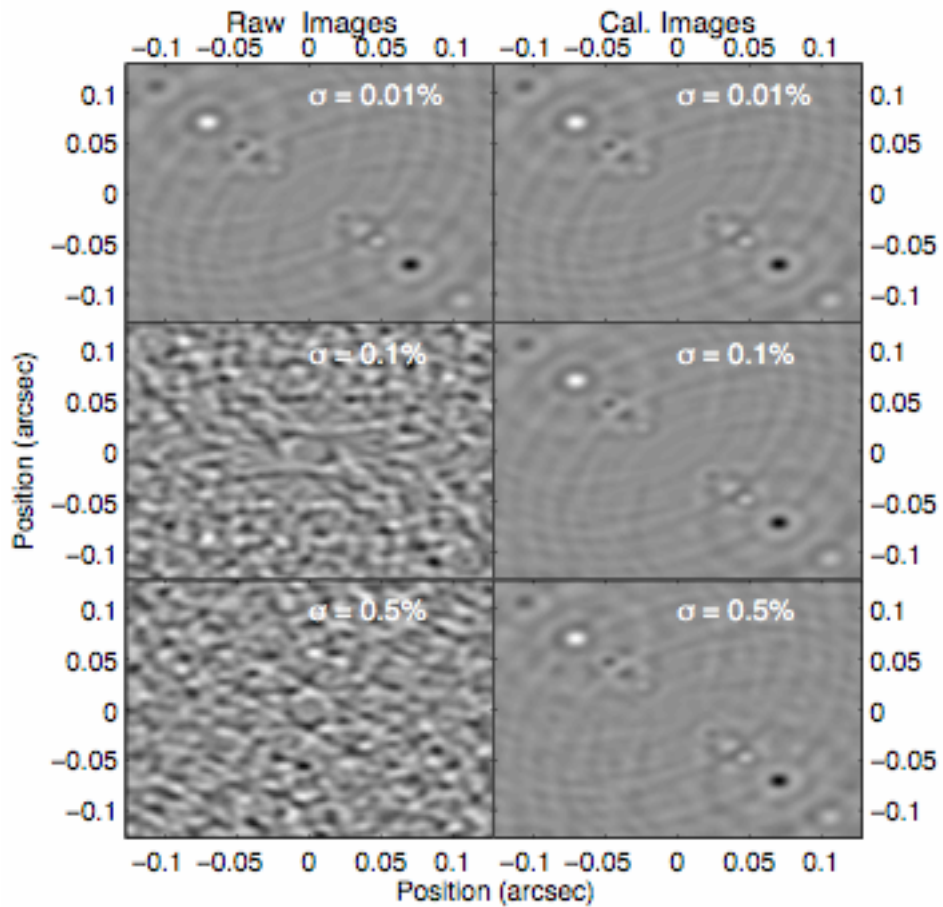
Figure 4-21. Simulated images reconstructed from raw and calibrated data, with three different noise levels. Top: 1 nm of phase noise and 0.01% amplitude mismatch. Middle: 10 nm of phase noise and 0.1% amplitude mismatch. Bottom: 50 nm of phase noise and 0.5% amplitude mismatch.

4.9 Imaging Properties

The primary motivation for the Terrestrial Planet Finder missions is their ability to directly detect photons from Earth-sized planets. Orbit determination requires that the emission can be localized and tracked over time. Spectroscopy is only meaningful if the photons can be attributed to the right object. This may be straightforward for the case of a single planet orbiting a star, but it will be very difficult to establish this a priori. The publication of the first spectrum from an exo-solar Earth would be heavily compromised by the possibility of spectral contamination by unresolved confusing sources, whether background objects, lumps in the exozodiacal dust emission, or other planets. It is, therefore, very important that TPF-I can resolve the emission from the multiple sources that might be present. This is why we must understand the
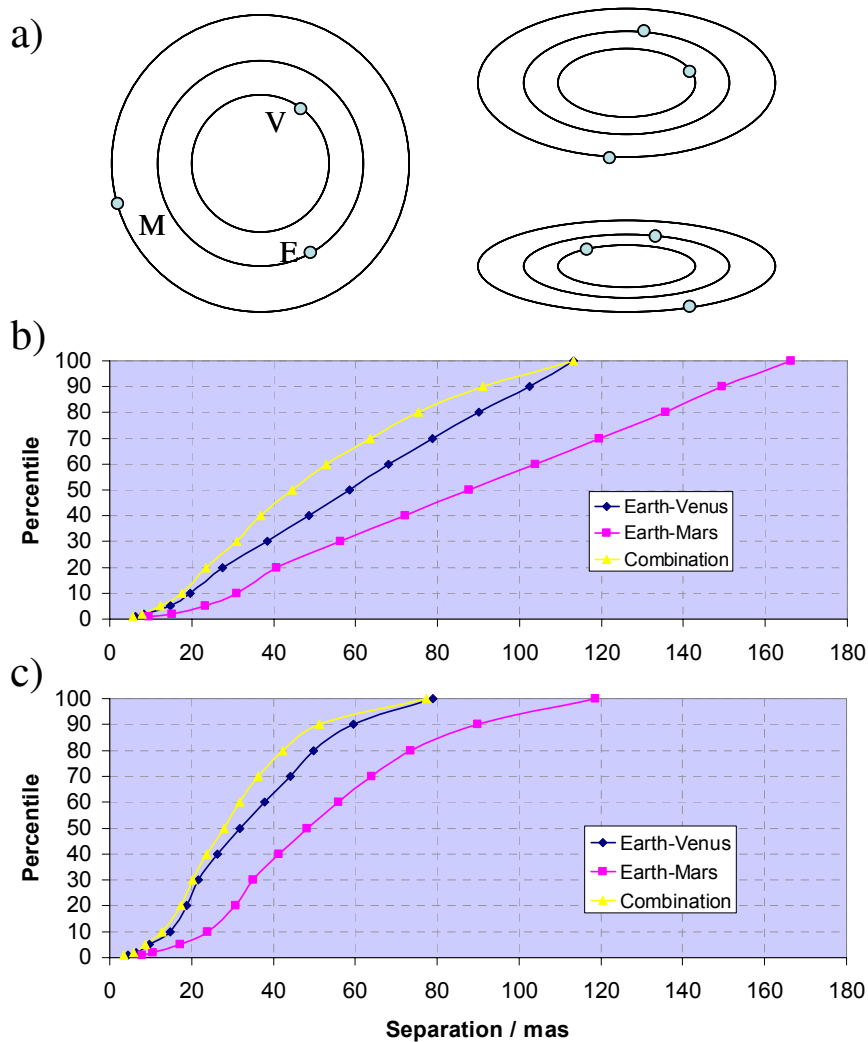
Figure 4-22. Angular separations of the Earth–Mars–Venus system viewed at 15 pc. (a) The angular separations are reduced as the orbits are viewed closer to edge-on. (b) Results of Monte Carlo simulation showing the probability that planets are separated by less than a particular value. For example, in 50% of cases we expect that two of the planets will be separated by 45 mas or less. (c) Same as (b), but includes the anti-star negative images of the planets.
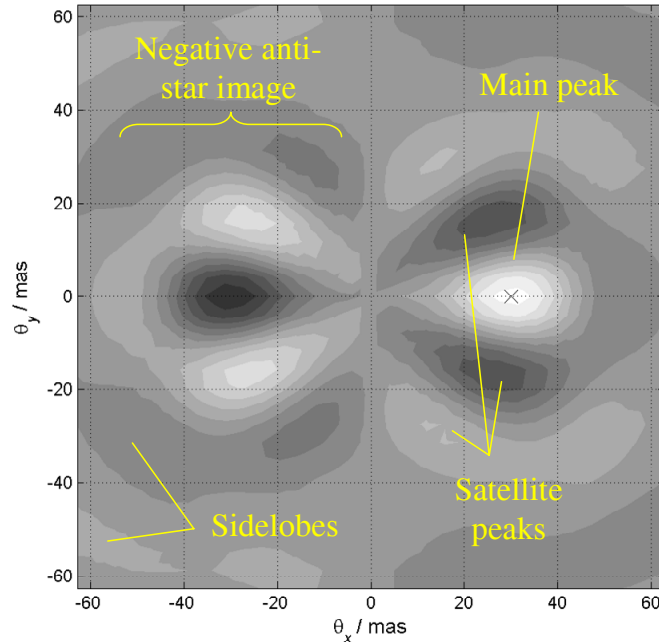
Figure 4-23. Example of the broad-band point-spread function for the X-array 2:1, obtained by co-adding the monochromatic PSFs from five wavelengths spanning 7 to 17 μm.

imaging properties of different array configurations. The following sections describe the distinction between the nulling and imaging baselines, the angular resolution needed to separate multiple planets, the properties of the point-spread function, the requirement on array size, and some of the approaches that have been proposed for image deconvolution.

4.9.1 Separating Multiple Planets

In this section we derive a criterion for the angular resolution that is desirable to resolve multiple planets. In the absence of measured planet data, we adopt the inner Solar System (Venus–Earth–Mars) as the benchmark case. Figure 4-22 shows the statistics for the relative angular separation of these three planets as viewed from a distance of 15 pc, averaged overall viewing angles. Figure 4-22b shows the cumulative statistics for the separations between the planets themselves. If we also include the negative anti-Sun image of each planet (a consequence of phase chopping – see next section), the average separations are reduced, as illustrated in Fig. 4-22c.

With an angular resolution of 20 mas, Fig. 4-22c indicates that an Earth at 15 pc will be confused with Venus or Mars approximately 25% of the time. We adopt this as the basis for a requirement on angular resolution. Since the mid-Habitable Zone subtends 67 mas at this distance, we require that the full-width-to-half-maximum (FWHM) of the PSF is less than or equal to 0.3 times the angle subtended by the mid-HZ:

$$\theta_{res} \leq 0.3\theta_{MHZ} \tag{2}$$

This is the requirement that drives the size of the array needed in most cases (Section 4.9.4).

4.9.2 Point-Spread Function

The point-spread function (PSF) described here is not the instantaneous response of the array on the sky. Rather, it is correlation map of the sky obtained from a point source after synthesis of all the observations (see Section 4.1). It is the analog of the PSF for an optical telescope, or the dirty beam of interferometric synthesis imaging. The PSF for a phased array is more complex than that of a standard imaging interferometer (which makes measurements from only pair-wise combinations of collectors). A full analysis that derives the structure of the PSF can be found in Lay (2005).

The basic features of the PSF for the X-array (2:1 aspect ratio) are depicted in Figure 4-23. This is the broad-band version of Figure 4-4, obtained by co-adding the PSFs for several spectral channels. The main peak is centered on the cross that denotes the actual location of the point source. This main peak is flanked by four satellite peaks, each of which has a set of sidelobes. Note that the sidelobes are suppressed in the broad-band PSF relative to the monochromatic case, but the satellite peaks are not. The phase chopping described in Section 4.1 results in an inverted anti-Sun image. The number, amplitude, and location of the satellite peaks relative to the main peak are determined by the shape of the nulling configuration. We define the angular resolution of the array to be the FWHM of the main peak, which can be predicted from the average length of the imaging baselines in the configuration:

$$\theta_{res} \approx 0.48 \frac{\lambda_{av}}{B_{img}}, \tag{3}$$

where the average wavelength was taken to be 12 μm. This relationship was used to determine the size of the array needed to observe a given star (see next section). In addition, the rms level of the satellite and sidelobe structure in the PSF was used as a metric to assess ease of deconvolution.

4.9.3 Array Size Criterion

Combining Eqs. (2) and (3) we obtain a requirement on the average length of the imaging baselines:

$$B_{img} \geq 1.6 \frac{\lambda_{av}}{\theta_{MHZ}}. \tag{4}$$

The criterion for inner working angle is

$$B_{null} \geq 0.9 \frac{\lambda_{av}}{\theta_{MHZ}}. \tag{5}$$

For most configurations, it is Eq. (4) that drives the size of the array needed to observe a given target. The big advantage of the X-array over other configurations is that the length of the imaging baselines is decoupled from the length of the nulling baselines; the long dimension of the array is stretched to meet or exceed the angular resolution requirement of Eq. (4), while the short dimension is held to just meet the inner working angle requirement of Eq. (5). For the other configurations in Fig. 4-8, the array size needed to meet Eq. (4) leads to null baseline lengths that greatly exceed the minimum requirement in Eq. (5) and incur a large penalty from increased stellar leakage.

4.9.4 Deconvolution Approaches

The ability to extract the information about the planet from the reflected light from a planet in orbit in the habitable zone of a star up to 30 pc away is crucial to the design and architecture of the TPF

interferometer. How this information is processed determines such fundamental properties as the proper geometry of the spacecraft and the size of the telescopes. It became clear early in the design stage that understanding planetary signal extraction (PSE) would be important in the Pre-Phase A design, if realistic designs were to be considered.

There is an extensive literature on signal processing from Earth-bound interferometers, both optical and radio. When TPF-I was first proposed, the problem of detecting a signal was already realized as being important. The work of the PSE Working Group was to determine whether these techniques were adequate, and if not, to develop improved methods. In addition, a set of metrics was developed which was independent of signal processing technique that could be used to evaluate different architectures without the computationally expensive process of actually testing each proposed architecture with several different PSE algorithms and many different target solar systems.

The basic performance parameter is SNR. In this effort, the signal is the planetary signal, which is the output of the phase-chopped interferometer. Noise comes from two sources (the star itself and extraneous light), and it comes in two ways (simple background and systematic errors). In the studies that we did, we considered only astronomic sources of background (local zodiacal and exozodiacal light), and we did not yet study systematic backgrounds and errors (imperfect maintenance of the null and thermal backgrounds from other spacecraft). The difficulty of the problem is that the SNR is inherently low, limited by finite observing times and the aperture of the telescopes, and that the most interesting signal bands are at the high and low wavelengths, where the sensitivity of the interferometer is lowest. The other fundamental problem is that any interferometer has limited coverage in the *u-v* plane, so the information obtained from the planetary system is fundamentally incomplete. This is exacerbated by the probability that there are multiple planets in the system, causing confusion in the signal. The combination of low SNR and incomplete information makes identifying a planet and extracting a spectrum a difficult, but not impossible, challenge. These challenges fundamentally drive the mission design.

The most basic source of noise is the stellar leakage from the finite suppression of the interferometric null, which is determined by the architecture of the interferometer. For these preliminary studies, we developed a simulation that included the effects of stellar leakage, exozodical dust, and local zodiacal background, and that could simulate the light from arbitrary planetary systems. Systematic effects were not included. This simulation was independently validated by comparison to several other calculations and simulations.

Many methods have been proposed for extracting the signal from background by different members of the TPF-I collaboration. In the literature, inconsistent assumptions have been made in testing various algorithms, so we decided to have a blind comparison of various algorithms using the JPL standard simulator and a small set of test cases which included solar systems which we thought would be both easy and difficult.

A group of scientists from JPL, The University of Arizona, Ball Aerospace, and eventually several other organizations formed a science working group and developed several new algorithms, in addition to a baseline cross-correlation/CLEAN (CC/CLEAN) algorithm. Each of these was tested against simulated planetary systems with a realistic SNR. It was found that the CC/CLEAN algorithm did reasonably well, and improved algorithms were both proposed and implemented. While none of these have yet turned out

to be a silver bullet for planet finding, the results are quite encouraging. It should be emphasized that this research is still in an early state.

In order to compare architectures without running time-consuming simulations (both generating planetary systems and analyzing them), we developed a set of metrics based on the PSF, which allowed us to calculate comparative planet-finding ability between proposed architectures. These metrics were validated against the CC/CLEAN algorithm and found to be representative of the performance of different spatial configurations and telescope apertures.

There is much work left to be done in this area. When this work wound down, the following items were still pending as possible future areas of research:

- Identify regular and pathological solar systems – what phase space needs to be tested?

- Add bumps in the zodiacal background.

- Incorporate prior knowledge of exozodiacal spatial covariance into a point process algorithm. This should suppress false positives.

- What is the density of background objects?

- Do spectroscopy.

- What is the optimal number of channels?

- How do you get a quick spectra?

- How do you obtain reliable spectra?

- How does variability of planets over observational time scales affect spectroscopy (and detection)?

- What is the optimal strategy for baseline selection?

- Investigate changing baselines to increase *u-v* plane coverage.

- How do we set confidence limits for false positives, false negatives?

- Start incorporating revisit information.

- Alternate approaches to cross-correlation for initial maps.

- Literature search—written survey of possibilities considered and discarded.

- Think of a better algorithm. Still open to new ideas.

This work led to two peer-reviewed papers. Draper *et al*. (2006) laid out the problem, defined important metrics (such as SNR, which is more complex in this problem than it might seem), and tested various solutions. In addition, Velusamy *et al*. (2005) came up with a new approach at analyzing the signal which seems very promising in initial tests.

4.9.5 Trade Study

A complete description of the trade study can be found in Lay et al. (2005). The scoring process is based on the Kepner-Tregoe methodology. The idea is simple. The options are judged against a set of mandatory criteria ("musts") and a set of discriminators ("wants"). Each must is scored as a pass/fail for each option, whereas the wants are weighted by importance and scored for each option on a scale of 1 to 10. Failing a mandatory criterion disqualifies the option from consideration. The highest weighted sum of the discriminator scores determines the best option.

The options in this case are the six architectures described in the Section 4.3. The list of mandatory criteria and discriminators was established through a lengthy process of iteration, based on initial inputs from a joint TPF/Darwin workshop and then edited in a series of meetings of the TPF-I Architecture and

Table 4-3. Scores for Nulling Architectures Considered in Trade Study

	Linear DCB		X-Array (2:1)		Diamond DCB		Z-Array		Triangle		Linear 3	
Overall score / 1000	**816**		**860**		**789**		**749**		**779**		**795**	
Performance	381		385		337		341		292		342	
Cost / risk	435		475		452		408		487		452	

Table 4-4. Key Discriminators in Trade Study, with Scoring Relative to Linear DCB Array

	Metric	Linear DCB	X-Array (2:1)	Diamond DCB	Z-Array	Triangle	Linear 3
Performance							
Number of planet systems characterized by spectroscopy at high angular resolution, beyond minimum required	Star count	0	0	-13	-4	-25	-19
Fidelity of image reconstruction	rms/peak (in Point Spread Function for planet at high res inner working angle)	0	-2	-6	-8	-14	-4
Redundancy / graceful degradation	Expected % of stars observed after loss of 1 spacecraft	0	4	-17	-6	-17	-17
General astrophysics potential	Dynamic range of baselines (max/min)	0	-4	-5	-10	-8	-4
Cost and Risk							
Number of types of spacecraft	# types	0	14	0	-9	0	0
Mass margin	Mass margin	0	0	3	3	15	6
Beam transport optics complexity	# hops to combiner	0	12	0	-10	0	0
Beamcombiner optics complexity	# parts (from schematic)	0	0	0	0	-10	-10
Number of mechanisms/ moving parts	# mechanisms / deployments	0	0	4	4	11	4
Difficulty of integration and test	# spacecraft	0	0	7	7	17	7
Complexity of flight operations	# spacecraft	0	0	4	4	10	4
		0	**43**	**-27**	**-66**	**-33**	**-22**

Design Teams. This process involved representatives from Ball Aerospace, Lockheed Martin and Northrop Grumman. Inputs were also solicited from the TPF-I Science Working Group. Participants were asked to weight the discriminators; an average of the responses was taken to determine the initial values, and the weights were normalized so that the sum of all weights equals 100. The weights represent the relative importance given to the discriminators and are separate from any consideration of the options.

Wherever possible, a discriminator was quantified using one or more metrics. For example, for the discriminator "Control system complexity" the metric chosen was the number of control loops needed for the basic array operation. These metrics helped to inform the scoring process, although scoring is fundamentally subjective. The scoring of the discriminators for each option was conducted at a 2-day meeting held at JPL in December 2004, with approximately 20 participants from JPL and the contractors. For each discriminator the best option was scored a 10, and a simple voting system was used to establish the scores for the other options. Sometimes the scores bore a linear relationship to the metrics; sometimes explicitly not. If there was little difference between the options then the scores were close together; large differences were reflected in a low score for the worst option. The contribution to the final score is given by the product of the weight and the score, with the weight reflecting the importance of the discriminator and the score showing the size of the difference between the options. The weighted sum of the scores has a maximum possible value of 1000 points for each option.

After the initial round of scoring there were multiple rounds of iteration in which both the weights and scores could be adjusted. This may sound like "gaming the system," but the intent is not that we turn the crank on the process and blindly accept the outcome; rather it is that the final table should reflect the collective engineering judgment of the group. The process is inevitably subjective (particularly the assigning of weights), but is highly transparent. It structures the analysis, focuses discussion on the key areas, and invites criticism and comment.
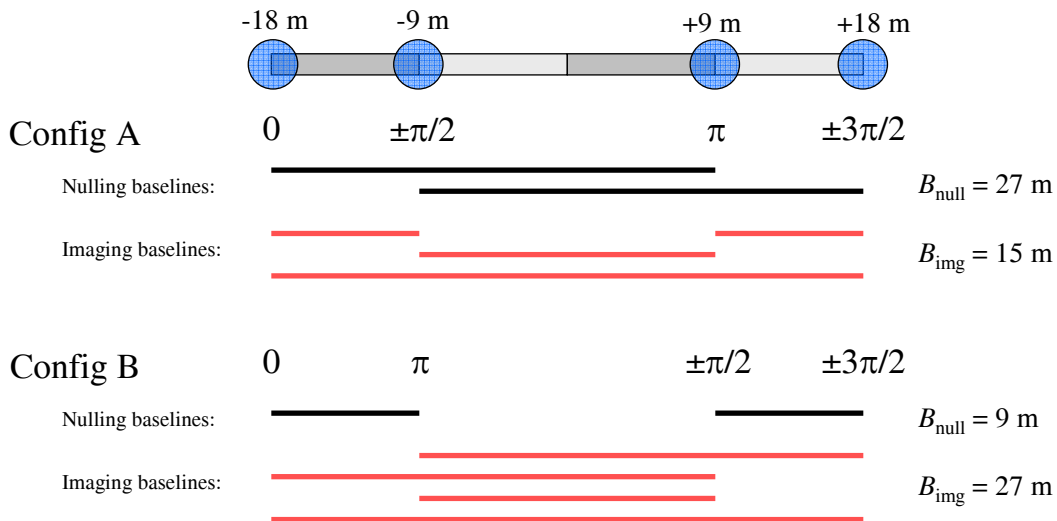
Figure 4-24. Schematic showing collector spacing for the Structurally Connected Interferometer. There are two different ways to phase the interferometer. In Configuration A, the nulling baselines are interleaved. In Configuration B, the nulling baselines are adjacent.

The full set of metrics and scores for each combination of option and discriminator is listed in Lay et al. (2005). The final scores are tabulated in Table 4-3, with the breakdown into performance and cost/risk. The X-Array scored the highest, followed by the Linear Dual Chopped Bracewell. Table 4-4 gives a breakdown of the key discriminators, ie. those responsible for most of the differentials in the final scores.

4.10 Structurally Connected Interferometer

Prior to 2004, the TPF-I project developed designs for both a formation-flying interferometer (FFI) and a structurally connected interferometer (SCI) architecture. In the following we briefly describe the SCI design and summarize a 2006 reassessment of its planet-finding performance.

4.10.1 Baseline design

The SCI architecture created by the TPF-I Design Team has four 3.2-m diameter collectors, spaced along a 36-m linear structure as depicted in Fig. 4-24. The light from the collectors can be phased as a Dual Chopped Bracewell Nuller in two different ways. Configuration A has longer nulling baselines and therefore a small inner working angle, but the short imaging baselines result in poor angular resolution.
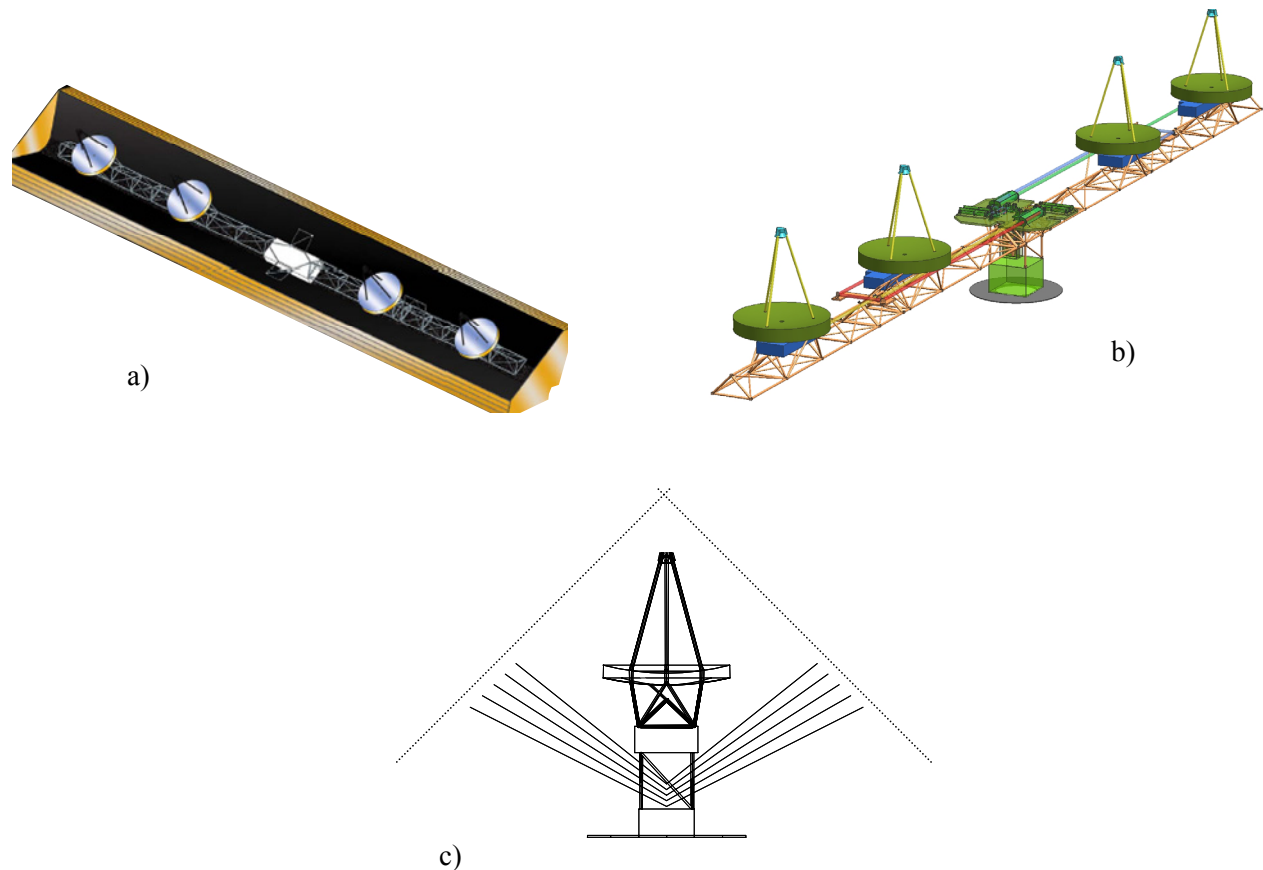
Figure 4-25. (a) SCI with deployed thermal shade. (b) SCI with thermal shade removed. (c) End view to illustrate the ±45 degree solar shading limit.

Configuration B has almost twice the angular resolution, but it has three times the inner working angle.

Different views of the SCI design are shown in Fig. 4-25. The combiner optics are located at the center of the structure, as is the spacecraft bus.

The 36-m length is constrained by the volume available in the shroud of the Delta IV Heavy launch vehicle (Fig. 4-26). The structure is folded at three hinge points. Further deployments are necessary for the thermal shades and secondary mirror supports.

4.10.2 Performance Assessment

With a maximum baseline of 36 m, the SCI has lower planet-finding capability compared to an FFI. The planet-finding process has three stages: (1) Detection of candidate planets, (2) Orbit determination, and (3) Spectroscopic characterization. Orbit determination and spectroscopy require greater angular resolution than the initial detection, and it is therefore these stages that most constrain the SCI performance.

Three criteria were applied to determine those stars for which an Earth-like planet could be detected and characterized: (a) Inner Working Angle (IWA) — at least 50% of the planet's orbit must lie outside the IWA, averaged over all inclinations, (b) Angular resolution — the planet should be unconfused with other planets at least 50% of the time, and (c) Spectroscopy time — no more than 100 days of integration time is allowed to achieve an SNR of 5 relative to the continuum over 9.5–10 μm (for detection of ozone). The angular resolution criterion was evaluated by calculating the fraction of time that a planet in an Earth-like orbit would be confused (i.e., not resolved as a separate entity) with either a Venus or Mars analog.
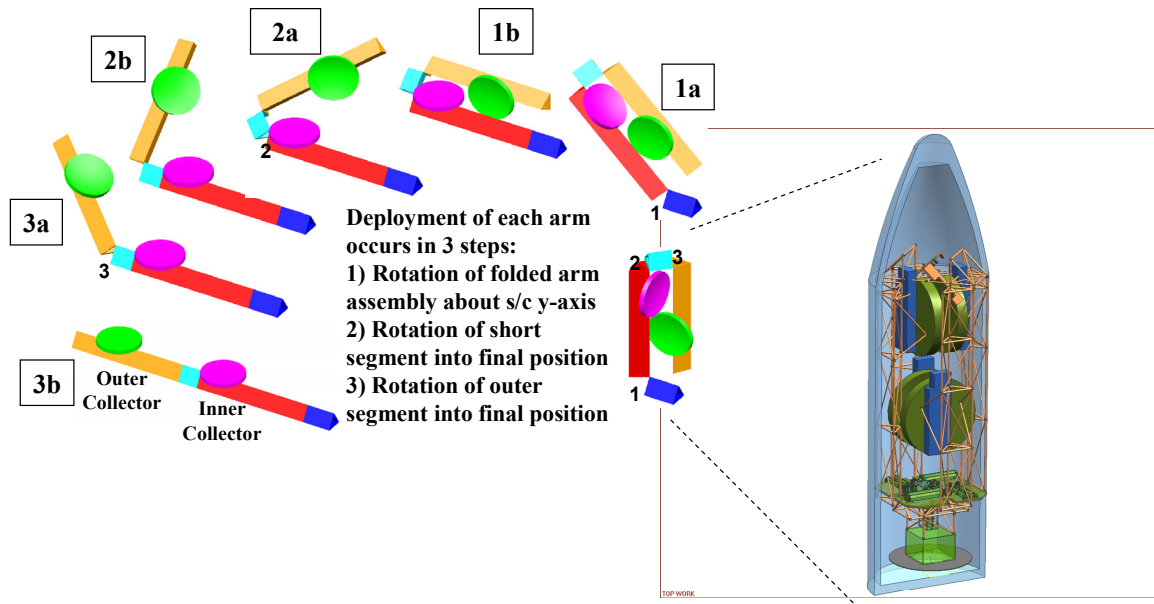
Figure 4-26. Stowed configuration for launch on a Delta-IV Heavy and schematic of on-orbit deployment sequence.
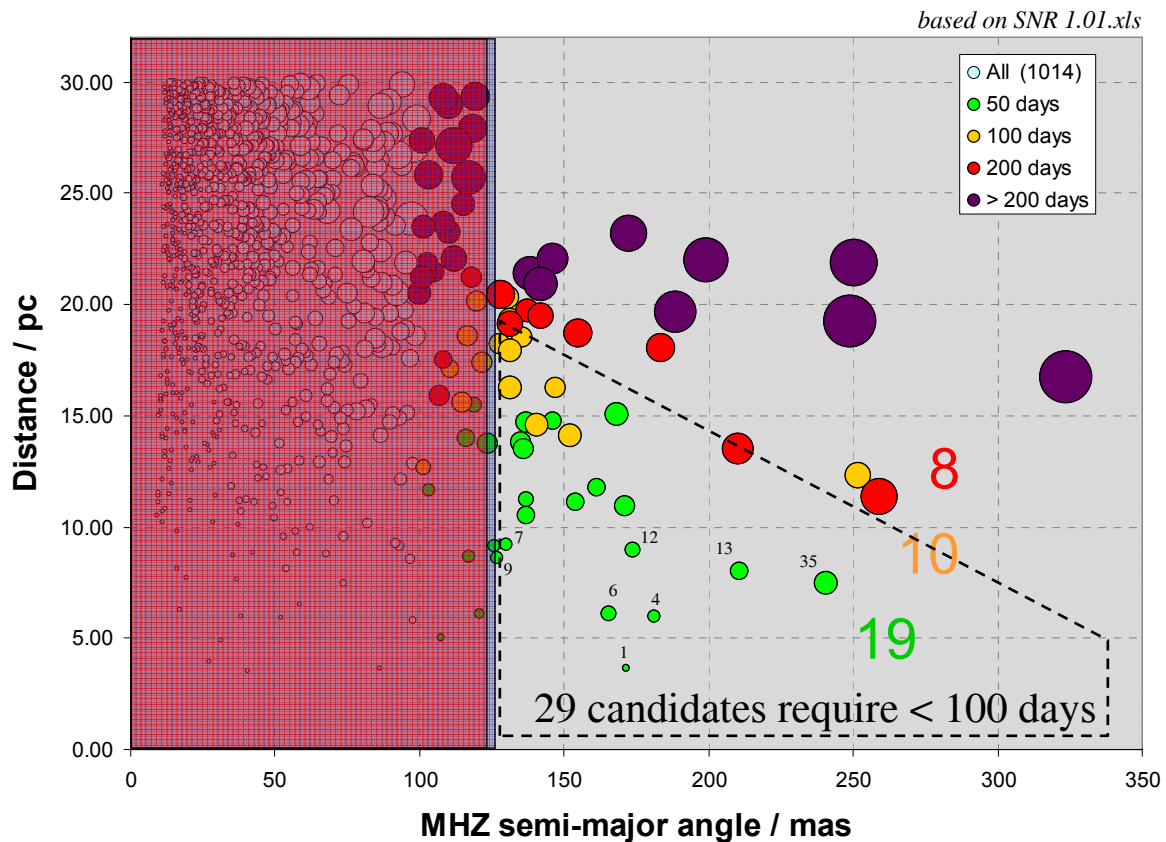
Figure 4-27. Candidate stars available for a 36-m SCI mission. Stars in the maroon area are excluded by the IWA criterion. Stars in the blue and maroon areas are excluded by the confusion criterion. The stars are color-coded according to the integration time needed to detect ozone with an SNR = 5 (see legend). The small numbers indicate the integration times for specific nearby examples. The large numbers show the number of observable targets in each integration bin. The dashed line encloses (almost) the region containing the 29 observable stars with characterization times of less than 100 days. See Section 5.9 for an introduction to this representation of the target stars.

For a planet orbit that just meets both the IWA and angular resolution criteria, only 1/16th of the orbit is available on average for orbit determination (planet lies inside IWA 50% of the time; planet is confused 50% of the time; and star is observable 25% of the time due to ±45 degree solar shading constraint).

Figure 4-27 shows how the application of the three criteria results in 29 candidate target stars for the Configuration B phasing (Fig. 4-24). For Configuration A, the smaller IWA pushes the red zone well to the left, but the poor angular resolution increases the confusion and extends the blue zone out to beyond 200 mas, greatly reducing the number of candidate targets. Figure 4-28 illustrates how the performance capability degrades rapidly as the length of the structure is reduced below 36 m.
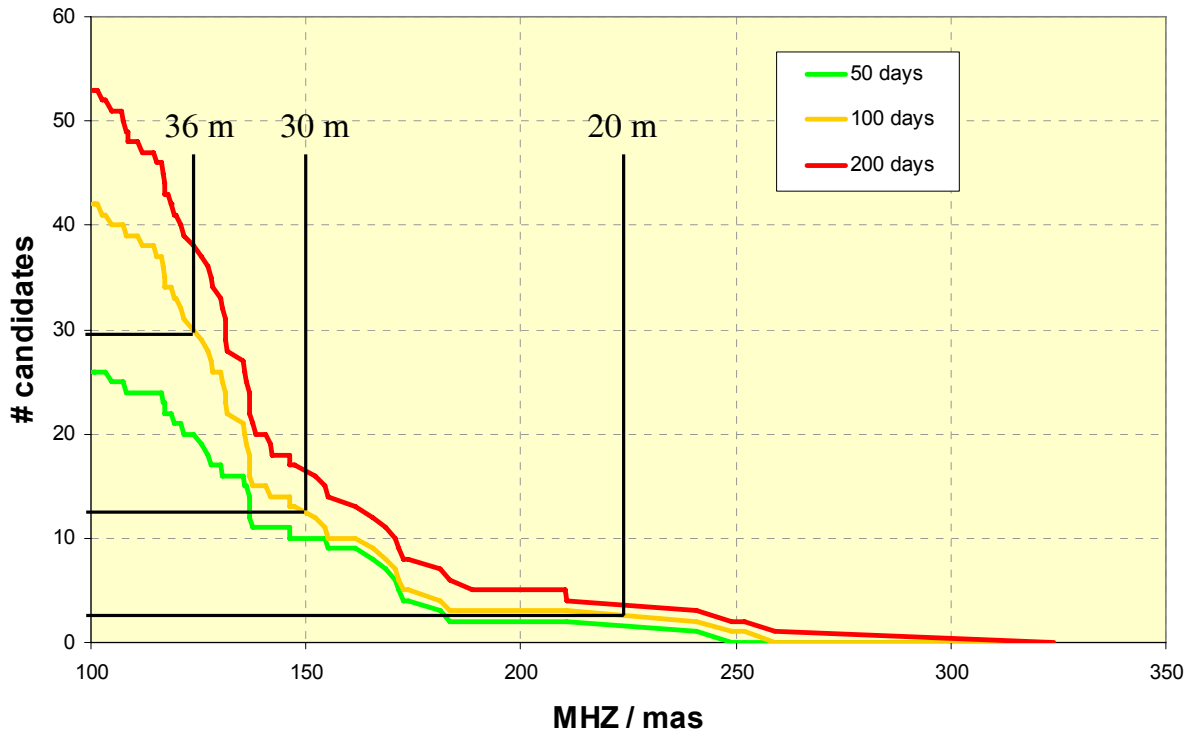
Figure 4-28. Dependence of the number of candidate target stars on the array length. For the 100-day limit on spectroscopic integration time (orange curve), the nominal 36-m design has access to 29 stars. Shrinking this to 30 m extends the maroon and blue areas to the right by a factor of 36/30 in Fig. 4-27 and reduces the number of stars available to 12. For a 20-m structure this is reduced to 3. Increasing the allowed integration time to 200 days does not dramatically improve the performance (red curve).

4.10.3 Summary

The major advantage of the SCI architecture is that it does not require the new technology of formation flying. The maximum size of 36 m is constrained by the volume of the launch shroud, and limits the IWA and angular resolution. The demands of orbit determination and spectroscopy limit the number of candidate stars to less than 30. This number falls off rapidly as the array size is reduced.

4.11 References

Angel, J. R. P., and Woolf, N. J., "An imaging nulling interferometer to study extrasolar planets," *Astrophys. J.* **475**, 373–379, (1997).

Beichman, C. A., Woolf, N. J., and Lindensmith, C. A., *Terrestrial Planet Finder: a NASA Origins program to search for habitable planets*, JPL Publication 99-3, Jet Propulsion Laboratory, Pasadena, CA (1999).

Draper, D. W., Elias, N.M., II, Noecker, C., Dumont, P. J., Lay, O. P. and Ware, B., "Planet Signal Extraction for the Terrestrial Planet Finder Interferometer," *Astron. J.* **131**, 1822–1836 (2006).

Dubovitsky, S., and Lay, O. P., "Architecture selection and optimization for planet-finding interferometers," *Proc. SPIE* **5491**, 284–295 (2004)

Hamlin, L. A., Henry, C. A., Adams, D. S., MacNeal, P. D., Cardone, J. M., and Holm, R. G. "Current status of the Terrestrial Planet Finder structurally connected interferometer concept," edited by R. B. Hoover, G. V. Levin, A. Y. Rozanov; *Proc. SPIE* **5555**, 231–240 (2004).

Karlsson, A. L., Wallner, O., Perdigues Armengol, J. M., and Absil, O., "Three telescope nuller based on multi beam injection into single-mode waveguide," New Frontiers in Stellar Interferometry, *Proc. SPIE* **5491**, 831–841 (2004).

Kelsall, T., Weiland, J. L., Franz, B. A., Reach, W. T., Arendt, R. G., Dwek, E., Freudenreich, H. T., Hauser, M. G., Moseley, S. H., Odegard, N. P., Silverberg, R. F., and Wright, E. L., "The COBE diffuse infrared background experiment search for the cosmic infrared background. II. Model of the interplanetary dust cloud," *Astrophys. J.* **508**, 44–73 (1998).

Kepner, C. H., and Tregoe, B. B., *The New Rational Manager*, Princeton Research Press, Princeton, NJ (1981).

Lay, O. P., "Systematic errors in nulling interferometers," *Appl. Opt.* **43**, 6100–6123 (2004).

Lay, O. P., and Dubovitsky, S., "Nulling interferometers: the importance of systematic errors and the X-array," *Proc. SPIE* **5491**, 874–885 (2004).

Lay, O. P., "Imaging properties of rotating nulling interferometers," *Appl. Opt.* **44**, 5859–5871 (2005)

Lay, O. P., Gunter, S. M., Hamlin, L. A., Henry, C. A., Li, Y-Y., Martin, S. R., Purcell, G. H., Ware, B. J., Wertz, A., Noecker, M. C., "Architecture trade study for the Terrestrial Planet Finder interferometer," *Proc. SPIE* **5905**, 8–20 (2005).

Lay, O. P. "Removing Instability Noise in Nulling Interferometers," *Proc. SPIE* **6268**, 62681A (2006).

MacNeal, P. D., Adams, D. S., Henry, C. A., Blackhall, H. G., and Cardone, J. M., "Structural configuration for the Terrestrial Planet Finder structurally connected interferometer concept," edited by J. Antebi and D. Lemke, *Proc. SPIE* **5495**, 383–393 (2004).

Noecker, C., Wei, Z., and Decino, J. "Stray light estimates for the TPF formation flying interferometer," *Proc. SPIE* **5526**, edited by P. T. C. Chen, J. C. Fleming, and M. G. Dittman, 249–256 (2004).

Noecker, C., and Lieber, M., "Terrestrial Planet Finder control system requirements for structurally connected interferometers," edited by W. A. Traub, *Proc. SPIE* **5491**, 373–382 (2004).

Noecker, C. and Leitch, J., "Beam transport for the TPF interferometer," *Techniques and Instrumentation for Detection of Exoplanets II*, edited by D. R. Coulter, *Proc. SPIE* **5905**, 590504 (2005).

Peters, R. D., Lay, O. P., Hirai, A., and Jeganathan, M., "Adaptive nulling for the Terrestrial Planet Finder Interferometer," *Proc. SPIE* **6268**, 62681C (2006).

Serabyn G., and Mennesson, B., "TPF Interferometer architecture drivers and implementation," *Proc. 2004 IEEE Aerospace Conf.*, Big Sky, MT, 4, 2144–2155, (2004).

Velusamy, T., Marsh, K. A., Ware, B., "Point Process Algorithm: A New Bayesian Approach for TPF-I Planet Signal Extraction," *Direct Imaging of Exoplanets: Science and Techniques*, *Proc. IAU Colloquium 200*, editors Aime C., and Vakili, F., Cambridge University Press, Cambridge, UK, pp. 621–626 (2006).

5 TPF-I Flight Baseline Design

5.1 Introduction

In this chapter we describe the design and performance capability of the nominal formation-flying interferometer (FFI) architecture. This is the stretched X-array configuration. Prior to the trade study described in the previous chapter, the baseline design was the linear dual chopped Bracewell configuration. The X-array 2:1 was the highest ranked in the trade study, but it was superseded by the stretched X-array, with its ability to eliminate instability noise.

The array geometry is summarized in the next section, followed by a description of the spacecraft design in Section 5.3 and the optics in Section 5.4. The sensitivity to planets is shown in Section 5.5 with the inner and outer working angles, and Section 5.6 shows the stars that can be surveyed for planets. The spectroscopic sensitivity is given in Section 5.7, followed by the imaging capabilities in Section 5.8.

5.2 Array Geometry

Figure 5-1 shows the stretched X-array geometry. All spacecraft lie in a plane normal to the direction of the incoming starlight. The beams are then routed to the central combiner spacecraft in a single hop. The aspect ratio is 6:1. This is still a dual chopped Bracewell design; the nulling baselines (π phase difference) are along the short dimension of the array, and the imaging baselines form the long sides and diagonals. The phases are inverted to switch between the two chop states. The collector spacecraft are identical, and have apertures with a diameter of 3.8 m, consistent with packaging into the shroud of a Boeing Delta IV
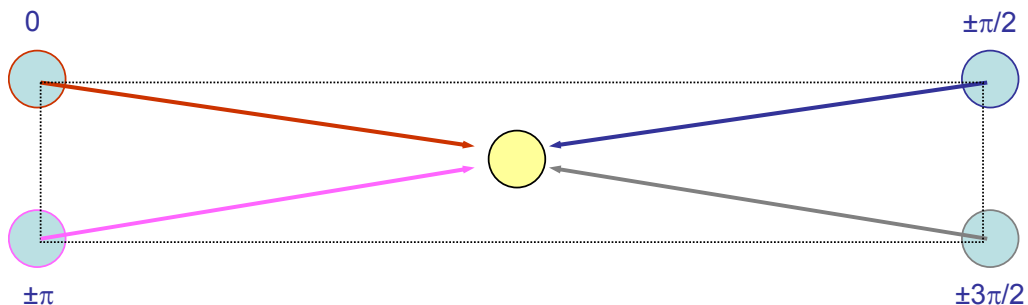
Figure 5-1. The stretched X-array configuration. Blue circles represent collector spacecraft, and the yellow circle is the central combiner spacecraft. Numerical values represent the relative phasing of each collector as implemented in the beam combiner

Heavy launch vehicle. The minimum array size of 120 × 20 m is constrained by the desire to maintain at least 20 m separation between the centers of the spacecraft. The maximum array size of 612 × 102 m is limited by the maximum distance (311 m) over which the beams can be relayed without introducing significant amounts of stray light for the thermal shields. These constraints result in a dynamic range of 5:1 in the array size.
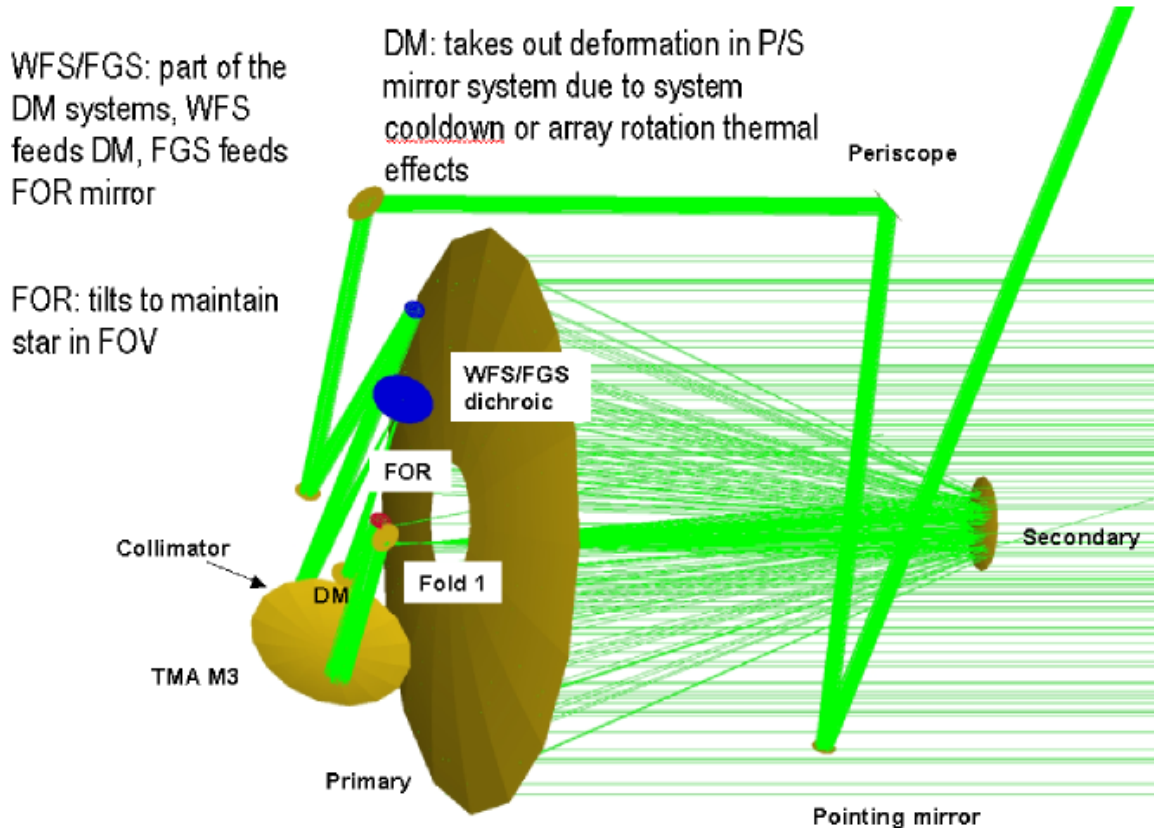
Figure 5-2. The main optical components of the collector telescope spacecraft.

5.3 Optical Beam Train

5.3.1 Collector Spacecraft

The beam train consists of the following main elements. First the collector telescopes, a three-mirror design. Beneath the telescope primary mirror, see Figure 5-2, are systems for maintaining pointing at the star and internal alignment and metrology systems. A deformable mirror (DM) is included in the beamtrain to allow wavefront correction; further analysis will be needed to examine the necessity for this unit and its range of operation. Following recollimation of the beam, a number of fold mirrors transmit the beam up to near the top of the telescope body and send it to the next spacecraft. The next spacecraft then relays the beam to the beamcombiner spacecraft.
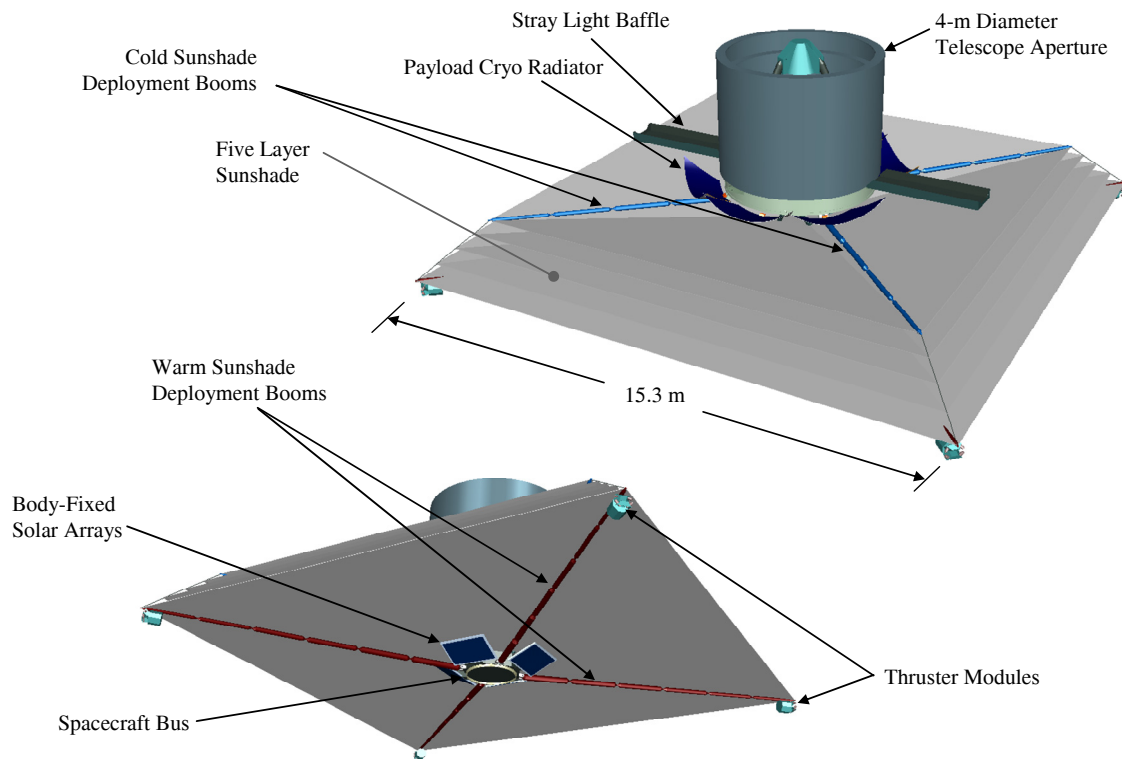
Figure 5-3. Collector Spacecraft.

CHAPTER 5

5.3.2 Combiner Spacecraft

On the beamcombiner spacecraft, the beam is first compressed from approximately 150 mm in diameter to 30 mm in diameter, and it passes through a multistage delay line. Following the delay line, it enters the adaptive nuller where the phase and amplitude are adjusted across the spectral band. After the adaptive nuller it enters a switch, which allows selection of T1–T2, T3–T4 or T1–T3, T2–T4 beam combination. Then it enters the nuller itself, at which point the fringe tracking light is separated from the science beams. After nulling and interfering the beams at the appropriate phases, the science light enters a single spatial mode fiber, and then it is dispersed spectrally before striking the science detector. Numerous beam train systems exist to maintain and adjust the alignment and the collector spacecraft phase of the beams. These will be discussed below.
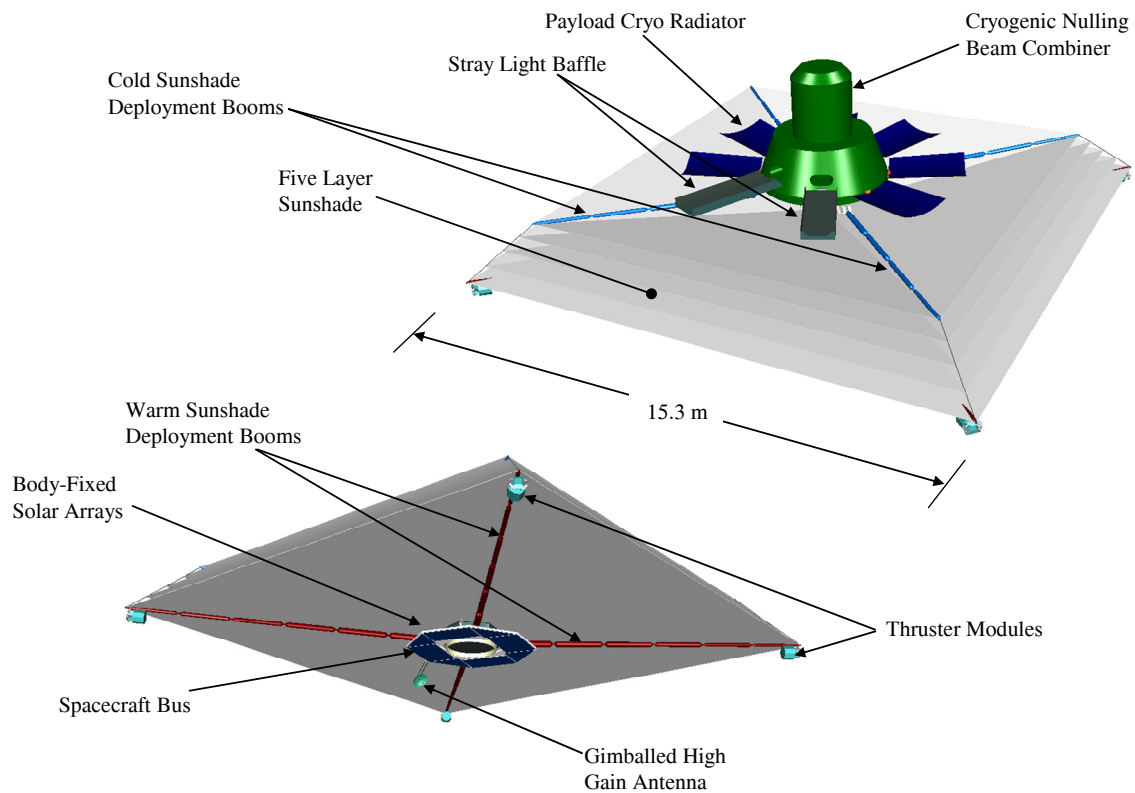
Figure 5-4. Combiner Spacecraft

5.3.3 Telescope Assembly

The telescope design is a three-mirror anastigmat design using conic sections: the primary is an ellipse; the secondary is a hyperbola; and the tertiary is an ellipse. After reflection from the secondary, the beam passes through a hole in the center of the primary and is folded into a plane beneath the primary. The primary mirror has a diameter of 4.0 m, and the secondary has a diameter of 0.3 m, giving an obscuration ratio of ~0.023, excluding spiders and mounts. An offset field angle used in previous designs was eliminated to reduce the number of differences between the left and right sets of collector telescopes. The new design was also required to have a very uniform wavefront performance across the field of view. This is to ensure that as the telescope drifts in space, the Strehl ratio remains the same, so that the coupling onto the single mode fiber at the end of the beamtrain does not vary. This ensures that the null depth will remain constant during the observation. It was not considered desirable to continuously operate the DM to compensate for these small wavefront changes. A mirror placed between the tertiary and the DM acts as a field of regard (FOR) mirror; it tilts to bring light from a chosen star into the main beam path and maintains that alignment continuously during observations.
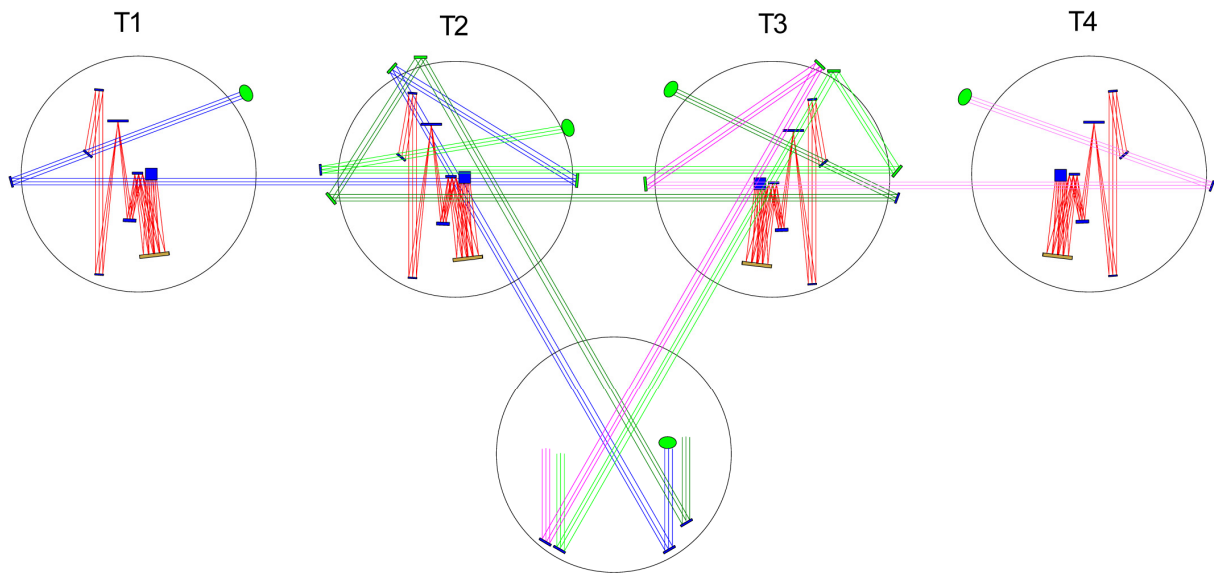
Figure 5-5. Beam transits between spacecraft are made as nearly as possible across diameters. The beam layout ensures that no angle changes as the formation expands. The layout also gives maximum shading from the sunshields; each mirror looks across the width of the spacecraft.

5.3.4 Beam Train Optics

Beneath the primary mirror, the beam strikes a fold mirror that tilts to bring the starlight into the main beam path. Next it strikes the third mirror of the three-mirror telescope and the FOR dichroic mirror. Behind this dichroic mirror are an alignment beam launcher and a metrology beam retro-reflector. Next, the beam strikes the DM, which corrects static wavefront errors. This pair of mirrors (the DM and the FOR) is controlled from the output of sensors placed behind the WFS/FGS dichroic, next in line, which separates out some light from the star for pointing and wavefront sensing. Next the beam is recollimated and transmitted to the top of the spacecraft. An active pointing mirror relays it to the next spacecraft.

5.3.5 Beam Transfer between Spacecraft

The active pointing mirror is controlled by beam shear sensors located behind a mirror on the next spacecraft. This continuously relays signals via an RF system to maintain accurate pointing. For interspacecraft transfers, the mirrors are arranged so that there is maximum shielding of the mirror from the sunshade of the next spacecraft. This is important for stray light mitigation. In earlier TPF-I designs, the number of folds and their angles were maintained in a symmetric fashion for each beamtrain. In this design, the fold angles are allowed to vary resulting in easier engineering of the layout and the consequential small asymmetries are compensated for by the adaptive nuller.
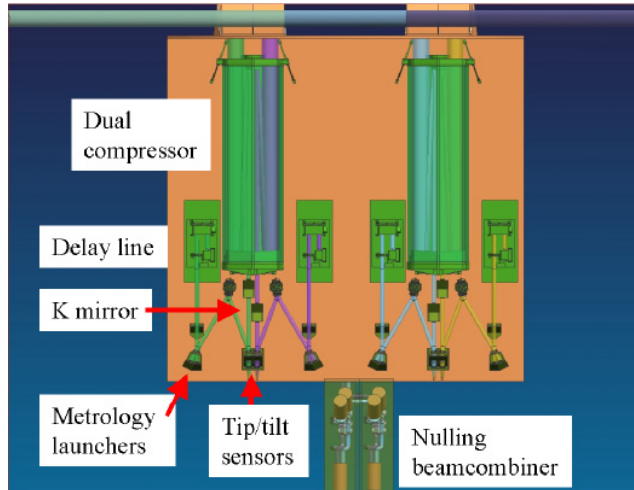
Figure 5-6. First side of vertical optical bench.   **Figure 5-7.** Second side of vertical optical bench.
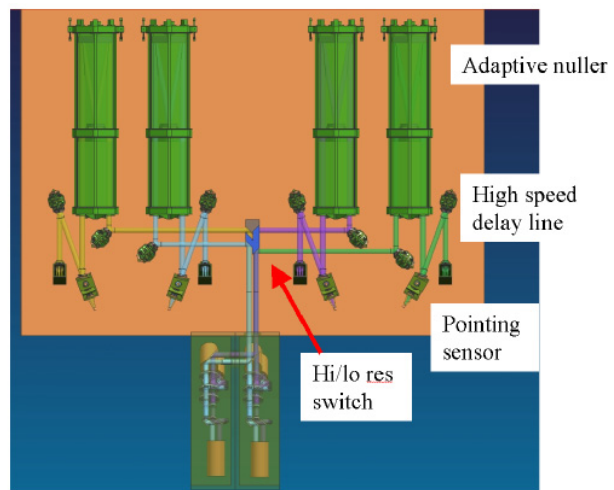
5.3.6 Stray-Light Modeling

Analysis showed that for a beam transfer mirror a view of the opposite spacecraft's sunshade, particularly the gap between the topmost shades, would admit an excessive number of stray-light photons into the science beam. This is because of the small imperfections of real mirrors and the need to detect extremely low levels of light from the target. Two stray-light analyses were performed, one a simple spreadsheet analysis and the other using an optical modeling code known as FRED (developed by Photon Engineering). Good agreement was obtained between these models for collector–collector transfers. Both models showed that for beam transfer heights 4 m above the sunshades, the collector–collector separation could be as much as 165 m. Baffle diameter was 125 mm at the transmitting spacecraft and 150 mm and the receiving spacecraft. Further analysis is needed for beam transfers between collector and combiner.

5.3.7 Combiner Spacecraft

The combiner spacecraft contains the majority of the optical systems. Each beam train is replicated exactly with minor differences at the simplified nuller. The top of the spacecraft receives the beams in a "maximum shading" arrangement and folds them down onto one side of a two-sided vertical main bench, see Figure 5-6. Here the beams are compressed to 30 mm diameter and passed through multistage delay lines before passing through to the opposite side of the bench and entering the adaptive nullers as shown in Figure 5-7. At the output of the adaptive nullers the beams are sent to the switch and into the nulling

beamcombiner. The exit pupil of the adaptive nuller forms the pupil of the beamcombiner system. The nuller bench is appended to the base of the vertical bench.

5.3.8 Beam Conditioning

The beam conditioning systems are: pupil stops and apertures to define the beams and restrict stray light, DM (on the collector spacecraft), adaptive nuller to tune amplitude and phase across the spectrum, delay lines for coarse through fine stages of fringe acquisition, and pointing and shear detectors for both interspacecraft beam transfers and for internal alignment principally on the beamcombiner spacecraft. Another system needed in the FFI design allows adjustment of the polarization angle of the incoming beams which can change as the spacecraft drift. The final system is the single mode spatial filter placed before the science detector. This selects the fundamental mode of the beam and reduces the sensitivity to shear and pointing misalignments as well as higher order beam asymmetries.

5.3.9 The Adaptive Nuller

The adaptive nuller consists of a deformable mirror placed at the focus of a parabolic mirror in an arrangement similar to a cat's eye delay line. At the focus, the input beam is dispersed in wavelength and separated into two orthogonally polarized stripes. By pistoning the mirror elements, phase can be added or subtracted from different spectral regions of the beam; and by tilting the mirror elements across the length of the stripe, the pointing of the output beam can be varied. By clipping the output beam against an aperture, the beam intensity can be varied for a particular range of wavelengths. One of these systems is placed in each beam, and it allows the correction of small differences in throughput and phase between beams arising from alignment changes and variations between optical components throughout the beam train. This capability operates independently on orthogonal polarizations.

5.3.10 Delay Lines

A multistage delay line is conceived for this system. A coarse stage of >20 cm range allows initial acquisition of the fringe and it is then parked. Subsequent stages allow range adjustment from 50 pm to 5 cm in three stages. The fine stage is a high speed stage based on a similar concept to stages used in JPL's Planet Detection Testbed3. These are re-actuated piezo-electrically driven stages capable of moving a 50 mm diameter mirror a distance of 3 mm at a rate of more than 2 kHz. The fine stage is a separate item mounted on the second side of the optical bench. The other two stages form a single unit with voice coil actuation. The operating ranges of the three stages overlap the regions 50 pm to 50 nm, 50 nm to 50 μm, and 50 μm to 50 mm.

5.3.11 Alignment System

Pointing and shear detectors are located at various stages in the system. A full-aperture alignment beam produced by a laser mounted on the collector spacecraft is co-aligned with the science light and used for beam shear or pointing sensing at interspacecraft transfers, after the compressors and after the adaptive nullers. The same beam is used for polarization angle sensing and correction on the beamcombiner spacecraft immediately after the compressors. Pointing adjustments are made at the last mirror before transmission to the next spacecraft, at the entrance to the compressor, and possibly at the entrance to the nullers (depending on the predicted stability). Pointing and shear corrections are made at the entrance to the adaptive nuller.
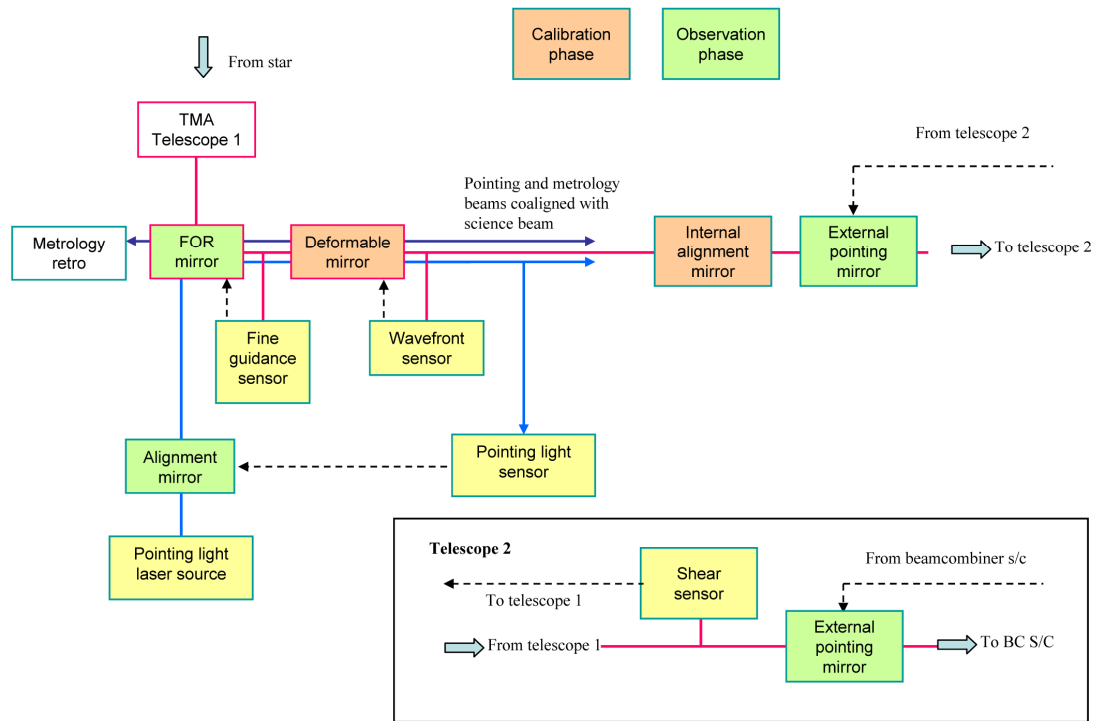
Figure 5-8. Control scheme: telescopes spacecraft.

5.3.12 Simplified Nuller

For the FFI design work, one desire was to try to simplify the MMZ nuller used for the SCI design. The main benefits would be that only one internal laser metrology beam would be needed for each beam of the interferometer rather than two, the attenuation or round trip insertion loss would be less for the metrology light, and the science light would emerge on only two beams rather than four, offering a small but significant improvement in signal to noise ratio at the detector. There would also be associated engineering simplifications. Because of the wide spectral band to be covered by TPF-I, the nuller is actually divided into two units stacked next to one another, one operating on the wavelength range 7 to 11 μm and the other on the range 11 to 17 μm. This arrangement necessitates an additional metrology path and possibly a second fringe tracking system. By splitting the spectrum, we generate less demanding coating requirements on the beamsplitters, which must give a near 50/50 split for the highest efficiency. Also, single spatial-mode filters (which cover these spectral bands) are expected to become available.

The simplified nuller uses a beamsplitter/compensator plate arrangement to obtain a near-match of optical path across the waveband. Residual error in reflection/transmission ratio (R/T) is taken up using one specially fabricated coating on one side of the compensator plate. Models showed that throughput could then be matched across the spectral band on both incoming beams to better than 1%. The residual amplitude and phase errors are then well within the compensation range of the adaptive nuller.

5.3.13 Science Detector and Fringe Tracking

The science detector operates on the two complementary outputs of the cross-combiner. Light emerging from the cross-combiner is focused through the single-mode spatial filter (subject of a TPF-I technology development effort) and then dispersed through a prism before being detected on the science array. Since only two beams are output from each cross-combiner, a single science detector array (nominally a Si:As array) can handle all four beams from the pair of cross-combiners.

The nuller layout includes a fringe-tracking camera which detects the phase on each nuller and on the cross-combiner. One beam from each nuller is extracted from the rejected light output (all the 7- to 17-μm wavelength starlight exits the system from this output) and is dispersed onto the camera array. From the cross-combiner, two beams are extracted, so a total of four beams are sensed at the array. For the second cross-combiner, a second fringe tracker would be needed unless a laser metrology could be used to transfer measured phase to the second nuller.

5.4 Control System

With so many moving parts the observatory requires an extensive control system. The basic requirements for nulling performance to meet our planet-detection goals imply amplitude control of the incoming beams to 0.1%, and phase control of the beams to 2 nm across the band. In turn, the amplitude control requirement can be broken down into a pointing and shear requirement at the input to the spatial filter. Mirrors that move cause translation of the beams at other mirrors and because of mirror imperfections and non-uniformities. This can change the phase and distribution of phase and amplitude across the passband, changing the null depth and introducing a noise component into the signal. The full complexity of these and other effects (for example, diffraction effects over long beam paths) is yet to be modeled, but the basic layout of the control system can be deduced from experience in the nulling laboratory and the modeling that has been done so far. In smaller systems null depths of 10^{-6}, adequate for the performance needs of TPF-I, have been reached using monochromatic light, and work is in progress to extend these results to broader spectral bands and to systems which null on two pairs of beams. The Keck Observatory's nuller control system also shares features of the TPF-I design although the layout is somewhat different. The Planet Detection Testbed incorporates a number of the control systems envisioned for TPF-I.

For deep nulling, the optical properties of the two incoming beams need to be matched to a high degree. The single-mode spatial filter can alleviate some of these requirements, so for example, incoming beam tilt and shear errors do not have to be so finely controlled as a simple analysis would suggest. Even so, for the flight design, the pointing requirement will be on the order of 1 arc seconds, and the shear requirement will be about 1.2% of beam diameter. The polarization rotation angle matching requirement is about 2 arc minutes. Before corrective action by the flight system, the telescope attitude can drift in space to angles as much as 1 arc min from the star, and this would result in a similar rotation of the polarization of the telescope's output beam. After transfer through the second collector and into the beamcombiner, and allowing for static errors in the setup, the requirement could be exceeded unless correction is possible.
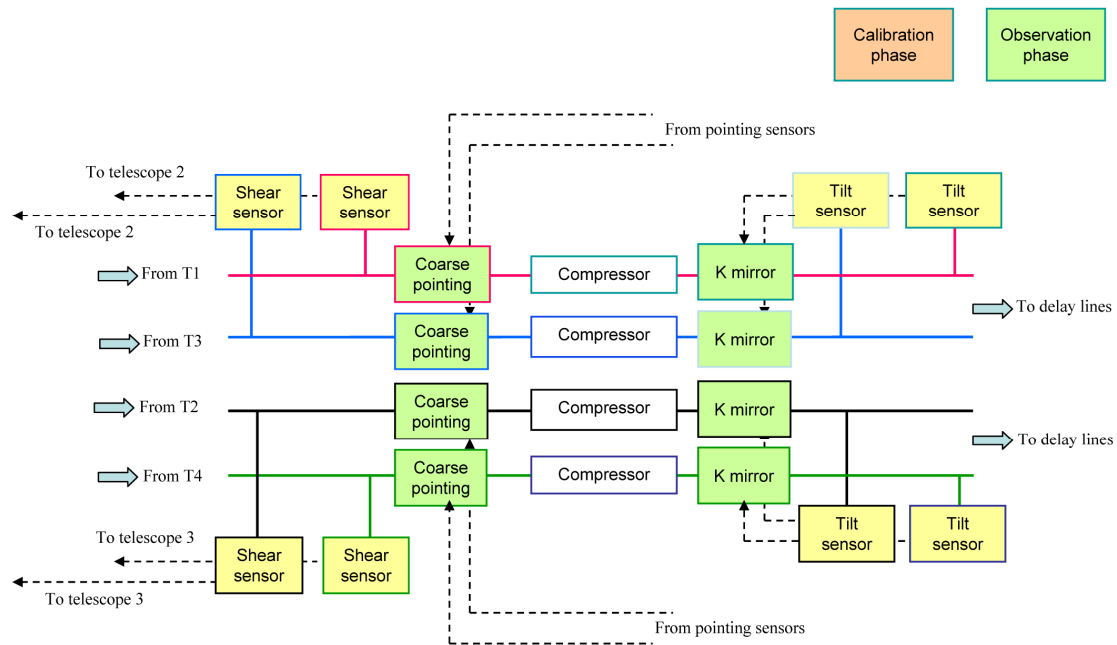
Figure 5-9. First section of beamcombiner spacecraft control system.

The basic control scheme is laid out in the series of Figures 5-8 through 5-11. Some alignments will take place continuously, and others will take place occasionally; these have been differentiated using different gray shades for calibration-phase and observation-phase processes. Calibration-phase processes might take place once every few hours up to once every few days, depending on the stability of the systems involved. Observation-phase processes will have characteristic times of milliseconds up to minutes.

5.4.1 System Summary

The system is briefly summarized here, and more detail is added in the following section. Referring to Figure 5-8, starlight enters the main beam train at the FOR mirror and starts its journey to the beamcombiner. A fine-guidance sensor behind the dichroic mirror controls the FOR mirror and maintains pointing on the star. A pointing light sensor and an alignment mirror allow the starlight and an alignment beam to be accurately co-aligned in the beamtrain. Also, a wavefront sensor allows sensing of any primary mirror aberrations which would be corrected by the DM. A metrology retroreflector reflects full-aperture metrology, co-aligned with the starlight, back to the beamcombiner spacecraft. An internal-alignment mirror is included to facilitate any necessary post-launch adjustments, and then the science beam and alignment beam leave the telescope spacecraft via a pointing mirror. This pointing mirror is controlled from a shear sensor located on the next collector spacecraft, requiring a control loop running through the radio frequency (RF) link. Similarly, a pointing mirror on the second telescope is controlled by a shear sensor on the beamcombiner spacecraft (lower box on Figure 5-8). Thus, the science light, alignment, and metrology beams arrive at the beamcombiner spacecraft.
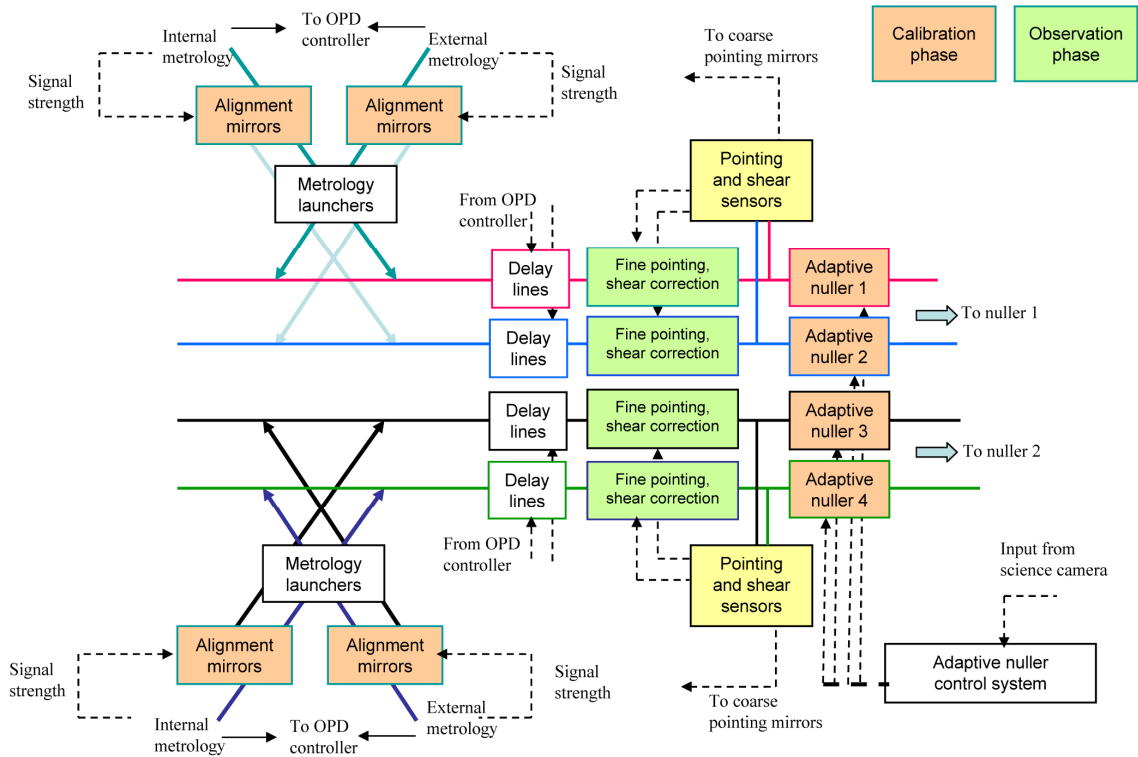
Figure 5-10. Second section of beamcombiner spacecraft control system.
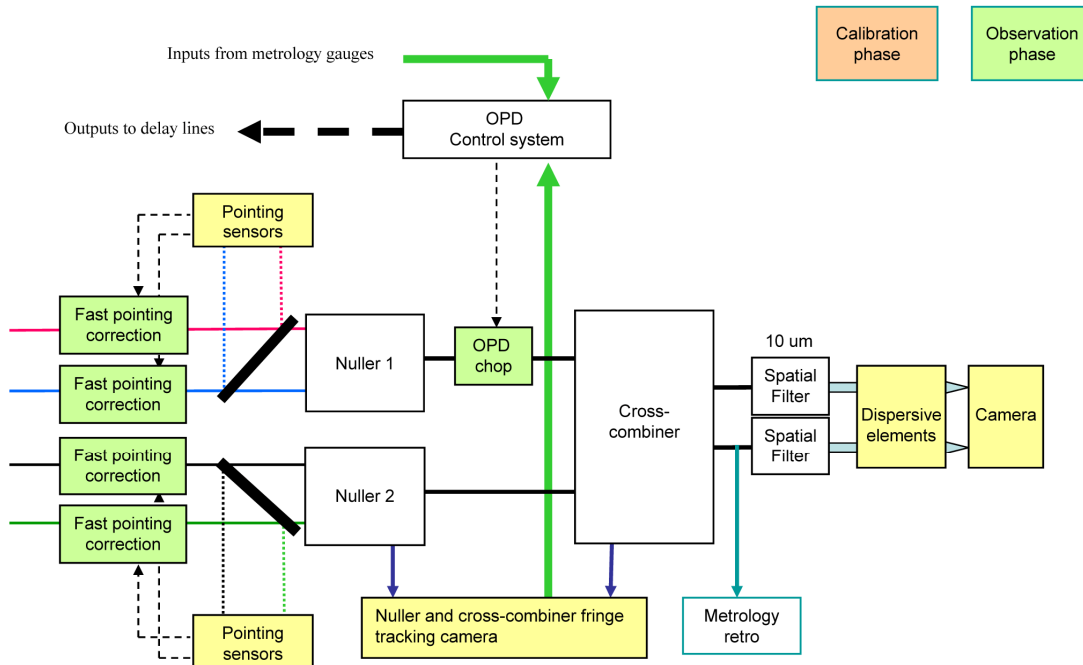
Figure 5-11. Final section of beamcombiner spacecraft control system.

Figure 5-9 shows the first section of the beamcombiner beamtrain. A coarse pointing mirror controlled from a sensor further down the beamtrain directs the light through the compressors and K-mirrors. The K-mirrors are controlled by tilt sensors located next in line, allowing small angular deviations in the polarization vector of the science beam to be controlled. Next the beams pass the metrology injection/extraction point (Figure 5-10) where laser metrology beams are directed up to the telescope retro and also down to the beamcombiner retro at the end of the beamtrain following the cross-combiner. The beams enter the delay lines, which are controlled by inputs from the downstream fringe trackers and also from the laser metrology gauges. The high-speed delay line is in fact located separately slightly further down the beamtrain. The beams are then accurately aligned in shear and pointing prior to entering the adaptive nullers. Accurate pre-alignment is necessary here because the adaptive nullers function by controlling beam shear at the output and require accurate pointing onto the focal plane, so these parameters must be fixed at the input. Therefore, the pointing and shear sensors immediately precede the adaptive nullers; these same sensors also control the coarse pointing mirrors previously mentioned. Each laser metrology beam has its own alignment mirror, which would only be adjusted occasionally.

The adaptive nuller is set up during the calibration phase using data acquired by the science camera, removing small amplitude and phase differences across the waveband so that the nulling performance can be optimized.

Figure 5-11 shows the final section of the beamtrain. Only one set of nullers is shown, but there would also be a split to separate the 7- to 11-μm waveband from the 11- to 17-μm waveband. After the split, a second set of pointing sensors is required to actuate fast-pointing mirrors, which control the final part of the beamtrain. The beams then enter the nullers, and at the exit an optical path chop (OPD is used rather than phase chop because there is only a small efficiency reduction) is applied in one beam, controlled by the OPD control system utilizing both fringe tracker and metrology data. The science beams are then cross-combined, and the internal laser metrology is retroreflected to the launchers. Finally, the science beam is filtered to a single spatial mode, angularly dispersed, and focused onto the science camera.

5.4.2 Optical Metrology

A polarized laser beam is launched from behind the FOR mirror on each collector towards the combiner. See Figure 5-11. This beam is used throughout the beamtrain for the pointing and shear metrology and for polarization rotation metrology.

5.4.3 Pointing Metrology

Short wavelength radiation from the star (0.8 to 1.0 μm) is focused onto a sensor behind the dichroic mirror on the collector spacecraft. Its position on the sensor is controlled by the FOR mirror, thus forming a loop controlling the angle of the starlight with respect to the beam train. A polarized laser beam of wavelength 850 nm is launched behind the FOR mirror and sensed on another sensor behind the dichroic mirror also shown in Figure 5-12. The laser beam is pointed using a tilt mirror behind the FOR mirror, thus forming another closed pointing loop. Calibrations can be made to co-align the stellar beam and the laser beam by integrating the starlight on the laser sensor with the laser turned off. Thus, a bright reference beam for the science beam is formed and can be used downstream for maintaining alignment.

The beam angle is also sensed and corrected on the beamcombiner spacecraft just before entering the adaptive nullers. Simple lens and quad cell assemblies suffice for sensing and a high speed tip/tilt mirror corrects the angle in conjunction with a coarse pointing mirror located at the input to the compressors. An additional stage of pointing correction is needed before entry to the beamcombiner to allow for misalignments introduced by the switch and the 11–17 μm split.
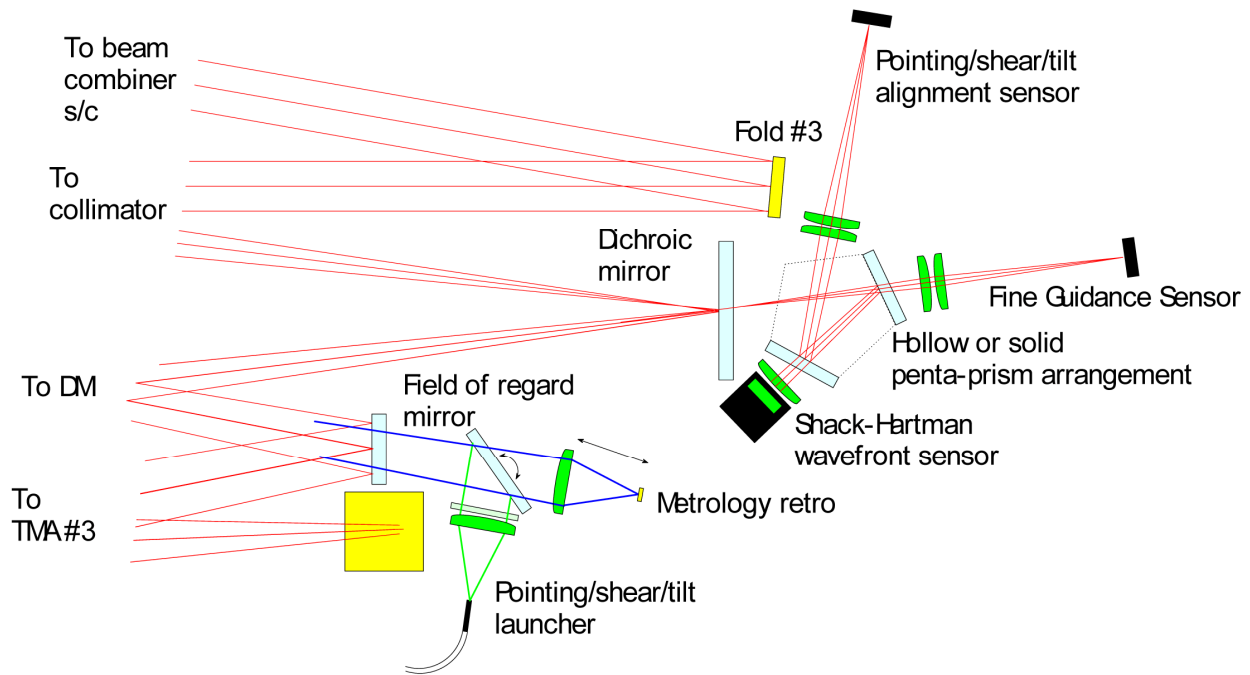
Figure 5-12. Telescope ancillary optical components.
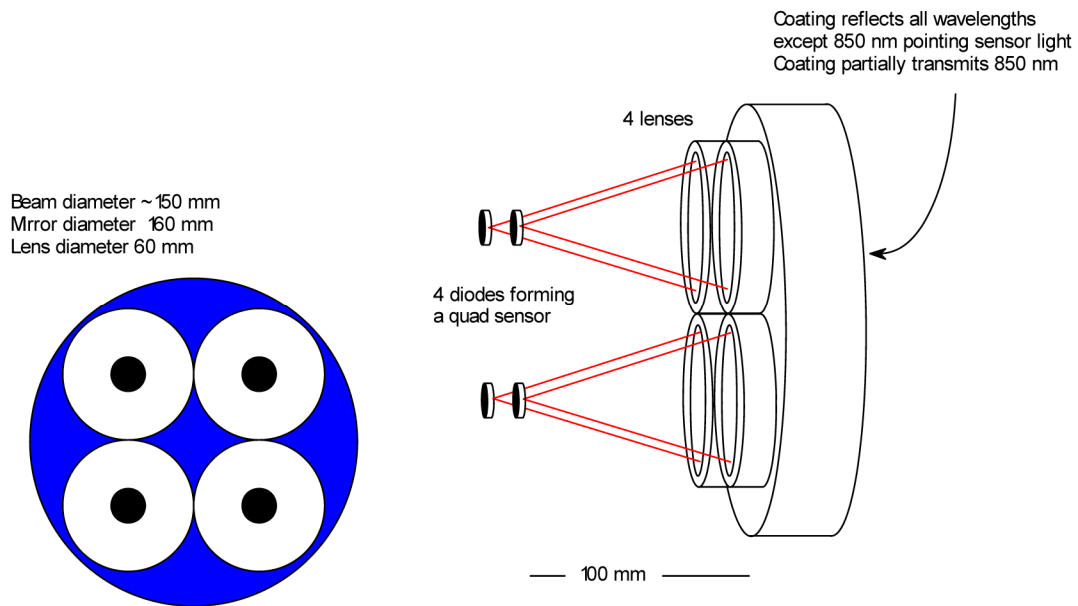
Figure 5-13. Transfer mirror shear sensor.

5.4.4 Shear Metrology

Shear metrology uses the same laser beam as the pointing system; the two systems are closely coupled. By placing a pupil stop at the FOR mirror, the alignment laser beam and the starlight have the same initial shear. Shear is first sensed after transfer to the next collector by a dichroic mirror with a set of lenses placed behind it (Figure 5-13). This dichroic lets through a portion of the 850-nm radiation, but the dichroic reflects most of it together with all the other useful light. The sensor output is run back to the transfer mirror on the first spacecraft to point the beam at the center of the dichroic shear sensor mirror. An identical method is used for transfer to the beamcombiner spacecraft. Once inside the beamcombiner, the shear is again sensed after the delay lines and corrected before entry to the adaptive nullers.

5.4.5 Polarization Rotation

Polarization-rotation metrology uses the same laser beam as the pointing system. The beam is initially polarized, and this forms a reference for beamtrain-induced rotations of the polarization angle. On arrival at the beamcombiner spacecraft, the beam is compressed and then passed through a K-mirror assembly, which allows the polarization angle to be rotated. A polarization-angle sensor is placed immediately after the K-mirror; thus, a loop can be formed to allow continuous correction of the polarization angle.
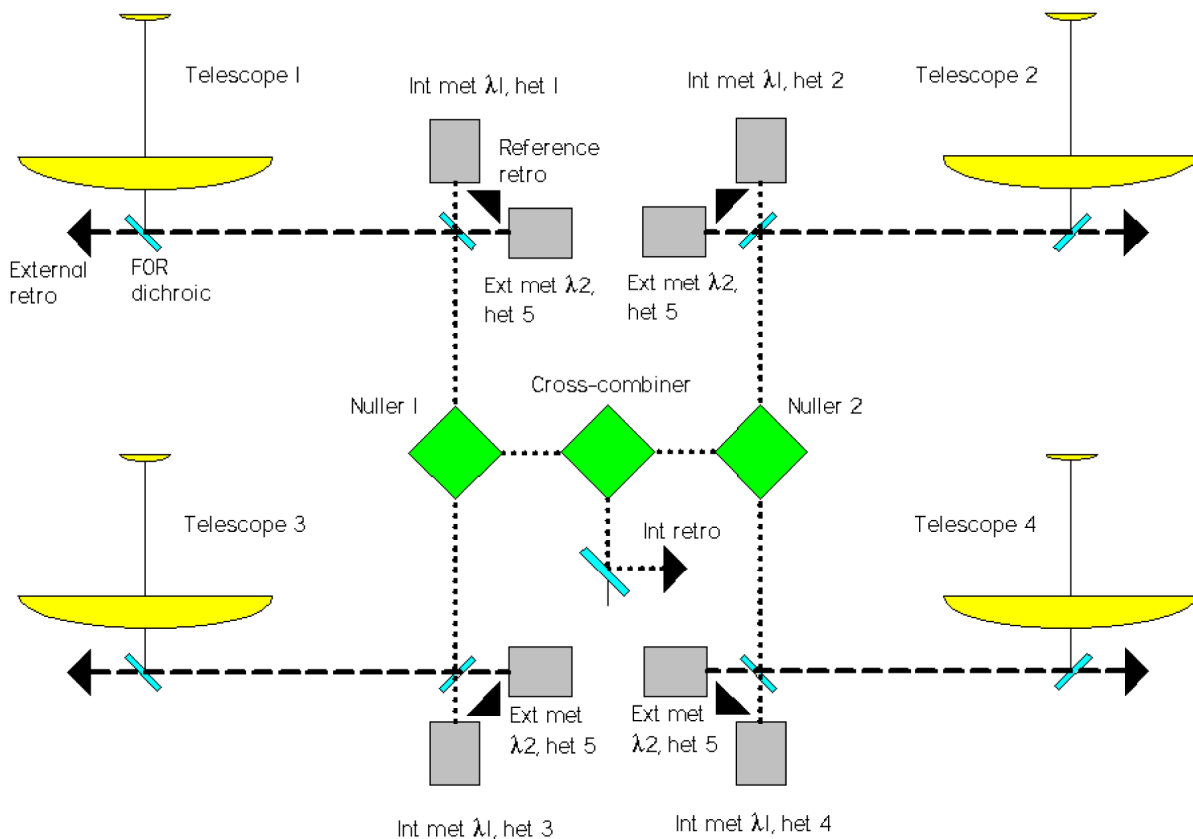
Figure 5-14. Metrology scheme for simplified nulling beamcombiner.

This polarization control loop is needed because although the adaptive nuller can (in principle) correct for the rotation error by adjusting intensities, it cannot do so on the timescales consistent with formation-drift motions. Note that there is an unsensed rotational component caused by clocking of the telescopes around the line-of-sight to the star; this would need to be known and sensed by means probably involving transfer-mirror angle knowledge.

5.4.6 OPD Metrology

The OPD metrology system forms part of the fringe tracking system and effectively extends the frequency response of that system up to several hundred hertz. The fringe tracker relies on light from the star and typically will sense some 107 photons per second. Calculations show that the response time of the fringe tracker will be ~ 0.01 second, and the OPD control-time constant will therefore be ~ 0.1 second. This is most likely inadequate given that the expected spacecraft vibration will extend to many tens of hertz with appreciable amplitudes (see below). Therefore, a laser metrology system operating at wavelengths near 1550 nm is used to sense and allow control of the higher frequency vibrations using principally the high-speed stage of the delay line.

Key elements of the metrology system are that it fills the aperture of the science beam, it measures down to the last beamsplitter, and it measures (as far as possible) only internal optical path. One area of the beam train is unsensed at present, that is the section from the FOR mirror to the primary mirror. It is worth noting that one possible motion cannot in any case be sensed, and that is high speed motion of the primary mirror with respect to the star; more on this issue later. The metrology system is divided into two components, internal and external, as shown in Figure 5-14. Internal metrology extends from the launchers just ahead of the delay lines down to a single retroreflector following a dichroic mirror placed after the cross-combiner beamsplitter. Beams from the four input paths are differentiated by having different heterodyne frequencies. External metrology extends from the same launch dichroic to a retroreflector placed behind the FOR mirror. These beams could all run at the same frequency shift, assuming no interference via the beamcombiner retroreflector, but would have a different wavelength from the internal metrology, nominally 1570 nm. The reference point for both internal and external metrology is at the launch dichroic, a complex custom optic. Metrology pointing and shear correction is active during calibration periods and consists of adjusting the mirrors placed behind the launch dichroic to maximize the return signal from the collector and combiner retroreflectors. Once set, these should require infrequent adjustment since the alignment is maintained by the separate alignment system.

5.5 Optomechanical Layout

5.5.1 Beamcombiner spacecraft

The four beams enter at the top of the spacecraft as far away as possible from the plane of the sunshades. The maximum shading principle is followed so that the beams cross over the center of the spacecraft. One side of the vertical bench supports the compressors and delay lines, the metrology launchers/receivers, the K-mirrors and the tilt sensors. The other side supports the adaptive nullers, the high/low resolution switch, and the shear and pointing sensors and actuators. The whole assembly will be contained within a cylindrical cover. The adaptive nullers are angled away from the bench because they have prisms at the entrance and exit, and these prisms refract the light away from the plane of the bench.
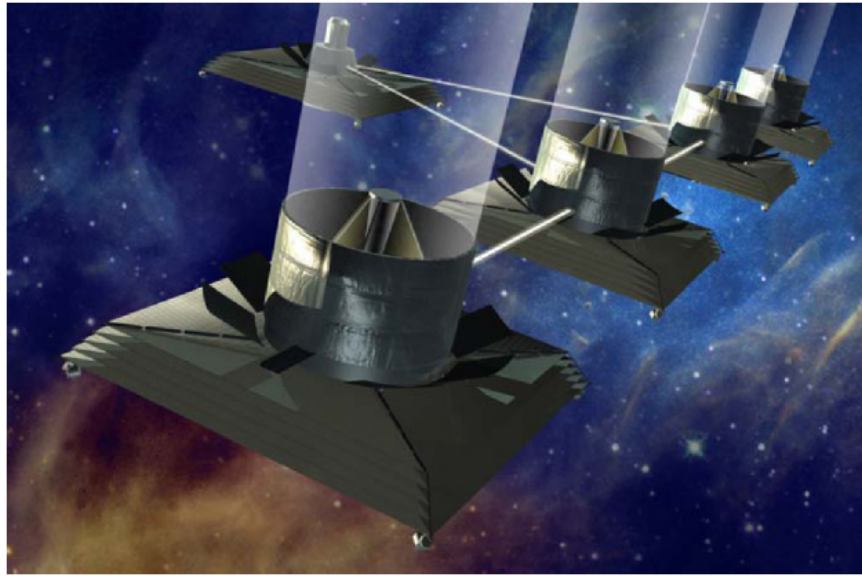
Figure 5-15. TPF-I Flight formation of telescopes for a linear dual-chopped Bracewell array.

The nullers are built as a separate unit attached to the base of the bench together with the fringe tracking cameras and the science detector. These detectors could (alternatively) be attached to the vertical bench, and the light would be brought in via optical fibers. Below the vertical bench is a thermal shield separating it from the spacecraft main bus and the other spacecraft systems, including the solar shade. Since the science detector requires cooling to 7 K, the bus also carries a cryocooler.

5.6 Spacecraft Design

The spacecraft are equipped with a five-layer square-shaped sunshade that permits the bulk of the optical system to be maintained at about 40 K by passive cooling. Some parts of the system on the beamcombiner are actively cooled to lower temperatures, notably the science detector at 7 K. These low temperatures minimize the self-radiation of the optical beam train which would add a noise signal to the science light. Spacecraft electronics and mechanical components are placed on the side of the spacecraft exposed to the Sun and are maintained near room temperature. Additional components include reaction wheels and small thrusters for formation flying. The spacecraft also have RF systems for communications both between themselves and the ground and RF sensors for coarse formation-flight control.

The spacecraft carry enough propellant to allow the complex maneuvering that the observations require for a mission duration of a minimum of 5 years. While some mission configurations have employed a single launch, for this study we allowed launching in two heavy vehicles, giving sufficient mass and size margin to allow larger telescopes to be carried. When the collector spacecraft are released from the cruise vehicle, two major deployments will take place. These will include the deployment of the sunshade and the deployment of the telescope secondary mirror, the beam transfer optics, and the cylindrical shade. The latter systems are folded down for launch to reduce the volume of the system. The principal deployment of the combiner spacecraft is the sunshade.
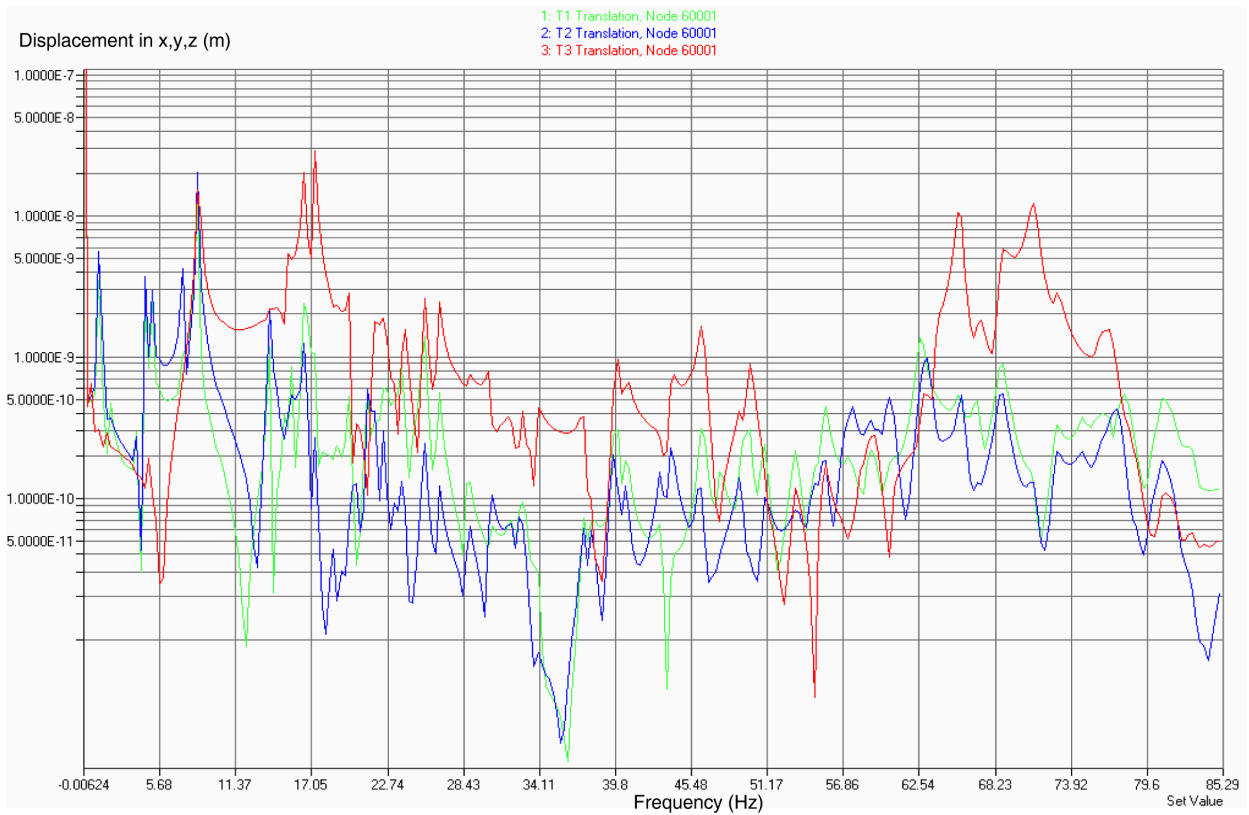
Figure 5-16. Induced vibrations of secondary mirror caused by reaction wheel vibration.

5.6.1 Thermal Modeling

A limited amount of thermal modeling has been done on this design. A model originally developed by Ball Aerospace was used to test the thermal environment with the spacecraft in close proximity and in a separated linear formation. Also, the X-array configuration has also been briefly studied. Results showed that the sunshades of the collector telescope spacecraft produce passive cooling down to 24 K at the secondary mirror, with little difference between close and widely separated formations. These temperatures meet our targets for the beamtrain optics, but the primary mirror (40 K) was at the target temperature, meaning that there is no margin here. The results exclude the influence of any cold-side heat sources which will need to be maintained at low power. Some changes would need to be made to improve this. For example, increasing the inter-shade angle (currently 0.5º) and spacing (currently 75 mm) per shade would reduce the primary mirror temperature. On the beamcombiner spacecraft, colder sections of the optics (a small part of the beamcombiner and the science detector) will be actively cooled by the cryocooler, and this must be added to the model. Additional work needs to be done to produce a thermal model of the instrument payload both on the collectors and combiner, including the optical benches with their optics, actuators, and sensors.

5.6.2 Structural Modeling

A limited amount of structural modeling has been performed on the collector telescopes to look at the effect of vibration from the reaction wheels on two of the main mirrors and at the effect of thruster firings on the optical path. From an instrument perspective, the main findings are that the motion of the

115

secondary mirror along the optical axis may exceed 1 nm over much of the spectrum, as shown by the uppermost trace in Figure 5-16. Below 28 Hz, the amplitude varies, but it peaks at more than 10 nm near 17 Hz. Also between 60 and 80 Hz, amplitudes are large. They exceed the rate that can be corrected by the fringe tracker, and they are in the section of the beamtrain that is not monitored by laser metrology, which stops near the FOR mirror. An error budget for the beamtrain has not been developed, but it is likely to be significantly less than 1 nm for frequencies greater than a few hertz. However, on the positive side, the vibration amplitudes are sufficiently small that it is possible that vibration mitigation efforts would reduce them sufficiently. Such mitigations might be (for example) improved isolation of reaction wheels, or no reaction wheels, and spacecraft controlled by proportional thrusters or another low vibration system. In the worst case, a laser metrology system could be added to the telescopes to measure much of the unmonitored path. Primary-mirror vibrations were typically an order of magnitude smaller, so they are much less likely to cause concern. Additional work to look at the major bending modes of the primary is also desirable.

5.7 Mission Description

The current concept of the TPF-I mission begins with the launch of a single heavy-class launch vehicle from Kennedy Space Center. The complete observatory, traveling as one integrated assembly, is flown to the Sun–Earth L2 point. At the L2 point the observatory is inserted into a halo orbit. L2 was chosen over an Earth drift-away orbit like that used by the Spitzer mission because L2 offers simpler telecommunications geometry, a lower insertion energy requirement, and the option to launch ground-based spare spacecraft to the orbit after the deployment of the original formation.

Figure 5-17 depicts a concept for the cruise stage. The cruise stage is used to transport the formation as packaged for launch from Earth to L2. The cruise stage also protects the optics from some potential contamination sources during launch. The stage includes a separate propulsion system, solar panels, and a mechanical structure. The electronics on the combiner spacecraft are used to control the cruise stage. On
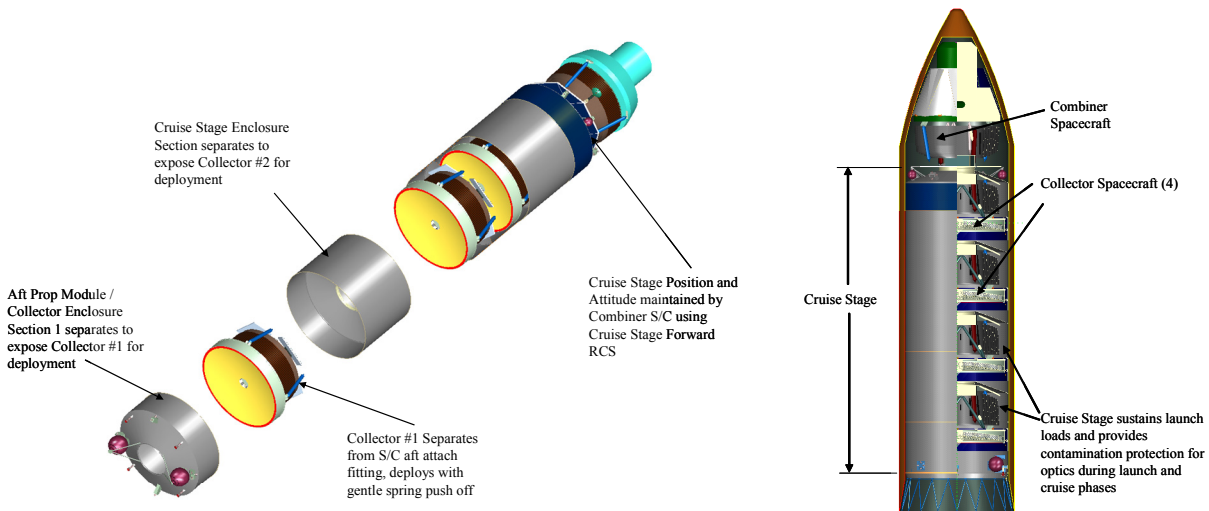
Figure 5-17. Cruise Stage (RCS is Reaction Control System).

the way to L2, the cruise stage performs a slow "barbecue" roll to maintain a benign thermal environment for the spacecraft within its shell. After arrival at L2, the cruise stage is used to deploy the individual spacecraft of the observatory one at a time. Ground operators verify successful deployment of each spacecraft before deploying subsequent spacecraft. After all the spacecraft are deployed, the formation is formed, and calibration begins. Following initial calibrations, the observatory is commissioned, and the prime mission begins.

Table 1-2 has a summary of the properties of the current TPF-I observatory concept. The prime mission lasts 5 years with approximately 3 years budgeted for star-system surveys and 2 years budgeted for detailed, follow-up studies of targets found by the surveys. Enough expendable resources are carried to permit extending the mission another 5 years if consumption of these resources is as predicted and the observatory remains healthy.

Observations consist of aligning the observatory's viewing axis to a target star, adjusting the formation baseline length to an optimum value (tuning), and then rotating about that axis for multiple hours until a sufficient signal-to-noise ratio (SNR) is attained. Depending on the length of the observation, data are either downlinked before slewing to the next target system or recorded and played back after completing the observation of a multiple-target set. It is envisioned that the observatory will be capable of completing slews and observations of multiple targets autonomously. However, it is not certain that this capability will be used since the frequency of calibrations requiring ground interaction has not been analyzed yet.

Geometrical thermal constraints will limit the target set to stars within ~± 45° of the ecliptic. This band of stars will be observed multiple times as the Earth/observatory system orbits the Sun. The target set includes many of the stars to be observed by the TPF Coronagraph.

5.8 Performance of Flight Baseline Design

5.8.1 Inner and Outer Working Angles

Figure 5-18 shows how the rms signal from a planet of unit flux varies with position relative to the star. The rms is taken over the full range of array-rotation angles. These maps of the 'rms modulation efficiency' show how the peak of the PSF varies with position. The example on the left is for the smallest array size of 120 × 20 m, at a wavelength of 10 μm. The response for the largest array size of 612 × 102 m is shown on the right. The overall response is a product of the primary beam taper and the effect of the interferometric fringes.

 The outer working angle (OWA) is taken to be the half-power point of the primary beam taper. With a collector diameter of 3.8 m, this is 280 mas, although the value is increased if we consider the non-uniform response of the single-mode fiber over the input aperture. The OWA is independent of the array size. At longer wavelengths the taper is reduced.
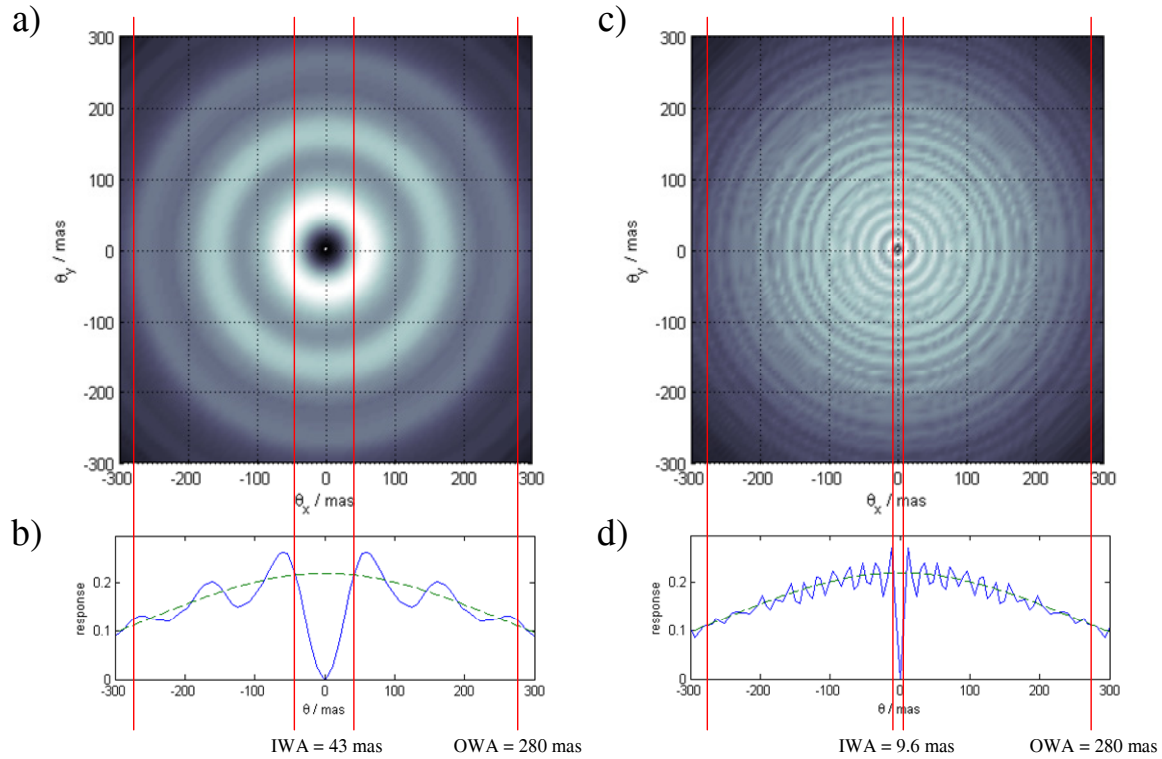
Figure 5-18. Response to planet emission at 10 μm for the stretched X-array. (a) Sky response for the minimum array size of 120 × 20 m at λ = 10 μm. (b) Section through the sky response for minimum array size. The IWA is 43 mas. The OWA is 280 mas. (c) Sky response for maximum array size (612 × 102 m). (d) Section showing IWA of 9.6 mas.

At the center of each response is the dark hole that represents the effect of the central null. The Inner Working Angle is defined to be the offset angle from the star at which the signal response (blue solid line) first crosses the asymptotic response (green dashed line), for a wavelength of 10 μm. This IWA scales approximately as B_{null}^{-1}. At the minimum array size of 120 × 20 m, the IWA = 43 mas; at the maximum array size of 612 × 102 m, the IWA = 9.6 mas.

Figure 5-18 shows the response to planet signal photons; this is not the same as the *sensitivity* to planet photons which depends on the signal-to-noise ratio. The noise sources described in Section 4.2 result in a statistically uniform distribution in the rms noise over the map. The noise level integrates down with time, so that the effective contrast that can be achieved scales with $T_{int}^{1/2}$. This is different from the coronagraph, which has a fixed contrast floor introduced by the instrument that ultimately limits the performance. For the interferometer, the powerful combination of fast phase chopping and spectral-fitting (described in Section 4.8) should ensure that any residual noise will be random in nature.
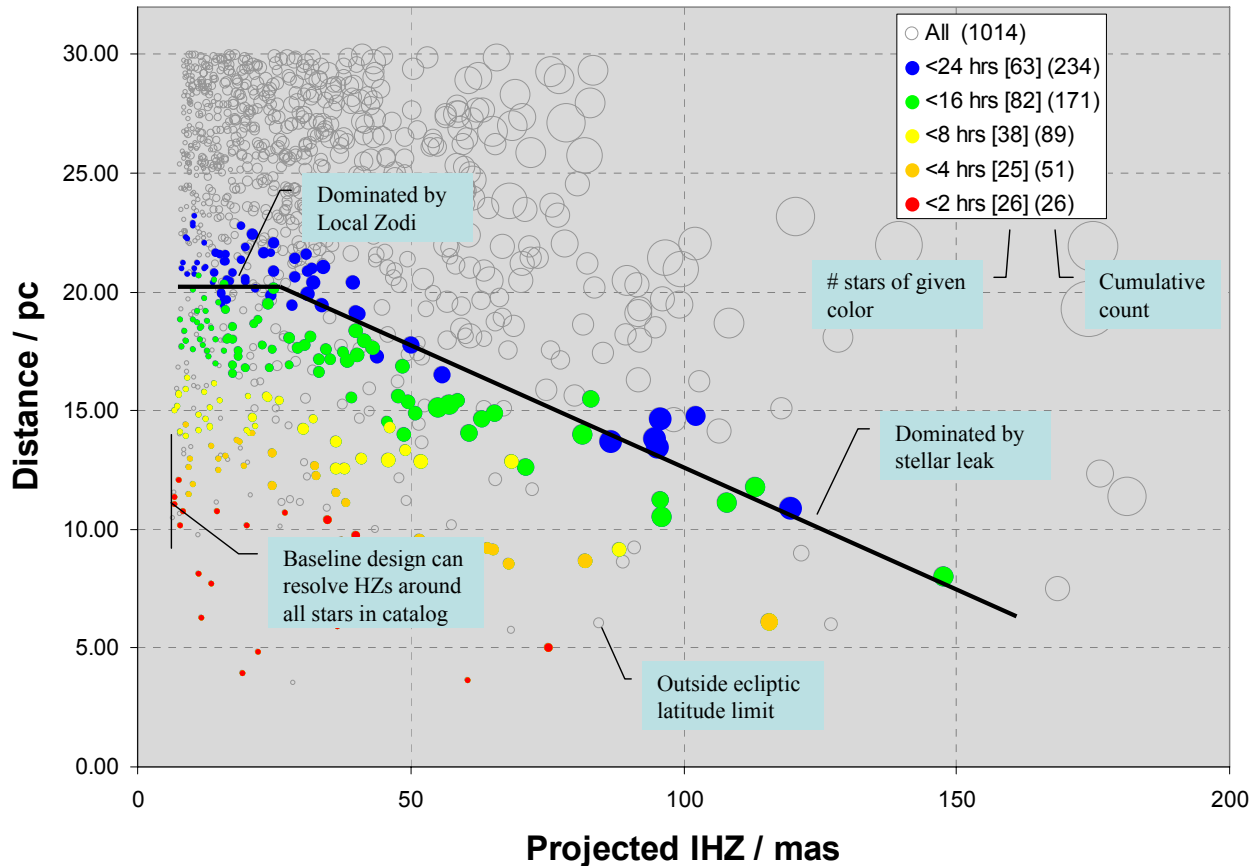
Figure 5-19. Integration times needed for 5σ detection of Earth-sized planet for each of the TPF-I candidate stars. Integration times longer than 24 hrs are not shown, but are not precluded.

5.8.2 Stars Surveyed

The star count model described in Section 4.2 was applied to predict the number of stars that can be surveyed for planets in the mission time available. Table 5-2 lists the parameters that were assumed.

It is also assumed that the array is continuously rotated about the line of sight to the star, with integrations carried out "on-the-fly" (i.e., not stop-and-stare). Several different observing strategies are now illustrated. In the nominal case, the search of each star is required to be complete at the 90% level with respect to Earth-sized planets. The integration times needed to achieve a 5σ broad-band detection in a single visit are shown in Fig. 5-19. The number of stars that can be surveyed in the 2-year mission period, with three visits each, is illustrated in Fig. 5-20. A total of 250 stars can be surveyed to 90% completeness for Earth-mass planets. Figure 5-20 also shows how we can choose to make a deeper survey of fewer stars. 163 stars can be surveyed for 0.5 Earth-mass planets, or 60 stars down to 0.1 Earth-mass (both still 90% complete). If, on the other hand, we fix the observation time to a single rotation of 50,000 s, then the corresponding mass sensitivity (at 90% completeness) is given by Fig. 5-21.

The coronagraph team has taken a different approach, in which the completeness around a given star is a free parameter, and the number of visits and observing times are optimized to maximize the number of

planets found. Figure 5-22 compares the planets surveyed by TPF-I and TPF-C, as well as the mass-sensitivity of the Space Interferometry Mission (SIM-PlanetQuest). The coronagraph approach of maximizing the number of planets found is currently being applied to the interferometer so that we can better compare the relative performance of the two missions.

Table 5-2. Parameters Assumed for the Prediction of the Number of Stars Surveyed

Parameter	Constraint
Mission time available for survey	2 yr
Fraction of survey time spent integrating	50%
Number of visits per star for 90% completeness	3
Solar shading constraint	±45 deg anti-Sun
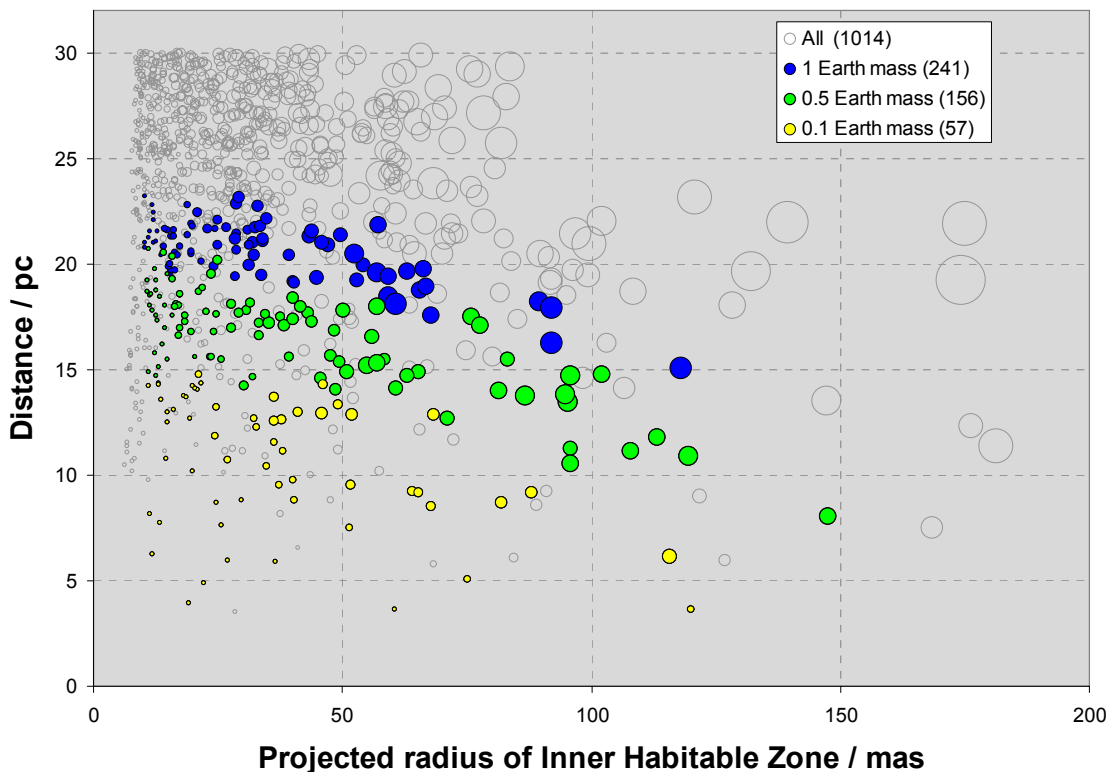
Figure 5-20. Number of systems surveyed in 2-year mission time as a function of the mass sensitivity. 57 stars are covered with a deep survey down to 0.1 Earth mass limit (yellow). 156 targets are covered with medium depth survey to 0.5 Earth mass limit (yellow + green). 241 targets are covered with shallow survey to 1 Earth mass limit (yellow + green + blue). These are mutually exclusive scenarios.
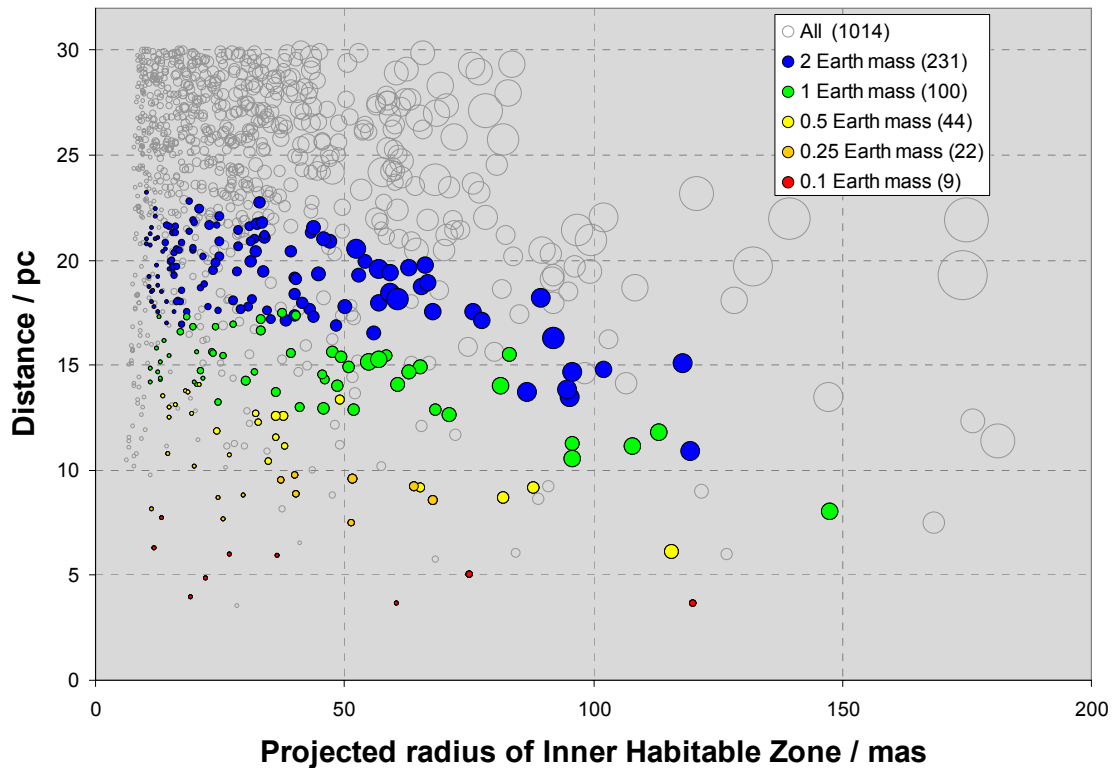
Figure 5-21. Planet mass sensitivity for a single array rotation of 50,000 s. 9 nearby stars can be surveyed for planets in the Habitable Zone with masses as low as 0.1 Earth mass. The mass sensitivity improves as $T^{0.75}$, assuming constant density of the planet.

A candidate selection will be followed up with further observations to determine the orbit and to rule out the possibilities of background sources and lumps in the exozodiacal emission. This phase of the planet-finding process is less well studied than the initial detection, but it should be greatly eased by the excellent angular resolution of the stretched X-array (see Section 5.8). The spectroscopic characterization phase is the subject of the next section.

5.8.3 Spectroscopy

Following detection and orbit determination, the goal is to obtain a spectrum of candidate planets. The outputs of the single-mode spatial filters are dispersed into ~100 spectral channels on a detector array. The array always observes at the full spectral resolution because the response on the sky is wavelength-dependent, and lower spectral resolution will restrict the useful field of view. The channels are co-added in the post-processing to maximize the SNR for detection and orbit determination, but this data also provides a first look at the spectrum, albeit with low SNR.
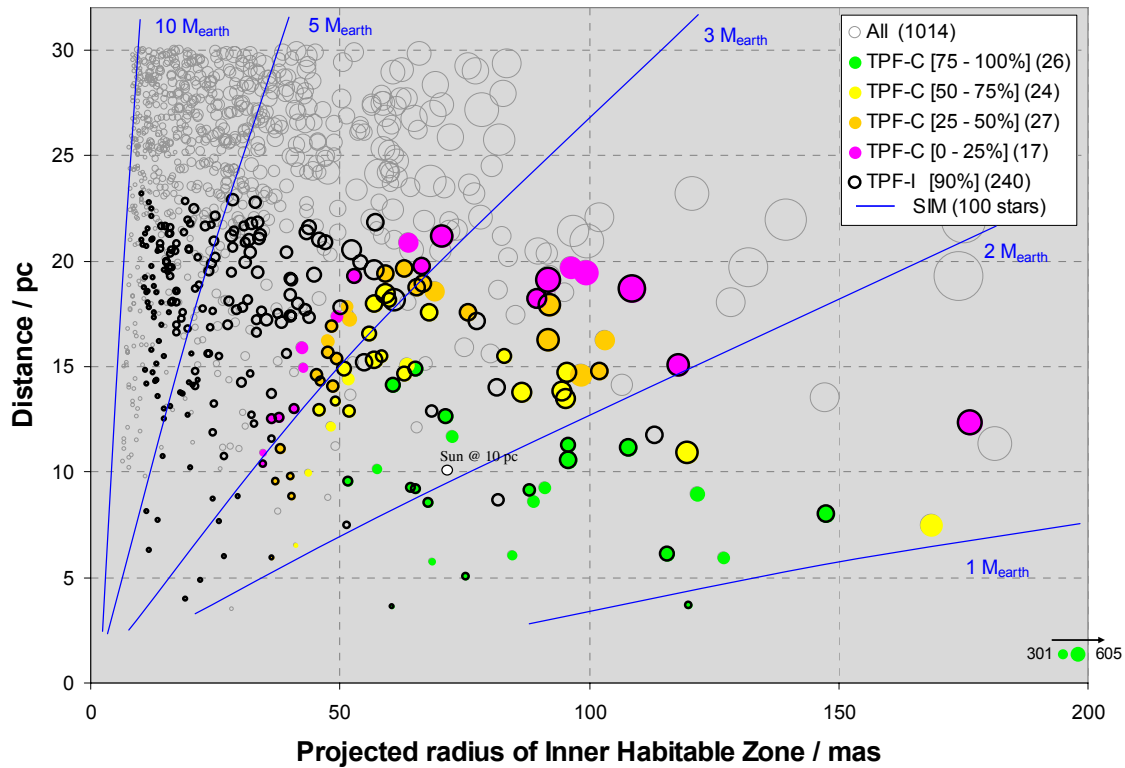
Figure 5-22. Comparison of TPF-I, TPF-C, and SIM Missions. The colored circles represent those stars for which an Earth-sized planet could be detected in the Habitable Zone by the TPF-C mission. The color indicates the completeness of the measurement, as indicated in the legend. For example, the yellow symbols show stars for which there is a probability of between 50 and 75% that a given Earth-sized planet in the habitable zone is detected. There are 24 such stars. The completeness diminishes with distance and proximity of the habitable zone to the star. The circles with a heavy outline denote the 240 stars that can be surveyed for Earth-sized planets in the habitable zone with 90% completeness by the TPF-I mission. The blue contours represent the planet mass sensitivity of the SIM mission for an Earth-equivalent orbit. The astrometric signature is proportional to the mass of the planet and the projected orbit radius, and inversely proportional to the mass of the parent star. For a star lying on the 3-Earth-mass contour, there is a 50% probability that a given 3-Earth-mass planet will be detected.

The spectroscopy observations are made in exactly the same manner as for detection and orbit determination: that is, the array is rotated continuously about the line of sight to the star and measurements are made "on-the-fly." Many rotations may be needed to accumulate the necessary integration time. Efficiency (integration time/mission time) is assumed to be 75%.

Figure 5-23 shows how the SNR in a 0.5-μm wide channel varies with wavelength, for an integration time of 29 days on an Earth-sized planet at 15 pc. Much of the variation in SNR (Fig. 5-23b) can be attributed to the variation in signal photon rate from the planet (modeled as a 265-K black body as shown in Fig. 5-23a). The SNR is reduced at short wavelengths by the increase in stellar leakage, since the width of the null is proportional to the wavelength. At long wavelengths the SNR is depressed by the increase in

a)

b)
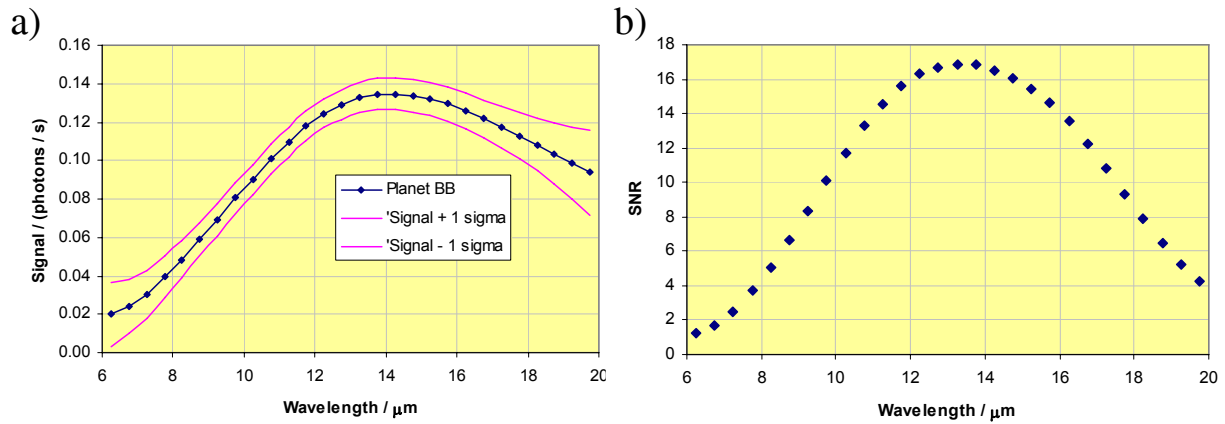
Figure 5-23. (a) Chopped planet signal rms vs. wavelength. The spectrum is divided into channels of width 0.5-μm. The planet is Earth-sized, at a distance of 15 pc, and with a 265-K black body spectrum. The magenta lines indicate the ±1 σ noise level after integrating for 29 days with the stretched X-array configuration. This time was chosen to give SNR = 10 in the 9.5–10 μm channel, corresponding to the ozone line, as shown in (b).

thermal noise emitted by the instrument, and, to a lesser extent, the local zodiacal emission. The peak sensitivity for spectroscopy is in the 12–15 μm region. The water-vapor features shortward of 8 μm will be very challenging to detect, given the low SNR, and will require integration times of many months. For this reason, the water-vapor features beyond 15 μm are more attractive.

Figure 5-24 is a histogram showing the integration times needed to achieve an SNR of 10 in the 9.5–10 μm ozone channel, for the nearest 200 candidate stars.
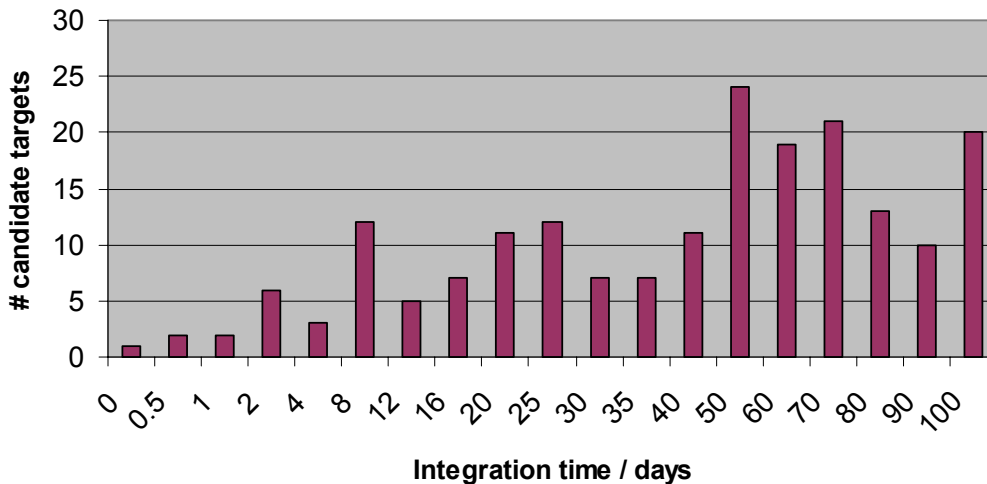
Figure 5-24. Histogram of spectroscopy integration times for 200 best candidate targets for SNR = 10 in the 9.5–10 μm channel.

123

5.8.4 Angular Resolution and Imaging

The imaging properties of nulling arrays are discussed in Section 4.9. Angular resolution—essentially the width of the main peak in the point spread function—is distinct from the IWA discussed in Section 5.8. A key feature of the stretched X-array is its excellent angular resolution, resulting from the long imaging baselines. Figure 5-25 compares synthesized dirty maps for the regular X-array 2:1 and the stretched X-array 6:1. The IWA is the same in each case, but the angular resolution is improved by a factor of 3. The angular resolution scales linearly with wavelength and is inversely proportional to the array size, as illustrated in Table 5-3.

High angular resolution is highly desirable for (1) separating the contributions of multiple planets; (2) rapid and unambiguous orbit determinations; and (3) discrimination against lumps in the exozodiacal disk.

For previous arrays with relatively poor angular resolution, image deconvolution was considered to be a major issue, since there can be substantial overlap between the PSFs of different sources. Sidelobes and satellite peaks can combine to produce false peaks or mutually cancel and prevent detection. The greatly enhanced angular resolution of the stretched X-array (Fig. 5-25b) minimizes these overlaps, and it should go a long way to retiring these issues.
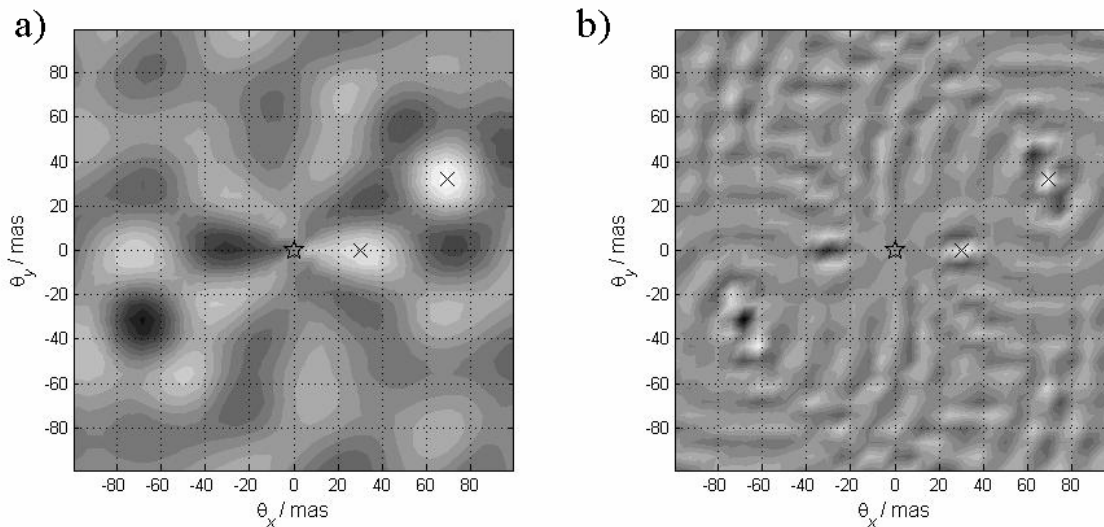
Figure 5-25. (a) Dirty map of two planets (indicated by the × symbols), synthesized from multi-channel observations of an X-array 2:1 array configuration (70 × 35 m); (b) Equivalent dirty map for the stretched X-array 6:1 configuration (210 × 35 m).
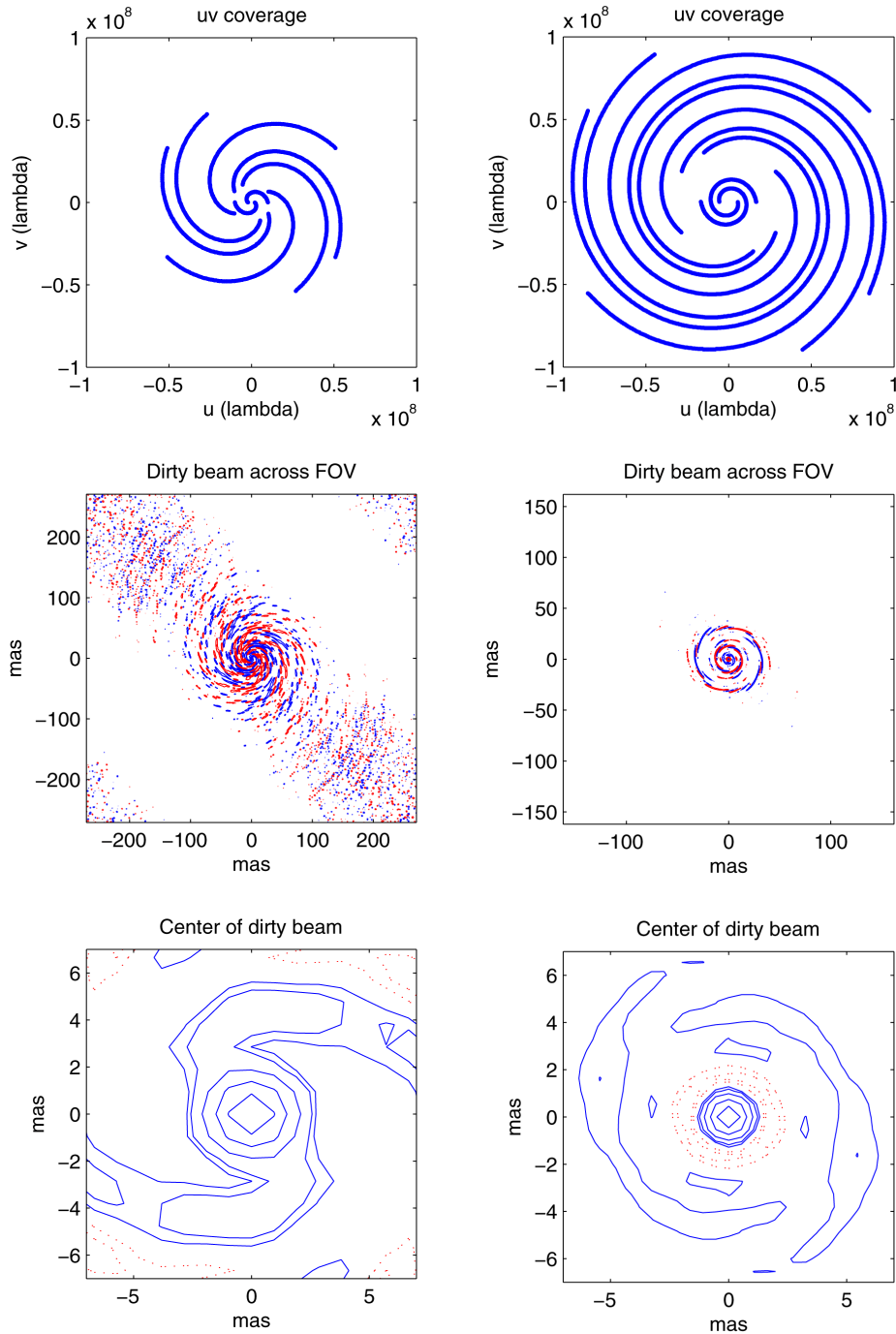
Figure 5-26. Examples of *u-v* coverage and dirty beam profiles for the stretched X-array in snapshort and full configuration. *Snapshot*: (left column) 10-μm wavelength, 5 h on 3 targets with calibrator (1.7 h per target), 180-degree array rotation over a baseline range from 20 to 60 m on the short side of the rectangle. Beam FWHM = 3.9 × 3.4 mas and highest sidelobe is 20%. *Full*: (right column) 6-μm wavelength, 12 h on 1 target with calibrator, 360-degree rotation over full baseline range (20 to 100 m on short side of rectangle). Beam FWHM = 1.5 × 1.2 mas and highest sidelobe is 10%.

Table 5-3. Angular Resolution (FWHM of PSF) of the Stretched X-Array

Array Size	Wavelength		
	6 μm	10 μm	18 μm
120 × 20 m	4.9 mas	8.2 mas	14.8 mas
612 × 102 m	1.0 mas	1.6 mas	2.9 mas

Here we have assumed that the 6:1 aspect ratio of the array is held fixed, which simplifies the input optics on the combiner. One design option would be to allow for a variable aspect ratio. The nulling baseline length would be set according to the angle subtended by the inner habitable zone, and the imaging baseline would be made as larger as possible. Fore general astrophysics without nulling, the imaging properties of the stretched X-array are depicted in Fig. 5-26.

5.8.5 Optimized Program Completeness

Each star on the TPF-I target list has a habitable zone, which scales by luminosity and is defined as the region around a star in which liquid water could exist. We model the habitable zone by populating this region with 1,000 pseudo-planets. The pseudo-planets have random inclination, eccentricity over the range [0, 0.1], and a semi-major axis in the range of $0.75\sqrt{L} \le x \le 1.8\sqrt{L}$. The planets are Earth-like in size and albedo. Program completeness is then defined to be the fraction of potentially observable planets that are detected over a mission. Our algorithm selects the most productive of the TPF candidate stars to observe in each week of the mission. It accounts for multiple visits, solar constraints, variable baselines, and planet orbital motion, removing many of the assumptions that were necessary in previous analyses. The procedure for this analysis is shown in Fig. 5-27.

The changes to previous methods of computing completeness include temperature-dependence of the planet across the habitable zone, a more realistic exozodiacal model, a tapered, wavelength-dependent representation of the IWA, and the optimization of visit timing. We perform this optimization by evaluating stars on the completeness per time that is provided by a given observation. We calculate the curve of completeness vs. integration time fore each star determining the best array size at each point. Several example curves are shown in Fig. 5-28. The curves start out flat due to overhead and a minimum integration time needed to observe any pseudo planets. The curves rise and then flatten out at different levels depending on the stellar type and distance to the star. (the IWA limits the possible planet observations for stars that are farther.) We define an instantaneous efficiency (change in completeness per hour, i.e., the red dot indicating the slope of the completeness curve in Fig. 5-28) for all available stars. The observation time per star is then defined as the time needed to observe the star up to the slope cut off point (t_1, t_2 or t_3 in Fig.5-28). The stars are then evaluated on net efficiency (i.e., the green dashed lines indicating overall completeness per observation time). Those stars with the largest net efficiency are then selected for a visit.
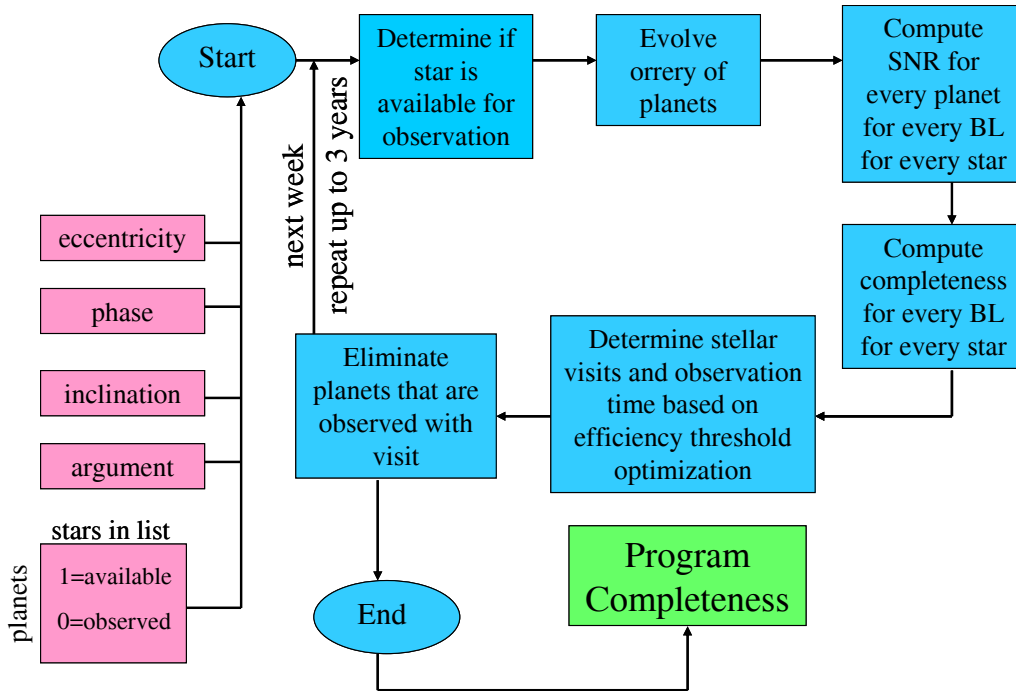
Figure 5-27. Flow diagram TPF-I completeness optimization. Pink boxes indicate inputs for the 1000 pseudo-planets. Blue boxes indicate steps in the program completeness computation. Green boxes indicate outputs. We compute completeness for every baseline (BL) for every star as a function of integration time.
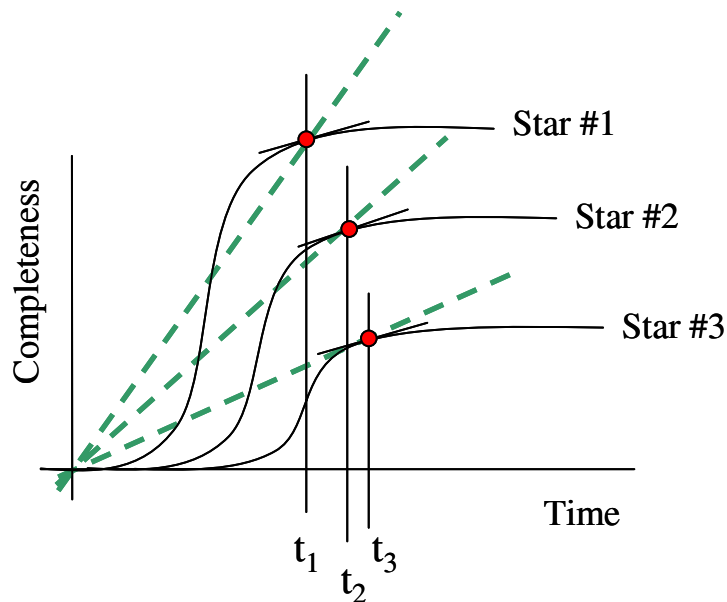
Figure 5-28. Each stellar curve is composed of the portion between time = 0 and the red dot on the curve. The red dot is located at a common slope point for all stellar curves. The green dashed lines show the net efficiency of a given stellar observation. The stars with the best completeness per time (t_1, t_2 or t_3) are then selected for a visit.

The optimization works by solving the following question: Given a set of completeness curves vs. time for the available stars in the current 1-week period, what is the optimum set of integration times that maximizes the number of planets found?

Solve by applying two rules: 1) For stars that are observed, we must be operating at a point on each completeness curve that has the same slope. Otherwise we can increase efficiency by transferring integration time from a target with shallow slope to one with steeper slope (i.e., $\Delta C/\Delta t = const$. 2) The observed stars are those with the highest net efficiencies. Otherwise we could increase overall completeness by swapping in a star with higher net efficiency (i.e., $\delta(C/t)$ is maximized).

We then repeat for different values of $\Delta C/\Delta t$ to find the most productive set of integration times.

The baseline mission concept includes a 2-year mission duration with an X-array (aspect ratio of 6:1) architecture. In this scenario, we assume a 70% integration time efficiency and a 4.3 hr slew time per target observation. With this baseline, we are able to obtain a total accumulated completeness of 192.0 habitable zones searched with 385 observations over 384 different targets. This is equivalent to stating that we would find 192 planets if each target had one Earth-like planet and 19 planets if one tenth of the targets had such a planet. Unlike previous simulations, all but one target (Hipp# 80337) are visited only
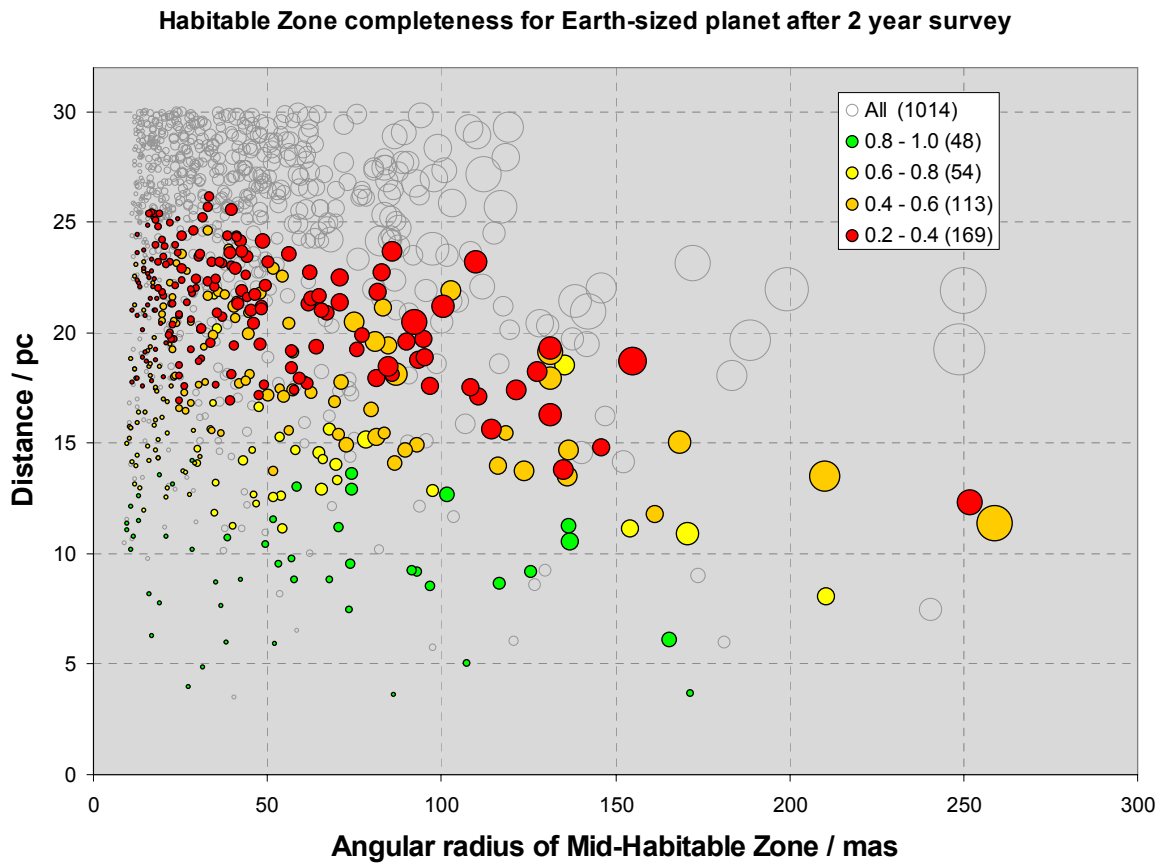
Figure 5-29. Completeness for visited stars.

once. Additionally, the completeness per star varies in the new simulation. In general, the closer stars are more complete than those that are further away. The completeness per star as a function of angular radius to the mid-HZ and distance to the star is shown in Fig. 5-29.

The completeness calculations for this simulation are lower than previous estimations because there is now more fidelity in the current model. We compute planet flux as a function of HZ distance in the new simulations. Because there is a sharp fall-off in the mid-IR flux in the outer HZ, fewer outer HZ planets are observable. Furthermore, if we map completeness across the HZ, there is a marked fall-off of completeness as a function of pseudo-planet distance. Future work includes a study of the effect of forced revisits on completeness.

5.9 References

Lay, O. P., "Imaging properties of rotating nulling interferometers," *Appl. Opt*. **44**, 5859–5871 (2005).

Martin, S., "The flight instrument design for the Terrestrial Planet Finder Interferometer," *Techniques and Instrumentation for Detection of Exoplanets II*, *Proc. SPIE* **5905**, edited by D. R. Coulter, 21–35 (2005).

6 Technology Roadmap for TPF-I

The *Technology Plan for the Terrestrial Planet Finder Interferometer* (Lawson and Dooley 2005) contains a detailed description of the areas of technical work that need to be developed for TPF-I prior to entering Phase A of its mission life cycle. The document describes the requirements and error budgets for the mission relevant to starlight suppression, formation flying, and cryogenic technology. Also included are testbed descriptions, and for each testbed, a schedule of milestones and technical gates.

The technology plan emphasizes the relationship between error budgets, theoretical predictions, and experimental results. The approach to technology development for TPF-I includes the notion that as our understanding of the instrument matures and our ability to model the experiments improves, the corresponding error budgets need be revised and updated, and the performance targets for each testbed need to be reassessed. Our understanding of instability noise and methods of its mitigation (described in Section 4.8) has evolved greatly since 2005. The technology plan is therefore overdue for revision, as it no longer reflects our current understanding of the mission requirements.

Also worth noting is that the scope of work on TPF-I has been greatly reduced since 2005 because of changes in the NASA budget. The ongoing work is focused on starlight suppression and formation flying and is described in the following sections.

6.1 Technology Gates

The technology goals for TPF-I in Pre Phase A are listed here. Within the plan the milestones are listed that lead towards major gates in technology development. These gates are shown below. It is worth emphasizing that our current understanding of mitigating instability noise should enable us to relax the null depth requirement by a factor of ~10 (Lay 2006) over the targets listed here. As such, the technology gates for starlight suppression now seem overly strict, but they are included here from the 2005 plan for completeness. A high-level overview of the flight requirements and testbed requirements, as they were described in 2005, is given in Table 6-1.

6.1.1 Optics and Starlight Suppression Gates

Starlight Suppression (Depth and Bandwidth at Temperature): Using the Achromatic Nulling Testbed, demonstrate that infrared light over a spectral bandwidth of $\geq 25\%$ can be suppressed by $\geq 10^6$ at ≤ 40 K. Accompany these results with an optical model of the Achromatic Nulling Testbed, validated by test data, to be included in the model of the flight-instrument concept. This demonstrates the approach to the broad-band starlight suppression needed to characterize terrestrial planets for habitability at a flight-like temperature. *Gate TRL 5*.

Table 6-1. Comparison of 2005 Flight Requirements with Pre-Phase A Nulling Testbed Requirements

Technology	Specifications	Performance to Date	Performance target prior to Phase A	Flight Performance (Preliminary)
Starlight Suppression				
	Average null depth	0.5×10^{-5} (25 % BW) 5.0×10^{-7} (laser)	Less than 1×10^{-6} *	Less than 7.5×10^{-7} *
	Amplitude control	0.2 %	0.12%	0.13
	Phase control	2.0 nm	2.0 nm	1.5 nm
	Stability timescale	Not tested	5,000 s	> 50,000 s
	Bandwidth	8.3–10.7 µm (25%)	8.3–10.7 µm (25%)	7–17 µm
Formation Flying				
	Number of s/c	2 robots	3 robots	5 s/c
	Relative control	7-cm range, 80-arcmin bearing	5 cm range, 60 arcmin bearing	2-cm range, 20-arcsec bearing

* The new stretched X-array design relaxes both these null depth requirements to 1×10^{-5}.

Planet Extraction: Using the Planet Detection Testbed (PDT), demonstrate extraction of a simulated (laser) planet signal at a star/planet contrast ratio of $\geq 10^6$ for a rotation of the flight formation lasting $\geq$ 5000 s. Accompany these results with a control system model of the Planet Detection Testbed, validated by test data, to be included in the control system model of the flight-instrument concept. Success shows flight-like planet sensing at representative stability levels within a factor of 20 of the contrast at 1/10 the flight observation duration. *Gate TRL 5*.

Dispersion Control at Temperature: Using the Adaptive Nuller**,** demonstrate that optical beam amplitude can be controlled with a precision of $\leq 0.2\%$ and phase with a precision of ≤ 5 nm over a spectral bandwidth of > 3 µm in the mid IR for two polarizations at ≤ 40 K. Accompany these results with a model of the Adaptive Nuller, validated by test data, to be included in the model of the flight-instrument concept. This demonstrates the approach for compensating for optical imperfections that create instrument noise that can mask planet signals at the temperature required for flight operations. *Gate TRL 5*.

6.1.2 Formation Flying Gates

Formation Flying (5-Spacecraft Simulation With Fault Recovery): Using the Formation Algorithms & Simulation Testbed, simulate the safing and recovery of a five-spacecraft formation subjected to a set of typical spacecraft faults that could lead to mission failures unique to formation flying such as collisions, sensor faults, communication drop-outs, or failed thrusters in on or off states. Simulations can be limited to single-fault scenarios. This demonstrates the robustness of formation control architecture, as well as fault-tolerance of the on-board formation guidance, estimation, and control algorithms to protect against faults that have a reasonable probability of occurring sometime during the TPF-I prime mission and that are unique to TPF-I's unprecedented use of close formation flying. *Gate TRL 5*.

Formation Flying (Multiple Robot Demonstration With Fault Recovery): Using the Formation Control Testbed, demonstrate that a formation of multiple robots can be safed following the injections of a set of typical spacecraft faults that have a reasonable probability of occurring during flight. Demonstrations can be limited to single-fault scenarios. This validates the software simulation of fault recovery for formation flight. *Gate TRL 5*.

6.1.3 Cryogenic Technology Gate

Cryocooler Development: With the Advanced Cryocooler Technology Development Program, demonstrate that the development model coolers meet or exceed their performance requirements to provide ~30 mW of cooling at 6 K and ~150 mW at 18 K. This demonstrates the approach to cooling the science detector to a temperature low enough to reveal the weak planet signals. *Gate TRL 5*. **Completed Q2 2005.**

6.1.4 Integrated Modeling Gate

Observatory Simulation: Demonstrate a simulation of the flight observatory concept that models the observatory subjected to dynamic disturbances (e.g., from reaction wheels). Validate this model with experimental results from at least the Planet Detection Testbed at discrete wavelengths. Use this simulation to show that the depth and stability of the starlight null can be controlled over the entire waveband to within an order of magnitude of the limits required in flight to detect Earth-like planets, characterize their properties, and assess their habitability. *Gate TRL 5*.

6.2 Nulling Interferometry

TPF-I is in Pre Phase A of its project life cycle, and its technology development is therefore directed at demonstrating the feasibility of the techniques that will be used. For starlight suppression it was thought impractical to demonstrate all that needed to be demonstrated on a single testbed. The effort has therefore been divided into tasks that can be addressed independently:

1. Deep broad-band two-beam nulling;

2. Planet detection with a four-beam nulling interferometer;

3. Adaptive correction of amplitude and phase; and

4. Suppression of higher-order wavefront modes using single-mode mid-infrared fiber optics.

The requirements for the nulling testbeds from the 2005 technology plan are summarized in Table 6-2.

6.2.1 State of the Art in Nulling Interferometry

Progress in nulling interferometry is summarized in Figure 6-1. The plot shows rejection ratio as a function of bandwidth, for laboratory experiments that have been undertaken since 1998. On the far left-hand side of the plot are shown the results obtained using lasers at visible, near-infrared, and mid-infrared wavelengths. Experiments with bandwidths as large as 28% are shown. Results from ground-based observations of astronomical targets are not included; the rejection ratio obtained from experiments at telescopes have been less than 1000:1, dominated by atmospheric fluctuations. Of principal concern to

Results of Laboratory Experiments
in Nulling Interferometry (1999-2007)
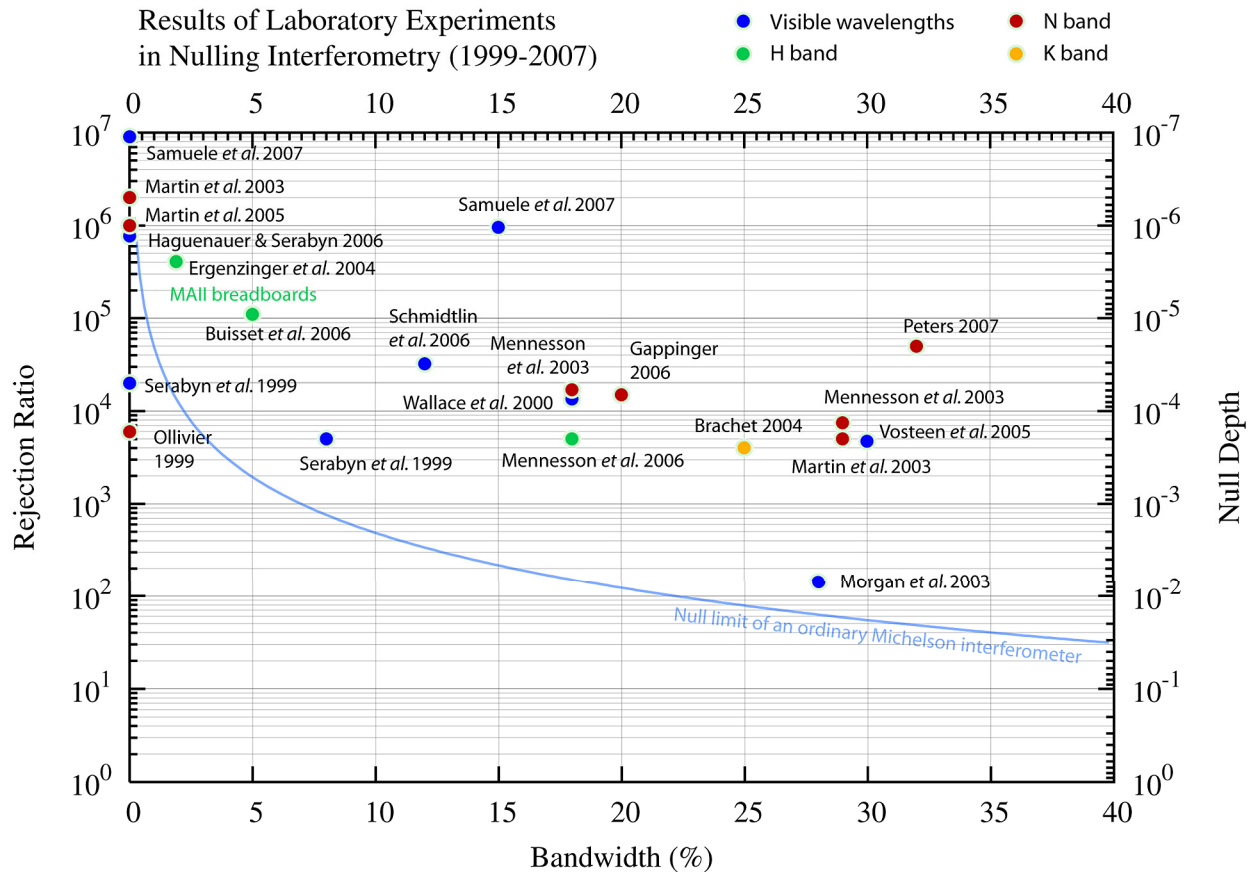
Figure 6-1. The State of the Art of Nulling Interferometry: Laboratory results showing null depth as a function of bandwidth for experiments at visible, infrared, and mid-infrared wavelengths. Results that are plotted with a zero bandwidth are laser measurements. Almost all results are limited to a single-polarization input. All but one of the results are from two-beam nulling interferometers. The result by Martin et al. (2005) is from the four-beam Planet Detection Testbed, described later in this Section. The result by Gappinger (2006) is an unpublished result from the Achromatic Nulling Testbed. The result by Peters (2007) is a preliminary and unpublished result from the Adaptive Nuller. The literature references, where available, are listed at the end of this chapter.

TPF-I are the experiments that have been conducted at mid-infrared wavelengths, which are indicated by the red circles in the plot.

From the results to date, we can draw the following conclusions.

1. Experiments have shown that achromatic effects (predominantly pathlength variations) can be controlled in the lab at a level that allows rejection ratios better than 1,000,000:1 to be achieved repeatedly. This level of performance exceeds the requirements for TPF-I. Narrow-bandwidth laser nulls have been attained with mid-infrared rejection ratios of 2,000,000:1 and at visible wavelengths of 10,000,000:1.

2. The best broad-band mid-infrared results were obtained in January 2007 with the Adaptive Nuller tesbed, noted in Fig. 6-1 as "Peters 2007." A null depth of 50,000:1 was obtained with a 32% bandwidth. This rejection ratio is only a factor of 2 from the 100,000:1 required for the stretched X-array. Broad-band nulling results to date are therefore extremely promising. Also of particular note is the result by Samuele et al. (2007) showing nulling at almost 10^{-6} with a bandwidth of 15%. This result, at a wavelength 20 times shorter than mid-infrared wavelengths, suggests there is no fundamental reason why similar null depths cannot be achieved in the mid-infrared.

The best broad-band mid-infrared null is arguably only a factor of two removed from Pre Phase A requirements for TPF-I, if one takes into account the relaxation of requirements due to advances in our understanding of instability noise. The literature references for the points noted in Fig. 6-1 are listed at the end of this Chapter. Descriptions of the TPF-I starlight suppression testbeds are given in the following pages.

Table 6-2 Comparison of 2005 Flight Requirements with Pre-Phase A Nulling Testbed Requirements

Parameter	Flight Performance	Achromatic Nuller	Planet Detection Testbed	Adaptive Nuller
Null depth	7.5×10^{-7}	1×10^{-6}	1×10^{-6}	1×10^{-5}
Amplitude control	0.13%	Derived	0.12%	0.2% (static)
Phase control	1.5 nm	Derived	2 nm	5 nm (static)
Stability timescale	50,000 s +	100 s	5,000 s	6 h
Bandwidth	7–17 μm	25%	$\lambda = 10.6$ μm	30 %

6.2.2 Achromatic Nulling Testbed (ANT)

Perhaps the most fundamental technical demonstration for TPF-I is to show that deep broad-band nulling is possible. For the ANT, a bandwidth of 25% was chosen at a central wavelength of 10 μm and a target null depth of 1×10^{-6}. The nuller being used is a compact two-beam Mach-Zehnder interferometer using opposite field flips in each arm with an arrangement of periscope mirrors. The interferometer is pictured in Fig. 6-2. The ANT has also implemented a dispersive plate nuller and a through-focus nuller. The best results to date have come from the periscope nuller, yielding broad-band nulls of 15,000:1 in unpolarized light. Our efforts to characterize the limitations of the periscope nuller have shown that the null is not dispersion limited; dispersion and chromatic effects are very well compensated within the nuller, and decreasing the bandwidth of the light source from 25% to 10% does *not* improve the null. However, there is evidence that polarization-dependent amplitude and phase errors are present in the testbed. Tests using the same optics, 10-μm laser light, and mid-infrared polarizers have yielded null depths of 200,000:1. It is difficult to model and predict these effects, as the predictions require knowledge of the material properties of the beamsplitter coatings, which unfortunately remains proprietary. The laser nulling results suggest, however, that a factor of 10 improvement in broad-band nulling is possible in the near future. This work is now in progress.
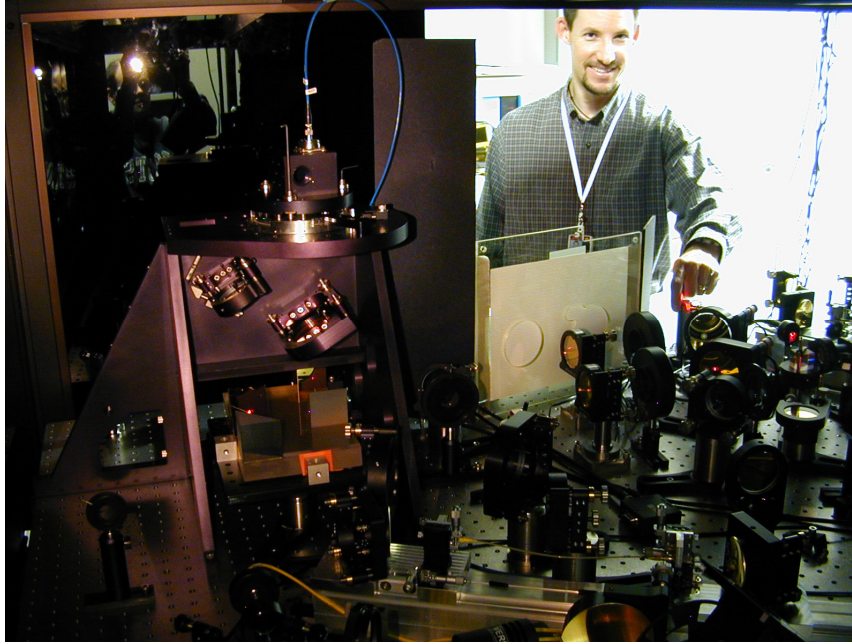
Figure 6-2. The Achromatic Nulling Testbed (ANT). The ANT includes three testbeds to explore technology for broad-band deep nulling. The goal of the testbed is to achieve mid-infrared null depths of 1000,000:1 using a bandwidth of 25 %, centered at a wavelength near 10 μm. The view of the ANT in the above photo shows the periscope assembly (on the left). Mid-infrared nulls of 15,000:1 have been achieved in unpolarized light with a 25% bandwidth. Mid-infrared laser nulls of 200,000:1 have been obtained using the exact same interferometer. The principal investigator (PI) of the ANT is Robert Gappinger, pictured here.

6.2.3 Planet Detection Testbed (PDT)

The leading candidate architectures for the TPF Interferometer (the X-array and the linear dual-chopped Bracewell) are both four-beam nullers that use interferometric chopping to detect planets in the presence of a strong mid-infrared background. The Planet Detection Testbed (PDT) was developed to demonstrate the feasibility of four-beam nulling, the required null stability, and the detection of faint planets using an approach similar to the ones contemplated for a flight-mission (Martin et al. 2006). A view of the PDT is shown in Fig. 6-3. The PDT includes numerous control loops that periodically degrade the null in the search of the best alignment for pathlength and tilt control of the four beams. The time-series of data from the PDT, plotted on a log-scale, show the signature of these modulations and yet the null degradations are so slight that deep nulling is maintained. As shown in Fig. 6-4, in 2005 the PDT demonstrated four-beam nulling with null depths of 250,000:1 and the detection of a simulated planet at a contrast level two million times fainter than its star.

Upcoming milestones for the Planet Detection Testbed include a demonstration of nulling stable to 0.1 % and phase chopping.
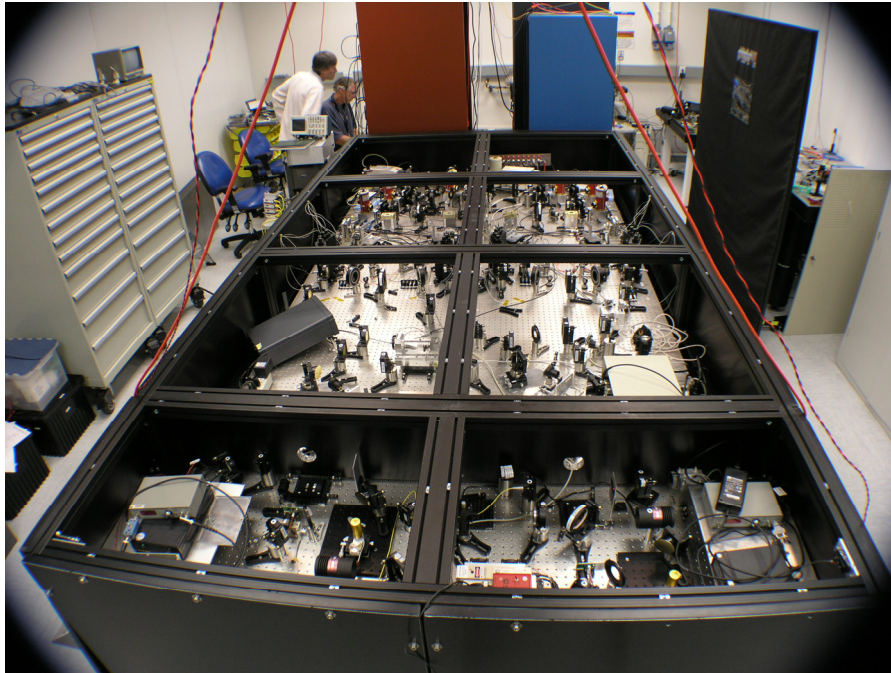
Figure 6-3. The Planet Detection Testbed (PDT). The PDT is a four-input nulling interferometer that uses 10-µm laser light and servo loops that modulate the null depth to perform experiments related to instability noise, interferometric chopping, and planet detection. The testbed configuration shown here was used to obtain 200,000:1 laser nulls and detect a simulated planet with a contrast ratio of 2000,000:1. The PI of the PDT is Stefan Martin, shown in the white lab coat.
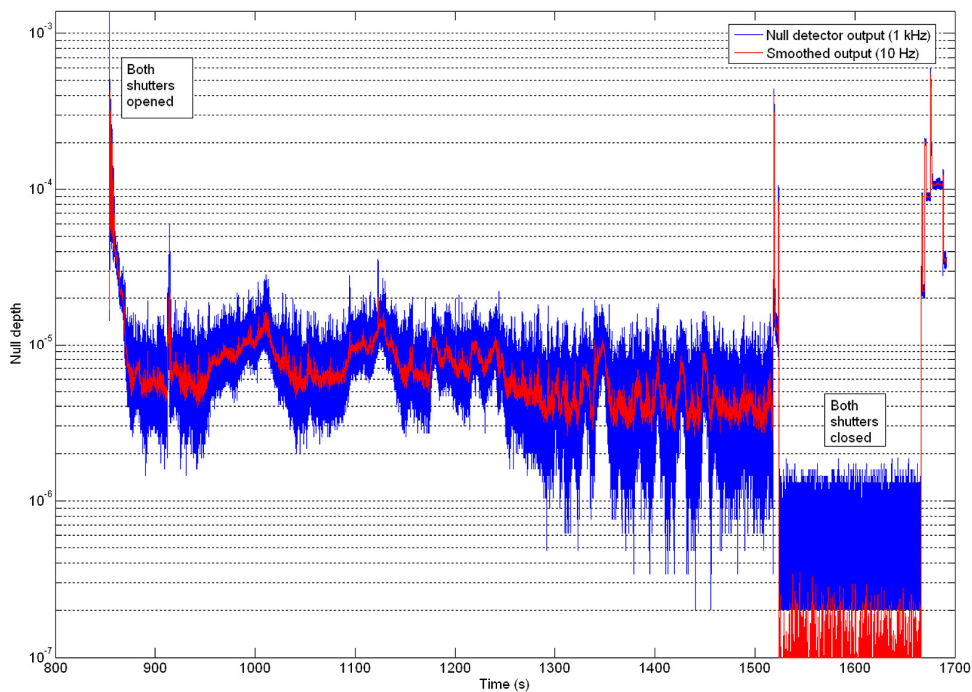
Figure 6-4. Four-beam nulling with the Planet Detection Testbed was achieved at a nul depth of 10^{-5} and demonstrated the ability to extract a planet signal two million times fainter than a simulated star.

137

6.2.4 Adaptive Nuller Testbed (AdN)

Deep broadband nulls require that the amplitude and phase of the electric field from each arm of the interferometer are very carefully matched over the full range of wavelengths and two polarization states. This becomes very challenging with large beamtrains — the tolerances on the surface figure and coatings of the many optical components is very tight. The Adaptive Nuller (Peters et al 2006) is a device inserted into each beamtrain that compensates the amplitude and phase errors independently for each spectral channel and polarization state. It effectively converts the broadband nulling challenge into a parallel set of narrow-band nulls, and enables robust deep nulling with mismatched optics and coatings. A deformable mirror is used to compensate amplitude and phase individually at each wavelength and polarization. The concept was first tested successfully at near-infrared wavelengths before moving to the mid-infrared system shown in Fig. 6-5. Testing is ongoing, but a null of 50,000:1 has already been demonstrated with mismatched optics over a bandwidth of 8–12 microns. Extending this to larger bandwidths should be simply a matter of adding more actuators to the deformable mirror.
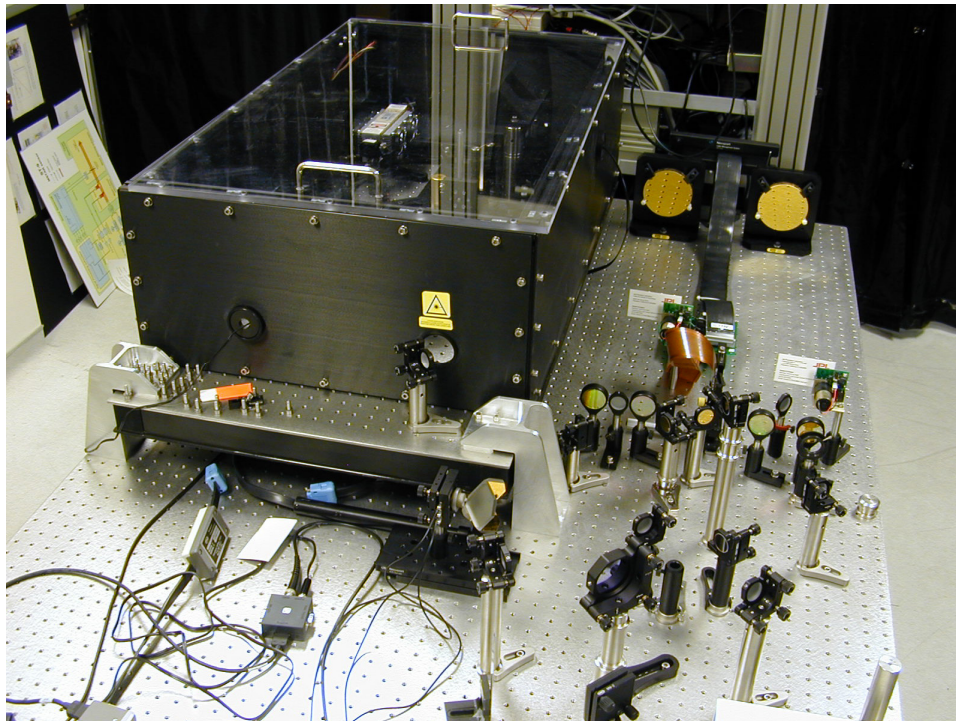
Figure 6-5. The Adaptive Nuller Testbed (AdN). The Adaptive Nuller has as its goal to demonstrate phase and intensity compensation of beams within a nulling interferometer to a level of 0.12% in amplitude and 5 nm in phase. This version of the AdN operates over a wavelength range of 8–12 μm. The AdN separates the two linear polarizations and produces spectra that are imaged one above the other at the surface of a deformable mirror. The long-focus parabolas, used in AdN are seen on the upper right. The PI of the AdN is Robert Peters.

6.2.5 Mid-Infrared Single-Mode Spatial Filters

The TPF-I project has had several contracts for the development and production single-mode mid-infrared fibers (Ksendzov et al. 2006). As a result of this work the project has approximately 16 high-quality single-mode fibers that include chalcogenide fibers from the Naval Research Laboratory (Aggarwal et al. 2005) and silver halide fibers from the University of Tel Aviv (Shalem et al. 2005). This is a significant change from the state of the art in 2002, when only one or two short samples of chalcogenide fibers had been produced by Le Verre Fluoré (Bordé et al. 2003). The technology for silver halide fibers is now advanced but still maturing. Computer control of the extrusion process for silver halide fibers has now greatly reduced inhomogeneities in the fibers. We have been pleased with test results of several bare samples, but only in 2006 were the first silver halide fibers received complete with casings and connectors. Nulling tests with these fibers are greatly anticipated because they hold the potential of extending the long-wavelength range of the testbeds.

6.3 Formation Flying

Formation flying and distributed collaborative systems have been an area of research at JPL dating back to the 1980s. Formation flying was originally sponsored by NASA as basic research within Code-R under the Distributed Spacecraft Technology (DST) element. When the two-spacecraft StarLight mission was in development, the DST efforts were focused towards key formation-flying controls technology, which at that time was at a relatively low technology-readiness level. A close collaboration between the DST and the StarLight Formation Guidance and Control (G&C) teams resulted in a rapid maturation of the scalable formation flying Control Architecture and key algorithms, including, Formation Guidance, Formation Acquisition, and Collision Avoidance.

The StarLight mission development effort was ended in 2003, and the continuing work became the TPF-I technology effort aimed at providing a robust demonstration of formation flying through ground-based laboratory work. This was divided into two complementary efforts: 1) the Formation Algorithms and Simulation Testbed (FAST), and 2) the Formation Control Testbed (FCT). The FAST, is a high-fidelity distributed realtime close-loop formation control simulation, while, the Formation Control Testbed (FCT) is a multi-robot system level hardware testbed to validate the FAST formation control architecture and algorithms. An overview of these efforts and the results to date are given in the following sections. Further details are provided in Appendix C.

6.3.1 Formation-Flying Requirements

The top-level "flight requirements" for TPF-I mission are summarized in Table 6-3. Requirements are listed separately for *knowledge* and *control* of range, bearing, attitude, and the first-derivative with respect to time (rates) of these quantities. The requirements depend on the operating mode of the array. In addition, a number of functional requirements were also imposed, such as maintaining collision-free operation at all times, using minimum resources (fuel, time/cryogen, etc.) to accomplish the mission and be robust to transient faults.

Table 6-3 Flight Requirements for Formation Flying with the TPF Interferometer

Ref	Parameter	Units	TPF-I Formation Flying Requirements per Operating Mode			
			Safe-Standoff	Reconfiguration	Hand-off	Observation
1	**Operating Envelope**					
2	Formation Sensor		Acquis. Sensor	Acquis. Sensor	Med Sensor	Fine Sensor
3	Inter-S/C Range	m	20–200	20–10,000	20–80	20–80
4	Inter-S/C Bearing	–	4π steradians	4π steradians	10° cone	10 arcmin cone
5	Inter-S/C Range Rate	< cm/s	200	200	5	0.2
6	Inter-S/C Bearing Rate	< arcmin/s	60	60	10	2.5
7	**Acquisition Time**	< s	5	30	10	10
8	**Range**					
9	Knowledge	cm	100	50	1	0.1
10	Control	cm	200	200	5	2
11	**Range Rate**					
12	Knowledge	cm/s	1	0.1	0.1	0.001
13	Control	cm/s	5	0.5	0.5	0.050
14	**Bearing**					
15	Knowledge	arcmin	1800	60	1	0.067
16	Control	arcmin	–	300	5	0.333
17	**Bearing Rate**					
18	Knowledge	arcmin/s	–	1	0.167	0.0007
19	Control	arcmin/s	–	5	1.000	0.0100
20	**Attitude (Abs. Sensor)**					
21	Knowledge	arcmin	1	1	0.1	0.1
22	Control	arcmin	60	60	3.0	1.0
23	**Attitude Rate (Abs. Sensor)**					
24	Knowledge	arcsec/s	1	1	1	1
25	Control	arcsec/s	5	5	5	5

There are four operating modes that have been defined: safe stand-off, reconfiguration, hand-off, and observation. The precise boundary between the different operating modes is to some extent arbitrary, since it depends on the capability of the sensors that are chosen. The *acquisition* sensor has the poorest resolution but the widest coverage in range and bearing angle. The acquisition sensor will be used primarily to establish the array configuration, reconfigure it, and recover from faults that would cause elements of the array to lose their station. The *fine* sensor has the most restricted coverage in bearing angle and is used to maintain the formation during science observations. The *medium* sensor has a capability allowing hand-off between the acquisition sensor and the fine sensor. It is the delay and delay-rate limitations of the interferometer during the science observations that drive the formation-flying requirements.

The requirements on formation flying are decoupled as much as possible from the requirements on nulling. The formation-flying system is envisioned as the "coarse stage" of a multi-layer control system that maintains the optical pathlengths. Centimeter-level variations in the relative positions of the spacecraft are sensed by the instrument's fringe tracking system and compensated for by the optical-delay lines in each beamtrain, each of which is required to provide a control range of ±10 cm of optical delay. The small changes in the relative bearing angles between the spacecraft are compensated by the articulation of steering mirrors on the collector and combiner spacecraft. The thrusters and reaction wheels will be important disturbance sources for the interferometer, but optomechanical modeling will be needed to establish the appropriate requirements.

The range and bearing control requirements during science observations are imposed by the limitations of the fringe sensor and delay line of the interferometer. If the fringes are allowed to move beyond the throw of the delay line, they will be lost. Similarly, if the fringes move too quickly for the fringe tracker to sense them, they will also be lost, even if they are within range of the delay line. The limitations of the delay line therefore impose requirements on range and bearing angle, and limitations of the fringe tracker impose requirements on range rate and bearing rate.

The optical path-difference is required to be controlled to ±1 cm along the beam path, for both in-plane and out-of-plane directions. This ±1-cm control requirement is shown in Table 6-3, row 10 under the 'Observation' operating mode. A bearing requirement of ±0.33 arcmin is equivalent to ±1 cm spacecraft position control at the shortest baseline with the collector spacecraft center-to-center separation of 100 m.

Specific requirements are also levied on the ground technology development during the current pre-Phase A efforts. Since the flight conditions can be simulated in a high-fidelity simulation, the Formation Algorithms and Simulation Testbed is identical to the flight requirements listed in Table 6-3. The requirements for the multi-robot based Formation Control Testbed are somewhat relaxed, though scalable to flight requirements, and are given in Table 6-4.

Table 6-4. Requirements of the Formation Control Testbed vs. Flight Requirements

Parameter	Flight Performance	Formation Control Testbed	Comments
Number of spacecraft	5	3	
Operational capability			
Standalone operations	5 yr	36 min	Total floatation time
Mission duration	5 yr	5+ yrs	
Observational duration	~20 hr	~15 min	For an "observation on the fly"
Availability	Continuous	8 hrs/day	Ground testbed facility
Motion DOFs	6	5+1	FCT:+ articulated DOF
Operating envelope	3D space	2D plane	FCT: with limited out-of-plane
Control	2 cm / 20 arcsec	5 cm / 60 arcmin	
Fault recovery	Active and passive	None	
Flight capability			
Sensor			
Inertial	Gyro/accel	Gyro/accel	
Celestial	Star tracker	Pseudo-star tracker	
Relative	Coarse, Med., Fine	Medium	
Actuator	Thruster, RWA	Thruster, RWA	
Control Architecture	Distributed	Distributed	
Control Algorithms	Flight	Flight	Developed by FAST
Dynamic DOFs	6	5	FCT: +1 articulated DOF
Range of motion			
Angular-in-plane	2π	2π	
Angular-out-of-plane	$\pm 45°$	$\pm 45°$	
Linear-in-plane	Limited by sensor range	Limited by lab space	
Linear-out-of-plane	Limited by sensor range	± 25 cm	Emulate deadband during observations
Maneuvers			
Acquisition	3D space	2D space	
Array rotation in-plane	Yes	Yes	
Array re-sizing	Yes	Yes	
Array re-targeting	Yes	Yes	
Collision Avoidance	3D space	2D space	

6.3.2 Formation Algorithms and Simulation Testbed (FAST)

Formation and Attitude Control System (FACS) lies at the heart of the formation-flying software. It is designed to provide three-axis inertial attitude and inter-s/c range and bearing control of each of the spacecraft in the TPF-I formation. Additionally, FACS provides the capability of initializing/reacquiring the formation through the acquisition of inter-s/c range/bearing knowledge, using the available on-board formation sensing capability. FACS ensures collision free operation of the formation throughout all nominal phases of the TPF-I mission. It is described in more detail in Appendix C. Here it is used for two software demonstrations that are described in the following pages.

Two high-level scenarios have been demonstrated in FAST. The first consists of two spacecraft functioning as a distributed interferometer. The second is a two-robot simulation of the FCT.
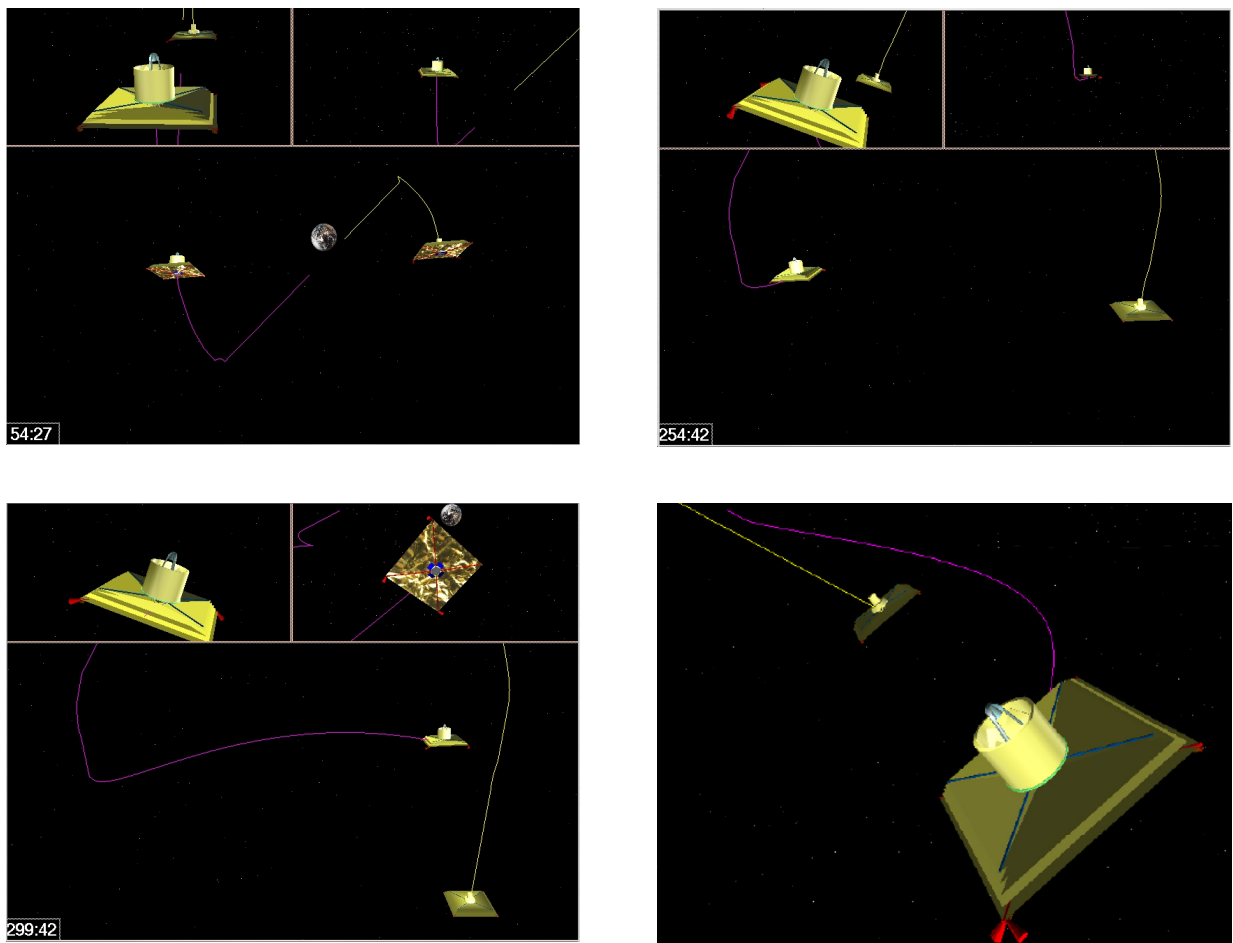
Figure 6-6. (top left) Spacecraft spring apart, arrest separation velocity, acquire relative sensor, and rotate formation to center Sun on panels; (top right) Beginning of second retarget: only relative position is controlled, the formation is drifting downwards; (bottom left) Approximately half-way through second retarget. Bowed trajectory is for collision avoidance; (bottom right) View after second retarget completed.

143

Two-Spacecraft Distributed Interferometer

The purpose of this simulation was to demonstrate nominal, ground-based operation of a distributed-interferometer formation with high-level commands and autonomous formation reconfigurations with collision avoidance. The spacecraft are in deep space and have several flexible modes due to a large sunshield with a fundamental mode at 0.5 Hz. An additional requirement for this FACS design was that all thruster firings for both attitude and relative position control across all spacecraft occur in the same 4-s window every 60 s. This requirement allows nanometer-level interferometer control loops to reacquire a fringe and make a science observation between impulsive disturbances due to thrusters. Subsequently, the selection of throttle-able ion thrusters that do not impart impulsive disturbances obviated this thruster quiescence requirement.

The spacecraft go through individual modes to become power positive (such as detumble, Sun-search, and Sun-point) and then begin to acquire the formation. In this scenario, the two spacecraft are assumed to be in a stack and to separate via springs. Propagation using accelerometers is used to determine an approximate position of the other spacecraft. With this knowledge, the spacecraft point their formation sensors at one another. The autonomous-formation flying (AFF) sensor was used in this simulation, which is RF-based with a Global Positioning System-like (GPS-like) signal structure. The field-of-view of the sensors is 70 deg. After acquiring relative sensor lock and establishing inter-spacecraft communication (ISC), a coarse control loop is closed to maintain a constant distance, and the formation rotates toward the Sun on the formation solar panels. This formation is held until a command is received.
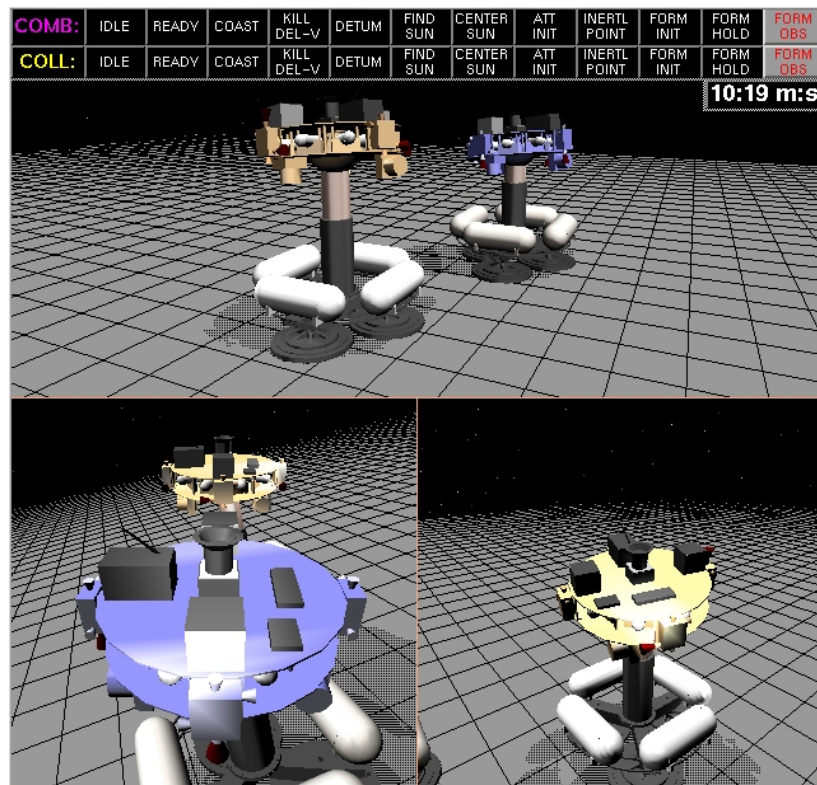
Figure 6-7. Visualization of FAST demonstration of two-robot FCT.

Two commands were sent in this demonstration, both of which specify stellar targets to observe. The stop-and-stare observations consist of holding a constant relative position with the thruster quiescence requirement. The commands include the baseline to hold while observing, and the time allotted for retargeting. In response to a retarget command, the formation guidance algorithm first plans collision-avoidance constrained, energy-optimal relative spacecraft trajectories to achieve the desired baseline. This process is non-trivial, since the unconstrained, energy-optimal trajectories for the second retarget lead to a collision. Figure 6-6 shows several visualizations from this distributed, real-time demonstration of formation flying.

Two-Robot FCT

The purpose of this demonstration is to validate the FACS used on the FCT robots before implementation on the actual robotic hardware, including flight-like ISC and control-cycle synchronization. The formation software used the Real-Time protocol, wireless links, and time-offset estimation via echo packets, and control cycle synchronization. Additionally, the sensors models use measured sensor noise values. For example, each fiber-optic gyroscope on the robots was calibrated, and measured values of rate-random walk, angle-random walk, and angle white noise were used in the gyroscope model. The control cycles were initially 0.5 s out of synchronization, and the clock models had a relative drift of 0.1 ms/s.

In addition to autonomous reconfiguration, synchronized rotations were demonstrated in which the formation rotation rotates as a virtual rigid body. Synchronized rotations are used for observations "on-the-fly" and can also be used to retarget a formation. In the latter case, the rotation axis is not along the formation boresight.

Figure 6-8 shows visualization from the two-robot FAST demonstration. The top of the figure shows the modes that the "Combiner" and "Collector" robots go through. In the figure, they are in Formation Observation mode and performing the first synchronized rotation. The lower part of the robots with the white tanks serves as a translation stage. The upper, cylindrical portions are referred to as the attitude stages and emulate spacecraft. As can be seen in the lower left, the attitude stages are a rotating and translating in a plane inclined to the experiment floor. This plane is normal to the star direction.

These two FAST simulations demonstrated formation software for autonomous formation flying with realistic inter-spacecraft communication and asynchronous clocks. In particular, formation algorithms for actuation-constrained formation control, autonomous collision-free reconfiguration, and synchronized rotation were demonstrated. This formation software has been integrated with the Formation Control Testbed robots for a flight-like, hardware demonstration of precision-formation flying.

6.3.3 Formation Control Testbed (FCT)

The Formation Control Testbed (FCT) is the testing-ground for flight software developed for formation flying for TPF-I. It includes the two robots pictured in Fig. 6-8. Each robot uses cylinders of compressed air and linear air bearings (the circular metal pads seen in the photo) to float freely above a polished metal floor. A spherical air bearing supports a stage (shown tilted in the photograph) upon which are housed the avionics and processors of each robot. The robots have a master–slave relationship and algorithms for autonomous guidance. They can either be operated independently or together in "cooperative" mode.
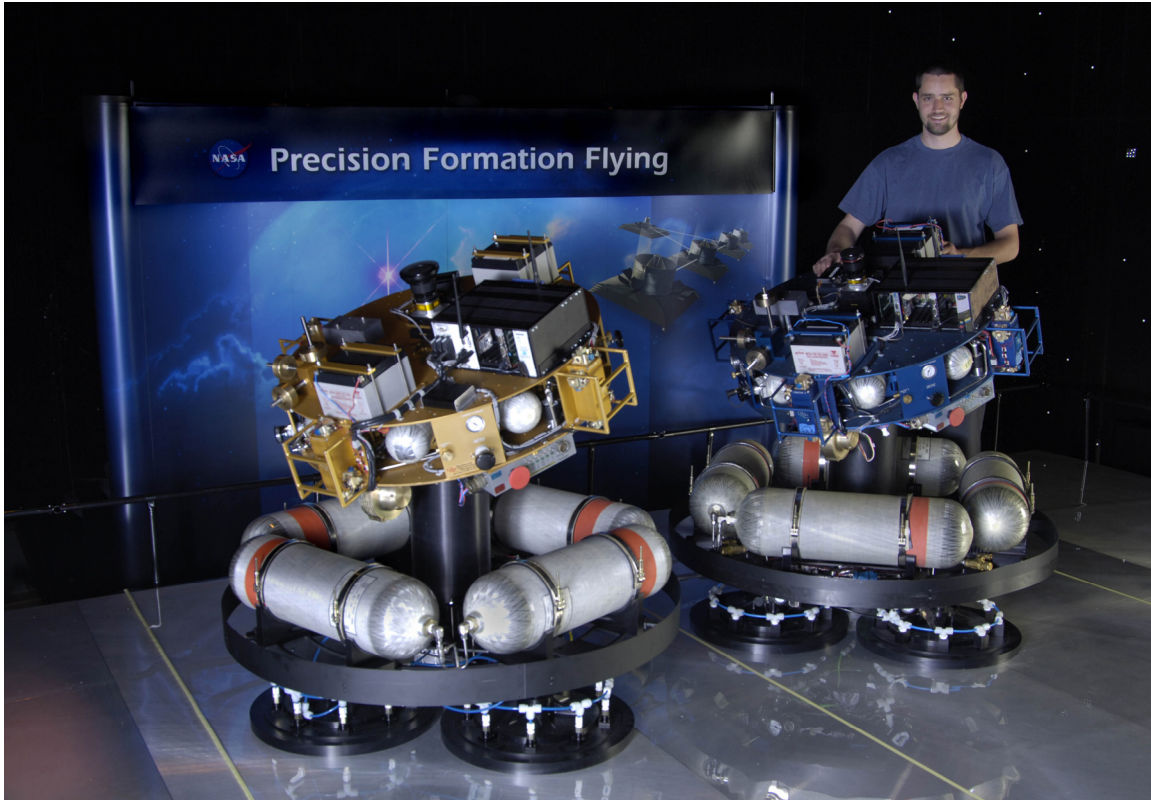
Figure 6-8: The Formation Control Testbed (FCT). Shown here are the two robots of the FCT, with Jason Keim. Each robot carries cannisters of compressed air that allow them to float off a polished metal floor. The floor is flat to within 2 one-thousandths of an inch (~50 μm) and spans a much larger area than shown here. The robots carry a platform (shown tilted for each robot) that is supported on a spherical ball bearing, also driven with compressed air so that the support of the platform is entirely frictionless. The robots serve as the hardware interface and testing ground for flight software developed for space applications in formation flying. The robots have completed their functional testing in cooperative mode and should achieve their major milestone of range and bearing control in mid 2007. The Principal Investigator of the Formation Control Testbed is Daniel Scharf.

The robots are being tested within a celestarium that had been used previously to calibrate star trackers used by spacecraft. The spherical ceiling of the interior building has an array of artificial stars on it that the robot cameras can use to derive absolute position information down to the level necessary to reach the testbed's performance milestone.

The FCT was planned as a ground-based laboratory consisting of three test robots in its fully deployed configuration. Much like in the distributed simulation under FAST, the FCT demonstrates formation acquisition, TPF-like formation maneuvering, and collision-free operations using the formation algorithms developed in the FAST. A high level of flight relevance was designed into the FCT avionics architecture, with on-board flight-like capabilities: (a) wireless communication emulating inter-spacecraft and spacecraft to ground communication; (b) on-board sensing and actuation using star tracker, gyros, thrusters, and reaction wheels for attitude and translation control; and (c) PowerPC flight control
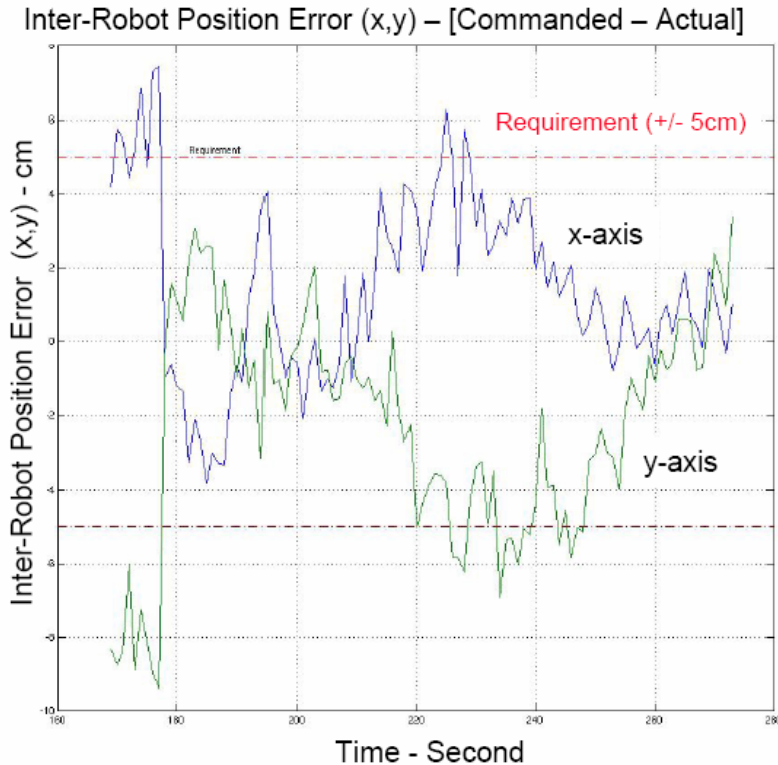
Figure 6-9. Inter-robot position error, showing performance slightly outside the range requirements. Ongoing upgrades to the robot thrusters should bring the performance within requirements.

computer on a compact peripheral communications interconnect (PCI) local bus under a vxWorks Realtime operating system. The on-board formation control software for the FCT is being developed by the Formation Algorithm and Simulation Testbed (FAST). To emulate the real spacecraft dynamics, the FCT was designed for realistic spacecraft-like dynamical behavior, mobility, and agility using linear and spherical air-bearings. With such 6-degrees-of-freedom dynamical motion and functional similarity to the TPF spacecraft, the FCT provides direct emulation of both individual spacecraft and formation behavior under autonomous on-board control. These architectural, functional, and dynamical similarities between the FCT and TPF-I provide a direct path of development to the TPF flight system.

The requirements for the FCT have been listed in detail in Table 6-4. The layout of the FCT emulates the distribution of the formation-flying telescopes, which is limited to a plane to minimize stray light from adjacent spacecraft. The vertical air bearing has a range of ±25 cm, and the pitch and roll axes of each robot's motion is limited to ±30°, which is a physical limitation due to the spherical air bearings.

The FCT is designed to demonstrate an end-to-end system level formation flying control capability (functional and performance requirements) scaleable to flight, within a ground-test environment. The ground-operating environment for the FCT provides a more severe disturbance environment compared to the conditions in space. The net linear disturbance force due to solar pressure of ~6 $\mu N/m^2$ (at 1 AU) for the TPF-I spacecraft (assuming a 5.7-m radius sunshade with a surface area of 102 m^2) is around 0.6 mN, comparable to the robot linear drift force of ~0.26N due to maximum residual floor slope of 80 µrad.
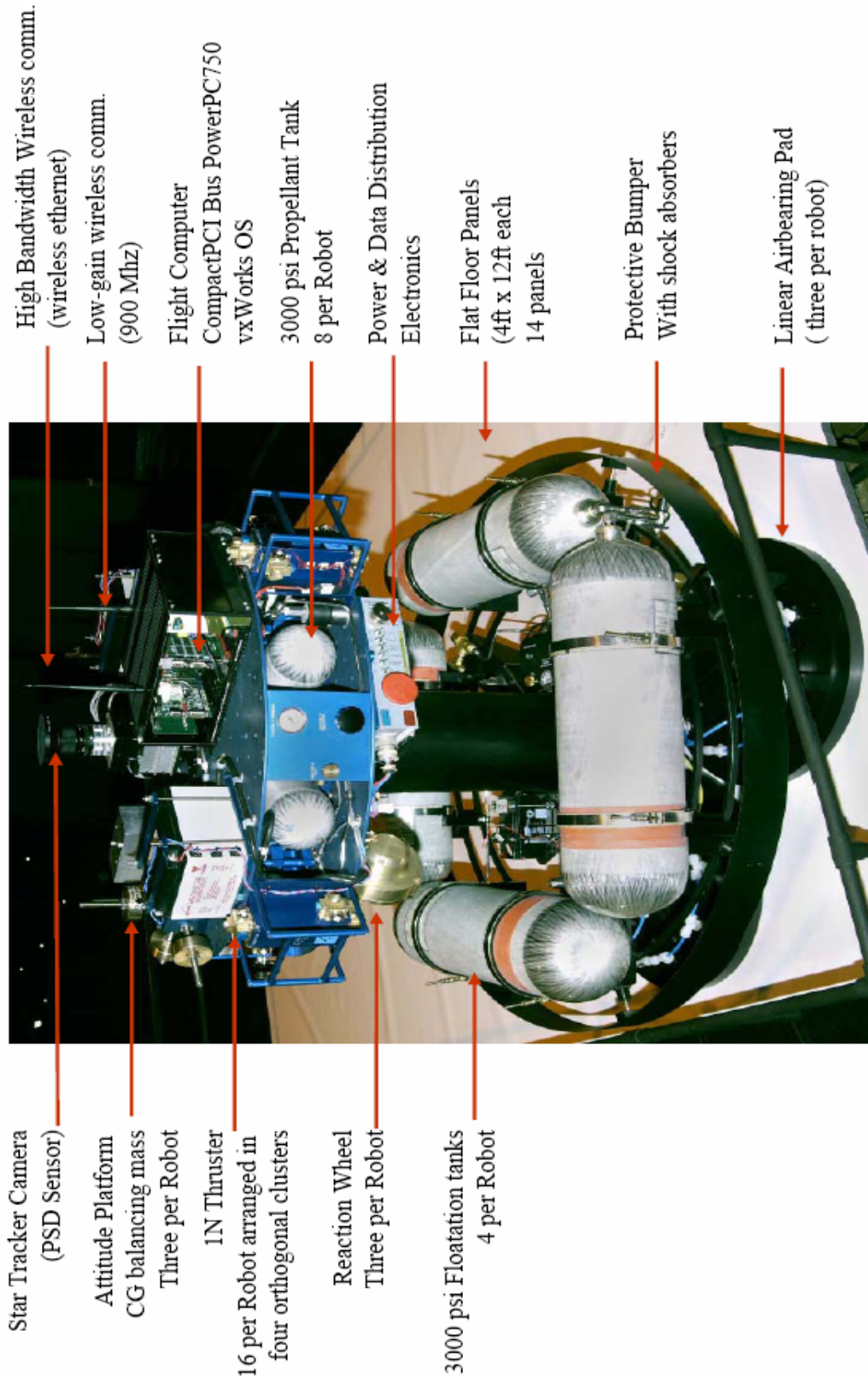
147

Figure 6-10. Detailed view of a Formation Control Testbed robot.

148

Moreover, the residual center-of-gravity (CG) mass imbalance torque of 5 mN-m of the top attitude platform of the FCT robot is about 33 times worse than the expected solar pressure induced torque of 0.15 mN-m on the TPF-I spacecraft sunshade due CG to center of solar-pressure offset of ~0.25 m.

The integration of the FACS software was successfully completed in February 2006, enabling the two FCT robots to operate in a formation mode for the first time. There are a number of calibration activities underway (inertia, thrusters, etc.); however, initial test results indicate that the closed-loop formation performance is very close to the required level (within factor of 2). Further formation tests will be performed once the ongoing calibration activities are completed.

Figure 6-9 shows the two-robot baseline-hold performance while pointing to a specified (non-zenith) position. The plot shows the performance during the baseline/target hold, after two robots have maneuvered to achieve the desired baseline (2 m) and target star pointing (20 deg. off zenith). The required performance bounds are also indicated on the plot.

The FCT currently does not have formation sensors to directly measure the inter-robot/spacecraft range and bearing. The range and bearing values for the FCT robots are currently derived from the position and attitude measurements from the star tracker on each robot — using parallax from the near-field FCT pseudo-star beacons mounted on the dome ceiling. An optical range and bearing sensor is currently under final hardware integration and test (I&T) phase to provide direct relative sensing capabilities in the near future. The difference of a factor of 60 in bearing control between the flight design and FCT requirement (1 vs. 60 arcmin) arises from the greatly reduced spacing between the 'spacecraft' in the testbed. The size of the control volume within which each spacecraft is constrained at a given time is comparable for the two cases. The technology gap between testbed and flight is really the precision of the bearing sensor that is needed to maintain the formation. Bearing sensing in the flight design will be achieved with a combination of inertial star trackers on each spacecraft and encoders on the steering mirrors that direct the science and metrology beams between the spacecraft, both of which are well within the current state-of-the-art.

In FY2006, using the two deployed FCT robots, FCT has functionally validated the FAST algorithms and the end-to-end formation-flying architecture, and the FCT team is currently in the process of validating the FAST predicted performance.

6.4 Future Hardware for General Astrophysics

The Terrestrial Planet Finder Interferometer (TPF-I) has immense potential to broadly transform astrophysics as well as to detect Earth-like planets. This potential relies on exploiting the high angular resolution and high sensitivity of TPF-I simultaneously in an imaging mode. Both hardware and software for aperture synthesis imaging capabilities must be developed to work well with a high-dynamic range over a small field-of-view (from one to a few diffraction-limited 'primary beams') using faint off-axis guide stars. This may require substantial modifications to the TPF system architecture beyond the minimum hardware architecture necessary for the baseline requirement of nulling interferometry over a narrow field (within one primary beam) around bright targets. However, the discovery potential for TPF-I will be so radically expanded by incorporating these additional imaging capabilities that they should be seriously considered as part of the overall TPF-I design. In this section we explore the potential hardware

that would expand the general astrophysics capability of the current baseline design. Although such hardware is not currently funded for development within the TPF-I project, its importance has been emphasized by the TPF-I SWG for funding in future years.

6.4.1 Off-Axis Phase Referencing

The most critical hardware requirement for maximizing general astrophysics will be the addition of phase referencing using an off-axis guide star, a capability not needed for the planet finding activity where the primary star acts as the phase reference. This capability is crucial to obtain the theoretical sensitivity limit that is needed for very faint objects, since current baseline designs require an external reference for monitoring OPD drifts internal to the spacecraft and perhaps for monitoring array geometry.

Having the capability of using an off-axis star, and hence an additional beam transport system, for phase referencing may not pose a problem if it is incorporated into the design process from the beginning, but it surely will require substantial modifications to the optics at the collector telescopes. TPF-I is a system optimized for low thermal background and off-axis phase referencing may require non-trivial changes to the current design of a "dual-star" module that is used to select the off-axis reference star while passing the on-axis light directly as is done with VLTI/PRIMA (Quirrenbach et al. 2004) and the Palomar Testbed Interferometer (PTI) (Colavita et al. 1999). Another possible approach would be to include a "fast switching" capability to the feed system or secondary mirrors on the collectors, to alternate between a guide star and the target star as is currently done in ground-based radio and mm-wave interferometry. A final option would be use an efficient dichroic to select a star in the field as a phase reference while allowing the mid-IR beam train to contain a different target. Further study is necessary to develop optimal designs for off-axis guiding that are consistent with the nulling requirements.

6.4.2 Wavelength Coverage

We must also consider the broadest possible spectral coverage when optimizing scientific return for general astrophysics. Based on the science case for terrestrial planet finding, the short wavelength side of TPF-I is generally restricted to ~5 µm due to: a) planets in the habitable zone have temperatures near room temperature, giving a peak in blackbody emission near 10 µm, and hence limited emission at short wavelengths; b) the performance requirements for the optics and wavefront quality that are driven for maximum performance around 10 µm to provide sufficient starlight suppression (deep nulling) to detect planets in the habitable zone.

Because these limitations are not relevant for general astrophysical observations, the final TPF-I design should consider incorporating a secondary beam combiner optimized for general astrophysics. While this could add significant cost and complexity to the system, one option might be to design the phase-referencing combiner for this purpose. This idea is further explained below.

It is likely that a 'fringe tracking' system will be incorporated into any baseline TPF-I design to control internal and external optical path difference (OPD) drifts. Most such designs operate by using off-band (near-infrared) light from the target itself (i.e., an "on-axis" guide star). In principle, this subsystem could be designed with its own separate beamcombiner that might function for example in the 1–5 µm band, to be used in parallel with the 5–15 µm beam combiner that is optimized for nulling and other lower-spatial-resolution astrophysics.

6.4.3 Spectral Resolution

Spectral resolution plays an important role both in allowing robust spectroscopy and also in aperture synthesis imaging, where the bandpass must be restricted to avoid "bandwidth smearing" distortion. Bandwidth smearing sets a minimum spectral resolution for imaging all objects within a single 'primary beam' (truly, the minimum field-of-view requirement): the requirement on spectral resolving power, i.e., $R \sim \lambda / \Delta\lambda \geq B / D$, where λ is the wavelength, $\Delta\lambda$ is the bandpass, B is the baseline length, and D is the diameter of the telescopes in the array. For 200-m baselines (12.5 mas resolution at 10 μm) and 4-m telescopes (primary beam of FWHM ~ 0.6"), we see that R > 40. This resolution can be obtained with a simple prism or grism that would likely be part of any detection system. Even extending the baseline to 1 km (2.5-mas resolution) would only require R > 200 spectrograph for imaging.

While this minimum spectral resolution for imaging is easy to achieve, higher spectral resolution in the infrared would be invaluable for many other scientific goals. A special combiner for general astrophysics (suggested in the last section) could host a spectrograph with multiple levels of dispersion depending on the science goal.

Figure 6-11. Beam combiner for pair-wise combination.

While it may difficult to obtain high spectral resolution (R>20000) for space-based telescopes due to weight and payload size limitations, the science gains from resolving ro-vibrational lines themselves could be immense by combining this kinematic information with the high angular resolution of the interferometer. As an alternative to deploying an echelle spectrograph, the interferometer could be used in a Fourier-transform spectrometer (FTS) mode to allow high-spectral-resolution interferometric observations, a potential gold-mine of information to probe the many mid-IR transitions of diatomic and polyatomic molecules associated with star formation and the extragalactic interstellar medium.

6.4.4 Beam Combination and Field-of-View (FOV)

There are readily available and proven techniques for imaging the entire field-of-view of the primary beam. However, this is a very small beam for TPF-I (~0.6″ at 10 μm) and thus would impose large costs in observing time to image a large FOV (such as Hubble Deep Field or nearby galaxies). Despite this limitation, the science case laid out in Chapter 3 is clearly transformational, resolving otherwise point-like objects across our Galaxy and indeed across the Universe. In this section we discuss options for imaging with TPF-I and explore ways to optimize the potential.

With a symmetric rotating array of four telescopes arranged in either a line or a rectangle, there are only three fully independent baselines. All of the necessary beam combinations can be generated with a straightforward two-level four-beam combiner, as shown in Figure 6-11. Indeed, one of the outputs is in fact redundant (allowing for application of this output to the lowest signal-to-noise combination). If

151
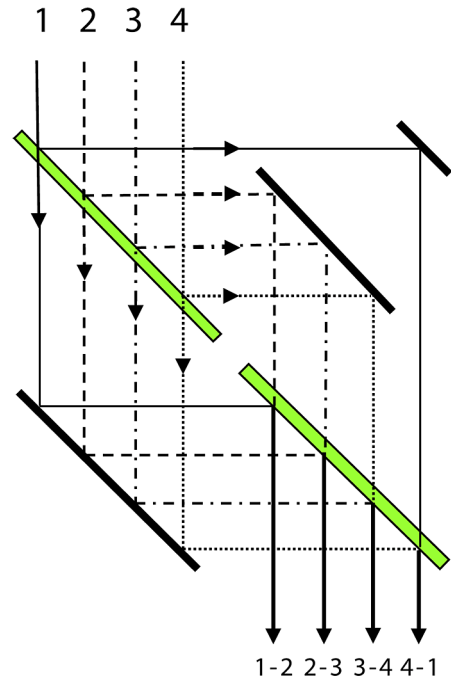
TPF-I is designed with the capability of arranging the telescope array into a non-redundant geometry, then an alternate beam combiner could be used that maximized the Fourier coverage and, thus, the imaging capabilities.

There are possibilities for giving TPF-I truly wide-field imaging capabilities, extending beyond a single primary beam. Wide-field imaging is best obtained using homothetic pupil mapping (Beckers 1986), which is difficult to implement in practice for a reconfigurable array geometry, although formation flying offers a possible context for application. An FOV intermediate between a single primary beam but smaller than the optical vignetting limits can be attained through pupil densification, so-called hyper-telescope concept (Labeyrie *et al*. 2000, 2003)

Novel optical arrangements have also been proposed that, when combined with special OPD modulation schemes, promise to provide a wide-field imaging capability simultaneous with high spectral resolution (e.g., the SPECS concept; Leisawitz et al. 2000). Recently, these schemes have been partially validated in the laboratory, clearly offering attractive features, and further research in this area should be pursued (Rinehart et al. 2006).

6.4.5 Double Fourier Interferometry

The mid-IR is rich in spectral features from source components in the solid state and gas phase. The spectrum includes atomic hydrogen recombination lines, ionized neon (Ne), argon (Ar), and sulfur (S) forbidden lines, H_2 rotational lines, and silicate, SiC and polycyclic aromatic hydrocarbon (PAH) features. These features appear on a continuum of thermal-dust emission. A wealth of information is available from the mid-IR spectrum, such as the radiation field intensity and hardness, the dust temperature, and the chemical state of the medium. Kinematic information is potentially available as well, but only when the available spectral resolution is $\sim 10^4$ for galaxies or $\sim 10^{5-6}$ for protostars and objects of similar size.

The spectral resolution of TPF-I can be increased by increasing the stroke of the delay line. R = 1000 at 10 μm requires only a 1-cm stroke, but $R = 10^6$ requires a 10-m delay-line stroke, a packaging challenge. Such very high resolutions probably require the addition of a grating.

The wide field-of-view double Fourier technique (e.g., Mariotti and Ridgway 1988) can enable a TPF mid-IR interferometer to provide high spatial resolution, high spectral resolution observations of spatially extended astrophysical sources. TPF-I could map protostars, debris disks, extragalactic star-forming regions, and protogalaxies on relevant spatial scales and simultaneously provide the spectroscopic data that would enable deep insight into the physical conditions in these objects. table 6-5 below shows desired measurement capabilities for a variety of targets and indicates that 10 mas is an interesting angular resolution and that ~1 arcmin is an interesting FOV for a wide variety of applications.

Table 6-5. Desired Measurement Capabilities for Desired Targets

Ancillary Science Target	Interesting Physical Scales	Typical Distance	Interesting Angular Scales (arcsec)	
			Desired Resolution	**Desired FOV**
Protostar (envelope, disk, outflow)	$1 - 10^4$ AU	140 pc	0.007	70
Debris disk	1 – 300 AU	3.2 pc (e Eri)	0.3	93
		30 pc	0.03	10
Extragalactic Giant H II Region	1 – 100 pc	5 Mpc	0.04	4
Coma cluster galaxy	0.01 - 10 kpc	107 Mpc	0.02	19
High-z protogalaxy	1/100th source to separation between merging systems	N/A	0.01	4

The idea behind the double Fourier technique is that a Michelson stellar interferometer equipped with a pupil-plane beamcombiner and a scanning optical delay line can be operated like a Fourier transform spectrometer (FTS). Instead of providing only a visibility measurement for the interferometer baseline established by the collecting aperture locations, such a device produces an interferogram whose 1-D Fourier transform is the spectrum of the target scene on the spatial scales to which the interferometer is sensitive. Combined, the interferograms from all the baselines provide a three-dimensional data cube where the cube has two spatial and one spectral dimension, like the data from the integral field units discussed above.

Using a conventional double-Fourier system, a TPF interferometer with 4-m diameter collectors operating at λ = 10 μm with a maximum baseline of 300 m could image a 0.6-arcsec diameter FOV at 4.8-mas spatial resolution. This field of view would be inadequate for the science programs mentioned above. However, the Wide-field Imaging Interferometry Testbed (WIIT) at NASA's Goddard Space Flight Center was designed to develop and demonstrate a technique for wide-field (i.e., FOV >> $1.2\lambda/D$) imaging in which a detector array is used to enhance the spatial multiplexing efficiency (Leisawitz et al. 2003). In this design, light from field angles θ >> $1.2\lambda/D$ relative to the principal axis of the interferometer focuses onto additional pixels in a detector array, which records interferograms shifted by a geometric delay corresponding to $|\mathbf{b}|$ times the sine of the component of θ aligned with the baseline vector $\mathbf{b}$. The field of view accessible to an interferometer like WIIT is given by $\theta_{FOV} = N_{pix}\theta_p/2$, where $\theta_p = 1.2\lambda/D$ is the primary beam diameter, N_{pix} is the number of pixels along one dimension of the detector array, and the factor 2 allows for Nyquist sampling of the primary beam. For a 256^2 pixel array

(N_{pix} = 256) on the interferometer described above (D = 4 m, λ = 10 µm), θ_{FOV} = 79 arcsec, a good match to the requirements outlined in Table 6-5.

The critical technology for wide field-of-view double Fourier interferometry is already mature. Detector arrays such as those aboard the Spitzer Space Telescope (IRAC and IRS instruments), the Wide-field Infrared Survey Explored (WISE) mission, and their planned successors are well suited for this application, both in sensitivity and pixel count. The moving scan mechanism in the Composite Infrared Spectrometer (CIRS) on the Cassini mission provides ~10 cm scan range. FTS scan mechanism technology has extensive heritage in space.

Caveat: The double-Fourier method is best suited for low to moderate spectral resolution. Resolution in the R = 10^4 –10^6 range is attainable with the double-Fourier method, but a long-delay line stroke is required, and the sensitivity is poorer than that available via dispersive methods and may be inadequate for certain sources and spectral lines.

6.5 Bibliography

6.5.1 References for Figure 6-1

Bokhove, H., Kappelhof, J. P., Vink, H. J. P., Vosteen, L. L. A., Sodnik, Z., "Broadband nulling using a prism phase shifter," *Towards Other Earths: Darwin/TPF and the Search for Extrasolar Terrestrial Planets*, edited by M. Fridlund, T. Henning, ESA **SP-539**, European Space Agency, Noordwijk, The Netherlarnds, 367–369 (2003).

Brachet, F., Labèque, A., Léger, A., Ollivier, M., Lizambert, C., Hervier, V., Chazelas, B., Pellet, B., Lépine, T., Valette, C., "Nulling interferometry for the Darwin misison: Polychromatic laboratory test bench," *New Frontiers in Stellar Interferometry*, edited by W. A. Traub, *Proc. SPIE* **5491**, 991–998 (2004).

Buisset, C., Rejeaunier, X., Rabbia, Y., Ruilier, C., Barillot, M., Lierstuen, L., Perdigues Armengol, J. M., "Multi-axial nulling interferometry: Demonstration of deep nulling and investigations of polarization effects, " *Advances in Stellar Interferometry*, edited by J. D. Monnier, M. Schöller, W. C. Danchi, *Proc. SPIE* **6268**, 626819 (2006).

Ergenzinger, K., Flatscher, R., Johann, U., Vink, R., Sodnik, Z., "EADS Astrium nulling interferometer breadboard for Darwin and GENIE," Proc. *Int. Conf. Space Optics 2004*. ESA **SP-554**, European Space Agency, Noordwijk, The Netherlarnds, 223–230 (2004).

Haguenauer, P., Serabyn, E., "Deep nulling of laser light with a single-mode-fiber beam combiner," *Appl. Opt.* **45**, 2749–2754 (2006).

Martin, S. R., Serabyn, E., Hardy, G. J., "Deep nulling of laser light in a rotational shearing interferometer," *Interferometry for Optical Astronomy II*, edited by W. A. Traub, *Proc. SPIE* **4838**, 656–667 (2003).

Martin, S. R., Gappinger, R. O., Loya, F. M., Mennesson, B. P., Crawford, S. L., Serabyn, E., "A mid-infrared nuller for Terrestrial Planet Finder: Design, progress, and results," *Techniques and Instrumentation for Detection of Exoplanets,* edited by D. R. Coulter, *Proc. SPIE* **5170**, 144–154 (2003).

Martin, S., Szwaykowski, P., Loya, F., "Testing exo-planet signal extraction using the Terrestrial Planet Finder Planet Detection Testbed," *Techniques and Instrumentation for Detection of Exoplanets II,* edited by D. R. Coulter, *Proc. SPIE* **5905**, 590508 (2005).

Mennesson, B., Crawford, S. L, Serabyn, E., Martin, S., Creech-Eakman, M., Hardy, G., "Laboratory performance of the Keck Interferometer nulling beam combiner," *Towards Other Earths: Darwin/TPF and the Search for Extrasolar Terrestrial Planets*, edited by M. Fridlund, T. Henning, ESA **SP-539**, European Space Agency, Noordwijk, The Netherlarnds, 525–529 (2003).

Mennesson, B., Haguenauer, P., Serabyn, E., Liewer, K., "Deep broad-band infrared nulling using a single-mode fiber beam combiner and baseline rotation," *Advances in Stellar Interferometry*, edited by J. D. Monnier, M. Schöller, and W. C. Danchi, *Proc. SPIE* **6268**, 626830 (2006).

Morgan, R. M., Burge, J. H., Woolf, N. J., "Final laboratory results of visible nulling with dielectric plates," Interferometry for Optical Astronomy II," edited by W. A. Traub, *Proc. SPIE* 4838, 644–655 (2003).

Ollivier, M., *Contribution à la Recherche d'Exoplanètes: Coronagraphie Interférentielle pour la Mission Darwin*, Ph.D. thesis, University Paris XI (1999).

Samuele, R., Wallace, J. K., Schmidtlin, E., Shao, M., Levine, B. M., Fregoso, S., "Experimental progress and results of a visible nulling coronagraph," *2007 IEEE Aerospace Conference*, Big Sky Montana, paper 1333 (2007).

Schmidtlin, E., Wallace, J. K., Samuele, R., Levine, B. M., Shao, M., "Recent progress of visible light nulling and first 1 million null result," *Direct Imaging of Exoplanets: Science and Techniques*, *Proc. IAU Colloq*. **200**, edited by C. Aime and F. Vakili, 353–360 (2006).

Serabyn, E., Wallace, J. K., Hardy, G. J., Schmidtlin, E. G. H., Nguyen, H. T., "Deep nulling of visible laser light," *Appl. Opt*. **38**, 7128–7132 (1999).

Vosteen, L. L. A., Vink., H. J. P., van Brug, H., Bokhove, H., "Achromatic phase-shifter breadboard extensions," *Techniques and Instrumentation for Detection of Exoplanets II,* edited by D. R. Coulter, *Proc. SPIE* **5905**, 59050A (2005).

Weber, V., Barillot, M., Haguenauer, P., Kern, P., Schanen-Duport, I., Labeye, P., Pujol, L., Sodnik, Z., "Nulling interferometer based on an integrated optics combiner," *New Frontiers in Stellar Interferoemetry, Proc. SPIE* **5491**, edited by W. A. Traub, 842–850 (2004).

Wallace, K., Hardy, G., Serabyn, E., "Deep and stable interferometric nulling of broadband light with implications for observing planets around nearby stars," *Nature* **406**, 700–702 (2000).

6.5.2 Achromatic Nulling Testbed

Gappinger, R. O., Wallace, J. K., Bartos, R. D., Macdonald, D. R., Brown, K. A., "Current progress on TPF-I nulling architectures at Jet Propulsion Laboratory," in *Techniques and Instrumentation for Detection of Exoplanets II*, *Proc. SPIE* **5905**, edited by D. R. Coulter, 55–61 (2005).

Wallace, J. K., Babtiwale, V., Bartos, R., Brown, K., Gappinger, R., Loya, F., MacDonald, D., Martin, S., Negron, J., Truong, T., Vasisht, G., "Mid-IR interferometric nulling for TPF," *New Frontiers in Stellar Interferometry*, *Proc. SPIE* **5491**, edited by W. A. Traub, 862–873 (2004).

Wallace, J. K., Bartos, R., Gappinger, R., F. Loya, S. Moser, J. Negron, "Progress in broadband infrared nulling technology for TPF," in *Techniques and Instrumentation for Detection of Exoplanets II, Proc. SPIE* **5905**, edited by D. R. Coulter, 47–54 (2005).

6.5.3 Planet Detection Testbed

Martin, S., "TPF Planet Detection Testbed: a four beam infrared testbed demonstrating deep, stable nulling and planet detection," *2005 IEEE Aerospace Conference*, Big Sky, Montana (2005)

Martin, S., "Progress in four-beam nulling: results from the Terrestrial Planet Finder Planet Detection Testbed," *2006 IEEE Aerospace Conference*, Big Sky, Montana, 4–11 March (2006).

Martin, S., Szwaykowski, P., and Loya, F., "Testing exo-planet signal extraction using the Terrestrial Planet Finder planet detection testbed," *Techniques and Instrumentation for Detection of Exoplanets II*, *Proc. SPIE* **5905**, edited by D. R. Coulter, 70–79 (2005).

Martin, S. R., Szwaykowski, P., Loya, F. M., and Liewer, K., "Progress in testing exo-planet signal extraction on the TPF-I Planet Detection Testbed," *Advances in Stellar Interferometry*, *Proc. SPIE* **6268**, edited by J. D. Monnier, M. Schöller, W. C. Danchi, 626818 (2006).

6.5.4 Adaptive Nuller Testbed

Lay, O. P., Jeganathan, M., Peters, R., "Adaptive nulling: a new enabling technology for interferometric exo-planet detection," *Techniques and Instrumentation for Detection of Exoplanets*, *Proc. SPIE* **5170**, edited by D. R. Coulter, 103–112 (2003).

Peters, R. D., Hirai, A., Jeganathan, M. Lay, O. P., "Near-IR demonstration of adaptive nuller based on deformable mirror," *New Frontiers in Stellar Interferometry*, *Proc. SPIE* **5491**, edited by W. A. Traub, 1630–1638 (2004).

Peters, R. D., Hirai, A., Jeganathan, M., Lay, O. P., "Adaptive nulling with a deformable mirror in the near-IR," *Techniques and Instrumentation for Detection of Exoplanets II*, *Proc. SPIE* **5905**, edited by D. R. Coulter, 62–69 (2005).

Peters, R. D., Lay, O. P., Hirai, A. Jeganathan, M., "Adaptive nulling for the Terrestrial Planet Finder Interferometer," *Advances in Stellar Interferometry, Proc. SPIE* **6268**, edited by J. D. Monnier, M. Schöller, W. C. Danchi, 62681C (2006).

6.5.5 Mid-Infrared Single Mode Spatial Filters

Aggarwal, D., Shaw, L. B., and Sanghera, J., "Chalcogenide glass for mid- and longwave IR fiber lasers," *Fiber Lasers II: Technology, Systems, and Applications*, edited by A. J. W. Brown, J. Nilsson, *Proc. SPIE* **5709**, 242–248 (2005).

Bordé, P., Perrin, G., Amy-Klein, A., Daussy, C., and Mazé, G., "Updated results on prototype Chalcogenide fibers for 10 micron wavefront spatial filtering," *Towards Other Earths: Darwin/TPF and the Search for Extrasolar Terrestrial Planets*, edited by M. Fridlund and T. Henning, ESA SP **539**, European Space Agency, Noordwijk, The Netherlands, pp. 371–374 (2003).

Ksendzov, A., Bloemhof, E,. White, V., Wallace, J. K., Gappinger, R. O., Sanghera, J. S., Busse, L. E., Kim, W. J., Pureza, P. C., Nguyen, V. Q., Aggarwal, I. D., Shalem, S., and Katzir, A., "Measurement of spatial filtering capabilities of single mode infrared fibers," *Advances in Stellar Interferometry*, edited by J. D. Monnier, M. Schöller, W. C. Danchi, *Proc. SPIE* **6268**, 626838 (2006).

Shalem, S., Tsun, A., Rave, E., Millo, A., Nagli, L., Katzir A., "Silver halide single-mode fibers for the middle infrared," *Appl. Phys. Lett*. **87**, 09113 (2005).

6.5.6 Future Hardware for General Astrophysics

Beckers, J. M., "Field of view considerations for telescope arrays," *Advanced Technology Optical Telescopes III*, *Proc. SPIE* **628**, edited by L. D. Barr, 255–260 (1986).

Colavita, M. M., *et al.* "The Palomar Testbed Interferometer," *Astrophys. J*. **510**, 505–521 (1999).

Lardière, O., *et al.* "VIDA (Vlti Imaging with a Densified Array), a densified pupil combiner proposed for snapshot imaging with the VLTI," *Interferometry for Optical Astronomy II*, Proc SPIE **4838**, edited by W. A. Traub, 1018–1027 (2003).

Leisawitz, D. *et al.*, "Scientific motivation and technology requirements for the SPIRIT and SPECS far-infrared/submillimeter space interferometers," *UV, Optical, and IR Space Telescopes and Instruments*, *Proc. SPIE* **4013**, edited by J. B. Breckinridge and P. Jakobsen, 36–46 (2000).

Leisawitz, D., Frey, B. D., Leviton, D. B., *et al*., "Wide-field imaging interferometry testbed I: purpose, testbed design, data, and synthesis algorithms," *Proc. SPIE* **4852**, 255–267 (2003).

Mariotti, J.-M, and Ridgway, S. T., "Double Fourier spatio-spectral interferometry," *Astron. Astrophys*. **195**, 350–363 (1988).

Martin, S., "The flight instrument design for the Terrestrial Planet Finder Interferometer," *Techniques and Instrumentation for Detection of Exoplanets II*, *Proc. SPIE* **5905**, edited by D. R. Coulter, 21–35 (2005).

Pedretti, E., *et al*., "First images on the sky from a hypertelescope," *Astron. Astrophys. Sup. Ser.***147**, 285–290 (2000).

Quirrenbach, A. *et al.* "The PRIMA astrometric planet search project," *New Frontiers in Stellar Interferometry*, *Proc SPIE* **5491**, edited by W. A. Traub, 424–432 (2004).

Rinehart, S. A. *et al.*, "The wide-field imaging interferometry testbed: recent results," *Advances in Stellar Interferometry*, *Proc. SPIE* **6268**, edited by J.D. Monnier, M. Schöller, and W. C. Danchi, 626836 (2006).

7 Preparatory Science for TPF-I

The development of precursor science for TPF-I is shown schematically in Fig. 7-1, which highlights the major project phases and gate reviews. In green, we indicate the most significant programmatic decisions the mission must face. In the sections below, we describe in more detail how scientific questions feed directly into the decisions that TPF-I faces during its development.

7.1 Pre-Phase A

In Pre-Phase A, the focus of TPF-I science will be to contribute to the Mission Concept Review that will allow TPF-I to enter Phase A of its project life cycle. Key questions will include the level of exozodiacal emission and its influence on the designs of interferometer architectures, an assessment (mostly complete) of the spectral markers for TPF-I, and an initial selection of appropriate target stars.

7.1.1 Priority 1: Exozodiacal Dust

For the interferometer, a driving requirement is the need to suppress or reject starlight so that planet light can be detected. Moreover, atmospheric spectroscopy must be possible within the bands of biomarkers that have been identified. A starlight rejection of $\sim 10^5$–10^6:1 is needed for a mid-IR interferometer. Previous architecture studies have shown that the brightness of dust in the habitable zone of the target star adversely affects the integration time necessary to detect planets. Thus, in addition to a critical assessment of the technology needed for each architecture, it is important to characterize and understand the brightness of the average exozodiacal emission surrounding potential target stars prior to the Mission Concept Review.

- A survey of a representative sample of target stars for dust on all orbital scales, from < 1 AU out to 100 AU, is important for both the mission concept review and selection of preliminary targets. Although selected stars may be studied through individual peer-reviewed proposals, a program coordinated between NASA and ESA is needed that will make the best use of missions such as Spitzer and Herschel.

- The TPF-I and Darwin Projects should also work to coordinate and make best use of upcoming ground-based facilities, such as the nulling instruments at KI and LBTI.

- Our understanding of levels of exozodiacal dust and the relation of those levels to the search for planets would be further bolstered by strong support for a wide-ranging program of theory and modeling.

7.1.2 Priority 2: Frequency of Terrestrial Planets

Improved knowledge of extrasolar planetary systems will allow us to predict with greater certainty the scientific return from TPF-I. This question has highest priority once each mission enters Phase A, and therefore should have a high priority in the preceding years.

- A comprehensive theoretical investigation into many aspects of the formation and evolution of planets and planetary systems must provide the framework within which to understand necessarily incomplete observational results. The combination of the existing and near-term radial velocity and transit programs—with theoretical insights into the orbital stability of planets, planetary migration, and the relationship between gas giants and rocky planets—will further enrich our understanding of extrasolar planetary systems.

- Our current understanding of the frequency of Earth-like planets is based on observations of higher-mass planets discovered through radial velocity surveys, transit surveys, and on inferences from gravitational microlensing results. These highly successful programs should be further supported and encouraged as new detections of lower-mass and longer-period planets continue to refine our estimate of the frequency of Earths.

- Radial velocity surveys would be better supported through the development of new specialized high-resolution échelle spectrometers to offset the current demand for these instruments. Investments in new equipment for radial velocity surveys, directed also at under-used 2–3-m class telescopes, would represent an excellent strategy in the development of workhorse instruments for exoplanet detection.

- The space-based missions CoRoT (CNES/ESA, launched in 2006) and Kepler (NASA, launch in 2009) hold great promise for identifying transiting planets down to an Earth radius around stars located 100–1000 pc away. With these missions we will determine the statistical incidence of terrestrial planets and, with suitable follow-up, new insights into the physical state of these distant planets. Ground-based transit surveys should also be encouraged. Of special interest is the development of a worldwide network of dedicated wide-field transit or microlensing search telescopes that would allow follow-up studies of bright targets.

7.1.3 Priority 3: Target Stars

The quality of science that will be derived from TPF-I will be partly determined by the stars included in the final target list. A preliminary list of stars will greatly assist in judging the technical feasibility of the mission concepts. This preliminary target list may include a larger number of stars than are retained in the final list.

- The TPF-I project needs to determine which stellar parameters are most relevant to the search for life. These parameters, once known, will need to be monitored over time for the stars included in the target list. Spectroscopic observations over a broad range of wavelengths will be needed with coordinated access to appropriate space observatories run by NASA and ESA. The TPF-I and Darwin projects should work with NASA and ESA to ensure a coordinated observing program to observe target stars.

- To complement the studies of nearby stars and potential targets, adequate support is needed for the development and maintenance of comprehensive databases and archives relevant to planet searches. A database, or central clearing-house, with active solicitations to provide missing information (colors, radial velocities, photometric variability, metallicities, binarity, interferometric measurements of diameters, etc.) should be established in Pre-Phase A.

7.1.4 Priority 4: Signs of Life

The technical requirements for the architectures of both coronagraphs and interferometers are dependent upon the wavelength range, or spectral bandpass, that is necessary to detect evidence of life. In particular, the shortest operating wavelength determines the required surface smoothness of optics and the mechanical stability of the observatory. The need for better starlight suppression would push the designs to use longer wavelengths, but amongst mid-IR biomarkers the relatively short-wavelength water-vapor band at 6.3 μm may prove the most sensitive and easiest to interpret—forcing a tightening of requirements of a mid-IR interferometer design. The necessary spectral bands of visible and mid-IR biomarkers must be known if the design team is to provide instruments tailored to TPF-I's needs.

To explore the plausible range of terrestrial planets that we may find, it is important to create self-consistent theoretical models of planetary characteristics and evolution. These models will help to refine
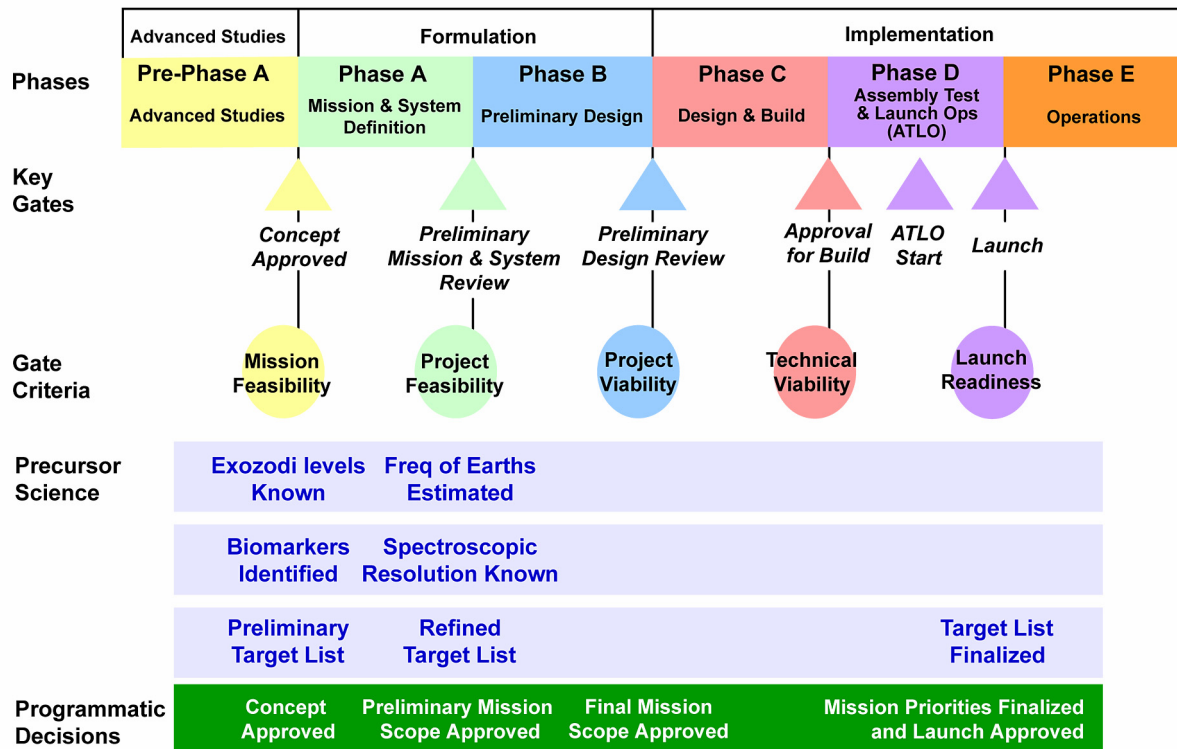
Figure 7-1. Summary schedule identifying the mission phases and science gates for the Terrestrial Planet Finder Missions.

the instrumentation requirements and search strategies for TPF-I, and they will ultimately provide a theoretical framework for analysis of the mission data.

7.2 Phase A

In Phase A the emphasis will be on specifying the detailed design of the optics of TPF-I, leading to the Preliminary Mission and System Review. The mission and system definition studies will refine the architecture so that it is ready for preliminary designs in Phase B. The overriding question to be resolved by the end of Phase A will be to define the capability of the mission and determine to what scale the observatory must be built. What volume of space should be searched for planets? How large of a collecting area will be needed? What angular resolution will be required? Scaling the architecture and defining the scope of the mission will be necessary before TPF-I continues to Phase B, C, and D.

7.2.1 Priority 1: Frequency of Terrestrial Planets

The scale of the TPF-I—the distance between the furthest collecting apertures of the interferometer—will determine the number of stars that are attainable. Defining the capability of a mission will involve a trade between the desire to explore a larger number of extrasolar planetary systems and the technological difficulty of building a larger observatory.

To better understand this trade, preparatory science activities *prior* to Phase A will include detections of planets by a variety of techniques. Coupled with advances in astrophysical theory, these data (including transit detections of several-Earth mass planets from CoRoT for nearby stars) will provide improved estimates of the frequency of Earth-like planets. The programmatic implications will be wide-ranging. More certain knowledge of the frequency of Earths will not only help set the scale of the observatories but will later assist in setting priorities in the initial phases of the missions.

7.2.2 Priority 2: Target Stars

The refined target list, to be developed for the mission during its Phase A, will assist in optimizing the trades (taking into account the expected performance limits) that will ultimately define the capability of TPF-I. The number of attainable target stars of different spectral types, their distances, and their detailed characteristics will largely determine the scientific return of each mission. This target list is more than just an output from a catalog search. There are many characteristics of stars that must be measured, and then carefully weighed in importance, before such a refined list can be constructed.

All nearby stars should be well characterized before the target lists for TPF-I can be chosen. A refined target list, with the farthest target identified, will be needed in Phase A to set the scale of the observatory. The distance to the farthest planet in the survey will be determined by the size of the observatory (its angular resolution) and the area of its collecting apertures (its sensitivity).

Table 7-1. Priorities of TPF-I Science Themes During Pre-Phase A and Phase A

Priority	Pre Phase A	Phase A
1	Exozodiacal Dust	Frequency of Terrestrial Planets
2	Frequency of Terrestrial Planets	Target Stars
3	Target Stars	Signs of Life
4	Signs of Life	Exozodiacal Dust

7.2.3 Priority 3: Signs of Life

In Phase A the details will need to be defined of the spectrometers, filters, dichroics, and operating wavelengths of various instruments within TPF-I. The instruments will be optimized for the detection of known biomarkers. Our understanding of biomarkers must have advanced sufficiently during Phase A to set requirements for the detailed instrument designs.

The spectroscopic resolution is another key parameter that defines the scientific scope. Because the planet signals are very faint, the spectroscopic resolution translates very directly into a sensitivity requirement. How long does it take to perform spectroscopic follow-up of a significant number of detected planets? The resolution needed is, of course, a question that must be answered using our best understanding of the geophysical, atmospheric, and astrobiological processes that may be present on planets that TPF-I detects.

7.2.4 Priority 4: Exozodiacal Dust

Observations to characterize exozodiacal dust will continue to be important during Phase A and also in the phases through launch. Activities in this science theme will contribute to characterizing the stars in the list of target stars.

7.3 Phases B and C/D

In Phase B, C, and D, preparatory science will emphasize the preparation of a mission whose capability is already well defined. Studies will emphasize further development of the target list, understanding the environment of the target stars, and determining the best strategy to maximize the scientific return of the mission.

A coordinated program will continue to observe and characterize all potential target stars and to establish a standardized database and archive of measurements. The target lists will be refined and prioritized to identify target stars most likely to harbor Earth-like planets. Observations with SIM PlanetQuest will be a particularly important component of this final step of characterization.

Up until launch, preparatory science activities will aid in preparations for each mission: undertaking complementary observations of the target stars, establishing databases of standardized measurements, and refining techniques for the detection of biomarkers. There will be a wide variety of activities focused on improving the scientific productivity of the missions.

8 Discussion and Conclusions

The goal of NASA's Navigator program is to find terrestrial planets and to search for life. We must *find potentially habitable planets*, (e.g., 0.5 to 10 Earth mass) located in or near the habitable zone of their parent stars, *characterize their physical properties* in terms of our growing knowledge of conditions that might be hospitable for the formation and stable evolution of life, and *determine their atmospheric constituents or surface composition* by looking for specific biomarkers (O_2, O_3, chlorophyll) or, more generally, the disequilibrium processes that might be attributable to the presence of life. As outlined in Chapters 1 and 2, this program is an ambitious one requiring the determination of masses via astrometry (with SIM PlanetQuest) and the detection of optical photons (with TPF-C) and mid-IR photons (with TPF-I/Darwin). In addition, TPF-I will address the cradle-to-grave evolution of stellar systems, specifically; the early evolution of star and planet formation, stellar and planetary death and cosmic recycling, the formation and evolution of Black holes, and galaxy formation and evolution.

The main areas of focus for TPF-I in the past 3 years have been on architecture selection with emphasis on reducing sources of systematic noise and on technology development in the areas of starlight nulling and formation flying. In a 5-year mission, the X-array architecture using four 3.5-m telescopes has the capability to:

a) Survey at least 150 F, G, K, and nearby M stars with at least three visits each;

b) Make spectroscopic observations of the planets detected around at least 10 stars looking for O_3, CO_2, H_2O, and possibly other species that are trace constituents in the Earth's atmosphere but which might be abundant in alien atmospheres such as CH_4 and N_2O;

c) Carry out a program for general astrophysics probing the 3-μm to 20-μm wavelength region with unprecedented μJy sensitivity and milli-arcsecond angular resolution.

We have also examined in a cursory way the scientific capabilities of a reduced TPF-I mission consisting of four 3.2-m telescopes on a 36-m boom. While this configuration would be severely limited compared to the full TPF-I/Darwin mission, because of its limited angular resolution, it would be able to measure the mid-IR emission of nearby terrestrial planets found with other missions (SIM and/or TPF-C) in a number of broad-band colors and to look for the broadest spectral lines in a few of the brightest planets. If terrestrial planets prove to be common, nearby, and bright, a reduced version of TPF-I might be worth considering as a first probe of the infrared properties of planets.

As outlined in this report a cadre of capable scientists and engineers around the country (and in Europe) are making steady progress on the precursor science and enabling technologies. Stable nulls deeper than10^{-4} have been achieved with a spectral bandwidth of 32%. Deeper nulls of 10^{-6} have been achieved in narrow laser bandpasses. Simulated planetary signals two million times fainter than a simulated star have been extracted using the Planetary Detection Testbed. The formation-flying testbeds are developing

the flight-like hardware and software components that will be needed to safely operate a multi-spacecraft interferometer with the necessary precision.

The scale of the TPF-I mission will be necessarily large, encompassing large cooled telescopes, multiple spacecraft operated in precision formation, and complex optomechanical systems. But the recent years of detailed study and technology development have revealed no fundamental impediments to carrying out TPF-I. The biggest risk this program faces is a highly uncertain funding environment over the next few years that threatens the steady technological progress that has been made.

Finally, it is important to note that the science and technology teams of the TPF Interferometer (NASA) and the Darwin mission (European Space Agency) continue to maintain an excellent working relationship. Both groups believe that it is in their mutual interest that the projects eventually be combined in a single mission under a Memorandum of Understanding signed between NASA and ESA. Such a formal working relationship is some years away, and in the meantime, each group is working separately to build support for their efforts within their own community, with TPF-I progressing towards the next Decadal Survey report and Darwin developing strong support within ESA's Cosmic Vision Program. Through efforts in the near term the technical teams of TPF-I and Darwin are collaborating to arrive at a common architecture for the interferometer.

With the strong public interest in the question of life beyond the Solar System, with the multi-disciplinary scientific interest in understanding the formation and evolution of life in environments different from our own, with the steady progress in key technologies, and with the promise of powerful capabilities for a broad range of astrophysical investigations, it seems inevitable that missions like TPF-I will, someday, be carried out.

Appendices

Appendix A
Technology Advisory Committee

Table A-1. TPF Technology Advisory Committee

Name	Institution
Ron Allen	Space Telescope Science Institute
Chris Burrows	Metajiva
Rich Capps	Jet Propulsion Laboratory
Dick Dyer	Schafer Corporation
Mike Krim	Perkin-Elmer, retired
Bruce MacIntosh	Lawrence Livermore National Laboratory
Pete Mason	California Institute of Technology
Dave Mozurkewich	Seabrook Engineering
Jason Speyer	UCLA

Appendix B
Flight System Configuration

Tables B-1 to B-5 describe the flight-system studied by the TPF-I design team in 2004. The interferometer under consideration was a four-telescope dual-Bracewell interferometer, depicted in Fig. 5-15.

Table B-1. Mission Summary

Parameter	Preliminary Requirements
Number of collector spacecraft	4
Number of combiner spacecraft	1
Design life	5 years
Mission orbit	L2 Halo
ΔV (TCMs and L2 injection)	105 m/s
Launch vehicle	Delta 4050H
Lift mass	9408 kg
Margin	30%

Table B-2. Design Team Power Allocations

DC Power	Collector	Combiner
Payload	75 W	475 W
Downlink	58 W	78 W
Housekeeping	537 W	557 W
Reserve	192 W	335 W
Total	862 W	1445 W

Table B-3. Design Team Mass Allocations

Mass	Collector	Combiner
Payload (each)	550 kg*	461 kg
Spacecraft (each)	605 kg	684 kg
Reserve (each)	276 kg	268 kg
Total (each)	1431 kg	1413 kg
Launch mass	5724 kg	1413 kg

*Collector payload includes a 391-kg primary mirror with an aerial density of 30 kg/m^2

Table B-4. TPF-I Combiner Spacecraft Design Summary

Parameter	Design Team Allocation
Architecture	Modular, process-driven, fully redundant
Attitude control	3-axis, zero-net-momentum
Attitude determination	Star trackers, inertial reference unit
Attitude control actuators	4 reaction wheels, 16 RCS thrusters
Formation acquisition sensors	S-band and sensors
Propulsion / RCS	Ion thrusters, Isp = 2500–3500 s
Delta-V capability	750 m/s
Solar array type / size	Rigid panel, 9.0 m^2
Solar cell type	Cascade multi-junction, 28% efficiency at beginning of life(BOL)
Array power at end of life (EOL)	1455 W (45° off-point)
Battery type / Capacity	Li-ion, 72.7 A-h
Thermal shield	5-layer, deployable sunshade
Telecommunications	X-band up / Ka and X-band down
Data rates up/down	2 kpbs / 1 Mbps (Ka-band) 16 kbps (X-band)
Inter-spacecraft telecommunications	UHF full-duplex, 2.0 Mbps

Table B-5. TPF-I Collector Spacecraft Design Summary

Parameter	Design Team Allocation
Architecture	Modular, process-driven, fully redundant
Attitude control	3-axis, zero-net-momentum
Attitude determination	Star trackers, inertial reference unit
Attitude control actuators	4 reaction wheels, 16 RCS thrusters
Formation acquisition sensors	S-band and sensors
Propulsion / RCS	Ion thrusters, Isp = 2500–3500 s
Delta-V capability	750 m/s
Solar array type / size	Rigid panel, 5.4 m^2
Solar cell type	Cascade multi-junction, 28% efficiency (BOL)
Array power (EOL)	862 W (45° off-point)
Battery type / Capacity	Li-ion, 19.8 A-h
Thermal shield	5-layer, deployable sunshade
Telecommunications	X-band up/down (contingency mode)
Data rates up/down	2 kbps / 16 kbps
Inter-spacecraft telecommunications	UHF full-duplex, 2.0 Mbps

Appendix C
Formation-Flying Algorithm Development

Formation Flying Control Architecture

Key requirement for the formation flying control architecture is to be scalable to more telescopes, yet robust while encompassing the traditional single spacecraft control functions and capabilities. This appendix describes details of the Formation and Attitude Control System (FACS) and the Formation Algorithms and Simulation Testbed (FAST).

The overall formation-flying control architecture, regardless of the specific implementation, retains the traditional single-spacecraft attitude estimation, attitude guidance, and attitude control functions within each spacecraft to allow for "standalone" mode, while providing a centralized "formation" guidance function on any of the selected spacecraft in formation, designated the formation "leader".

The leader/follower control architecture was selected for TPF-I since it is effective for smaller formations (~2–10 s/c) and its stability properties are well-understood. In the leader/follower architecture, the centralized "formation" guidance functions ensure resource-efficient, collision-free, and coordinated formation maneuvering across all spacecraft within the formation via leader (combiner) generated commands, which are communicated over the inter-spacecraft communication (ISC) links to all the follower spacecraft (collectors). During formation experiments, the centralized formation-guidance commands, once received over the inter-s/c communication links, are implemented locally on each spacecraft through a local six-DOF control function. In the event of ISC dropouts or failure, each spacecraft within the formation reverts back to local "standalone" on-board attitude control mode to maintain power-positive Sun-pointing, while still being capable of performance ground-commanded linear delta-V maneuvers. The overview of the formation-flying control architecture is shown in Fig. C-1 within context of the s/c uplink/downlink and the ISC. Key features of the FACS architecture are summarized below:

1. Hybrid Control Architecture
   a. Centralized translation guidance
   b. Decentralized attitude guidance
   c. Decentralized translation control
   d. Decentralized attitude control

2. Identical FACS flight software load on all S/C

    a. Each S/C FACS S/W is capable of taking on the formation leader/follower role.

Formation and Attitude Control System (FACS) Algorithms

Formation Estimator

The formation estimator optimally combines measurements from multiple sensors and produces estimates of different accuracy and bandwidth using an extended Kalman filter – to produce inter-s/c range and bearing estimates. In the case of the TPF-I mission, each of the spacecraft will have a variety of sensors for different phases of the mission. The formation-estimator algorithm will optimally combine the available sensor signals to provide the best inertial attitude estimate of each spacecraft and also the s/c-to-s/c relative position estimate. A high-level architecture and representative simulation is shown in Fig. C-2.

Formation estimation consists of estimating both local spacecraft attitude and the relative position of all the other spacecraft in the formation. The latter we refer to as translation estimation.

Attitude Estimation

The attitude estimator determines the attitude of a spacecraft body frame with respect to an inertial frame, given star tracker and gyroscope measurements. Each spacecraft estimates its own attitude, and only local information is required.

Estimation in general consists of a propagation step based on the physics-based dynamic model and an update step in which sensor measurements are combined with the propagated estimate. The spacecraft attitude depends on applied torques (e.g., from thruster and reaction wheels), which are governed by Euler's equations. Although Euler's equations are an accurate representation of the spacecraft dynamics, the input torques due to thruster firings are difficult to model. Hence, Euler's equations do not provide an accurate means of propagating the attitude states of the spacecraft. Instead a kinematic model is used (i.e., relating angular velocity to attitude) where the angular velocity is measured by the gyroscopes. The sensor measurement for the update step comes from the star tracker(s).

Another important aspect of the attitude estimation problem is that gyroscopes have biases. The bias of each gyroscope must be added to the attitude estimation problem to obtain accurate estimates. Combining a gyroscope model with the kinematic attitude equation, one can obtain an equation for the errors in the attitude and bias estimates. Based on the above model, an optimal Kalman estimator has been designed.

Translation Estimation

On each spacecraft the translation estimator estimates the position of every other spacecraft in the formation with respect to itself. One complication in relative translation estimation is that it is coupled one way to attitude estimation. Relative sensors provide measurements between sensor frames on respective spacecraft. However, since a center-of-mass to center-of-mass (CM) relative position vector is desired for control, the estimator must transfer from the two sensor frames (one on each spacecraft involved in the measurement) to an inertial frame. This transfer requires the attitudes of both spacecraft.
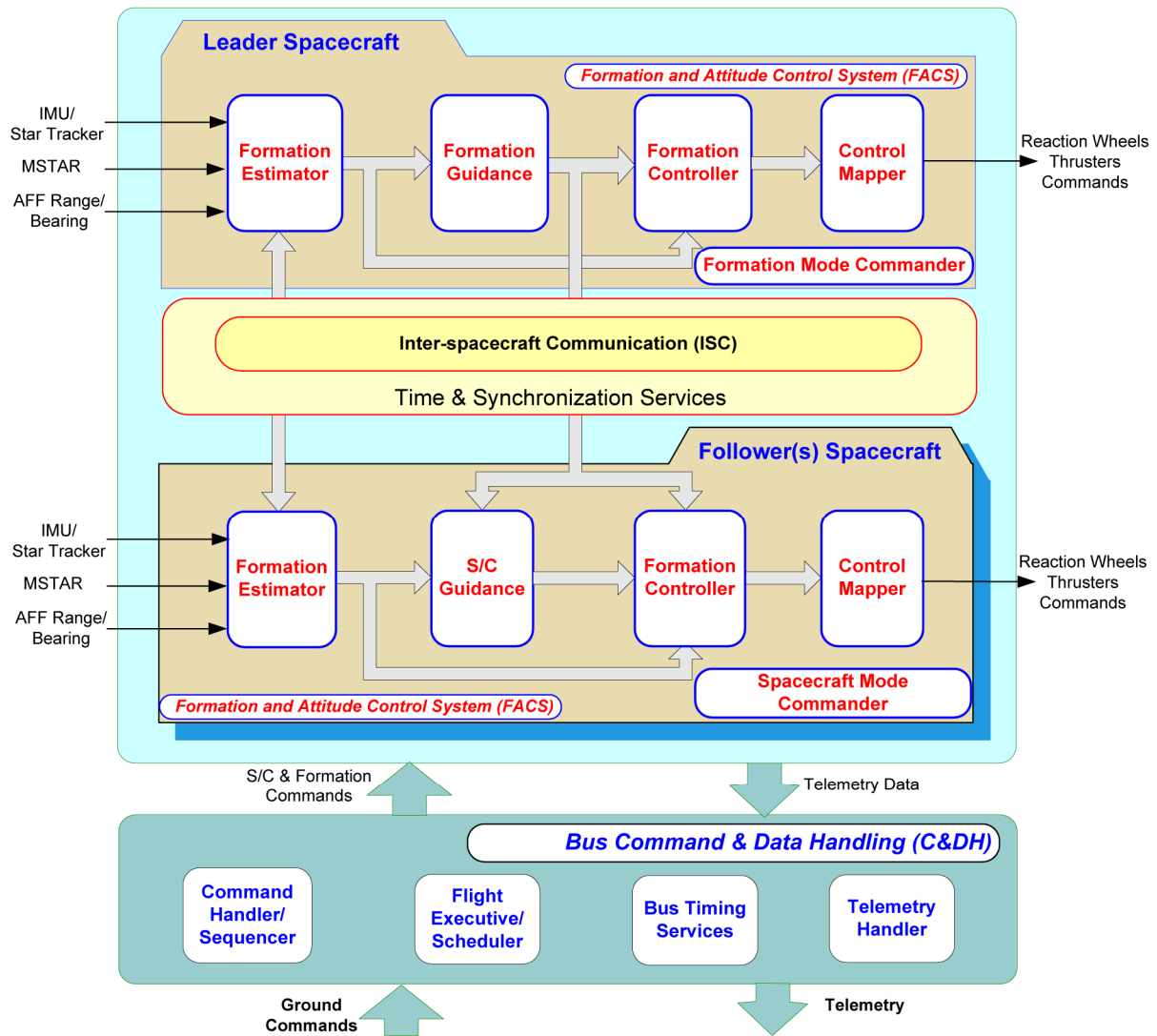
Figure C-1. Formation & Attitude Control System Architecture.

The measurement update for the translation estimator is much more complex than for the attitude estimator because there are three levels of inter-spacecraft sensing (acquisition, medium, and fine) and these measurements are in terms of range and bearings; whereas, the state is in terms of Cartesian relative position. Each sensor measurement must also be transformed.

The relative translation estimator has two components: 1) a Kalman filter; and 2) an acceleration data processing (ADP) algorithm, which produces bias-corrected CM acceleration estimates.

1. Including all the necessary transformations and incorporating communicated data, an optimal Kalman estimator has been designed for the translation degrees of freedom. As each more precise level of sensing is acquired, the error in the estimate decreases. With the precision sensors locked, the resulting error that has been simulated is on the order of a few tens of millimeters, which meets the requirements for TPF-I.

2. Recall that the coefficients needed for estimator propagation are the outputs of the ADP algorithm. The ADP takes the raw accelerometer measurements, corrects for accelerometer bias and the location of the accelerometer (when not at the spacecraft CM, accelerometers also sense centripetal acceleration), and rotates the acceleration into the inertial frame. The ADP serves two additional functions. First, when no thrusters are firing, it estimates the accelerometer bias. Second, when the thrust levels are very low and the accelerometer signal-to-noise ratio (SNR) is poor, the ADP estimates the acceleration based on thruster on-times.

Formation Guidance

For TPF-I there are three mission phases: formation acquisition, formation reconfiguration, and observation. Formation acquisition, also known as formation initialization, is the process of obtaining relative dynamic state information and establishing communication. It occurs after deployment or a fault condition. Formation reconfiguration moves the formation from one configuration to a new configuration. Reconfigurations occur after acquisition to move the formation to its initial science configuration, and after a science observation to retarget. Finally, the observation phase consists of rotating the formation as a rigid body and changing its baseline to synthesize a synthetic aperture. The observation phase is unique in that spacecraft attitudes must be synchronized with relative positions for the interferometer to operate. In each of these three phases, formation guidance must command the formation, that is, provide attitude and relative translation paths for all the spacecraft.

There are three main constraints that the attitude and relative translation paths must satisfy: the collision-avoidance constraint (CAC), the Sun-avoidance constraint (SAC), and the relative thermal constraint (RTC). For the CAC, exclusion spheres are placed around each spacecraft, and relative translation paths must not cause the spheres to intersect. The SAC protects the infrared optics. It requires the payload "boresights" to remain within a cone about the anti-Sun line.

Additionally, recall that TPF-I is an infrared interferometer. The optics are cooled to 40 K. The hot side of each spacecraft's sunshield is approximately 300 K. If the hot side of one spacecraft's sunshield were to illuminate the cold optics of another it would heat the optics. Then the formation would have to sit idle while the optics re-cooled. For each spacecraft, the RTC requires that relative position vector to the other spacecraft remain approximately 85° or more away from the sunshield normal. The RTC is a time-varying attitude constraint that depends on the relative positions of the formation.

Spacecraft (Attitude) Guidance

The attitude-guidance algorithms on each spacecraft are extensions of the attitude-guidance algorithm designed for the Cassini mission. On each spacecraft a base frame is defined by aligning (1) a body-fixed direction with an inertial direction, and (2) a second body fixed direction as much as possible with a second inertial direction. Attitude turns are then commanded by specifying a new attitude relative to either the current or base frame.

When a new attitude is commanded, the guidance first checks if the new attitude violates the SAC. If it does, the command is rejected. If not, then an attitude path is first planned based on an Euler turn. If during this turn the SAC is violated, then the turn is broken into three Euler turns that do not violate the SAC. This algorithm does not address the RTC. However, the RTC is only active after the spacecraft are in science
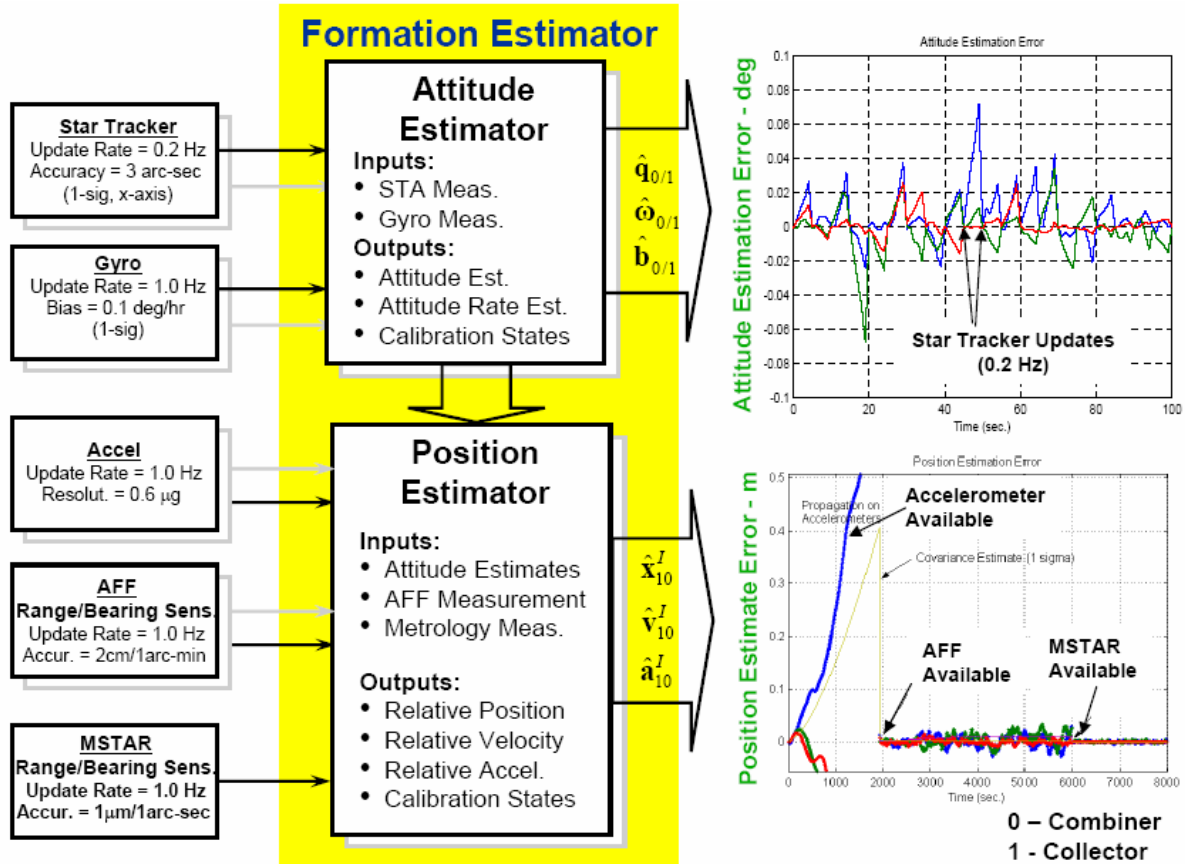
Figure C-2. Formation Estimator Architecture and representative results.

configuration. In science configuration attitude maneuvers are synchronized with relative positions so that the RTC is satisfied.

Translation Guidance

We consider each of the three mission phases. For formation acquisition, the baseline acquisition sensor has an unlimited FOV. Further, the baseline TPF-I design includes omni-directional communication. As a result, formation acquisition consists of turning these systems on. If there is an acquisition sensor antenna failure or a spacecraft occultation, then communication and relative sensing will not be immediately established. Deployment of spacecraft from the cruise stage can be planned to avoid occultations. In the event of an acquisition sensor antenna failure, the limited-FOV acquisition algorithm of Ploen et al. (2004) can be used. Another possibility may be that the spacecraft are out of range of their acquisition sensors. In this case, ground intervention is needed.

For *formation reconfiguration*, a general deep space, energy-optimal formation reconfiguration algorithm with collision avoidance has been developed (Singh et al. 2001). This algorithm does not address the RTC. However, the RTC is not active initially. Therefore, the algorithm of Singh et al. (2001) is used to plan trajectories to move the formation from its post-acquisition configuration to its initial science configuration.

179

Once the formation has assumed the *science configuration* and optics have cooled, the RTC is active. Reconfigurations are then needed to retarget the formation between observations. Planning coupled relative translation/attitude reconfigurations with an RTC is an open area of research. Therefore, for retargeting reconfigurations we rotate the formation as a virtual rigid body. This approach satisfies the CAC and RTC, and avoids communication and sensor occultations. Finally, since the initial baseline direction for a new science target is unconstrained, an Euler rotation of the formation, in which the individual spacecraft behave as if embedded in a virtual rigid body, can always be found that satisfies the SAC for the spacecraft.

In science configuration, each spacecraft aligns its payload boresight (body z-axis) with the formation boresight *s*. The collectors must also be aligned along the current baseline vector *b* with their body x-axes aligned with the baseline. When an initial baseline for Target 2 is specified, an Euler retargeting rotation can cause the aperture boresights to leave their SAC cones. However, when the initial baseline for Target 2 is free, an Euler rotation can always be found that satisfies the SAC during the entire retargeting. If a future mission operational design constrains the initial baseline for a new target, then a sequence of three Euler rotations can be found to satisfy the SAC. The algorithm for formation rotations is discussed in more detail as part of the observation phase.

For observations the formation must be rotated about the formation boresight vector, and attitudes must be synchronized with relative positions. For retargeting the formation can be rotated about an arbitrary axis, and there is no attitude/relative position synchronization requirement. As a result, the same relative translation guidance algorithm is used for both observation and retargeting rotations. Synchronized attitudes are achieved by commanding each spacecraft to align its body z-axis with the formation boresight and either (i) its body x-axis with the baseline vector or (ii) an assigned body vector with the direction to a neighboring spacecraft.

A formation rotation algorithm has been developed that rotates the formation about the energy-optimal point. The spacecraft travel on a polygonal approximation to arcs, where the number of polygonal segments is commandable.

Formation Controller

The Formation Controller controls the s/c and formation to follow the desired inertial attitude and formation range/bearing profiles as prescribed by formation guidance. The formation controller implements the desired path by computing and commanding the needed forces/torques to bus for mapping to available actuators. See the papers by Scharf et al. (2004) and Lurie (2003).

Attitude control (as opposed to guidance) is decoupled from relative translation control. Therefore, independent attitude controllers can be designed. Attitude control is completely decentralized.

In operation, each collector estimates its relative position with respect to the combiner and its inertial attitude. Based on relative translation guidance from the combiner and local attitude guidance, each follower's controllers drive performance errors to within the requirements. The combiner controls its attitude and applies feed-forward accelerations as dictated by formation guidance.

There is an important, non-standard constraint on relative position and attitude control. Observations are performed entirely using thrusters. Since the thrusters are not throttle-able, their firing can cause spacecraft

vibrations that interrupt the interferometer. To allow for both actuation and science, all thrusters on all spacecraft for both attitude and relative position control may only fire in a 6 s window every 54 s. Data gathering occurs during the 54 s between thruster firing windows. This requirement is referred to as the thruster synchronization constraint (TSC).

For control design, both relative translation and attitude dynamics are well approximated by independent double integrator models. Relative translation control design is simplified since TPF-I will be in orbit about a Sun-Earth Lagrange point. In these orbits, the relative translation dynamics are well approximated by decoupled double integrator models (Scharf et al. 2002). Similarly, since the TPF-I spacecraft are three-axis stabilized, have small off-diagonal inertias, and rotate slowly, the small angle approximation is valid. In this approximation, the attitude quaternion is decomposed into independent body axis angle errors, and the dynamics of each angle error are approximated by a double integrator model. Since each relative translation and rotational degree of freedom is modeled by a double integrator, one SISO controller can be designed for all degrees of freedom and then scaled to the correct double integrator model (e.g., by multiplying by the inertia about a principal axis).

Since the attitude and translation dynamics have the same control design model and constraints, we used the same design process for each as described next.

Control design is done via a classical approach augmented with nonlinear dynamic compensation (Lurie 2003). A controller is divided into two parts: a fast controller that runs at the 1 Hz FACS rate, and a slow controller that runs at 1/60th of a Hertz. The slow controller output is scaled and applied over 4 s of the 6 s window with 2 s reserved for margin. Both controllers are stable individually and in parallel. Switching between the fast and slow controllers is done using non-linearities in the controller, and so no additional mode commander is necessary. The fast controller turns off when the position tracking error is small. Then actuation only occurs every 60 seconds per the RTC. There may be regions of the phase space where no control is active. The current design is such that the maximum drift time is 17 s. These regions could be removed at the cost of increased controller complexity, but the regions do not affect steady-state tracking performance.

The fast controller is a PD with nonlinear dynamic compensation and includes rate limits in the event of large tracking errors. The slow controller is a PID and also has nonlinear dynamic compensation. The nonlinear compensation in both the fast and slow controllers allows a conditionally stable loop to be designed that is stable in the event of saturations. In effect, high gain controllers have been designed based on the Bode integral constraints that reduce their gain as tracking errors become large.

The control design was simulated to demonstrate its performance. The scenario considered was the control of a collector during an observation with a formation rotation period of 48 hours and the formation plane perpendicular to the Sun-line. Recall that during an observation the spacecraft are traveling on a circle and rotating about their body z-axes to keep their body x-axes aligned with the formation baseline. Therefore, the attitude commands, which are in the body frame, are zero in the body x- and y-axes and a ramp in the body z-axis. Relative translation commands, which are in the inertial frame, are sinusoids in the inertial x- and y-axes, and zero in the inertial z-axis. For convenience, the inertial x-y plane has been chosen to coincide with the formation plane. The full simulation model includes: (i) actuator misalignments of 10 arcsec, (ii) estimation noise based on the estimator performance, (iii) an extra delay of one RTI, (iv) a sunshield mode at 0.48 Hz, (v) a solar torque of 0.15 mN m about the body x-axis and a differential solar
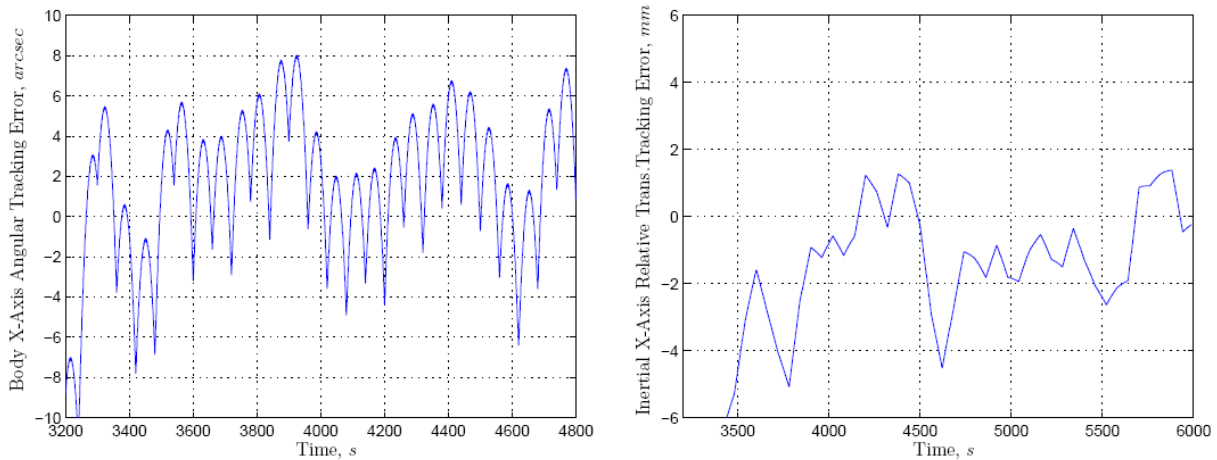
Figure C-3. Example of controller tracking error for both attitude and translation control, the TPF-I requirements can be met with the TSC.

pressure of 0.5 mN in the inertial z-axis, (vi) mass and inertia uncertainties of 3%, and (vii) kinematic decoupling errors, which result from realizing inertial force commands with body-fixed thrusters and imperfect attitude knowledge. To ensure performance with margin, the solar-induced disturbances are larger than will be expected in practice.

The steady-state simulation results are given in Fig. C-3, which show, respectively, the body x-axis angular tracking error and the inertial x-axis relative translation tracking error. There is a considerable transient (not shown) due to the low bandwidth of the controllers required by the TSC. However, the transient will be reduced when the controllers are integrated with the formation guidance, which provides feed-forward accelerations.

Mode Commander (Formation/S/C)

The Mode Commander (MDC) coordinates the algorithms with the current mission phase and hardware capabilities. For example, it lets the FACS algorithms know when the star tracker can provide measurements or when all spacecraft are ready for a synchronized rotation for covering the *u-v* plane. All FACS modes are contained within the two main modes (namely "standalone" and "formation") and these two nodes enable the end-to-end operations of the FACS across all mission phases, including the various anticipated system hardware configurations.

In standalone mode, each of the spacecraft in TPF-I formation can perform basic system checkout at a safe separation. Upon successful spacecraft system checkout, the spacecraft will be ground commanded to a closer range, within the formation sensor acquisition range (nominally at 10 km), while still in standalone operational mode. At this closer range, the ISC and formation sensors signals are to be acquired. Once formation knowledge and inter-s/c communication is established, the flight system can be commanded to enter the formation operational mode.

While in the formation mode, the spacecraft within the TPF-I formation can be ground commanded to re-configure to any desired safe formation separation. While in formation mode, a loss of ISC or range and bearing (spacecraft-to-spacecraft position) knowledge will result in automatic transition back to the

standalone operational mode to allow for safe operations. Similarly, attitude knowledge loss of partner's attitude, while still having range/bearing knowledge, will result in precautionary safing of self while still maintaining the formation operational mode.

At any time, while in either cluster or separated configuration, loss of spacecraft attitude knowledge will result in an attempt to regain inertial knowledge by nulling any residual attitude rates and acquisition of celestial and inertial attitude sensors.

Control Mapper

The control allocator takes the requested force and torque from the controller and generates low-level commands to the thrusters and/or reaction wheels. Forces can only be implemented by the thrusters. Torques can be implemented by thrusters, reaction wheels, or a combination of both. The current FACS control allocator allows torques to be implemented by only thrusters or only reaction wheels. This limitation is more operational, and if blended thruster/reaction wheel torques are desired (e.g., in the event of multiple reaction wheel or thruster failures), the FACS control allocator could be extended. If torques are generated by reaction wheels, the commanded torques are simply passed to the reaction wheels. As such, the principal FACS control allocator algorithm takes forces and torques to thruster on-times.

The thruster allocation problem is formulated as a convex optimization problem by minimizing a cost function consisting of force and torque errors and a weighted sum of thruster on-times. The latter creates the convexity of the cost function and is a measure of the fuel consumed. The constraints are that the on-time for each thruster must be between a high and low value. This constraint is also convex as desired. Using the problem structure, a gradient descent algorithm is used to solve the constrained optimization problem. Hence, if the thrust allocation algorithm is interrupted in real-time while it is optimizing, the current value of thruster on-times in the optimization will be better than the previous value. The gradient descent starts at the unconstrained solution, which can be determined analytically.

FAST – Distributed Real-Time Simulation

The Formation and Algorithms and Simulation Testbed (FAST) is a hard real-time, distributed simulation environment for precision formation algorithm design and validation. FAST is built upon several PowerPC 750 flight-like processors running a flight-qualified, real-time OS. (The Mars Reconnaissance Orbiter is currently flying the radiation-hardened version of the PPC 750.) A ground console is used for commanding a formation and for processing the telemetry. The dynamics of spacecraft, sensors, actuators, up-links, down-links, and inter-spacecraft communication are also simulated on distributed processors using the Hierarchical Distributed Re-configurable Architecture (HYDRA) simulation environment (Martin et al. 2003). In particular, the dynamics of each spacecraft are integrated on separate processors, thereby enabling a fully scalable, distributed simulation architecture. With the open-architecture HYDRA, FAST can be used to simulate a five-spacecraft formation in low-Earth orbit or, with the addition of processors, a thirty-spacecraft formation in deep space. Furthermore, the distributed architecture enforces truly distributed algorithms and prevents inadvertent data sharing.
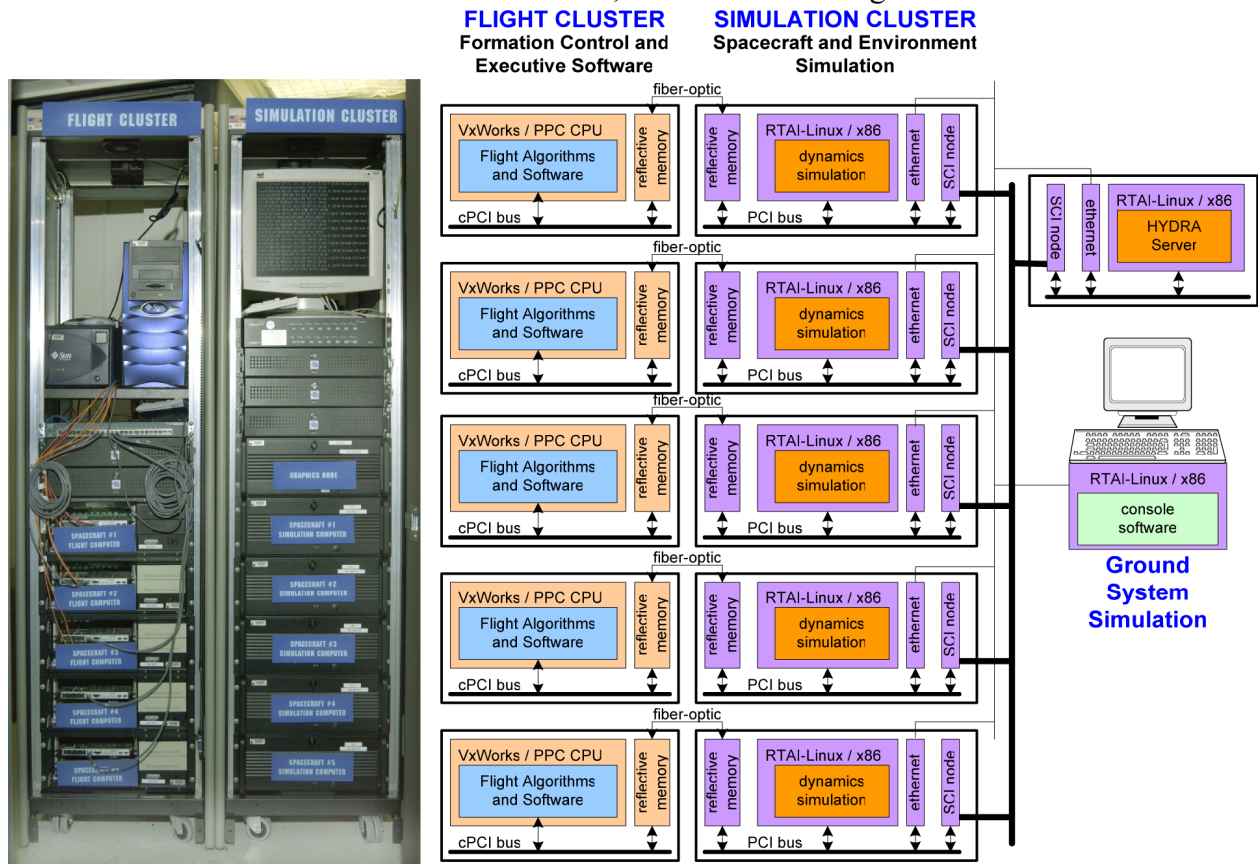
Figure C-4. FAST Flight and simulation clusters (left) and schematic (right).

The FAST configuration is representative of one that would be used in a flight project to test and debug the real-time flight code before proceeding to full flight-system testing. Essentially an extension of a single-spacecraft flight software testbed to formations, FAST can evaluate end-to-end performance, functionality, and long-term robustness of precision formations.

The next section presents the FAST hardware in detail. Then, the functional architecture of FAST is discussed, including HYDRA and its distributed timing architecture. Next, the software executive and the FACS currently used in FAST are reviewed. Finally, two-spacecraft distributed interferometer and two-robot FCT simulation results are given.

FAST Functional Architecture

The functional architecture of FAST is shown in Fig. C-4. The five spacecraft computers are shown, each hosting a software executive and formation software. The formation software on each spacecraft computer is referred to as a Formation and Attitude Control System (FACS), described previously. The simulation computers have models for sensors, actuators, spacecraft dynamics, environmental forces, and communication. Standard single-spacecraft actuators, sensors, and uplink/downlink models are included. For formations, additional models for inter-spacecraft communication (ISC) and relative sensing are

required. Relative sensing and ISC are the unique hardware models that couple individual spacecraft simulations. This coupling differentiates a formation simulator from a constellation simulator.

As the number of spacecraft in a formation increases, the overhead required to manage communication and synchronization between distributed simulation components grows rapidly. A scalable, flexible, and easily extensible architecture is needed to automate communication and manage connections between distributed applications. HYDRA automates the connection of distributed simulation elements using a publish–subscribe, client-server paradigm. As each client application is started, it provides the HYDRA server with a list of offered and desired services. The HYDRA server commands two clients to form a connection when they have advertised compatible services. Adding a simulated spacecraft to the formation only requires starting up another spacecraft client. HYDRA allows the user to override default behaviors at several layers. While HYDRA is similar to other distributed architectures (such as CORBA and HLA), it was specifically designed for the needs of high-speed, distributed simulation.

In HYDRA, client applications communicate through connectors that abstract message passing over a variety of protocols and infrastructure, including Scalable Coherent Interface (SCI) and transmission control protocol/internet protocol (TCP/IP). Each spacecraft simulation in FAST is a HYDRA client. A sixth simulation computer functions as the HYDRA server. All clients register with the server over the Ethernet local-area network (LAN). The majority of inter-process communication in is handled by HYDRA, including:

1. ISC traffic over the SCI connection,

ii) 2. Uplink, downlink, time coordination, and relative sensor traffic over Ethernet, and

3. Inter-process traffic within a computer. Simulation computer-to-spacecraft computer traffic over the fiber-optic reflective memory cards is controlled via an interface specification.

Each simulation computer simulates the dynamics for only its associated spacecraft. The spacecraft dynamics are integrated using the Dynamics Algorithms for Real-Time Simulation (DARTS) software package (Jain and Rodriguez 1992). DARTS is a multi-platform software library written in C and is based on spatial operator algebra. It provides efficient numerical algorithms for both rigid-body and flexible-body dynamics. Spacecraft mass and inertia properties are input to DARTS using a Tool Command Language (TCL) script. A lightweight interface to DARTS provides external actuator and sensor models access to force and torque inputs and state outputs. A numerical integrator is used to propagate the system state based on accelerations computed by DARTS. FAST currently provides either a fixed-step, fourth-order Runge-Kutta integrator or the variable-step CVODE integrator (Cohen and Hindmarch 1996). The fixed step integrator provides real-time, deterministic performance while the variable step integrator provides higher accuracy.

A critical function of HYDRA is the synchronization of the separate spacecraft simulations for relative sensing (Sohl et al. 2005). Specifically, relative sensing requires synchronization of the dynamics integrators running on separate computers to provide consistent state information at a given time. A second crucial function coupled to state synchronization is the simulation of local spacecraft clocks (SCLKs). Spacecraft clocks are used to time-tag measurements and initiate digital control cycles. As spacecraft clocks will have different offsets and drifts, control cycles on spacecraft will start at different true times and will move with respect to one another. In addition, ISC will have jitter and dropouts. These characteristics must be accurately simulated to evaluate formation robustness.

The "true" time of the simulation environment is based on the processor clock of the HYDRA server. This clock is synchronized to the JPL GPS-based Network Time Protocol (NTP) server to within 1 ms.

Each spacecraft also has its own local concept of time. The processor clock of the associated simulation computer serves as the basis of local time. These processor clocks are synchronized to the HYDRA server clock's true time via NTP. The processor clock of a simulation computer drives the local SCLK model, which adds an offset and a drift. All interrupts required by the software executive and formation software are based on the SCLK time and are provided by the simulation computer as interrupts across the reflective memory interface. This timing architecture emulates an actual formation of disparate spacecraft. A control cycle with a desired duration of 1 s can be 0.995 s on one spacecraft and 1.005 s on another.

The SCLK time is also used to control the local numerical integrator. This design allows all local sensor and actuator rates to be based on the local SCLK as they would be in practice. However, as a formation simulation progresses through M seconds, some spacecraft would have integrated $0.995M$ of true time and others $1.005M$. To eliminate this problem, the Timing Coordinator on the HYDRA server sends a pulse every second of true time. When the coordination pulse arrives, the drift of the local SCLK with respect to true time is determined. Subsequent integration intervals are updated to reflect this drift. For example, assume a SCLK runs 5% faster than true time. If the local integrator needs to advance 0.1 s, then the integration actually propagates only 0.095 s of SCLK time forward.

Since the simulation computers provide timers and interrupts to the spacecraft computers, simulation can be accelerated while maintaining real-time accuracy. Real-time execution of the entire formation is scaled by appropriately scaling the pulse per second (PPS) in the Time Coordinator. Note that all real-time deadlines are still enforced; only the entire schedule has been compressed. Formation-flying maneuvers will often require hours to execute; we have been able to compress the nominal 1-Hz control cycle rate of FACS by up to a factor of 32. This capability has significantly increased the usability of FAST.

Formation Software

The FAST was developed using a process similar to what might be found on a flight project. The top-level software architecture has four components.

1) Ground console for commanding the formation and receiving telemetry;

2) Simulation.

3) Flight-like software component of FAST consists of the Formation and Attitude Control System (FACS); and

4) Software Executive (SE).

The use of the shared memory interface between the SE and the simulation environment is controlled by an interface specification, allowing different formation control systems to be designed, coded, and tested.

The FACS includes (i) a mode commander block with supervisory logic for coordinating high-level functions such as detumbling and formation acquisition, (ii) a guidance block providing constrained attitude and formation path-planning and collision avoidance, (iii) a formation and attitude estimator block, (iv) an attitude and formation controller block using a leader/follower architecture and providing a synchronized actuation capability for disturbance reduction, and (v) a thruster allocator to map force and

186

torque commands into thruster and reaction wheel commands. The FACS software is the same for all spacecraft, and so any spacecraft can assume the role of leader in the formation-control architecture.

The FAST will be validated by simulating FCT formation scenarios. The FACS residing on the FCT robots has two additional subsystems, an absolute translation system (ATS) for positioning the robots independently on the experiment floor, and a formation drift controller (FDC) that keeps the formation approximately centered on the experiment floor without affecting formation performance. A secondary mode commander, called the FCT-FACS MDC, coordinates these additional subsystems. The ATS uses raw sensor data, and so it does not require an estimator.

The Software Executive (SE) provides a flight-like environment for execution of the FACS and is designed to support a wide variety of formation-control architectures and algorithms. The SE provides commanding, telemetry handling, device-level communication, inter-spacecraft communication, and scheduling within the real-time VxWorks operating system. A TCL command interpreter functions as the command executive. The formation-control algorithms are also commanded via TCL commands. These commands are simple to implement, and we have found that adding new commands can be done in less than an hour. Telemetry is available in ASCII or binary format, and the process for generating telemetry has been automated in Matlab. In addition, telemetry identifiers, telemetry generation, telemetry decoding, and telemetry display code are all automatically coded from a telemetry specification written in a standard spreadsheet tool. We are able to automatically code the memory map describing the interface between the simulation and the VxWorks hardware boards, again based on a spreadsheet specification. The auto-coding tools were written in Java.

Two crucial services provided by the SE are spacecraft-to-spacecraft clock offset estimation and control-cycle synchronization. Clock offsets are necessary for formation estimation. Control-cycle synchronization, which is the process of making control cycles on separate spacecraft start at the same true time, is required for the highest precision formation control. By using time echo packets similar to NTP, the SE Time Manager determines the clock offsets between spacecraft. Then, each spacecraft communicates the time at which its most recent control cycle started. With this data the SEs determine the amount to lengthen their control cycles. No shortening is allowed. The SEs then command their SCLKs to appropriately delay the next control-cycle interrupt to bring all the control cycles into synchronization. For example, if control cycles are 1 s in duration and SC1's control cycle starts 100 ms before SC2, then the SE on SC1 would command the SCLK to send the next control cycle interrupt in 1.1 s. A refined version of this basic scheme has been implemented wherein the control cycles are resynchronized periodically. In steady state with no additional SCLK drift added to the inherent processor clock drift, cycle shifts are on the order of a few milliseconds.

The SE also hosts the ISC manager. Currently, a time division multiple access (TDMA) architecture is implemented for sharing the wireless link between the ISC, the console uplink and downlink, the time-echo packets, and the control cycle synchronization messages. Existing communication protocols (such as TCP and user datagram protocol (UDP)) are not satisfactory since TCP can disrupt real-time performance through continual packet resends, and UDP is not robust to packet drops. A new protocol was developed called real-time UDP that adds timeouts and a limit to packet resends.

References

Cohen, S., and Hindmarsh, A., "CVODE, a Stiff/Nonstiff ODE Solver in C," *Computers in Physics* **10** (2), 138–143 (1996).

Jain, A., and Rodriguez, G., "Recursive Flexible Multibody System Dynamics Using Spatial Operators," *Journal of Guidance, Control and Dynamics* **15**, 1453–1466 (1992).

Lay, O. P., and Blackwood, G. H., "Formation-Flying Interferometry," *Interferometry in Space*, edited by M. Shao, *Proc. SPIE* **4852**, 481–491 (2003).

Lurie, B., "Multi-Mode Synchronized Control for Formation Flying Interferometer ," *AIAA Guidance, Navigation, and Control Conference*, Austin, TX, 11–14 August 2003, paper 5365 (2003).

Martin, B. J., and Sohl, G. A., "HYDRA: High-Speed Simulation Architecture for Precision Spacecraft Formation Simulation," *AIAA Modeling and Simulation Technologies Conf.,* Austin, TX, 11–14 August, paper 5380 (2003).

Ploen, S. R., Scharf, D. P., Hadaegh, F. Y., and Bikdash, M., "Guaranteed Initialization of Distributed Spacecraft Formations," *Journal of the Astronautical Sciences* **52** (4), 495–515 (2004).

Scharf, D. P., Acikmese, A. B., Ploen, S. R., and Hadaegh, F. Y., "A Direct Solution for Fuel-Optimal Reactive Collision Avoidance of Collaborating Spacecraft," *American Control Conference*, Minneapolis, MN, 14–16 June (2006).

Scharf, D. P., Hadaegh. F. Y. and Kang, B. H., "On the Validity of the Double Integrator Approximation in Deep Space Formation Flying," *First International Symposium on Formation Flying Missions and Technologies*, Centre National d'Etudes Spatiales, Toulouse, France, (Oct. 29–30, 2002).

Scharf, D. P., Hadaegh, F. Y., Rahman, Z. R., Shields, J. H., Singh, G., and Wette, M. R., "An Overview of the Formation and Attitude Control System for the Terrestrial Planet Finder Formation Flying Interferometer," *2nd International Symposium on Formation Flying Missions and Technologies*, Washington, D.C. (September 2004).

Scharf, D. P., Ploen, S. R., Hadaegh, F. Y., and Sohl, G. A., "Guaranteed Spatial Initialization of Distributed Spacecraft Formations," *AIAA Guidance, Navigation and Control Conference*, Providence, RI, 16–19 August 2004, paper 4893 (2004).

Singh, G., and Hadaegh, F. Y., "Collision Avoidance Guidance for Formation-Flying Applications," *AIAA Guidance, Navigation, and Control Conference,* Montreal, PQ, 6–9 August, paper 4088 (2001).

Sohl, G. A., Udomkesmalee, S., and Kellogg, J. L., "Distributed Simulation for Formation Flying Applications," *AIAA Modeling and Simulation Technologies Conference*, San Francisco, CA, 15–18 August 2005, paper 6494 (2005).

Appendix D
Acronyms

ACS	Attitude Control System
AdN	Adaptive Nuller Testbed
ADP	acceleration data processing (algorithm)
AFF	autonomous formation flying
AGB	asymptotic giant branch
AgCl	silver chloride
AGN	Active Galactic Nucleus (or Nuclei)
ALMA	Atacama Large Millimeter Array
ANT	Achromatic Nulling Testbed
AO	adaptive optics
Ar	argon
ARR	Assembly Readiness Review
ASO	Astronomical Search for Origins
ATLO	Assembly, Test, and Launch Operations
ATS	absolute translation system
AU	astronomical unit; approximately the mean distance between the Earth and the Sun
BC	beam combiner
BL	baseline
BOL	beginning of life
CAC	collision-avoidance constraint
CCD	charged couple device
CCl_2F_2	freon 13
CCL_3F	freon 12
CDR	Critical Design Review
CG	center-of-gravity
CH_3Cl	methyl chloride
CH_4	methane
CIRS	Composite Infrared Spectrometer (on the Cassini mission)
CM	center of mass
CMC	center-of-mass to center-of-mass (relative position)
CNES	Centre National d'Etudes Spatiales
CO_2	carbon dioxide
CoRoT	Convection Rotation and Planetary Transits (CNES, France)
CTE	coefficient of thermal expansion
DAC	degenerate Angel cross
DARTS	Dynamics Algorithms for Real-Time Simulation

DC	direct current
DCB	dual chopped Bracewell
DM	development model
DM	deformable mirror
DOCS	Dynamics Optics Controls Structures
DOD	Department of Defense
DOF	degrees of freedom
DST	Distributed Spacecraft Technologies
EIRB	External Independent Readiness Board
ELT	Extremely Large Telescope (approximately 30-m diameter or larger aperture)
EM	engineering model
EMFF	electromagnetic formation flying
EOL	end of life
ESA	European Space Agency
ESTEC	European Space Research and Technology Centre
ExNPS	Exploration of Neighboring Planetary Systems
EZ	Exozodiacal (dust emission)
FACS	Formation & Attitude Control System software
FAST	Formation Algorithms and Simulation Testbed
FCT	Formation Control Testbed
FDC	formation drift controller
FDDS	Formation Dynamics and Devices Simulation software
FF	formation flying
FFI	formation-flying interferometer
FGS	Fine Guidance Sensor
FFTL	Formation Flying Technology Laboratory
FIRES	Faint Infra Red Extra-galactic Survey
FIT	Formation Interferometer Testbed
FOR	field of regard
FOV	field of view
FST	Formation Sensor Testbed
FTS	Fourier-transform spectrometer
FWHM	full width at half maximum
FY	fiscal year
GAC	generalized Angel cross
G&C	guidance and control
GPS	Global Positioning System
GSFC	Goddard Space Flight Center
H_2	hydrogen
H II	ionized hydrogen (regions)
HST	Hubble Space Telescope
H_2O	water
HQ	Headquarters
H_2S	hydrogen sulfide
HYDRA	Hierarchical Distributed Re-configurable Architecture
HZ	Habitable Zone
Hz	hertz

190

IHZ	Inner Habitable Zone
IMF	initial mass function
IMOS	Integrated Modeling of Optical Systems
IMU	inertial measurement unit
IO	integrated optics
IPM	Interferometer Performance Model
IR	infrared
IRAC	Infrared Array Camera (on Spitzer Telescope)
IRAS	Infrared Astronomical Satellite
IRS	infrared spectrograph (on Spitzer Space Telescope
ISAMS	Improved Stratospheric and Mesospheric Sounder
ISAAC	Infrared Spectrometer and Array Camera
ISC	inter-spacecraft communication
ISM	interstellar medium
ISO	Infrared Space Observatory
I&T	integration and test
IWA	inner working angle
JCMT	James Clerk Maxwell Telescope
JPL	Jet Propulsion Laboratory
J-T	Joule-Thomson
JWST	James Webb Space Telescope
kHz	kilohertz (1000 Hz)
KI	Keck Interferometer
L2	Sun-Earth Lagrange-2 point
LAMP	Laser-Augmented Mobility Power
LADAR	laser detection and ranging
LAN	local-area network
LBT	Large Binocular Telescope
LBTI	Large Binocular Telescope Interferometer
LBV	Luminous Blue Variable
LISA	Laser Interferometer Space Antenna
LMC	Large Magellanic Cloud
LRR	Launch Readiness Review
mas	milli-arcsecond
MACHO	massive astronomical compact halo object
MDC	mode commander
MATLAB	Matrix Laboratory
MIPS	Multiband Imaging Photometer for SIRTF
MIR	mid-infrared
MIRI	Mid-Infrared Instrument (for JWST)
MIT	Massachusetts Institute of Technology
MiXI	Miniature Xenon Ion thruster
M_{Ju}	Jupiter mass
MMZ	Modified Mach-Zehnder (design)
MS	main sequence (stars)
$M_{\oplus}$	Earth mass

NaCl	sodium chloride
NAR	Non-Advocate Review
NASA	National Aeronautics and Space Administration
NASTRAN	NASA Structural Analysis Program
Ne	neon
NGST	Northrop Grumman Space Technology
NICMOS	Near Infrared Camera and Multi-Object Spectrometer
nm	nanometer (10^{-9} meters)
N_2O	nitrous oxide
NRA	NASA Research Announcement
NRL	Naval Research Laboratory
NTP	Network Time Protocol
O_2	oxygen
O_3	ozone
OB association	association of spectral class O and B stars
ObSim	Observatory Simulation model
OPD	optical path difference
OASES	Outpost for the Analysis and Spectroscopy of Exoplanetary Systems
OPD	optical path difference
OWA	outer working angle
PAH	polycyclic aromatic hydrocarbons
PAL	present atmospheric level
pc	parsec (3.259 light-years, or 30.83×10^{12} km)
PCI	peripheral communications interconnect local bus
PDR	Preliminary Design Review
PDT	Planet Detection Testbed
PI	principal investigator
PMSR	Preliminary Mission Systems Review
POP	Program Operating Plan
ppb	parts per billion
PPS	pulse per second
PRIMA	Phase-Referenced Imaging and Micro-arcsecond Astrometry
PSD	power spectral density
PSE	planetary signal extraction
PSF	point spread function
PSR	Pre-Ship Review
P-V	peak to valley
QE	quantum efficiency
R&A	research and analysis
RCS	Reaction Control System
RF	radio frequency
RFI	Request For Information
RFP	Request for Proposal
RMS, rms	root mean-square
R/T	near reflection/transmission (ratio)
RTC	relative thermal constraint

RWA   reaction wheel assembly

S   sulfur
SAC   Sun-avoidance constraint
SBIR   Small Business Innovative Research
SCI   structurally connected interferometer
SCI   Scalable Coherent Interface (protocol)
SCLKs   simulation of local spacecraft clocks
SCUBA   Submillimetre Common-User Bolometer Array (on the JCMT in Hawaii)
SE   Software Executive
Si:As   silicon:arsenic
SiC   silicon carbide
SIRTF   Space Infrared Telescope Facility (now Spitzer Space Telescope)
SIM   Space Interferometry Mission
S/N   signal-to-noise ratio
SNR   signal-to-noise ratio
SPIE   International Society for Optical Engineering
SWG   Science Working Group

TAU   Tel Aviv University
TCL   Tool Command Language
TCP/IP   transmission control protocol/internet protocol
TDMA   time division multiple access
TMA   tertiary mirror assembly
TOM   thermo-optical mechanical
TOO   target of opportunity
TPF   Terrestrial Planet Finder
TPF-C   Terrestrial Planet Finder Coronagraph
TPF-I   Terrestrial Planet Finder Interferometer
TRL   technology readiness level
TRP   Technology Review Panel
TSC   thruster synchronization constraint

UA   University of Arizona
UDP   user datagram protocol
u-v   spatial frequency coordinates, in wavelengths

VLA   Very Large Array, National Radio Astronomy Observatory
VLT   Very Large Telescope, European Southern Observatory
V&V   verification and validation

WFE   wavefront error
WFS   wavefront sensor
WFS&C   wavefront sensing and control
WIIT   Wide-field Imaging Interferometry Testbed

YSO   young stellar objects

Appendix E
TPF-I Review Papers

The following publications provide a broad overview of progress with technology development for TPF-I since 2002. The papers are listed in reverse chronological order.

Lawson, P. R., Ahmed, A., Gappinger, R. O., Ksendzov, A., Lay, O. P., Martin, S. R., Peters, R. D., Scharf, D. P., Wallace, J. K., and Ware, B., "Terrestrial Planet Finder Interferometer: Technology status and plans," *Advances in Stellar Interferometry*, *Proc. SPIE* **6268**, edited by J. D. Monnier, M. Schöller, and W. C. Danchi, 626828 (2006).

Beichman, C., Lawson, P., Lay, O., Ahmed, A., Unwin, S., Johnston, K., "Status of the Terrestrial Planet Finder Interferometer," *Advances in Stellar Interferometry*, *Proc. SPIE* **6268**, edited by J. D. Monnier, M. Schöller, and W. C. Danchi, 62680S (2006).

Henry, C., "Terrestrial Planet Finder Interferometer 2005: Overview of system design studies and technology development," in *Techniques and Instrumentation for Detection of Exoplanets II*, edited by D. R. Coulter, *Proc. SPIE* **5905**, 1–7 (2005).

Henry, C., Lay, O. P., Aung, M., Gunter, S. M., Dubovitsky, S., and Blackwood, G. H., "Terrestrial Planet Finder interferometer: Architecture, mission design, and technology development," *New Frontiers in Stellar Interferometry*, *Proc. SPIE* **5491**, edited by W. A. Traub, 265–274 (2004).

Blackwood, G. H., Serabyn, E., Dubovitsky, S., Aung, M., Gunter, S. M., Henry, C., "System design and technology development for the Terrestrial Planet Finder infrared interferometer," *Techniques and Instrumentation for Detection of Exoplanets*, *Proc. SPIE* **5170**, edited by D. R. Coulter, 129-143 (2003).

Beichman, C. A., Coulter, D. R., Lindensmith, C., Lawson, P. R., "Selected mission architectures for the Terrestrial Planet Finder (TPF): Large, Medium, and Small," *Future Research Direction and Visions for Astronomy*, *Proc. SPIE* **4835**, edited by A. M. Dressler, 115–121 (2002).

Appendix F
Contributors and Credits

The editors are grateful to the individuals who were responsible for specific chapters, as listed below.

Introduction

Charles Beichman, California Institute of Technology
Kenneth J. Johnston, U.S. Naval Observatory
Peter R. Lawson, Jet Propulsion Laboratory
Oliver P. Lay, Jet Propulsion Laboratory

Exoplanet Science

Charles A. Beichman, California Institute of Technology
Kenneth J. Johnston, U.S. Naval Observatory
John Bally, University of Colorado
David Crisp, Jet Propulsion Laboratory
Lisa Kaltenegger, Smithsonian Astrophysical Observatory
Peter R. Lawson, Jet Propulsion Laboratory
Oliver P. Lay, Jet Propulsion Laboratory
Huub Röttgering, University of Leiden
Eugene Serabyn, Jet Propulsion Laboratory

Transforming Astrophysics with TPF-I

John Bally, University of Colorado
Huub Röttgering, University of Leiden
Charles Beichman, California Institute of Technology
Maria-Rosa Cioni, University of Edinburgh, UK
Malcolm Fridlund, European Space Agency
Roland den Hartogg, European Space Agency
Jan-Willem den Herder, Space Research Organization Netherlands
M. Hoogerheijde, University of Leiden
Ivo Labbé, Carnegie Observatories, Pasadena
Oliver Lay, Jet Propulsion Laboratory
Réne Liseau, Stockholm University

Alice Quillen, University of Rochester
Stephen Serjeant, The Open University, Milton Keynes, UK
C. P. de Vries, Space Research Organization Netherlands
Rachel Webster, Michelson Science Center

Design and Architecture Trade Studies

Oliver P. Lay, Jet Propulsion Laboratory
Stefan Martin, Jet Propulsion Laboratory
Benjamin Lane, Massachusetts Institute of Technology
Kenneth Marsh, Jet Propulsion Laboratory
Charley Noecker, Ball Aerospace
Eugene Serabyn, Jet Propulsion Laboratory
Velu Velusamy, Jet Propulsion Laboratory
Brent Ware, Jet Propulsion Laboratory

TPF-I Flight Baseline Design

Stefan Martin, Jet Propulsion Laboratory
Oliver P. Lay, Jet Propulsion Laboratory
Sarah Hunyadi, Jet Propulsion Laboratory

Technology Roadmap for TPF-I (Nulling Interferometry)

Peter R. Lawson, Jet Propulsion Laboratory
Robert Gappinger, Jet Propulsion Laboratory
Alexander Ksendzov, Jet Propulsion Laboratory
Oliver P. Lay, Jet Propulsion Laboratory
Stefan Martin, Jet Propulsion Laboratory
Robert Peters, Jet Propulsion Laboratory

Technology Roadmap for TPF-I (Formation Flying)

Asif Ahmed, Jet Propulsion Laboratory
Matt Wette, Jet Propulsion Laboratory
Dan Scharf, Jet Propulsion Laboratory
Behcet Acikmese, Jet Propulsion Laboratory
Eddie Benowitz , Jet Propulsion Laboratory
Chuck Bergh, Jet Propulsion Laboratory
Allan Eisenman, Jet Propulsion Laboratory
Jason Keim, Jet Propulsion Laboratory
Arin Morfopolous, Jet Propulsion Laboratory
Joel Shields, Jet Propulsion Laboratory
Guru Singh, Jet Propulsion Laboratory

Technology Roadmap for TPF-I (Future Developments)

William C. Danchi, Goddard Space Flight Center
Peter R. Lawson, Jet Propulsion Laboratory
David Leisowitz, Goddard Space Flight Center
John Monnier, University of Michigan
Stephen C. Unwin, Jet Propulsion Laboratory

Discussion and Conclusion

Charles Beichman, California Institute of Technology
Kenneth J. Johnston, U.S. Naval Observatory

Copyright Permissions

Figure 2-1 – Figure by W. A. Traub and K. W. Jucks. Reprinted, by permission of the American Geophysical Union, from *Atmospheres in the Solar System: Comparative Aeronomy* (2002).

Figure 2-2 – Figure by L. Kaltenegger *et al*. Reprinted, by permission of the American Astronomical Society, from *Astrophysical Journal* (2007), in press.

Figure 2-3 – Figure by Giovanna Tinetti (Institut d'Astrophysique de Paris) for this publication.

Figure 2-4 – Figure by L. Kaltenegger *et al*. Reprinted, by permission of the American Astronomical Society, from *Astrophysical Journal* (2007), in press.

Figure 2-5 – Figure by A. Segura *et al*. Reprinted, by permission of the publisher, from *Astrobiology* **3**, 689–708 (2003).

Figure 2-6 – Figure by L. Kaltenegger *et al*. Reprinted, by permission of the American Astronomical Society, from *Astrophysical Journal* (2007), in press.

Figure 2-8 – Figure by C. A. Beichman *et al*. Reprinted, by permission of the American Astronomical Society, from *Astrophysical Journal* **652**, 1674–1693 (2006).

Figure 2-10 – Figure by C. A. Beichman *et al*. Reprinted, by permission of the American Astronomical Society, from *Astrophysical Journal* **639**, 1166–1176 (2006).

Figure 2-11 – Figure by G. Bryden *et al*. Reprinted, by permission of the American Astronomical Society, from *Astrophysical Journal* **636**, 1098–1113 (2006).

Figure 2-12. – Figure by M. C. Wyatt *et al*. Reprinted, by permission of the American Astronomical Society, from *Astrophysical Journal* (2007), in press.

Figure 3-1 – Original figure from the article "Protostars," by Thomas Greene *American Scientist* 89 (4) 316 (2001), used by permission of the publisher.

Figure 3-3 – Original by Dejan Vinkovic (Institute for Advanced Study), used with permission.

Figure 3-3 – Original by Lucio Mayer (ETH Zürich), used by permission.

Figure 3-5 – Figure by M. J. Reid and K. M. Menten. Reprinted, by permission of the American Astronomical Society, from *Astrophysical Journal* **476**, 327–346 (1997).

Figure 3-6 – Figure by A. M. Ghez *et al*. Reprinted, by permission of the American Astronomical Society, from *Astrophysical Journal* **620**, 744–757 (2005).

Figure 3-7 – Original by Huub Röttgering (Leiden Observatory), for this publication.

Figure 3-8 – Figure by H. Röttgering et al. Reprinted by permission of the European Space Agency, from ESA SP-539, *Towards Other Earths: Darwin/TPF and the Search for Extrasolar Planets*, pp. 299–308 (2003).

Figure 3-9 – Original by Huub Röttgering (Leiden Observatory), for this publication.

Figure 3-10 – Original by Eugene Serabyn (JPL), for this publication.

Figure 4-14 – Figure by P. Haguenauer and E. Serabyn. Reprinted, by permission of the Optical Society of America, from *Applied Optics* **45**, 2749–2754 (2006).

Figure 4-16 – Figure by B. Mennesson *et al*. (2006), Jet Propulsion Laboratory

Figure 4-20 – Figure by B. F. Lane, M. W. Muterspaugh, and M. Shao. Reprinted, by permission of the American Astronomical Society, from *Astrophysical Journal* **648**, 1276–1284 (2006).

Figure 4-21 – Figure by B. F. Lane, M. W. Muterspaugh, and M. Shao. Reprinted, by permission of the American Astronomical Society, from *Astrophysical Journal* **648**, 1276–1284 (2006).

Figure 5-26 – Original by R. L. Akeson (Caltech), for this publication.